Mechanism of Action Studies of Phenotypic Whole-cell Active Antimalarial Leads Through Target Identification

Thesis presented for the degree of

DOCTOR OF PHILOSOPHY

in the Department of Chemistry

UNIVERSITY OF CAPE TOWN

CONSTANCE MAWUNYO KORKOR

SUPERVISORS

Professor Kelly Chibale and Professor Timothy John Egan

JULY 2022

Declaration

Mechanism of Action Studies of Phenotypic Whole-cell Active Antimalarial Leads Through Target Identification

I, Constance Mawunyo Korkor, hereby:

I. Grant the University of Cape Town a free license to reproduce this work, in whole or in part, for research;

II. Declare that no part of this work has been presented or is intended to be submitted at this or another university for the award of a degree;

III. Declare that the above-titled report is based on my work, both in concept and execution, with the standard guidance from my supervisors. In cases where input from others has been included, they were duly acknowledged.

I hereby present this report in fulfilment of the requirements for the degree of Doctor of Philosophy in the Department of Chemistry at the University of Cape Town.

Signature: Signed by candidate **Date:**

Dedication

To my loving husband, Jefferson Edem Attipoe, for being my source of love, strength, and support throughout this experience. Thank you for your enduring patience, understanding, and encouragement and for being my greatest cheerleader.
I am truly blessed to have you.

To my mother, Ms. Gloria Odum, for your unconditional love and support for me my entire life. Thank you for your constant prayers on my behalf and for always putting my siblings and I first. Your sacrifices have brought me this far. I love and appreciate you, and I pray the good Lord blesses you abundantly.

To the loving memory of my daddy, Mr. Felix Yao Korkor, my father in-law, Mr. William Attipoe, and my co-supervisor, Professor Timothy John Egan, all of whom passed away this year. Your love, sacrifices, and passion got me here.

You will forever be in my heart.

Acknowledgments

My Ph.D. journey has been successful due to the help and support from various individuals to whom I am indebted. Of utmost importance to this research have been my supervisors. First and foremost, I would like to express my in-depth appreciation to my supervisor Professor Kelly Chibale for funding me and providing all the needed resources for completing this work. His intellect is unmatched, and I am thankful for his invaluable contribution to this project. His exemplary mentorship created the environment for growth and the numerous opportunities for which I am grateful. My time in his group has been truly transformative. I am also highly thankful to Professor Tim Egan for his impact on this work. I have profited significantly from his broad knowledge and immense attention to detail. Professor Tim Egan can explain away every result, no matter how discouraging and unexpected, which always came in handy in this project.

I would also like to thank the administrative team, Elaine Rutherfoord-Jones, Saroja Naicker, Ayesha Banderker, Deidre van Rooyen, Deidre Brooks, and others not mentioned here for ensuring the smooth running of administrative processes that have made this thesis possible.

I also want to thank our collaborators, Professor David Fidock from Columbia University, for his team's help in generating the resistance selection result, Dr. Sergio Wittlin of the Swiss Tropical and Public Health Institute for carrying out some pharmacological assays relevant to this work, and for providing parasite pellets for use in this work and Dr. Marcus Lee for His work on cross-resistance studies using DNA barcoded mutants. Furthermore, my appreciation goes to Professor Dirk Lang, Susan Cooper, and Dr. Caron Jacobs of the University of Cape Town imaging facility for their assistance. For analytical work, I would like to thank Tariq Ganief and other members of the Blackburn laboratory, University of Cape town, for assisting with MS and proteomics analysis.

A special thanks to Dr. Godwin Dziwornu for the recommendation that made my Ph.D. candidature a reality and for his mentorship and support during my Ph.D. Also, a big thanks to Dr. Richard Amewu and Professor Dorcas Osei-Safo for their mentorship, advice, and criticism that has brought me this far.

I also want to acknowledge the contribution of Dr. Lauren Arendse, Dr. Kathryn Wicht, and Dr. John Woodland to this work. Their experience in the field has guided this project, and I have learned a lot from them.

To all the KC academic research group members and members of the ''Heme Team'' who have positively impacted my research experience, I appreciate the feedback, constructive criticism, and, above all, friendship. A special thanks to research scientists and post-docs at the Drug Discovery and Development Center (H3D) for their friendship, support, and assistance in many aspects of this work.

I am thankful to Novartis Pharma AG and the University of Basel for the opportunity to partake in the 2019 Next Generation Scientist Program. A big thanks to Ms. Akiko Keller and all members of the NGS core team for putting together an overall educative and successful program. A special thanks to my mentors, Philip Skaanderup, Romain Gambert, and others in chemical biology and therapeutics. I appreciate the knowledge they imparted and the experience of working in a world-class pharmaceutical company.

To my family and my Ghanian family in Cape Town. Thank you for the support, encouragement, and prayers during my Ph.D. May God richly bless you all.

Finally, I would like to thank H3D, Medicines for Malaria Venture (MMV), Merck, and the UCT Post-graduate Funding Office for the financial assistance throughout my Ph.D. This work would not have been possible without it.

Publications, Conferences & Training Programs

Publications

- Korkor, C. M.; Garnie, L. F.; Amod, L.; Egan, T. J.; Chibale, K. Intrinsic Fluorescence Properties of Antimalarial Pyrido[1,2-a]Benzimidazoles Facilitate Subcellular Accumulation and Mechanistic Studies in the Human Malaria Parasite *Plasmodium falciparum*. *Org. Biomol. Chem.* **2020**, *18* (42), 8668–8676.
- Dziwornu, G.; Coertzen, D.; Leshabane, M.; Korkor, C.; Cloete, C.; Njoroge, M.; Gibhard, L.; Lawrence, N.; Reader, J.; van der Watt, M.; Wittlin, S.; Birkholtz, L.-M.; Chibale, K. Antimalarial Benzimidazole Derivatives Incorporating Phenolic Mannich Base Side Chains Inhibit Microtubule and Hemozoin Formation: Structure-Activity Relationship and Oral Efficacy Studies. *J. Med. Chem. 64* (8), 5198–5215.
- Parth; Kaur, N.; Korkor, C.; Mobin, S. M.; Chibale, K.; Singh, K. Fluorene-Chloroquine Hybrids: Synthesis, in Vitro Antiplasmodial Activity, and Inhibition of Heme Detoxification Machinery of Plasmodium Falciparum. *ChemMedChem* **2022**, *17* (19).
- Singh, V.; Mambwe, D.; Korkor, C. M.; Chibale, K. Innovation Experiences from Africa-Led Drug Discovery at the Holistic Drug Discovery and Development (H3D) Centre. *ACS Med. Chem. Lett.* **2022**, *13* (8), 1221–1230.

Conferences & Training Programs

1. Norvatis Next Generation Scientist (NGS) Program. Novartis AG – Basel, Switzerland. 22 Fabriskstrasse, Chemical Biology & Therapeutics, NIBR (1ST June - 30th August 2019). Project Title: Building a Modular System of Chemically Modified dCas9 for Epigenetic Gene Regulation.
2. Keystone Symposium, G1 The Malaria Endgame. Innovation in Therapeutics, Vector Control & Public Health Tools. Addis Ababa, Ethiopia (30th October - 2nd November 2019)
3. ITRG 2290 Malaria Research Symposium. Crossing Boundaries-Wallenberg Research Center, STIAs, Stellenbosch, South Africa (30th September-1st October 2019).

4. Keystone Symposium, D2 Malaria: Confronting Challenges from Drug Discovery to Treatment. Beaver Run Conference Center, Breckenridge, Colorado, USA (10 – 13th April).

Abstract

Chemotherapy has remained the backbone of malaria control and prevention. Over the past century, potent antimalarial drugs with different mechanisms of action have been successfully developed and used to treat malaria. However, the ability of the most virulent species, *P. falciparum,* to resist these available antimalarial chemotypes and compromise their potency has raised the importance of using combination therapies and developing new, safe, and efficacious molecules with novel modes of action for the treatment of malaria.

Phenotypic whole-cell screening, followed by medicinal chemistry optimization efforts, identified the pyrido[1,2-a]benzimidazole compounds **KP68** and **KP124** and the benzimidazole compound **DM253** as efficacious antimalarial leads. However, the essential details of their mechanism of action against *P. falciparum* remain unresolved. This thesis employs 'omics-based techniques with support from fluorescence live-cell imaging, compound docking, and heme fractionation studies to generate insights into the action of these compounds against *P. falciparum*.

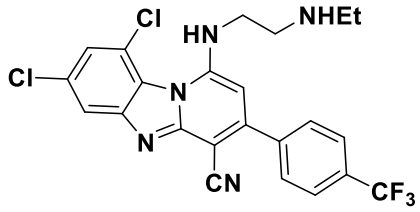

KP68

P*f*NF54 IC_{50} = 0.03 µM
P*f*K1 IC_{50} = 0.04 µM
in vivo P. berghei (p.o) 4x50 mg/kg = 98.0%
3/3 malaria infected mice cured

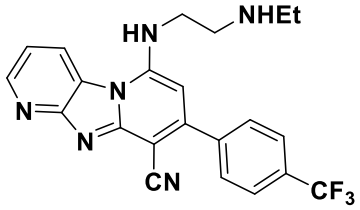

KP124

P*f*NF54 IC_{50} = 0.14 µM
P*f*K1 IC_{50} = 0.13 µM

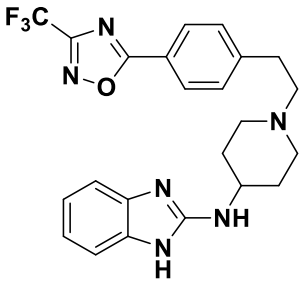

DM253

P*f*NF54 IC_{50} = 0.012 µM
P*f*K1 IC_{50} = 0.040 µm
in vivo P. berghei (p.o) 4x50 mg/kg = 99.52
Mean survival days = 14 days

The previous mechanism of action studies on these antimalarial chemotypes has focused mainly on the inhibition of hemozoin biocrystallization in the acidic digestive vacuole of the parasite. However, the intrinsic fluorescence properties of **KP68** and **KP124** were used to comprehensively study the subcellular accumulation of these compounds in an infected erythrocyte. Using the inherent fluorescence properties of these compounds is advantageous because accurate localization due to the compounds is observed with no

influence from an external fluorophore. On the other hand, **DM253** required the attachment of an external fluorophore for live-cell imaging. As such, a novel fluorescent derivative was designed and synthesized with guidance from extensive structure-activity relationship studies previously conducted in this series. 7-Nitrobenz-2-oxa-1,3-diazole (NBD) was identified as an appropriate external fluorophore and was attached to the compounds investigated. The spacer chain length between the compounds and the fluorophore was varied to find suitable fluorescent derivatives that would appropriately represent the parent compounds.

The photophysical and physicochemical properties of all fluorescent compounds were evaluated. Although the fluorescent derivatives lost antiplasmodium potency relative to their parent compounds, all but NBD-labelled **KP124** retained antiplasmodium activity in the chloroquine-sensitive strain of *P. falciparum*. Furthermore, a detergent-mediated assay indicated that all fluorescently labelled derivatives retained activity against β-hematin formation compared to the parent molecules. These results suggest that except for **KP124-NBD**, all fluorescent compounds and the fluorescent analogues were suitable for live-cell fluorescence accumulation studies.

Live-cell imaging showed selective accumulation of all fluorescent compounds within *P. falciparum*-infected red blood cells. Different accumulation patterns were observed when using the inherent fluorescence of the structurally related **KP68** and **KP124**. **KP124** was observed to colocalize in the parasite's digestive vacuole and associate with hemozoin crystals, whiles **KP68** which differs from **KP124** by the replacement of the imidazole[1,2-*a*:4,5-*b*′]dipyridine core with the benzimidazole core, as well as the presence of chloro substituents, showed no accumulation in the parasite's digestive vacuole. Quantitative colocalization studies of parasite cells co-stained with **KP124**, **DM253-NBD,** and LysoTracker Red demonstrated an excellent colocalization between these signals. This indicates a preference for these compounds in the parasite's acidic compartment. Furthermore, the quantitative analysis also revealed that none of the compounds localized in the nucleus, eliminating the nucleus as a site of action for these compounds. To mitigate the limitations of resolution, Airyscan and super-resolution structured-illumination microscopy (SR-SIM) were employed. Fluorescence imaging using the ER-Tracker Red revealed a broad colocalization between **KP124** and **DM253-NBD** and the tracker dye,

suggesting that both compounds accumulate in the endoplasmic reticulum (ER). However, no significant amounts of **KP68** were localized in the ER. The mitochondrion was, however, implicated in the action of **KP68**. Although colocalization was not observed between the MitoTracker Deep Red and **KP68**, significant amounts of the compound localize around the mitochondrion membrane. Finally, all compounds were assessed in the cellular heme fractionation assay. Results from this assay indicate that inhibition of hemozoin formation is a mechanism of action for **KP124** but not for **KP68** and **DM253**.

The recent growth in genomics and genetics has provided powerful tools for mode of action studies. *In vitro* resistance selections represent one of the genomics tools for target deconvolution of hit and lead molecules. The mechanism of resistance of the pyrido[1,2-a]benzimidazoles was investigated through resistance selection. Whole-genome sequencing of the mutant clones generated from **KP68** under drug pressure showed a single nucleotide polymorphism in the mitochondrion carrier protein. It also revealed a few copy number variations, including the deamplification of the mitochondrial-processing peptidase and the *P. falciparum* multidrug resistance transporter P*f*MDR1.This result, coupled with the significant amounts of **KP68** observed to accumulate around the parasite's mitochondrion, confirms the mitochondrion as an organelle of interest in the compound's mode of action in *P. falciparum*. Furthermore, no cross-resistance was observed between **KP68** and chloroquine, suggesting that both compounds may act through different resistance mechanisms and possibly different mechanisms of action. Similarly, no cross-resistance was observed between the mutant clones generated for **KP68** and **KP124**, meaning that the parasite's mode of resistance and the action of both compounds may be mediated through different mechanisms. This also confirms the live-cell imaging and heme fractionation assay results, which support hemozoin inhibition as a mode of action for **KP124** but not **KP68**.

Finally, chemical proteomics was employed to identify the protein binding partners of these antimalarial compounds in *P. falciparum*. Here, drug-labelled matrices were used to capture protein binding partners of **KP68** and **KP124** from *P. falciparum* cell lysates. Several protein binding partners specific to these compounds were detected from the parasite lysate prepared and identified by mass spectrometry and proteomic analysis. Out of the many proteins identified as protein binding partners for **KP68,** the high molecular

weight EMP1-trafficking protein, P*f*EMP1 is of significant interest. This is because it is essential for the parasite's survival and has been implicated in the action of other antimalarials such as dihydroartemisinin. These results suggest that these compounds may impact different parasite pathways and processes. Besides hemozoin formation, **KP124** has also been implicated in interfering with the parasite's protein synthesis.

Overall, this work has developed new tools that have aided in understanding the mechanistic details of these compounds. The observations described here, and further studies using the techniques and approaches to target deconvolution discussed here may facilitate the identification of novel targets for treating malaria. Also, once chemically validated, the protein targets identified in this work can serve as suitable starting points for target-based antimalarial drug discovery efforts.

List of Abbreviations

ART	Artesunate
ABPP	Activity-based protein profiling
ACTs	Artemisinin combination therapy
APBs	Activity-based Probes
ACTs	Artemisinin combination therapy
ADME	Adsorption, Distribution, Metabolism, Excretion, and Toxicity
AST	Astemizole
ATQ	Atovaquone
BHIA	Beta-hematin inhibition assay
BODIPY	Boron-dipyrromethene
CCCP	Compound centric chemical proteomics
CNVs	Copy number variances
Cas9	CRISPR-associated protein 9
$CDCl_3$	Chloroform (deuterated)
CRISPR	Clustered regularly interspaced short palindromic repeats
Cas9	CRISPR-associated protein 9
CQ	Chloroquine
CQS	Chloroquine-sensitive
CQR	Chloroquine-resistance
DART	Drug Affinity response target stability
DCM	Dichloromethane
DDT	Dichlorodiphenyltrichloroethane
DIPEA	N, N-diisopropylethylamine dichloromethane
DFT	Density functional theory
DHFR	Dihydrofolate reductase
DHPS	Dihydropteroate synthase
DMSO	Dimethyl sulfoxide
DMAST	Desmethylastemizole
DNA	Deoxyribonucleic acid
DNDi	Drugs for neglected diseases initiative

DV	Digestive vacuole
EDS	Energy dispersive x-ray spectroscopy
ER	Endoplasmic reticulum
ESI	Electrospray ionisation
FRET	Fluorescence resonance energy transfer
HCl	Hydrochloric acid
HDP	Heme detoxification protein
HEPES	(4-(2-hydroxyethyl)-1-piperazineethanesulfonic acid)
HPLC-MS	High-Performance Liquid Chromatography-Mass Spectrometry
HEPES	(4-(2-hydroxyethyl)-1-piperazineethanesulfonic acid)
HRP	Histidine rich protein
Hz	Hemozoin
MCP	Mitochondrial carrier protein
MOA	Mechanism of action
MoR	Mechanism of resistance
NBD	Nitrobenz-2-oxa-1,3-diazole
NMR	Nuclear magnetic resonance
PBI	Pyrido[1,2-a]benzimidazole
pLDH	Parasite lactate dehydrogenase
pRBC	Parasitized red blood cell
PYR	Pyrimethamine
RBC	Red blood cell
RIF	Rifampicin
SAR	Structure-activity relationship
SDS-PAGE	Sodium dodecyl sulphate -polyacrylamide gel electrophoresis
SNP	Single nucleotide polymorphism
SR-SIM	Super-resolution structured illumination microscopy
UV	Ultraviolet

Table of Content

Lists of Figures

Lists of Schemes

Lists of Tables

Chapter one

Introduction and Literature Review

1.1. Chapter Overview

Malaria, an infectious disease caused by *Plasmodium* parasites, remains a major cause of morbidity and mortality in the world's population that is already plagued with other disease burdens and poverty. Currently, the outbreak of the COVID-19 pandemic and restrictions related to its response has caused major disruptions in malaria relief services. Even in several high-income countries, health care systems became overwhelmed with the efforts required to stop transmission and cope with the increased number of hospitalizations caused by the pandemic. Consequently, there are global health concerns regarding the potential consequences of the pandemic on malaria treatment and eradication efforts in low- and middle-income countries. This, coupled with the emergence of resistance to all available antimalarial chemotherapies, has created an urgent need for new chemotypes with activity across multiple stages of the parasite's life cycle and novel modes of action. Benzimidazoles and pyrido[1,2-a]benzimidazoles have been identified as efficacious antimalarials. However, their mechanism (s) of action (MOAs) has remained unresolved.

This study aims to utilize innovative tools available in genomics, proteomics, and fluorescent microscopy to generate insight into the MOA of this class of antimalarials represented by pyrido[1,2-a]benzimidazoles **KP68** and **KP124** and benzimidazole **DM253** (Figure 1.1).

This chapter provides background to the global burden of malaria in the context of its epidemiology, ultrastructural physiology, and chemotherapy. The life cycle of the most virulent member of the genus, *Plasmodium falciparum*, will be discussed with a focus on the intraerythrocytic stage, where clinal symptoms are observed. During this stage of the parasite's life cycle, it digests considerable amounts of the host's hemoglobin and generates a toxic by-product, ferriprotoporphyrin. This process and challenges faced by the parasite in disposing of this by-product are relevant to this work and are discussed herein. Approaches to fuelling the malaria drug discovery pipeline with safe and

efficacious molecules and tools available to deconvolute the MOA of phenotypic whole-cell active leads will be described. The final subsections describe the design and discovery of antimalarial benzimidazole-based astemizole analogues, repositioned for malaria and pyrido[1,2-a]benzimidazole analogues, identified as phenotypic whole-cell active antimalarial leads. Finally, this chapter describes the research program and justifies study while stating the research question, aims, and specific objectives.

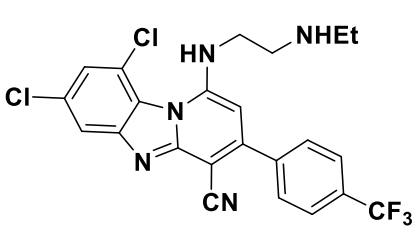

KP68

*Pf*NF54 IC_{50} = 0.03 μM
*Pf*K1 IC_{50} = 0.04 μM
in vivo P. berghei (p.o) 4x50 mg/kg = 98.0%
3/3 malaria infected mice cured

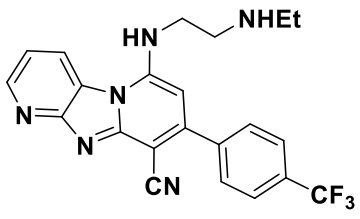

KP124

*Pf*NF54 IC_{50} = 0.14 μM
*Pf*K1 IC_{50} = 0.13 μM

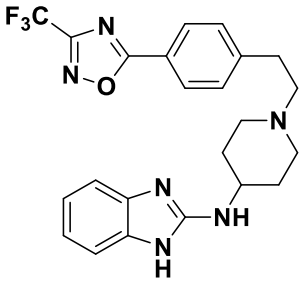

DM253

*Pf*NF54 IC_{50} = 0.012 μM
*Pf*K1 IC_{50} = 0.040 μm
in vivo P. berghei (p.o) 4x50 mg/kg = 99.52
Mean survival days = 14 days

Figure 1.1. Structures of the phenotypic whole-cell active antimalarial leads investigated in this study.[1]

1.2. Global Malaria Burden in 2021

2020 represented a milestone for several World Health Organisation (WHO) interventions aimed at reducing and eliminating the malaria scourge where possible. While there have been tremendous successes in reducing malaria cases and deaths between 2000 and 2020, the disease still accounted for 627 000 deaths in 2020 with an estimated 241 million cases, increasing from 227 million in 2019.[2,3] The WHO African region accounted for 95% of all recorded cases with pregnant women and children under five being the most affected.[3] Notably, these figures represent two decades of global progress and some challenges in the fight against malaria. By the end of 2019, the WHO reports an estimated 1.5 billion malaria cases and about 7.6 million deaths being prevented since the year 2000.[3] Although malaria is still endemic in 85 countries, it has seen a decline from 108 malaria-endemic countries since 2000.[3] Recently, China and El Salvador have reported three conservative years of zero indigenous cases and have been granted WHO certification of malaria elimination (Figure 1.2). Twenty-five more countries are on course

to end malaria transmissions, including the Islamic Republic of Iran, Malaysia, and Timor-Leste, which have also reported no local cases for the second time and are well on their way to elimination. While these are significant milestones toward global malaria eradication, progress has stalled in recent years and is compounded by the world still battling with high malaria burdens and other health concerns in the COVID-19 pandemic era. As initially suspected, the WHO confirms an estimated 14 million more cases and 47,000 more deaths in 2020 compared to 2019 due to the disruption to malaria services during the pandemic.[2,3] Also, evidence of the parasite's resistance to artemisinin-based combination therapies (ACTs) in the WHO African Region is of worrying global concern and calls for urgent and consolidated efforts in the prevention, treatment, and subsequent eradication of the disease.

Figure 1.2. Categorization of countries with local malaria cases in 2000 and their status by 2019. Adapted from the WHO malaria report, 2021[2]

1.3. The Malaria Parasite Life cycle

Five malaria species are known to cause infection in humans. These include *Plasmodium. falciparum*, *Plasmodium vivax, Plasmodium. ovale*, *Plasmodium malaria, and Plasmodium knowlesi*.[4] Of these, *Plasmodium falciparum* is the most virulent in terms of morbidity and mortality. This specie presents a complicated life cycle divided into two parts, the sexual

life cycle in the female *Anopheles* mosquito and the asexual life cycle in the human host (Figure 1.3).

In the human host, the life cycle begins with the injection of sporozoites from the mosquito's salivary gland directly into the bloodstream or the subcutaneous tissue.[5] They then enter the pre-erythrocytic stage by migrating to the liver, invading hepatocytes, and initiating a period of asymptomatic infections. Each sporozoite multiplies into tens of thousands of merozoites within one week[6], after which the merozoites are further released into the bloodstream, marking the start of the asexual cycle. This cycle is characterized by the adhesion of infected red blood cells (RBCs) to endothelium cells and reduced potential of the spleen to clear infected cells, resulting in potentially fatal clinical manifestations of malaria such as severe malaria that can result in organ failure and cerebral malaria if left untreated.[7,8] Some merozoites in the intraerythrocytic stage develop into sexual blood stage gametocytes ingested by mosquitoes during a blood meal.

In the vector's gut, gametocytes mature into male (microgametes) and female gametes (macrogametes), which later fuse to form a zygote. The zygote develops into motile ookinetes and, later, oocysts within the mosquito's mid-gut. Sporozoites are produced upon the division of the oocyst and later concentrate in the vector's salivary glands. During a blood meal, these sporozoites are inoculated into the bloodstream of the next human host.[9] In *P. ovale* and *P. vivax*, the parasites present a distinct hepatic dormant stage called hypnozoites which may carry on for weeks, months, or even years before getting reactivated to initiate the intraerythrocytic stage of infection.[10] Each point in the parasite's life cycle lends itself to be exploited as a potential drug target (s). The expectation from an ideal next-generation antimalarial is to combat relapse by targeting hypnozoites, relieve clinical symptoms by targeting the intraerythrocytic stage of the life cycle, and block transmission from person to person via the mosquito vector.

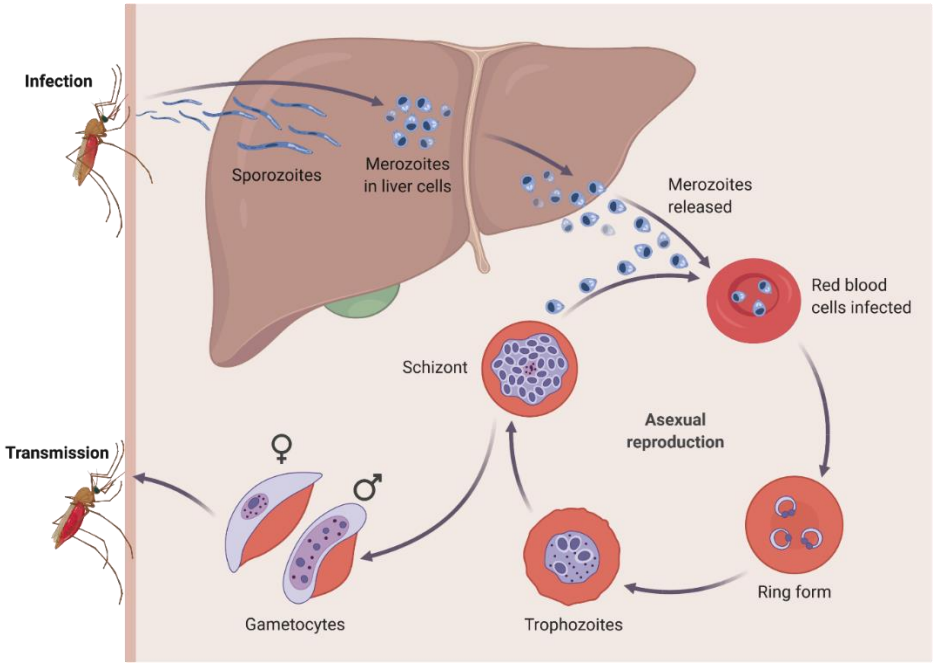

Figure 1.3. The Life cycle of *Plasmodium falciparum*.[5]

1.3.1 Asexual Erythrocytic Stage

As previously described, the intraerythrocytic stage of *P. falciparum* begins with the invasion of host RBC with merozoites released from the liver. Merozoites are ellipsoidal in structure and possess dimensional similarities to the large bacterium.[11]

Merozoites released from hepatocytes into the bloodstream re-invade the host RBCs and undergo an asexual erythrocytic cycle (Figure 1.4). The adhesion of merozoites to the surface of RBCs precedes the invasion process. The parasite then makes apical contact, moves into a deep pit formed on the surface of the RBC, and eventually gets sealed by the merozoite. Once inside the RBC, the parasite engulfs itself in a separate compartment from the erythrocytic cytosol bounded by the parasitophorous vacuole.[12] This invasion process is catalyzed by micronemes, rhoptry surface membranes, and a cluster of secretory organelles (Figure 15A). Other organelles, including ribosomes, single acrystate mitochondrion, an apicoplast, and a nucleus, are also present in the merozoites.[12]

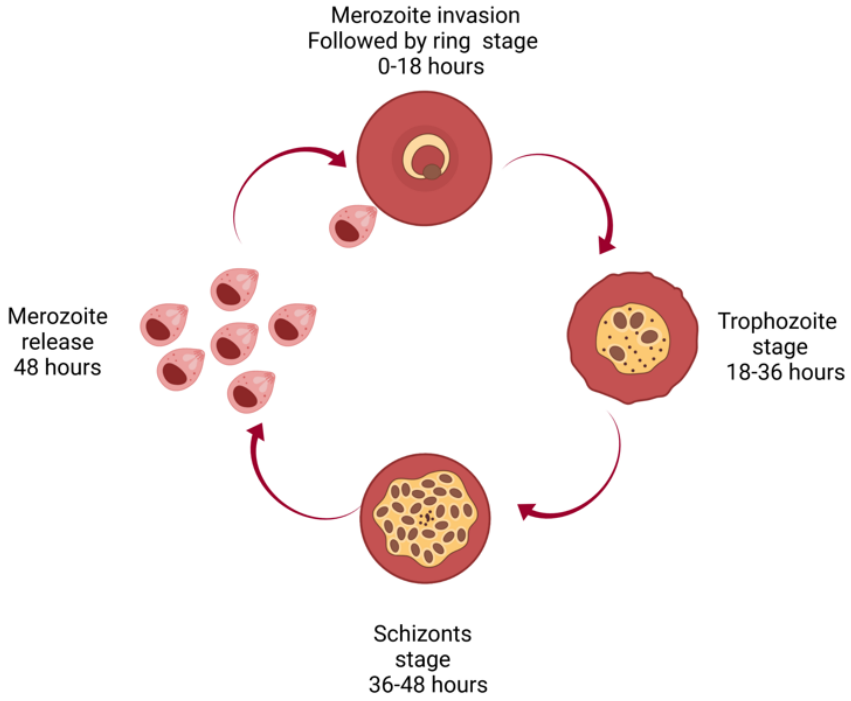

Figure 1.4. An Illustration of the major stages of the intraerythrocytic life cycle of *P. falciparum*. Merozoite invasion of the red blood cells is followed by their development into rings, trophozoites, and schizont stages. Created with BioRender.com

Following the establishment of *in vitro* continuous cultures in 1979,[13] there has been extensive research into providing a definitive ultrastructural description of the parasite through immunolabelling, serial electron tomography, and other microscopic and imaging techniques. These techniques have collectively contributed vast insights into understanding the structure of *P. falciparum*.

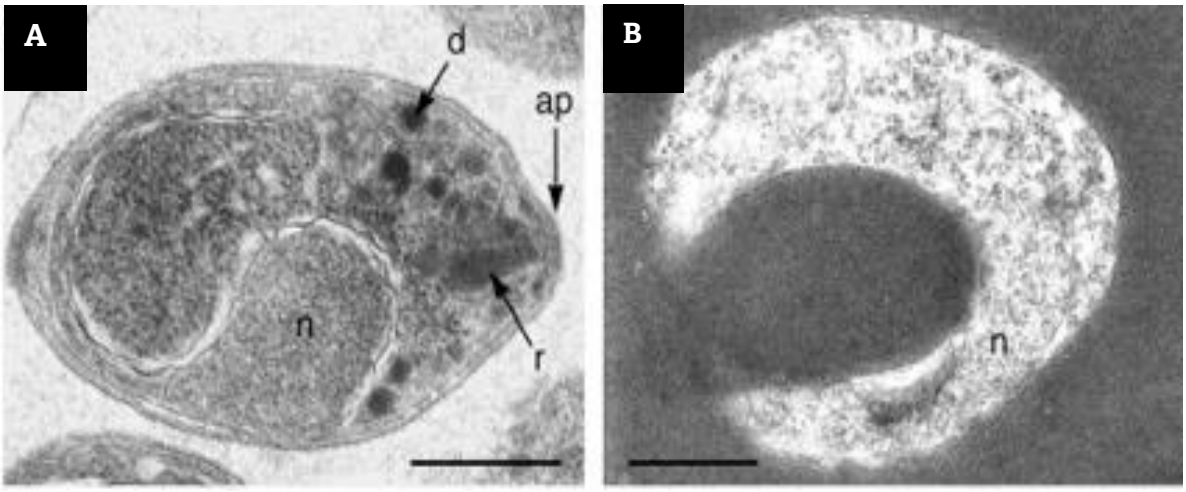

Figure 1.5. Electron micrographs of the merozoite and ring stages of the blood stage of *P. falciparum*. (A) A Merozoite showing the apical prominence (ap) with a rhoptry (r) dense granules

(d) and an indented nucleus (n). (B) A ring-stage parasite exhibiting the nucleus (n), surrounded by ribosomes and endoplasmic reticulum. Scale bars represent 0.5 μm. Reproduced from Bannister et al., Parasitol. Today, 2000, **16**, 427 with permission from Elsevier.

After the invasion, the parasite develops into a thick rim of cytoplasm, which accommodates its major organelles, such as the nucleus, plastids, mitochondrion, ribosomes, and endoplasmic reticulum (ER). The thickened perimeter of the cell and the position of the nucleus when Giemsa-stained slides of the parasite are viewed under the microscope depicts a signet ring-like structure, thereby earning this stage its name. Also, at this stage, the parasite begins to feed on its host RBC through the cytostome, which is broken off and digested later within the parasite's acidic digestive vacuole (DV).[14–17] Initially, several small DVs are observed, which fuse to form a single large vacuole as the parasite develops.[18] As the parasite grows, there is an increase in protein synthesis, characterized by the proliferation of ribosomes and ER.[11]

The trophozoite stage occurs about 18-38 hours after the invasion (Figure 1.6A). The main distinction between the ring and trophozoite stages of the parasite is in their size and shape as well as the many transcriptional and metabolic variation that occur from the ring to trophozoite stages.[19] Like the ring stage, the trophozoites feed on the host's RBC and change it by gradually transporting several parasite proteins into the cytoplasm and cell surface of the host RBC. This stage is characterized by a more enlarged and unusual Golgi body complex near the nucleus. While still attached, the mitochondrion and plastids lengthen, resulting in the overall enlargement of the surface area of the trophozoite.[11] A more developed and distinct DV is observed, characterized by the presence of hemozoin crystals, an inert by-product of the hemoglobin degradation process, which continues during this stage.[11] The process of hemoglobin degradation is further discussed in detail in the following section. By the mid-trophozoite stage, the parasite makes several alterations to the host RBC due to increased protein export across the parasitophorous membrane into the erythrocyte cytoplasm. These proteins are transported into small compartments within the parasite known as the Maurer's clefts that are created to accumulate lethal proteins en route to the host membrane.[20] On the other hand, the plasma membrane of parasitized RBCs becomes distorted by structures known as knobs.[20] These are essential in aiding the adhesion protein, *P. falciparum* erythrocyte membrane protein-1 (*Pf*EMP1), a protein required for parasite virulence. The trophozoite

stage presents an exceptional opportunity for drug discovery. This is because, the parasite becomes transcriptionally active as it matures and 80% of the parasite's genome is actively transcribed at this stage, representing several processes that can be uniquely targeted for antimalarial drug discovery.[20,21]

Finally, mature trophozoites develop into a schizont stage, characterized by mitotic nuclear division to produce approximately 16 to 32 daughter merozoites (Figure 1.6B).[11] At this stage, the parasite completely takes up the host RBC and compacts its acidic DV into a single rounded mass. Also, a merozoite forming foci forms around the parasite's circumference.[12] The proliferation of the rough ER, ribosomes, and the multiplication of the plastids and mitochondrion, also progresses. This allows a copy of each of these organelles to be inherited by a daughter merozoite when the cell divides. The merozoites are then released from the erythrocyte into the host bloodstream when the parasite plasma, parasitophorous vacuolar, and erythrocyte plasma membranes rupture.[12]

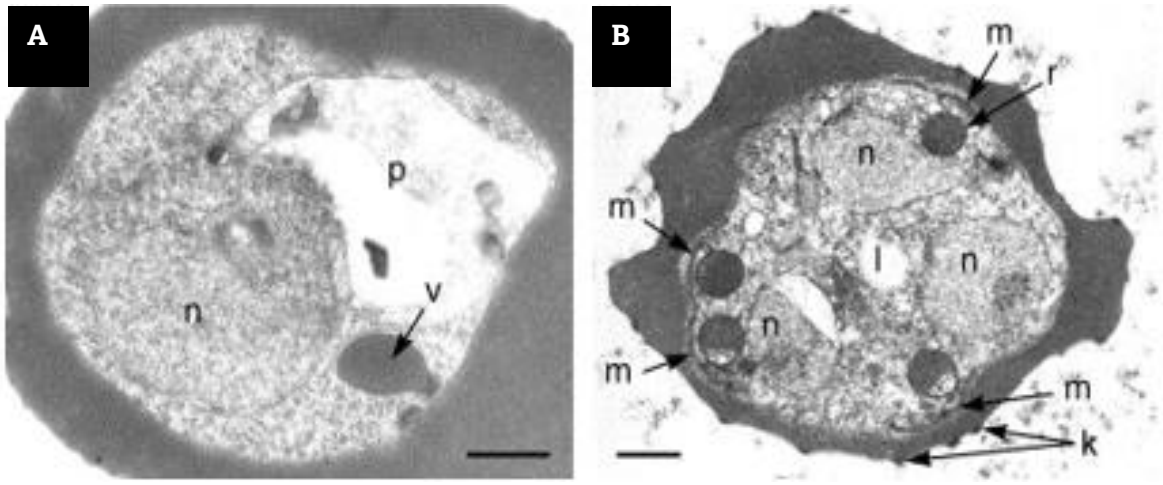

Figure 1.6. Electron micrographs of the trophozoite and schizont stages of intraerythrocytic *P. falciparum*. (A) Mid-trophozoite stage showing the nucleus (n), digestive vacuole (p), and a cytostome with a forming digestive vacuole vacuole (v). (B) A schizont showing a series of nuclei (n) and developing merozoites (m). Note the irregular appearance of the host cell surface and the presence of knobs (k). Scale bars represent 0.5 μm. Reproduced from Bannister et al., Parasitol.

1.3.1.1 The Hemoglobin Degradation Pathway

The human RBC presents a suitable accommodation for the parasite and provides ample protection from the human immune system. In addition to lacking almost any organelles, the host erythrocyte provides an immeasurable source of hemoglobin that is digested by

the parasite for nutrients and to free up physical space for its growth and division.[22,23] The parasite takes up about 65-75% of the host's RBC and only utilizes about 16% of the amino acids derived from the digestion, resulting in metabolic challenges for the parasite. The unused amino acids are released from the infected cell into the external medium.[12] This proteolytic process, in addition to providing some essential amino acids for the parasite's use, releases toxic iron (II) protoporphyrin IX (Fe(II)PPIX) or heme (Figure 1.7).[24] The absence of a functional heme oxygenase to enzymatically cleave the released heme leads to the parasite's unique metabolic challenge regarding waste disposal. Fe(II)PPIX build-up, which is toxic to the parasite's survival, is first oxidized to an equally toxic Fe(III)PPIX. To deal with this influx of vast amounts of Fe(III)PPIX, the parasite converts this toxic ''free heme'' into an inert and insoluble crystal known as hemozoin.[25]

Hemoglobin catabolism occurs in the parasite's lysosome-like compartment known as the DV. Over the years, several competing theories about the formation of the DV have emerged.[26–28] However, it is generally agreed that this process depends on the cytostomal invagination of the double membrane between the parasite's cytosol and the erythrocyte (Figure 1.7). The uptake of hemoglobin occurs when the cytostome pinches off hemoglobin-containing vesicles. Once internalized, it is transported via the parasite cytosol into the DV, where it is broken down.

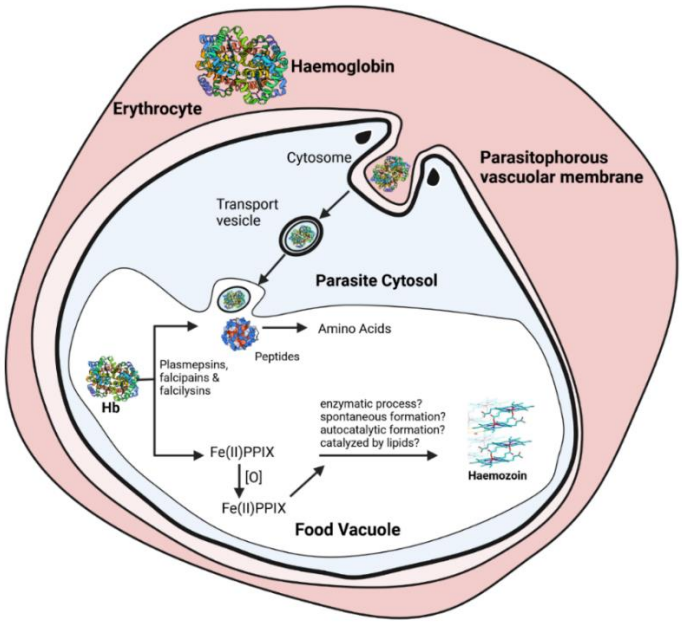

Figure 1.7. An Illustration of the process of hemoglobin (Hb) degradation within a host erythrocyte infected with *P. falciparum*. Created with BioRender.com

In the DV, two families of proteases play significant roles in the digestion of hemoglobin. Four aspartic proteases, known as plasmepsins, and three cysteine proteases called falcipains, are found in the [29,30] and are involved in the catabolism of hemoglobin. The zinc metalloprotease falcilysin, followed by the dipeptidyl aminopeptidase, digests the ingested hemoglobin into smaller peptides and dipeptides. Some of these dipeptides are transported to the cytosol and broken down into amino acids by aminopeptidases. This pathway presents a vulnerable target for malaria drug discovery. This is because it is parasite-specific, ensuring selectivity and is essential to the parasite's survival. Interfering with the parasite's ability to convert free heme to hemozoin leads to the build-up of toxic free heme and the subsequent death of the parasite. Also, inhibiting hemoglobin degradation proteases and amino peptidases will interfere with hemoglobin hydrolysis and with globin-derived peptides, leading to the parasite's death.

1.3.1.2 Hemozoin Formation and its Relevance in *P. falciparum*

Due to hemoglobin catabolism, heme is degraded through biliverdin reductase or the heme-oxygenase pathway in some eukaryotic and eubacteria organisms.[31] Malaria and several other blood-feeding organisms, including helminths[32] (*Schistosoma mansoni*) and protozoans[33] (*Haemoproteus columbae*), sequester about 85% of the (Fe(III)PPIX) produced to hemozoin in the parasite's DV. In *P. falciparum*, it is believed that the negatively charged propionate group of a hematin moiety interacts with the positively charged Fe(III) metal center of an adjacent hematin molecule through the carboxylate group. This initiates an assembly of hemozoin crystals through subsequent dimerization of hematin molecules.[34] Hemozoin does not form spontaneously under physiological conditions from either heme or hemoglobin.[35,36] Although the structure of hemozoin has been fully elucidated, the biochemistry of its formation remains unclear. Over the years, several hypotheses have been proffered to explain hemozoin crystallization. Sullivan *et al.* identified and cloned two histidine-rich proteins, HRP2 and HRP3, in purified DVs,[37] believed to precipitate hemozoin formation. However, it has been reported that *P. falciparum* clones lacking both HRP2 and HRP3 still proceed to form hemozoin crystals.[38,39] Furthermore, *P. vivax* and *P. berghei*, which equally produce hemozoin, lack

orthologs of HRP2. Finally, contrary to what was suggested by Sullivan *et al.*, only a small fraction of HRP2 is found in the DV, which serves as the site for hemozoin formation.[40] These, taken together, exclude the potential role of this protein in hemozoin formation.

Slater and Cerami later proposed an enzyme-catalyzed process of hemozoin formation when an extract of isolated *P. falciparum* trophozoite was incubated with heme in the presence of sodium acetate under acidic conditions. The authors suggested that this reaction yielded a product with hemozoin-like properties and was further confirmed with Fourier-transform infrared spectroscopy to be hemozoin.[41] However, Dorn and co-workers quickly challenged this finding, suggesting that heat treatment of trophozoite extract had minimal effect on the reaction. They proposed that hemozoin formation is an autocatalytic chemical process of heme dimerization rather than an enzymatic process.[42]

One hypothesis that has enjoyed support is hemozoin formation by lipid catalysis. Bendrat *et al.* implicated lipids in the catalysis of heme detoxification by demonstrating that an acetonitrile extract from hemozoin contained several lipids, including oleic, palmitic, and stearic acids. They also showed that these lipids promoted the formation of β-hematin,[34,43] especially when Fe(III)PPIX is introduced near the interface between the lipids and aqueous solution. Other studies have also supported the involvement of lipids in β-hematin formation.[42,44,45] Neutral lipid bodies have been shown to play significant roles in the interior and exterior of the DV regarding hemozoin formation.[46–48] Pisciotta and co-workers identified neutral lipids near hemozoin using transmission electron micrograph (TEM) images.[49] This was later confirmed by de Villiers and co-workers at neutral lipid interfaces using monomyristoylglycerol.[50] Further work using TEM and confocal images showed β-hematin formation in lipid-water emulsions, thereby providing in-depth insights into the mechanism of hemozoin crystal formation.

Later, Leiserowitz *et al.* employed grazing incidence X-ray diffraction to show that β-hematin crystals align with their 100-face parallel to the air-water interface.[51] Compared to monoacylglycerides, diacylglycerides mediate β-hematin formation faster.[52] This has been attributed to the lower activation energy of diacylglycerides compared to monoglycerides.[53] Furthermore, a density functional theory (DFT) experiment supports the role of diacylglycerides in mediating heme aggregation, a possible essential first step in crystal nucleation.[54] Finally, the size of β-hematin crystals has been shown to correlate

with the diameter of lipid droplets, with crystal length representing about 60% of the lipid droplet diameter.[55] With an Avrami constant of 4, sigmoidal kinetics of β-hematin modelled using the Avrami equation suggested that crystal nucleation is a sporadic process and crystal growth occurs in three dimensions. de Villiers and Egan compared this to biomineralization, which typically proceeds through an amorphous phase, suggesting that acetate may be a phase-transfer catalyst, a role that lipids could play *in vivo*.[56] The Avrami equation is used to describe how solids transform from one phase to another at a constant temperature and explicitly describes the kinetics of crystallization.

In 2008, a new theory was exploited by Jani *et al.* when they identified and characterized heme detoxification protein (HDP). This *Plasmodium* protein was shown to be a producer of hemozoin.[57] The authors demonstrated that this protein is highly conserved across the *Plasmodium* genus and efficiently produces hemozoin. They also showed that HDP is trafficked to the site of hemozoin formation through a peculiar route.[57] HDP is believed to be critical to the parasite's survival and could be a suitable target for antimalarial drug development. Chugh *et al.* probed this hypothesis further when they showed that HDP functions with falcipain 2 to convert hemoglobin to hemozoin.[58] However, more recently, a homologue of lipocalin, PV5, was reported to be involved in hemozoin crystallization. Disruption of this protein has been shown to affect the external morphology of hemozoin crystals.[59] The authors showed that PV5 is trafficked into the digestive vacuole and that interfering with the levels of PV5 expression in the cell could affect the parasite's sensitivity to antimalarial drugs during intraerythrocytic stage infection.[59] While the debate continues as to whether hemozoin formation is protein or lipid-mediated, it has also been reported that β-hematin can be prepared in the absence of either. Earlier work by Egan and co-workers suggested that carboxylic acids mediate the conversion of amorphous heme to β-hematin.[56]

1.4. Global Efforts in Malaria Treatment and Prevention

The milestones in reducing the malaria scourge outlined in Section 1.2 have been attributed to over two decades of unprecedented scale-up in malaria intervention strategies. At the 1992 Ministerial Conference in the Netherlands, policymakers endorsed a Global Strategy Malaria Control to guide malaria response.[60] Later, WHO member states proposed the inclusion of malaria control as an essential component of primary health

care[61], leading to the launch of the ''Accelerated Implementation of Malaria Control''.[62] These and many more policies developed over the decades have shaped the fight against malaria. In addition to sustainable policies, vector control, mass drug administration, malaria chemotherapy, and efforts into vaccine development have aided in the control and treatment of malaria.

1.4.1. Vector Control

Malaria is a vector-borne disease that can only be transmitted through a female *Anopheles* mosquito. Consequently, vector control efforts can only be achieved by preventing contact between the vector and the host. Vector control has successfully contributed to managing and eradicating malaria in some parts of the world.[63] The vector control options available include; chemical, biological, environmental management, and the use of natural plant products. The use of insecticides remains a primary tool in most vector control programmes.[64]

Indoor residual spraying (IRS) with insecticides contributes to malaria control. It has been instrumental in reducing malaria incidence rates.[65–67] Stable formulations of insecticides are sprayed to the interior sprayable surfaces of households such as walls and roofs to kill mosquitoes. To augment the efforts of IRS, insecticide-treated nets (ITNs) have been used to protect households from mosquitoes by creating a physical barrier between mosquitoes and humans. ITNs were later developed into long-lasting insecticidal nets (LLINs) to mitigate the rapid loss of efficacy of ITNs due to constant washing. The biological activity of LLINs has been shown to last as long as the net itself. It is also more effective in reducing human to mosquito contact by reducing sporozoite and parasite infection rates.

1.4.2. Chemoprophylaxis and Vaccine Development Efforts

Malaria prophylaxis can be achieved using vaccines, personal protection, and chemoprophylaxis. There have been extensive efforts directed toward vaccine development over the decades. Although there had not been any licensed products for over five decades, the WHO's recent recommended use of RTS,S/AS01 is a testament to the steady progress that has been made, specifically with regards to understanding the molecular and cellular mechanisms involved in protection, both in humans and animal models. Currently, RTS,S, formulated with an efficacious liposomal adjuvant system, AS01 is the most extensively tested vaccine for preventing *P. falciparum* malaria.[68] It has

been in development since 1987 by GlaxoSmithKline (GSK) to direct immune responses against the circumsporozoite protein (*Pf*CSP), which covers the surface of the infecting sporozoite. RTS,S/AS01 has demonstrated a 40-80% prophylactic protection in malaria-naïve individuals.[69] However, the protection observed is partial, dwindles over time, and may depend on the recipient's age. The vaccine showed reduced protection in lower infants 6-12 weeks of age than in younger children from 5 to 17 months old.[70] The WHO also identified two safety risks in a phase III trial. These included meningitis and cerebral malaria. The cause remains unknown and is anticipated to be addressed in a follow-up WHO-recommended large-scale pilot implementations phase III trial. This is to further provide an in-depth evaluation of the current doses' viability and the vaccine's potential to reduce childhood malaria deaths.[71] About five sub-Saharan African countries are participating in this pilot clinal trial by integrating RTS, S/AS01 into their national immunization programmes over five years.[71] These countries include Ghana, Kenya, and Malawi. Recently, the WHO recommended the widespread use of RTS, and S/AS01 among children in sub-Saharan Africa and other regions with moderate to high *P. falciparum* malaria transmission. This comes after results from the ongoing pilot programme in Ghana, Kenya and Malawi have reached more than 800,000 children since the trial started in 2019. This represents a monumental moment in child health, malaria control, and public health. While there are other vaccines in development, none is as potent as RTS, S.[68]

There are antimalarial drugs designed to mitigate the risk of developing malaria in people travelling to endemic regions. Since the vaccines are yet to be fully developed, and personal protection, although necessary is not enough, chemoprophylaxis remains the primary means to prevent and treat malaria. Although chemoprophylaxis can be applied to all malaria species, there is a difference between *falciparum* prophylaxis and that of the relapsing malaria species such as P. *vivax* and P. *ovale*.[72] Currently, no drugs besides primaquine are available for *P. vivax* prophylaxis, and the emergence of resistance, cost, and adverse reactions to medications complicates *P. falciparum* prophylaxis. There are two phases of malaria chemoprophylaxis, primary and terminal prophylaxis. Primary prophylaxis requires using antimalarial drugs at a recommended dose of 2-20 days before departure to malaria-endemic areas. For effective prevention, travellers are encouraged to continue taking the doses during their stay and complete it 1-4 weeks after return.[73]

Atovaquone-proguanil, mefloquine, doxycycline, primaquine, and chloroquine at their recommended doses have been successfully used for *P. falciparum* prophylaxis.[74] Terminal prophylaxis, on the other hand, requires using primaquine for two weeks after returning from an endemic zone to clear *P. vivax* and *P. ovale* hypnozoites that can cause relapse. Although no prophylactic antimalarial drug can guarantee complete protection, it significantly reduces fatal disease.[75,76]

1.5. Current Malaria Chemotherapy

Chemotherapy remains the most effective way to treat malaria and has evolved since the advent of the first antimalarial drug. Due to the complex nature of the parasite's life cycle, different developmental stages can be targeted using drugs or a combination of drugs to treat the disease. The current antimalarial chemotypes can be grouped into various classes. These include the quinolines (quinoline methanols, 4-aminoquinolines, and 8-aminoquinolines), antifolates, artemisinins, acrylaminoalcohols, antibiotics, and compounds that inhibit the cytochrome bc1 complex in the parasite's electron transport pathway.

Quinine is the first drug to be used in the treatment of malaria, with its use dating back to the 17th century. It was isolated from the bark of the cinchona tree native to South America. Quinine and other quinoline methanols, including quinidine, cinchonine, and cinchonidine, have all been effective against malaria.[77] Over the years, the malaria parasite slowly developed resistance to quinine. The first report of parasite resistance to quinine was in 1910.[78] Since then, resistance to quinine has been documented in Asia,[79] South America,[80] and least commonly in Africa.[81] Despite the challenges associated with resistance to quinine, it remains an essential antimalarial drug after almost 400 years of its first use. Currently, quinine is used in combination with doxycycline, tetracycline, or clindamycin as a second-line treatment for uncomplicated malaria.[82]

Following the emergence of resistance to quinine, an 8-aminoquinoline named pamaquine was developed by Bayer in 1925 using methylene blue as a prototype. Other derivatives, quinacrine, and acridine were also later developed.[83] As parasite resistance to quinine progressed, a new molecule called resochin was developed but later found to be too toxic for use in humans. However, during the second world war, the world's leading source of quinine was cut off by the Japanese after they took over the cinchona plantation

cultivated by Dutch colonials. Consolidated efforts from American, British and Australian scientists to develop new antimalarials renewed interest in resochin, which was later renamed chloroquine (CQ).[83,84] Since then, CQ has been clinically used to treat all forms of malaria until the emergence of resistance in the 1950s.[85,86] Parasite resistance to CQ first appeared simultaneously in Southeast Asia and South America. Later, CQ resistance spread to all malaria-endemic regions.[87] Resistance to CQ is attributed to the efflux of the drug in resistance parasites.[88] Parasite membrane transporters have been shown to traffic substrates in and out of the parasite and the host cell. *P. falciparum* chloroquine-resistance transporters (*Pf*CRT) and *P. falciparum* multidrug resistance transporter (*Pf*MDR1) have been particularly implicated in the mechanism of resistance of CQ.[89] Fidock *et al.* pioneered the identification of *Pf*CRT as the primary driver of parasite resistance to CQ when they analyzed a genetic cross between sensitive and resistant strains of *P. falciparum* clone.[90] The authors showed that *Pf*CRT is localized at the parasite's digestive vacuole membrane.[90] It is made of 424 amino acids and contains 10 transmembrane domains that can be phosphorylated.[91] At least six different geographic regions with chloroquine resistance strains have reported different polymorphisms in the *Pf*CRT gene of *P. falciparum*. All alleles are characterized by the replacement of a lysine residue with a threonine residue at position 76.[90] CQ resistance has been attributed to reduced accumulation of the drug caused by *Pf*CRT polymorphism in chloroquine resistance strains. This suggests that the gene possibly controls access of CQ to its target.[90] CQ is still used for treating *P. vivax* in areas where resistance has not developed.[92] Subsequent research identified primaquine, an aminoquinoline for prophylactic use. It is also the recommended treatment for *P. vivax* and *P. ovale* malaria.[93]

Mefloquine was developed later in the 1970s to treat chloroquine-resistant (CQR) malaria as a curative and prophylactic agent. It is structurally related to the quinoline antimalarials and interferes with the hemoglobin degradation pathway, leading to the toxic build-up of heme in the parasite.[94] In some parts of the world, where there is decreased sensitivity to quinoline antimalarials, mefloquine is combined with antibiotics tetracycline or clindamycin to increase the cure rate.[95] Parasite resistance to mefloquine was first reported in the 1986.[96]

Research into the development of efficacious antimalarial drugs during the second world war led to the discovery of antifolate antimalarial drugs. This class of antimalarials is subdivided into inhibitors of dihydropteroate synthase (DHPS) and inhibitors of dihydrofolate reductase (DHFR).[97] Proguanil, an antimalarial antifolate agent, is a prodrug that metabolizes to its triazine form known as chlorcycloguanil. Chlorcycloguanil inhibits the parasite's DHFR.[98] Chlorproguanil and clociguanil were developed after structure-activity studies of proguanil revealed that chlorination of the phenyl ring and increasing the linker between the phenyl ring and the diaminopyrimidine ring increases the activity of this class of antimalarials. The most widely used antifolates, a 2,4 diaminopyrimidine, pyrimethamine, is used in combination with other antimalarials for the treatment of malaria, and in exceptional instances, it is used in monotherapy.[99–101]

Currently, ACTs are the frontline treatment for malaria. Artemisinin was first isolated from *Artemisia annua*, a Chinese medicinal plant.[102] Although the antimalarial properties of this plant date as far back as the 1970s, it wasn't until 2000 that the WHO approved its use for the treatment of uncomplicated malaria.[103] ACTs have been credited for reducing the malaria burden over the last two decades. They are active against all multidrug-resistant forms of the parasite. The most popular semi-synthetic derivatives are artemether, artesunate, and arteether. Once in a biological system, these prodrugs metabolize to the active dihydroartemisinin.[104] The MOA of artemisinin and its derivatives have been closely linked to their endoperoxide groups. As a result of hemoglobin degradation in the parasite, ferrous ions catalyze the cleavage of the peroxy groups to form carbon-free radicals.[95] These free radicals inhibit the cysteine proteases in the parasite's DV.[95] Over the years, there has been evidence of other possible MOA (s). This includes a computational study that identified *P. falciparum* Ca(2+)-ATPase (*Pf*ATP6) as a plausible target of the artemisinins.[105] Another study identified artemisinin as a potent inhibitor of *P. falciparum* phosphatidylinositol-3-kinase (*Pf*P13K).[106] Artemisinins are best known for acting rapidly and clearing blood parasites below detection. Therefore, artemisinins are combined with slower-acting antimalarials drugs like lumefantrine, sulfadoxine-pyrimethamine, mefloquine, amodiaquine, and piperaquine to delay parasite resistance to the drug and achieve high efficacy. These combination partners are recommended to have a different MOA from artemisinin and a slower *in vivo* elimination to aid in clearing any latent parasites that were not cleared by the fast-acting artemisinin.[107,108–110]

Unfortunately, evidence of parasite resistance to artemisinin-based chemotypes has emerged in Southeast Asian countries like Cambodia, Thailand, Vietnam[111] and some parts of Africa.[112]

While malaria chemotherapy has continued to play a major part in curbing the disease, it has been plagued with the threat of parasite resistance to all existing antimalarial chemotypes.[113] Also, most antimalarial drugs currently in use only act mainly at the intraerythrocytic stage of the parasite's life cycle to alleviate the clinical symptoms of the disease. However, drugs capable of targeting multiple stages of the parasite's life cycle with novel MOA (s) are needed if the ambitious goal of malaria eradication is to be achieved.[114] Furthermore, some antimalarials, both in clinal use and development, have life-threatening limitations that urgently require the search for better alternatives. For example, amodiaquine has been associated with agranulocytosis and hepatotoxicity, resulting from the drug's metabolism to its quinone imine and reactive aldehyde metabolites.[115–117] Primaquine, currently the only clinical agent used for treating the hepatic forms of *P. vivax*, has been shown to cause fatal hemolysis among patients deficient in glucose-6-phosphate (G6PD), an enzyme involved in regulating cellular oxidative stress.[118] Consequently, new product development partnerships (PDPs) have fuelled the drug discovery pipeline with new antimalarial chemotypes. PDPs such as the Medicines for Malaria Venture (MMV) and the Drugs for Neglected Diseases initiative (DNDi), with financial support from organizations like the Bill and Melinda Gates Foundation and governmental and non-governmental organizations, have led to the development of several new chemical entities in various stages of development.

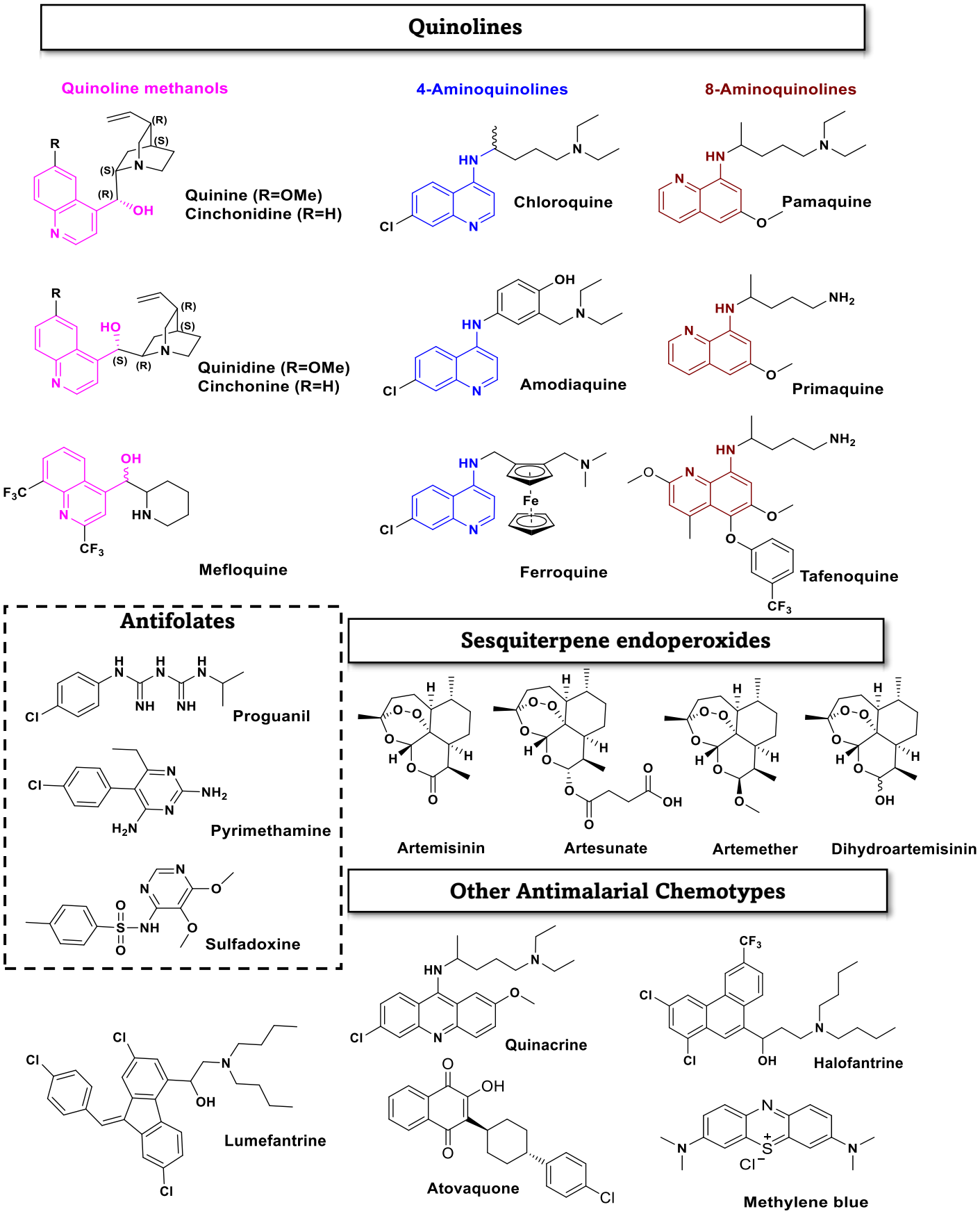

Figure 1.8. Chemical structures of some past and current antimalarial drugs.

1.6 Approaches to Antimalarial Drug Discovery

Many strategies are employed to identify novel chemical entities for antimalarial drug discovery. Notable among them are phenotypic whole-cell and target-based screening approaches to drug discovery. This section will discuss these approaches of relevance to this work and their contributions to discovering new molecule entities for treating malaria.

1.6.1 Target-Based Drug Discovery Approaches

Target-based drug discovery (TBDD) is a commonly used approach toward hit identification. This approach fundamentally involves screening compound libraries against a protein target, after which the hit compounds are optimized against the enzyme for selectivity over any human orthologue, pharmacokinetic parameters, and cellular potency.[119] Targets are primarily proteins with essential functions in the cell for which their inhibition results in cell death. In general, there are four levels of target validation. These include genetic, phenotypic, *in vivo*, and, most importantly, clinical validation. Genetic validation is usually determined by genetic knockdown experiments to assess the effect of the absence of that gene function or a reduction in its expression on the growth of the cell in a culture or a host. The second level of target validation, chemical validation, is determined by chemical inhibition studies demonstrating a chemical compound's potential to inhibit the target and induce the desired phenotypic response (cell death).[119,120] *In vivo* validation or *in vivo* proof of concept demonstrates the ability of a compound to induce the expected pharmacodynamic effect in an animal model. For malaria drug discovery, this is measured by a compound's ability to reduce parasitemia over a given period. Finally, the fourth level of target validation is clinical validation, where a compound is successfully used against the target in patients.[120] Following the identification of a valid target, a biochemical assay is developed using the recombinant protein produced to identify chemical compounds that inhibit the function of the target. The availability of a crystal structure for the protein of interest further enhances the process and aids in guiding the design of potential chemical inhibitors. More importantly, the availability of a crystal structure helps in designing specific and selective inhibitors against the parasite proteins as opposed to the host proteins.

The target-based approach to drug discovery has been used in malaria drug discovery after identifying validated targets. *P. falciparum* DHFR and cytochrome bc1 are clinically

validated protein targets inhibited by the antifolates (pyrimethamine and proguanil) and atovaquone, respectively.[121,122] Inhibiting *Pf*DHFR inhibits folate synthesis, which is essential to replicating the parasite's deoxyribonucleic acid (DNA). Targeting this protein successfully in previous studies has led to the development of an *in-silico* method which ultimately led to the discovery of a potent inhibitor of mutant DHFR, **P218**. Currently, **P218** has completed a Phase I clinical trial with promising results.[123]Also, the parasite's dihydroorotate dehydrogenase (DHODH), a mitochondrial enzyme, was explored as a possible antimalarial target. This is because it catalyzes the fourth step in the *de novo* pyrimidine biosynthesis pathway, which is essential to the parasite's survival.[124] Earlier, high-throughput screening efforts identified several possible inhibitors of DHODH. However, their enzymatic activities did not directly translate into activity in cell proliferation assays.[125] This is one of the major drawbacks of the target-based approach. Later, the triazolopyrimidines, a new class of compounds from the original screens, were identified through phenotypic whole-cell assays with sub-nanomolar activity against both the chloroquine-sensitive (CQS) strain and multidrug-resistant strains of *P. falciparum*. It also had a greater than 5000-fold selectivity for the parasite's DHODH over the host's DHODH.[126] Although this class of compounds was not initially potent in the *in vivo P. berghei* model, a series of chemical modifications and further binding optimizations using a drug-enzyme co-crystal structure delivered a potent lead, **DSM265**.[126,127] The compound was active against both drug-sensitive and resistant strains of the parasite and showed comparable activities with chloroquine in the humanized SCID mouse model.[128]

1.6.2 Phenotypic-based Drug Discovery

Phenotypic-based drug discovery (PBDD) is one of the most successful approaches in delivering first-in-class medicines in various disease areas and is the most relevant to this work. In response to the presumed ''failure'' of TBDD in delivering new molecule entities, PBDD presents a more holistic approach to screening target compounds to determine whether or not they induce any phenotypic response in the whole cell of interest.[129] In PBDD, the microorganism under study (in this case, a culture of the *Plasmodium* parasite) is exposed to the test compound, and incubated for a short period.[129] The ability of the compound to induce the appropriate phenotypic response (killing the parasite) is then assessed. Due to technological advancements over the past few decades, the search for

new drug candidates has been accelerated. High throughput screening (HTS) capabilities of very large compound libraries have been facilitated by advances in liquid handling technologies, automated robotics systems, and the ease with which whole-cell assays are performed.[130]

While drug discovery campaigns have relied on both target-based and phenotypic-based methods of HTS, phenotypic screens have the advantage of naturally eliminating all non-membrane permeable drugs and drugs with efflux issues.[130,131] It also provides an opportunity to identify compounds acting synergistically or acting on multiple targets. Furthermore, it is a worthwhile approach to discovering drugs to treat many rare and understudied diseases.[131] Finally, phenotypic screens do not require previous knowledge of the drug candidate's molecular targets and MOA, thereby increasing the biological space where the probability of identifying first-in-class molecules with potentially new targets and novel MOA is high.[129,132]

Ultra-HTS efforts involving million compound libraries have previously targeted the F (ABS) of the parasite's life cycle more than any other stage. This is because, the ABS of *P. falciparum* life cycle is easily maintained, in *in vitro* erythrocytic cultures that are compatible with automated liquid handling technologies.[13] Therefore, it was no surprise that the first ultra-HTS exploring the antimalarial activities of compound libraries was performed against the ABS of the parasite.[133] This screen exploited the absence of nuclei in erythrocytes by using a nucleic acid intercalating dye to stain the parasite's DNA. Fluorescent signals detected are then attributed to parasite growth. Several other high-throughput screens have employed similar nucleic acid staining techniques to identify antimalarial hits for subsequent progression.[134–136] These HTS phenotypic screens identified several compounds that were later evaluated and optimized from hits to leads. Some compounds obtained from these screens subsequently progressed to clinical trials.

Cipargamin, the spiroindolone compound was shown to inhibit the P-type cation transporter, ATPase4, was identified as a potent and fast-acting antimalarial agent with median parasite clearance half-life of 0.9 hours.[137,138] To put this in context, only about 1% of patients treated with an oral dose of artesunate for *P. falciparum* malaria showed a parasite clearance half-life of less than an hour.[138] **Cipargamin** is currently in phase II clinical trials.[138]

Although initial phenotypic HTS efforts were previously only aimed at the ABS of the parasite's life cycle, there has been an increase in the development of assays that are compatible with compound activity against other stages of the life cycle with the same throughput as the blood stage screens.[139] A major breakthrough was achieved in studying liver-stage parasites, with the ability to set up and maintain *in vitro Plasmodium* sporozoite infections in hepatic cells.[140,141] Consequently, the first *in vitro* liver-stage phenotypic screen was performed employing antibody staining of the malaria parasite in hepatic cells in conjunction with high content imaging[142] or infrared imaging.[143] High content imaging of antibody-treated parasite-infected hepatic cells was employed to screen over 4000 compounds made of previous positives from an ultra-high throughput ABS screen. This phenotypic screen identified the imidazolopiperazine chemical series, from which further lead optimization efforts led to the development of **KAF156** with good potency against the blood-stage parasite. This compound is currently in clinical trials.[144,145] Although resistance to **KAF156** is mediated by mutations in the *P. falciparum* cyclic amine resistance locus (*Pf*CARL), its MOA remains elusive.[146] Targeting the liver stages of the parasite's life cycle facilitates the discovery of prophylactic drugs.

Furthermore, methods for assessing compound activity against the sexual stage gametocytes have been developed using the metabolic indicators,[147–149] genetically engineered parasite lines with specific reporters for gametocytes,[147,150] and the detection of stage-specific markers using antibodies.[151] Plouffe and co-workers developed an example of this assay.[152] Here, the sexual blood stage gametocytes were treated with a fluorescent dye capable of only illuminating the mitochondrion with an active membrane potential. This indicates cell viability.[152] The emanating fluorescent signal is then measured by high content imaging and correlated to viable gametes.[152] Several other assays have been developed over the years.[153] However, the standard membrane feeding assay (SMFA) remains a useful method for validating the ability of compounds identified from gametocytocidal or gametocidal screens to block transmission.[154] In this assay, the compound under study is incubated with mature stage V gametocytes for about 24 hours, after which they are fed to the *Anopheles* spp. mosquitoes through an artificial membrane. Subsequently, the parasite's midgut is dissected, and parasite infection in the mosquito is assessed by counting the number of oocysts with a light microscope.[154] This is done about

a week after the blood meal. Although there are no current HTP methods for SMFA, there are promising developments in that area.[154]

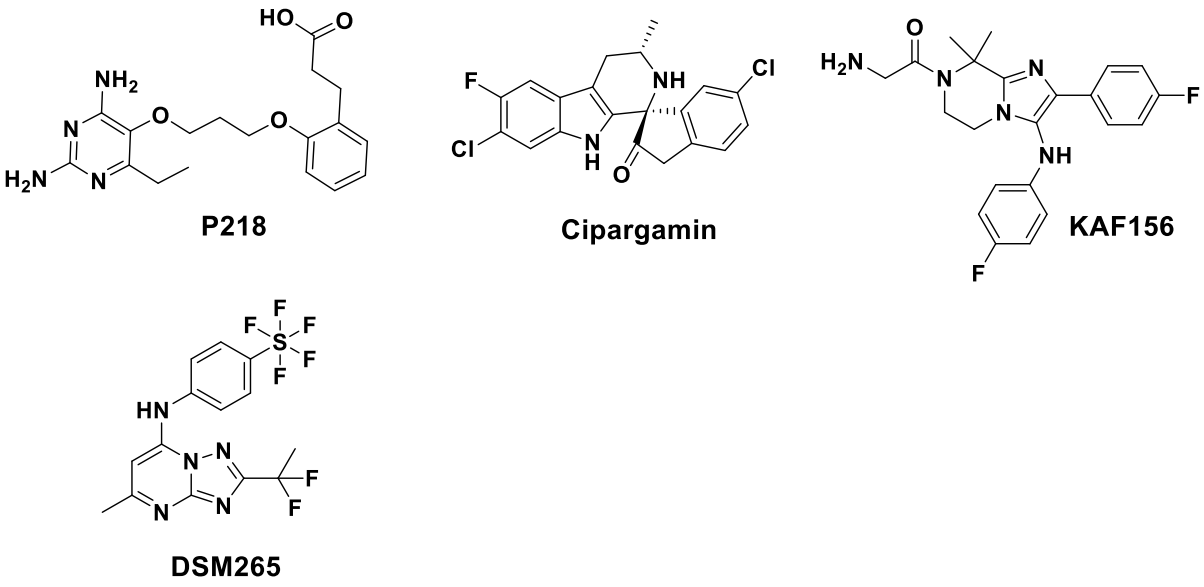

Figure 1.9. Chemical structures of some new antimalarial candidates obtained through phenotypic and target-based approaches to drug discovery.

1.7. Target Deconvolution After Phenotypic Screening

While effective in the discovering new drug candidates, phenotypic whole-cell screening is burdened with the daunting and time-consuming task of target deconvolution of hits to leads. There are several advantages to identifying the molecular target of a drug candidate. Knowledge of the biological target (s) is enormously helpful in understanding the molecular etiology of the disease and aids in the performance of efficient chemical optimization of lead drug candidates guided by SAR studies. It also helps in the identification of any potential toxicity issues or undesirable side effects.[155] Failure to identify the molecular target (s) keeps the potential for target-based optimizations untapped and may leave a drug discovery effort stranded with no suitable starting points.[156] For these reasons, major efforts have been directed at developing new technologies in the omics-based approaches including proteomics and genomics,[157,158] in combination with other techniques such as fluorescence localization[159] and heme fractionation studies[159] to identify and validate relevant target (s) of phenotypically active leads and understand their MOA (s).

1.7.1. Proteomics Approaches

Various techniques have been developed over the years to discover protein targets relevant to drug discovery. The first and oldest proteomic approach was to label the target proteins with radioactive isotopes in cultured cells. This was followed by purifying these proteins from the cell lysates using two-dimensional gel electrophoresis (2D GE).[160] The radiolabelled proteins are then located and subsequently identified by mass spectrometry (MS).[160] Further development of chemical proteomics techniques has identified affinity chromatography as a means to "pull down" target proteins from cell lysates. This technique depends on the design of affinity probes with the small molecule of interest on one end and a crosslinking probe or bead on the other end. The functional groups on the small molecule present a way to "trap" target proteins while the crosslinker functions as a solid phase for target purification. Purified proteins are then identified by MS.[161] The development of affinity matrix-based techniques led to the discovery of a more direct binding method for small molecules to their target termed drug affinity responsive target stability (DARTS). This method developed by (Lomenick et al. 2009; Lomenick et al. 2011)[162] analyzes the direct binding of a small molecule of interest to its target protein without needing modification or immobilization of the molecule.[162]

1.7.1.1. Two-dimensional Gel Electrophoresis and Mass Spectrometry

Traditional two-dimensional (2D) gel electrophoresis, performed as a combination of sodium dodecyl sulphate polyacrylamide gel electrophoresis (SDS-PAGE) and isoelectric focusing, has been the only available method for analyzing the proteome of organisms for decades.[163,164] The use of this proteomics-based technique has helped to separate thousands of proteins that are expressed in a cell or tissue. It has been used frequently to separate complex protein mixtures such as cell lysates.[165] This is the most commonly used proteomic technique in which protein spots obtained from stained gels are cut out by hand and subjected to proteolytic digestion to break down complex proteins into peptides.[165] MS data from the peptide mixtures helps to identify these proteins. 2D gel electrophoresis has been used extensively for the selective analysis of the proteome of the *Plasmodium* parasite. Rabilloud *et al.* used 2D gel electrophoresis to analyze and compare the proteomes of *P. falciparum*-infected and uninfected red blood cells[166] to

identify essential membrane proteins that function to acquire nutrients, contribute to cytoadherence and immune evasion, and could serve as potential drug targets[167,168]

To compare the protein expression patterns of *P. falciparum* extracellular and intracellular proteins from both CQS (MRC2) and CQR (RKL9) strains based on differences in their protein expressions, Hiasindh *et al.* utilized 2D gel electrophoresis separation methods.[169] Furthermore, 2D gel electrophoresis in conjunction with MS revealed the downregulated levels of ribosomal proteins after treating *P. falciparum* with an isocryptolepine-derived antimalarial compound.[170] This contributed to the understanding of the compound's MOA. While 2D gel electrophoresis has been successful in protein identification and contributed significantly to understanding the MOA (s) of small molecules, this technique has major limitations. These limitations include the poor resolution of low abundance proteins, proteins with large molecular masses, and those with large numbers of transmembrane domains. The technique is also complex, labour-intensive, and very limited in quantifying proteins.[171] Further, 2D electrophoretic techniques assume that only one protein is present in each spot. However, the comigration of proteins has disproved such assumptions.[172] In light of these drawbacks, alternative proteomics methods are required for large-scale protein expression analysis.

1.7.1.2. Chemical Proteomics

Chemical proteomics, also referred to as functional proteomics, is a combinatory HTP proteomics approach that relies on MS, synthetic organic chemistry, and cell biology to identify proteins bound to small molecule entities in screening assays. These assays are designed to probe biological pathways and identify potential drug targets.[173,174] Chemical proteomics has experienced rapid growth in the field and has provided valuable techniques for target identification and discovering novel inhibitors for human diseases. Over the past decade, chemoproteomics approaches have gained much attention in the mechanistic deconvolution of hits/leads and for the HTP identification and analysis of expressed proteins from cells.[173] The primary goal of this field of proteomics is to understand the function, structure, cellular localization, expression, interacting partners, and the regulation of proteins produced from a complete genome.[173] Fluorescently labelled chemical probes (Figure 1,10), or those attached to solid-support matrices such as agarose beads, are used to bind proteins from either whole cells or fractionated lysates.

This allows libraries of small molecule entities to be screened for specific binding and selectivity against entire proteomes.[173]

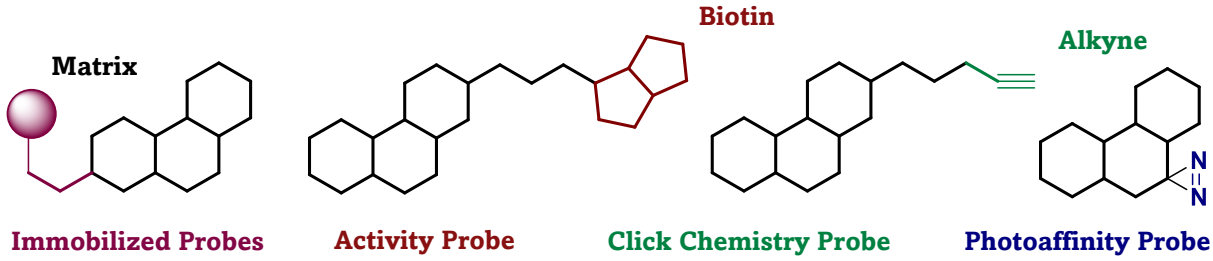

Figure 1.10. General chemical structures of different types of chemical probes designed for proteomics.

1.7.1.2.1. Classification of Chemical Proteomics Techniques

Chemical proteomics techniques are classified into activity-based protein profiling (ABPP) and compound-centric chemical proteomics (CCCP) approaches. (Figure 1.12) ABPP studies enzyme activities whiles CCCP contributes to the direct elucidation of interactions between small molecule entities and their molecular targets.[175,176] Activity-based probes (ABPs) employed in ABPP usually consist of three essential elements: a tag, a linker, and a warhead. (Figure 1.11) The tag serves as a means of identifying and purifying the enzymes. At the same time, the warhead is made of reactive functional groups that covalently interact with the active site of an enzyme.[177] A linker is required to connect the tag and the warhead to provide selectivity in binding interactions and prevents steric overcrowding or off-target interactions. The warhead is integral to an ABP and should be reactive enough to modify latent nucleophiles.

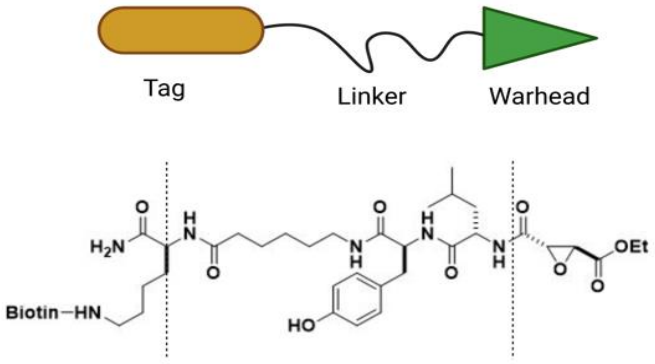

Figure 1.11. Example of an activity-based probe showing its warhead, linker, and warhead. Created with BioRender.com

Most ABPs employ electrophilic groups that are mainly obtained from enzyme inhibitors. These groups can form covalent bonds with nucleophiles in the enzyme's active site.[177] The tag presents an opportunity to visualize and purify proteins.[177] Many tagging methods are available to suit a specific need. These include using small organic fluorophores such as rhodamine and fluorescein to illuminate labelled targets.[178] Affinity tags also provide another means of enriching and isolating targets obtained from ABPs. Commonly used affinity probes include biotin, which takes advantage of its strong affinity for avidin or streptavidin to aid in purification.[178,179] Affinity tags are limited by certain drawbacks. Their bulky nature sometimes limits their uptake by proteins. They also poorly permeate the cells *in vivo*, disrupting their distribution in tissues and cells. Consequently, this limits their application to the analysis of crude protein extracts.[180]

In contrast to ABPP, CCCP is an affinity chromatography-based chemical proteomics technique based on the affinity binding of small molecule entities. The compound of interest is first immobilized on a solid support through key synthetic intermediates of relevance to the molecule being studied. This affinity matrix is then incubated with cell lysates to pull down the proteins interacting with the molecule of interest. Subsequently, the target proteins are purified, visualized by staining agents, and identified through MS methods (Figure 1.12).[176] CCCP methods have been successful in large-scale identification of protein-drug interactions. However, on the downside, this technique requires large amounts of cell materials from which a lysate is prepared. All target proteins in the prepared lysate are required to be soluble for their effective interaction with the molecule of study. Also, additional synthetic steps are required to introduce functional groups necessary for immobilization to the affinity matrix.[176] More importantly, CCCP presents the challenge of nonspecific binding of highly abundant proteins to the molecule of interest and binding to the affinity matrix.[176] To counteract these issues, negative affinity experiments are conducted in parallel using inactive analogues of the small molecule of interest as a control. The proteins captured using active and inactive drug analogues are compared to differentiate between specific interactions and background contamination.[181,182] Optimization of the affinity linker,[183–185] competition binding

techniques, and the application of serial affinity chromatography methods[186] are other approaches employed to mitigate the risk of background protein contaminations.[187,188]

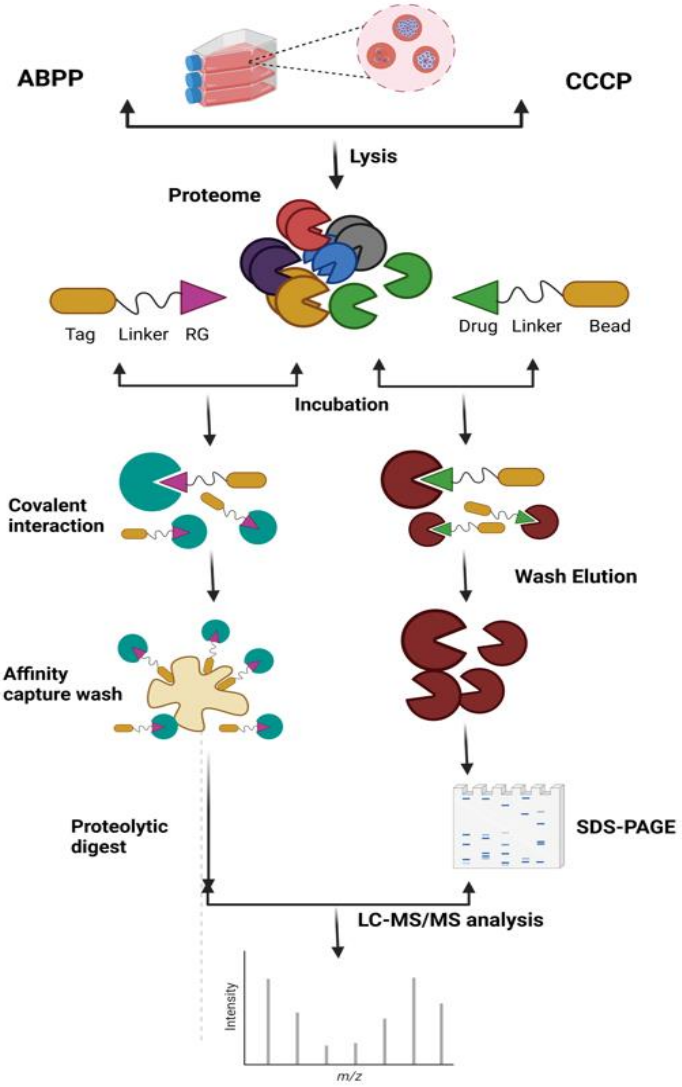

Figure 1.12. Comparison between activity-based protein profiling (ABPP) and compound-centric chemical proteomics (CCCP) proteomics techniques. Created with BioRender.com

1.7.1.2.2. Applications of Chemical Proteomics in Target Identification

In antimalarial drug discovery, chemical proteomics approaches have been utilized for over a decade. Both CCCP and ABPP techniques provide comprehensive and impartial analyses of the proteome of organisms including that of *P. falciparum*. Synthetic organic chemistry strategies are essential to designing suitable chemoproteomics probes to enhance target deconvolution and validation. For example, Greenbaum and co-workers employed chemical proteomics to identify and analyze the activity of all cysteine

proteases in *P. falciparum* extracts.[189] Cysteine proteases are essential for parasite survival and serve many functions. This makes them attractive drug targets in antimalarial drug discovery.[190] The authors, in a separate study, screened *Plasmodium* proteins bound to chemical probes designed to imitate cysteine protease inhibitors.[191] These electrophilic probes were designed to covalently bind to their target after which the affinity labelled proteins are separated by SDS-PAGE. This is followed by in-gel tryptic digestion and MS identification (Figure 1.12).[191] This study identified several cysteine proteases, including falcipain-1, which was found to be active in the invasive merozoite stage of the parasite's life cycle. Also, when falcipain-1 was selectively inhibited, parasite invasion of red blood cells was blocked, validating this protein as a drug target.[191]

Penarete-Vargas and colleagues employed click chemistry to design a photoreactive bifunctional probe for the proteomic investigation of albitiazolium. (Figure 1.13) Albitiazolium is a clinical antimalarial agent obtained from a series of choline analogues, synthesized to target and inhibit the *Plasmodium* phospholipid metabolism.[192] Potential drug target (s) of albitiazolium in *P. falciparum* were identified via MS and their functions were further analyzed using bioinformatic techniques.[192] CCCP approaches, assisted by *in vitro* evolution and whole-genome sequencing, were employed to identify *P. falciparum* phosphatidylinositol-4-kinase (*Pf*PI4K) as the target of clinical candidate MMV390048, a 2-aminopyridine. (Figure 1.12) This compound is an effective antimalarial agent with activity across all stages of the *Plasmodium* life cycle except the hypnozoite stage.[193]

Furthermore, Wang *et al.* employed alkyne-tagged artemisinin analogues combined with fluorescent probes to observe protein binding. Biotin was used for protein purification and identification (Figure 1.13). Through this approach, the authors identified 124 covalent binding partners of artemisinin, of which 33 had been previously implicated as antimalarial drug targets.[194] In a follow-up study, Ismail *et al.* designed probes with retained biological activities to alkylate the molecular targets of artemisinin in *P. falciparum* 3D7 parasites.[195] The alkylated target proteins identified are essential in hemoglobin degradation, protein synthesis pathways, glycolytic, and antioxidant defence, suggesting that artemisinin interacts with multiple metabolic pathways.[195,196]

More recently, Yoo and co-workers designed an affinity-based probe of the antimalarial natural product Salinipostin A, as a tool to study the proteome of the *Plasmodium* parasite

and identify the compound's molecular target. The authors attached an alkyne group to the terminus of the compound hence allowing for the affinity isolation of the covalently modified protein, using biotin as a tag. Using this approach, the authors identified α/ß Serine hydrolases as the protein target (s) of Salinipostin A. These proteins are essential in lipid metabolism in *P. falciparum* parasites.[197]

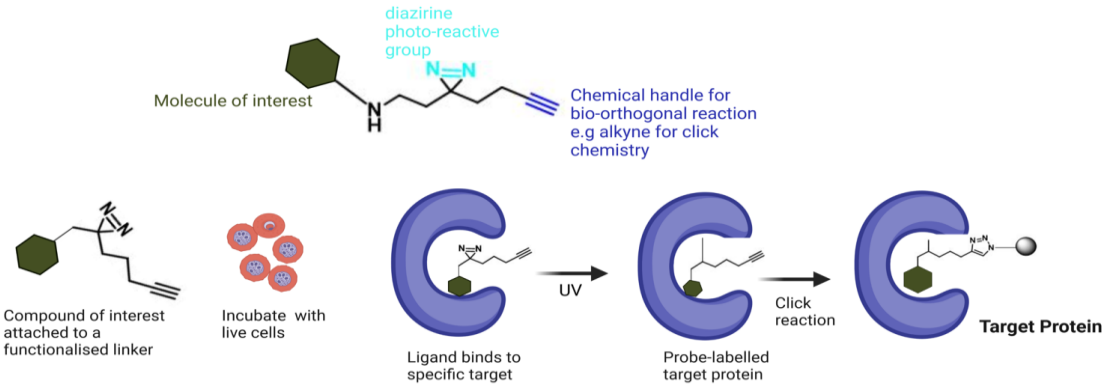

Figure 1.13. Chemical proteomics technique employing alkyne tagged drug lead for protein target identification. Created with BioRender.com

1.7.1.2.3. Label-free Chemical Proteomics Techniques

New proteomics techniques, tailored to target identification without reliance on the chemical derivatization of the drug molecule of interest, have been developed. These techniques, such as drug affinity responsive target stability (DARTS), thermal proteome profiling (TPP), cellular thermal shift assays (CETSA), and bioinformatics-based analysis, are employed to circumvent the need to derivatize small molecules.[198] (Figure 1.14)

DARTS is a simple yet universally adaptable approach to target the identification of small molecules. It analyses a compound's direct binding to targets. Since drug-bound proteins might be less liable to proteolysis than drug-free proteins,[199,200] DARTS uses this stability to identify protein targets without needing modification or immobilization of the molecule of interest.[200] Using affinity precipitation and DARTS, Sun *et al.* identified the targets for Torin 2 in *P. falciparum*. Torin 2 was identified as a lead compound with activity in the low nanomolar ranges against the gametocyte stages of *P. falciparum*. Phosphoribosyl pyrophosphate synthetase transporter and aspartate carbamoyl transferase were identified as proteins of interest in the action of Torin 2. (Figure 1.14A) This validates DARTS as a label-free, chemical proteomics technique in malaria drug discovery.[201]

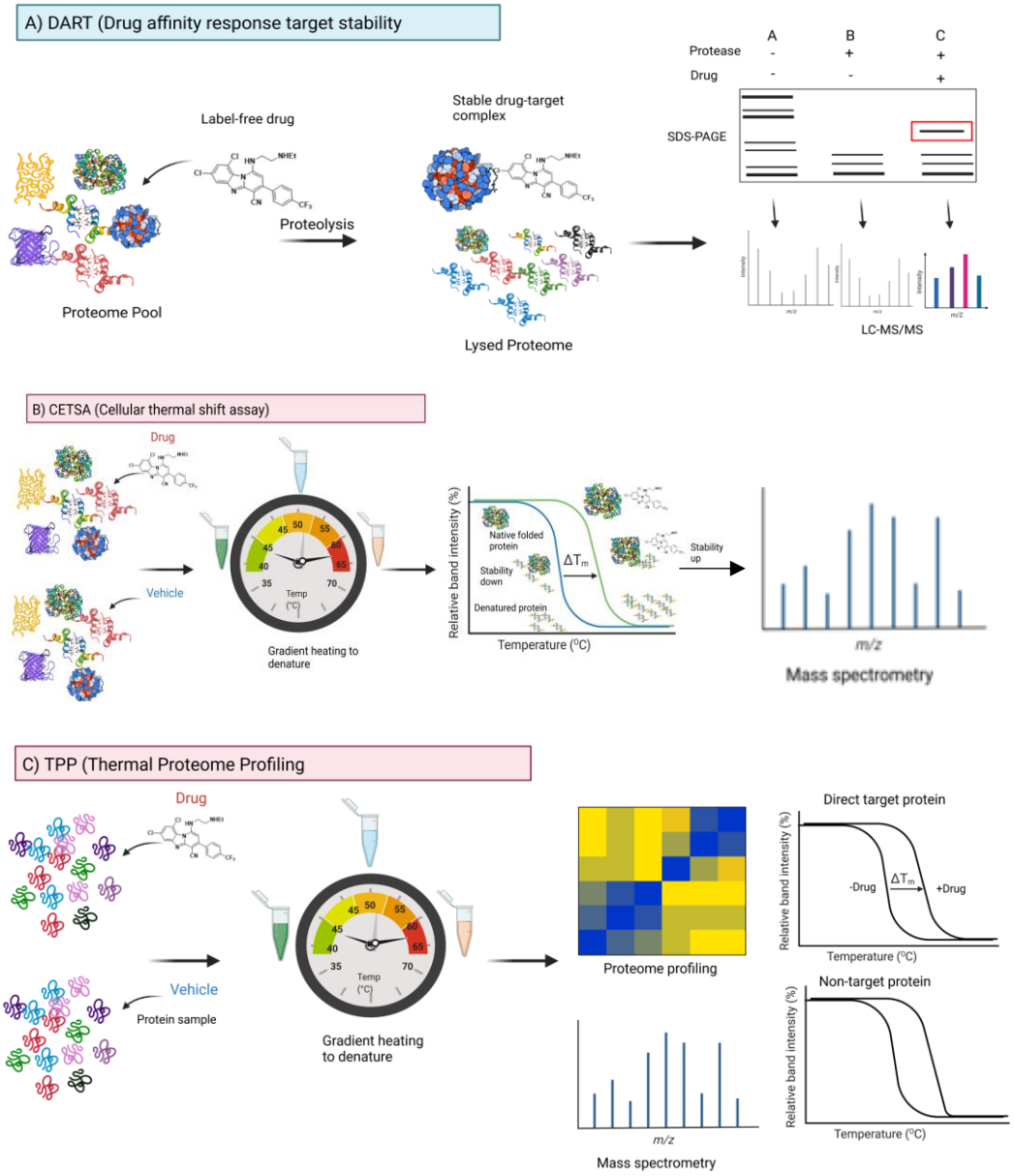

Figure 1.14. A representation of label-free chemical proteomics techniques. Created with BioRender.com

TPP on the other hand provides an opportunity to quantify the change in thermostability caused by the interaction between a ligand and a protein on proteome-wide scale.[202] This proteomics approach relies on the biophysical properties of proteins where interaction of a target with a ligand changes its structural stability`(Figure 1.14C). This ensures an ultracentrifugation step which separates soluble and insoluble proteins protein fractions for MS quantification.[203] Recently, TPP has been applied to study the MOA and identify the protein target (s) of several antimalarial agents.[204,205]

An alternative approach to TPP is CETSA. This technique is based on the observation that the melting curves of proteins in intact cells can be measured following a heating step. Normally, a dose-dependent thermal stability change is determined using the median melting temperature. (Figure 1.14C) This thermal change is then quantified by the amount of soluble protein remaining using MS. This strategy has been used to validate the known MOA of pyrimethamine as a folic acid antagonist and also identified *P. falciparum* purine nucleoside phosphorylase as a novel antimalarial target of quinine and mefloquine.[204]

1.7.2. Genomics Approaches

The increased use of genomics and genetic tools in studying the biology of *Plasmodium* species has provided valuable tools to deconvolute the molecular determinants that confer antimalarial resistance. It also aids in the identification of drug targets of phenotypic whole-cell active antimalarial leads. These tools, when used in combination with other ''omics'' tools such as chemoproteomics, metabolomics, transcriptomics, and epigenomics, provide great avenues for studying essential physiological processes in *P. falciparum* parasites.[206,207]

Genomics approaches have been invaluable in understanding mechanisms of antimalarial drug resistance and other important processes such as RBC egress, evasion, and intracellular protein trafficking.[208–210] Whole-genome approaches such as genome-wide association studies, experimental genetic crosses, and *in vitro* resistance selection (Figure 1.15) have been the foundation of recent investigations into antimalarial drug resistance and malaria biology, which sheds light on the MOA of a phenotypically active lead.[211] While these genomics and genetics approaches contribute significantly to target identification and MOA studies, much focus is placed on *in vitro* resistance selection and whole-genome sequence analysis for this thesis.

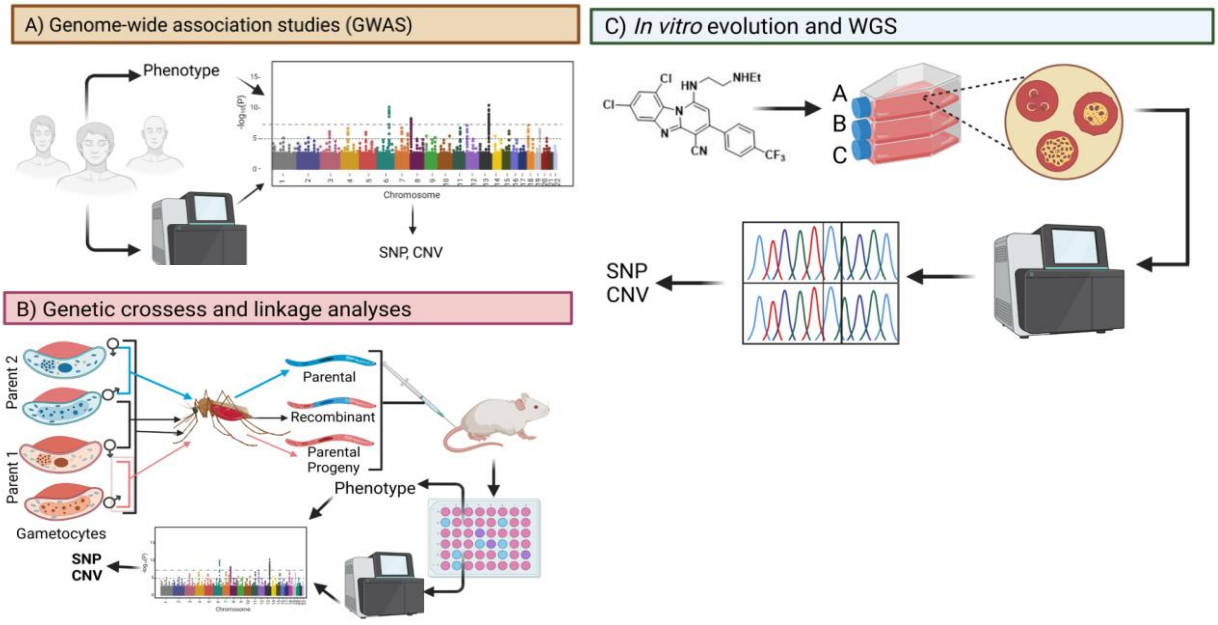

Figure 1.15. Genomics approaches to studying the mechanism of parasite's resistance to drugs.[211] Created with BioRender.com

1.7.2.1. *In vitro* Resistance Selection and Whole-genome Sequence Analysis

In vitro evolution of resistance, followed by whole-genome sequencing (WGS) of parasite clones, remains one of the primary genomics approaches to identify genetic determinants that drive antimalarial drug responses.[212] In this approach, *Plasmodium* parasites are continuously exposed to sublethal doses of drug pressure until the onset of recrudescent resistant parasites. The genomic data of the resistant clones generated via limiting dilution are compared to their isogenic parent parasites to identify mutations that occurred during the process of acquiring resistance. These mutations are observed through genome-encoded changes such as single nucleotide polymorphisms (SNPs) and copy number variations (CNVs) that may be driving the resistance phenotype. (Figure 1.15C)

Not only does this method generate hypotheses about the resistance mechanisms of drug candidates but also about their potential target (s) and MOA (s).[213,214] For example, this approach identified the translation elongation factor 2 (eEF2) as the molecular target for **DDD107498**, a phenotypic whole-cell active antimalarial lead with activity across multiple stages of the parasite's life cycle, good pharmacokinetic properties, and acceptable safety margins. eEF2 is essential for protein synthesis and its identification as a plausible target in antimalarial drug discovery presents the opportunity to develop new

chemical agents to target this pathway.[136] Further applications of this approach identified phenylalanyl-tRNA Synthetase (PheRS),[215] a polyadenylation specificity factor subunit 3 (*Pf*CPSF3),[216] and the double functional farnesyl/geranylgeranyl diphosphate synthase as promising antimalarial targets. Also, WGS data identified Na^+-dependent ATPase as the target of several antimalarial chemotypes including the methylisoquinoline, **MB14**[217] and *Pf*PKG as the primary target of **MMV030084** and **ML10**.[218,219] (Figure 1.16) A drawback to this approach is that further time-consuming studies may be required if the identified mutation is in an uncharacterized gene to assess whether the gene is a drug-resistant gene, drug target or just a background mutation. Also, since the success of this method depends on the ability to raise resistant mutants easily, other techniques are required to study the MOA of ''irresistible compounds''.

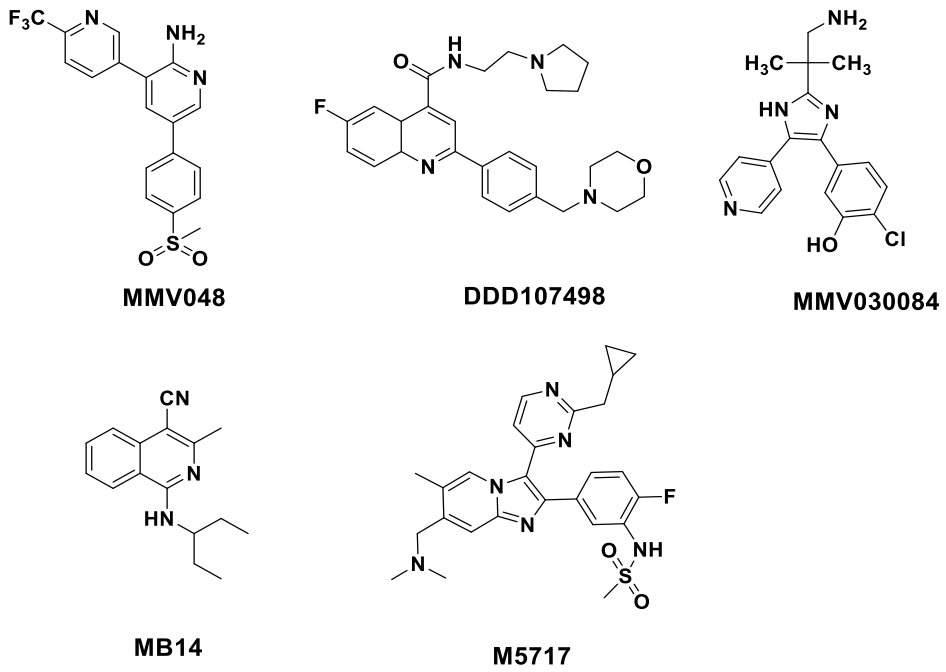

Figure 1.16. Chemical structures of some new antimalarial drug candidates whose molecular target (s) were identified using the in vitro resistance selection approach to target identification.

1.8. Pyrido[1,2-a]benzimidazoles a Potent Antimalarial Chemotype

Pyrido[1,2-a]benzimidazole (PBI) compounds contain a benzimidazole motif that interests medicinal chemistry campaigns. The benzimidazole nucleus is structurally made up of naturally occurring purine nucleotides, which can interact effectively with a wide range of biological systems.[1] This has led to numerous reports of the biological activities of the scaffold, including anticancer,[220] antifungal,[221] antimycobacterial,[222] antiviral,[223] and

anxiolytic[224] activities. Previous work by Sandlin and co-workers on 144,330 chemotypes in the Vanderbilt University Institute of Chemical biology's library and by Fong *et al.* using compounds in the MMV Malaria Box identified the benzimidazole chemotype as a potent inhibitor of βH formation.[225,226] After the earlier discovery of benzimidazole analogues with potent *in vitro* antiplasmodium activity,[227] there has been increased interest in exploring and developing this chemotype to discover new antimalarial agents with potentially novel modes of action. N-aryl-2-aminobenzimidazoles were identified by Ramachandran and co-workers as phenotypic whole-cell active antimalarial leads against the ABS of *P. falciparum* when an AstraZeneca corporate compound library was screened.[228] In a separate effort, a series of benzimidazole analogues were found to possess antiplasmodium activities against multiple stages of the parasite's life cycle when Leshabane and co-workers screened these analogues against the blood stages and the transmissible gametocyte stages of the parasite.[229]

PBIs on the other hand, represent a novel class of antimalarial chemotypes, that have equally been investigated previously for their antiviral, antifungal and antitumour properties. The antimalarial properties of PBIs were first reported by Ndakala and co-workers in 2011, when a small library of 1440 chemically diverse compounds were screened against a panel of protozoans *in vitro* as part of a collaboration with the Belgian company Tibotec. This yielded compound **TDR15087** with moderate activity against both *P. falciparum* CQS (GHA) and CQR (W2) strains. Further SAR exploration on the **TDR15087** core yielded about 535 PBI analogues screened against the CQR strain, K1. This identified 49 antimalarial PBIs, with IC_{50} below 0.1 μg/ml. Chiefly among them were **TDR35885** and **TDR44047** (Figure 1.17)**.** However, none of the three analogues were successful *in vivo* proof-of-concept in a *P. berghei* mouse malaria infection model up to high doses of 4 x100 mg/kg Ip. This was attributed to poor solubility and metabolic stability.[230]

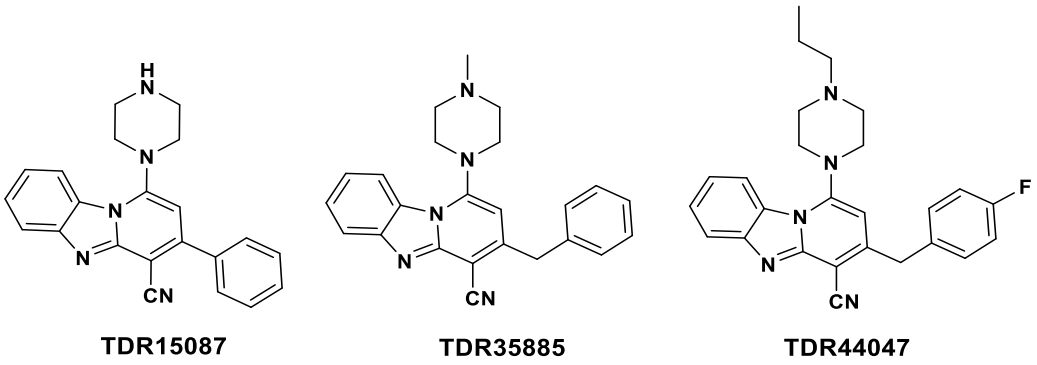

Figure 1.17. Chemical structures of PBI hits with potent antiplasmodium activity.

The authors explored further SAR optimizations around the PBI core to identify PBI analogues that retained potency in the *P. berghei* model. This exploration was focused on 3-aryl derivatives with alkylamino side chains possessing sub-micromolar activities. The most active analogue was compound **PBI-1** with IC_{50} of 0.047 μM against the CQR strain K1. However, this compound was metabolically unstable in liver microsomes and quickly formed its mono-desethyl metabolite, **PBI-2** through *N*-dealkylation (Figure 1.18). **PBI-2** retained activity and microsomal stability in murine models compared to **PBI-1**. However, its pharmacokinetic liabilities such as low bioavailability probably due to solubility-limited absorption decreased its *in vivo* activity. *In vivo* efficacy studies of the orally administered salt of **PBI-2** against *P. berghei* using both single and multi-doses showed that the activity plateaus with doses above 25 mg/kg (50.2%, 71.2% and 79.8% reduction in parasitemia on days 3, 4 and 5 respectively, at 50 mg/kg dose).

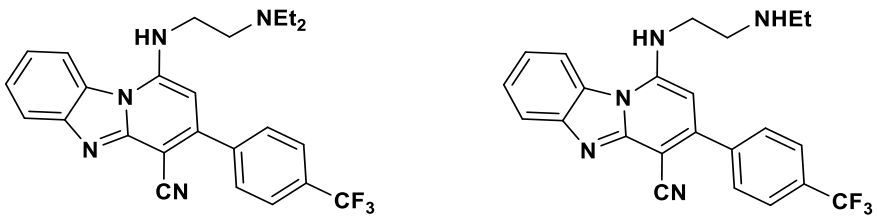

Figure 1.18. Chemical structures of the lead PBI compound **PBI-1** and its metabolite **PBI-2** identified by Ndakala and colleagues in 2011.[222]

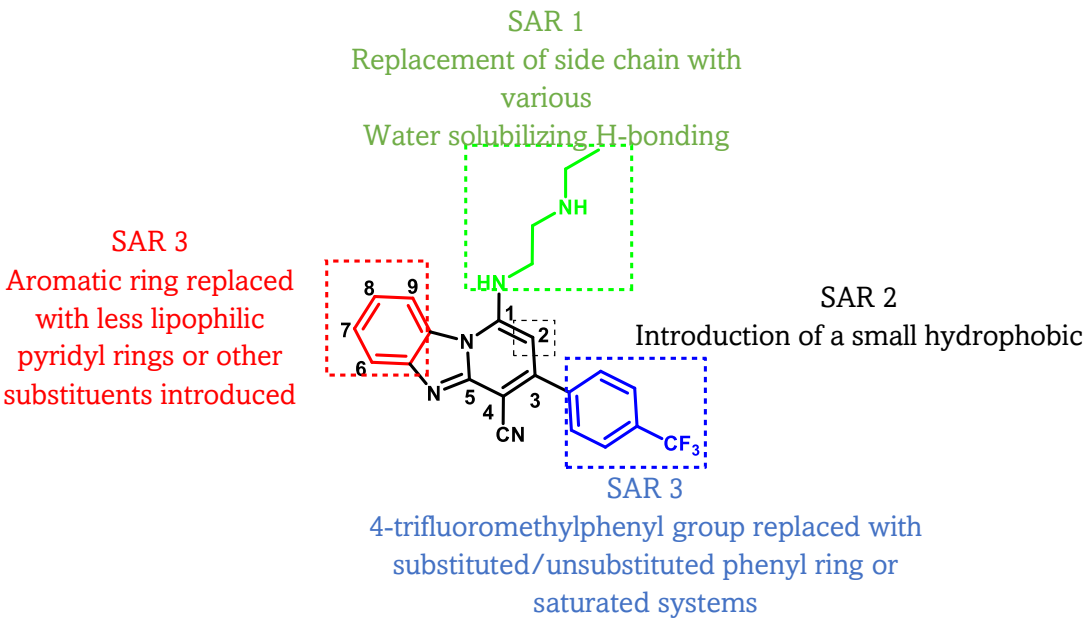

Figure 1.19. Chemical structure of **PBI-1** showing the various SAR explorations aimed at designing compounds with improved physicochemical and pharmacological features.[1]

As shown above, these two leads identified by Ndakala *et al*. have laid the foundation for SAR exploration and optimization around the PBI core to identify analogues with improved pharmacokinetic profiles. SAR investigations on the PBI core as illustrated in Figure 1.19, were made to investigate the effects of modifications on other parts of the molecule that were not previously investigated. The physicochemical and pharmacological properties of the new analogues synthesized based on these modifications were evaluated. Four SAR strategies were explored to deliver PBI analogues with improved pharmacological and physicochemical properties.[1]. These SAR explorations yielded a series of potent antimalarial PBI analogues including compounds **KP68**, and **KP124** (Figure 1.20). **KP68** is the most active of the two, with halogen substitution on the benzimidazole core (P*f*NF54 IC_{50} = 0.03 μM; P*f*K1 IC_{50} = 0.04 μM). It was metabolically stable with reasonable kinetic solubility at pH 6.5. When assessed for its *in vivo* efficacy in a *P. berghei* mouse model, dosing orally at 4x 50 mg/kg, there was 98% reduction in parasitemia after 30 days. Although the efficacy of compound **KP124** was not assessed in an *in vivo* mouse model, the compound exhibited a good *in vitro* antiplasmodium activity (*Pf*NF54 IC_{50} = 0.14 μM; *Pf*K1 IC_{50} = 0.13 μM) with moderate physicochemical properties. The striking structural similarities between these PBIs leads, **KP68** and **KP124** to CQ, which comprises of the presence of both a basic amino side

group and a planar heterocyclic group suggest that they can undergo, π-π stacking interactions with heme to form a heme-drug complex Consequently, both compounds could inhibit β-hematin *in vitro* assay and hemozoin *in vivo* in *P. falciparum*.

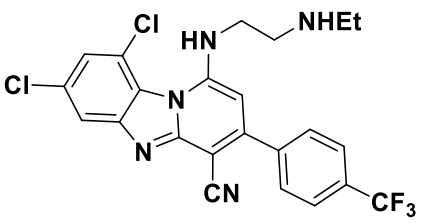

KP68

*Pf*NF54 IC_{50} = 0.03 μM
*Pf*K1 IC_{50} = 0.04 μM
in vivo P. berghei (p.o) 4x50 mg/kg = 98.0%
3/3 malaria infected mice cured

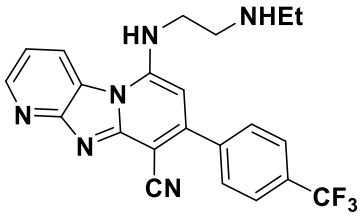

KP124

*Pf*NF54 IC_{50} = 0.14 μM
*Pf*K1 IC_{50} = 0.13 μM

Figure 1.20. Chemical structures of phenotypic whole-cell active PBI leads of relevance to this study, obtained after further SAR studies and optimizations on **PBI-2**.[1]

1.8.1. Repositioning Astemizole for Antimalarial Drug Discovery

Astemizole (AST, Figure 1.21) represents a second-generation selective H_1-receptor antagonist. However, in addition to its antihistamine properties, it causes fatal side effects such as cardiac arrhythmias hERG K^+ channel blockade, QTc prolongation, torsades de pointes, and sudden death. This led to its withdrawal, from the market.[231,232] Chong and co-workers first identified the antimalarial properties of AST and its metabolite Desmethylastemizole (DMAST, Figure 1.13).[233]

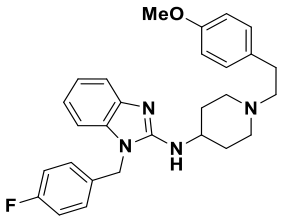

AST

*Pf*3D7 IC_{50} = 0.227 μM
*Pf*Dd2 IC_{50}= 0.457 μM
*Pf*ItG IC_{50} = 0.734

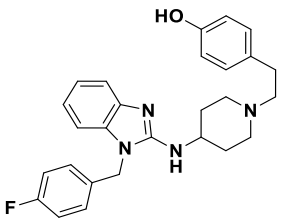

DMAST

*Pf*3D7 IC_{50} = 0.117 μM
*Pf*Dd2 IC_{50} = 0.106 μM
P*f*ItG IC_{50} = 0.057 μM

Figure 1.21. Chemical structures of astemizole (AST) and desmethylastemizole (DMAST).

AST and DMAST showed sub-micromolar *in vitro* activities against three strains of *P. falciparum*; 3d7, Dd2, and ItG. The compounds showed *in vivo* efficacy in the standard 4-day parasite suppression assay in both CQS *P. vinckei* and CQR resistance *P. yoelii*. Up to 80% reduction in parasitemia was observed in AST and DMAST against the sensitive strain at 15 and 30 $mg.kg^{-1}.day^{-1}$. However, parasite recrudescence was observed on day 4 when treatment stopped.

Several drug discovery efforts have since undertaken various medicinal chemistry approaches to deliver potential antimalarial AST analogues. As such, our research group utilized astemizole as a template to design and synthesize new antimalarial agents with improved activity, physicochemical properties, and reduced cardiotoxicity (hERG) risk through an in-dept SAR exploration. **DM253** was identified as one of the frontrunners of the series. The compound showed sub-nanomolar activities against the parasite's CQS and multidrug-resistant strains. (*Pf*NF54 IC_{50} = 0.012 µM; *Pf*K1 IC_{50} = 0.040 µM) with favourable absorption, distribution, metabolism, and excretion (ADME) properties. **DM253** also presents with high metabolic stability with >93% remaining, CLint = <11.6 $\mu l.min^{-1}.mg^{-1}$, *E*H < 0.42 once the 3-/5-CF_3 group in the oxadiazole moiety blocked the metabolic hotspot. In the *P. berghei* mouse model, **DM253** was efficacious with about 99.5% reduction in parasitemia when a standard 50 $mg.kg^{-1}$ dose was administered orally for four consecutive days. The compound's efficacy was determined by the level of parasitemia in the treated animals and their untreated control after infection.

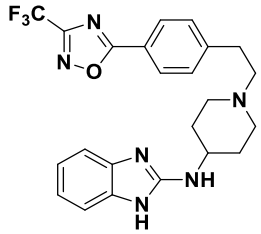

DM253

*Pf*NF54 IC_{50} = 0.012 µM

*Pf*K1 IC_{50} = 0.040 µM

in vivo P. berghei (p.o) 4x50 mg/kg = 99.52

Mean survival days = 14/days

Figure 1.22. Chemical structure of phenotypic whole-cell active astemizole-derived benzimidazole lead of relevance to this study, obtained after further SAR studies and optimizations on AST

1.9. Research Program

1.9.1 Justification of Research

As discussed earlier in this chapter, malaria continues to negatively affect the health and living conditions of the people who suffer it. While chemotherapy remains the most effective way to control the disease, resistance to already existing antimalarial drugs on the market renders them ineffective against the parasite. The currently recommended ACTs for treating uncomplicated malaria have already started showing evidence of parasite resistance due to the reduced clearance rates observed from Southeast Asia and have already spread to Africa. Therefore, there is a high possibility of this resistance spreading to malaria endemic areas, of which the consequence will be enormous. In addition, the COVID-19 pandemic has negatively impacted malaria relief services in endemic regions, increasing malaria incident rates in these regions. These reiterate the urgent need to develop new compound classes with novel modes of action, efficacy at low doses, good safety profiles, and activity at various stages of the parasite's life cycle.

The pyrido[1,2-a]benzimidazole chemotype is one of the privileged scaffolds being developed as a potential source of new antimalarial leads, as reported by Ndakala and co-workers.[230] However, the mechanistic details of the MOA of this scaffold are yet to be elucidated. The structural resemblance of the representative compounds to chloroquine and the previous work on this scaffold has shown that they interact with the hemozoin biocrystallization pathway in the intraerythrocytic *P. falciparum* by inhibiting the conversion of heme to hemozoin. The build-up of toxic free heme then leads to the parasite's death. However, Singh and co-workers could not provide conclusive evidence that inhibiting the formation of hemozoin is the primary MOA of PBIs but concluded that it is a contributory MOA.[1]

The discovery of the antimalarial properties of astemizole has increased interest in repositioning it as an antimalarial drug. Medicinal chemistry approaches were utilized to improve its efficacy, and solubility and reduce its hERG liability, thereby increasing its overall potential as an antimalarial drug. SAR studies focused on the various parts of the core astemizole have delivered many analogues with antiplasmodium activity and suitable physicochemical properties. These separate phenotypic screens have identified whole-cell active leads that could potentially be developed into new generation

antimalarial drugs. However, these compounds' molecular target (s), and MOA need to be studied and understood. Consequently, this work explores omics-based approaches to target identification, such as genomics and proteomics through resistance selection and affinity-based chromatography. Also, using both extrinsic, and intrinsic fluorescence of the compounds, their subcellular accumulation in parasite-infected erythrocytes is assessed provide in-dept information about the compounds' action against the parasite. Finally, the heme fractionation assay and docking of the compounds were employed to provide further details on the compounds' MOA.

1.9.3. Research Question

This research seeks to answer the question; can chemical proteomics, genomics, and fluorescent localization studies, aided by computational docking and heme fractionation studies, be used to identify molecular target (s) and hence elucidate the MOA of the antimalarial leads derived from phenotypic whole-cell screening approach to drug discovery.

1.9.4. Main Objective

This project aims to identify molecular targets of antimalarial pyrido[1,2-a]benzimidazole and related leads obtained from phenotypic whole-cell screening using proteomics, genomics, and fluorescent localization studies.

1.9.5. Specific Objectives

- Synthesis and characterization of derivatized precursors suitable for the coupling with fluorophores to generate analogues of whole-cell active antimalarial leads using hydrophobic and hydrophilic fluorophores.
- Attachment of precursor analogues to agarose beads.
- Validate the fluorescent derivative of drug leads as a suitable analogue (s) of the parent molecule by evaluating its interaction with Fe(III)PPIX and its antiplasmodium activity.
- Determine the photophysical properties of the fluorescent analogues including wavelength maxima, for excitation and emission, quantum yield, quenching by Fe(III)PPIX.
- Evaluate compounds' intrinsic fluorescence and their suitability for subcellular accumulation studies.

- Study the subcellular accumulation of the compounds and fluorescent analogues using confocal, Airyscan, and super-resolution microscopy of infected erythrocytes.
- Identify protein binding partners using both SDS-PAGE and proteomics methods.
- Identify genes that may be implicated in conferring parasite resistance to the lead compounds.

2.0. References

(1) Singh, K.; Okombo, J.; Brunschwig, C.; Ndubi, F.; Barnard, L.; Wilkinson, C.; Njogu, P. M.; Njoroge, M.; Laing, L.; Machado, M.; Prudêncio, M.; Reader, J.; Botha, M.; Nondaba, S.; Birkholtz, L.-M.; Lauterbach, S.; Churchyard, A.; Coetzer, T. L.; Burrows, J. N.; Yeates, C.; Denti, P.; Wiesner, L.; Egan, T. J.; Wittlin, S.; Chibale, K. Antimalarial Pyrido[1,2- a]Benzimidazoles: Lead Optimization, Parasite Life Cycle Stage Profile, Mechanistic Evaluation, Killing Kinetics, and in Vivo Oral Efficacy in a Mouse Model. *J. Med. Chem.* **2017**, *60* (4), 1432–1448.

(2) World Health Organization. *World Malaria Report*; Geneva, 2021.

(3) World Health Organization. *World Malaria Report*; Geneva, 2020.

(4) Tuteja, R. Malaria − an Overview. *FEBS J.* **2007**, *274* (18), 4670–4679.

(5) Miller, L. H.; Baruch, D. I.; Marsh, K.; Doumbo, O. K. The Pathogenic Basis of Malaria. *Nature* **2002**, *415* (6872), 673–679.

(6) Bousema, T.; Okell, L.; Felger, I.; Drakeley, C. Asymptomatic Malaria Infections: Detectability, Transmissibility and Public Health Relevance. *Nat. Rev. Microbiol.* **2014**, *12* (12), 833–840.

(7) Tilley, L.; Dixon, M. W. A.; Kirk, K. The Plasmodium Falciparum-Infected Red Blood Cell. *Int. J. Biochem. Cell Biol.* **2011**, *43* (6), 839–842.

(8) Greenwood, B. M.; Fidock, D. A.; Kyle, D. E.; Kappe, S. H. I.; Alonso, P. L.; Collins, F. H.; Duffy, P. E. Malaria: Progress, Perils, and Prospects for Eradication. *J. Clin. Invest.* **2008**, *118* (4), 1266–1276.

(9) Matuschewski, K. Getting Infectious: Formation and Maturation of Plasmodium Sporozoites in the Anopheles Vector. *Cell. Microbiol.* **2006**, *8* (10), 1547–1556.

(10) Biamonte, M. A.; Wanner, J.; Le Roch, K. G. Recent Advances in Malaria Drug Discovery. *Bioorg. Med. Chem. Lett.* **2013**, *23* (10), 2829–2843.

(11) Bannister, L. .; Hopkins, J. .; Fowler, R. .; Krishna, S.; Mitchell, G. . A Brief Illustrated Guide to the Ultrastructure of Plasmodium Falciparum Asexual Blood Stages. *Parasitol. Today* **2000**, *16* (10), 427–433.

(12) Banniter, L. H.; Mitchell, G. H. The Malaria Merozoite, Forty Years On. *Parasitology* **2009**, *136* (12), 1435–1444.

(13) Trager, W.; Jensen, J. Human Malaria Parasites in Continuous Culture. *Science (80-.).* **1976**, *193* (4254), 673–675.

(14) Kohler, S. A Plastid of Probable Green Algal Origin in Apicomplexan Parasites. *Science (80-.).* **1997**, *275* (5305), 1485–1489.

(15) Aikawa, M. Plasmodium: The Fine Structure of Malarial Parasites. *Exp. Parasitol.* **1971**, *30* (2), 284–320.

(16) Goldberg, D. E.; Slater, A. F.; Beavis, R.; Chait, B.; Cerami, A.; Henderson, G. B. Hemoglobin Degradation in the Human Malaria Pathogen Plasmodium Falciparum: A Catabolic Pathway Initiated by a Specific Aspartic Protease. *J. Exp. Med.* **1991**, *173* (4), 961–969.

(17) Yayon, A.; Timberg, R.; Friedman, S.; Ginsburg, H. Effects of Chloroquine on the Feeding Mechanism of the Intraerythrocytic Human Malarial Parasite Plasmodium Falciparum 1. *J. Protozool.* **1984**, *31* (3), 367–372.

(18) Slomianny, C. Ultrastructure of Malaria-Infected Erythrocytes: Commentary. Three-Dimensional Reconstruction of the Feeding Process of the Malaria Parasite. *Blood Cells* **1990**, *16* (2–3), 369–378.

(19) Painter, H. J.; Chung, N. C.; Sebastian, A.; Albert, I.; Storey, J. D.; Llinás, M. Genome-Wide Real-Time in Vivo Transcriptional Dynamics during Plasmodium Falciparum Blood-Stage Development. *Nat. Commun.* **2018**, *9* (1), 2656.

(20) Hanssen, E.; McMillan, P. J.; Tilley, L. Cellular Architecture of Plasmodium Falciparum-Infected Erythrocytes. *Int. J. Parasitol.* **2010**, *40* (10), 1127–1135.

(21) Bozdech, Z.; Llinás, M.; Pulliam, B. L.; Wong, E. D.; Zhu, J.; DeRisi, J. L. The Transcriptome of the Intraerythrocytic Developmental Cycle of Plasmodium Falciparum. *PLoS Biol.* **2003**, *1* (1), e5.

(22) Krugliak, M.; Zhang, J.; Ginsburg, H. Intraerythrocytic Plasmodium Falciparum Utilizes Only a Fraction of the Amino Acids Derived from the Digestion of Host

Cell Cytosol for the Biosynthesis of Its Proteins. *Mol. Biochem. Parasitol.* **2002**, *119* (2), 249–256.

(23) Lew, V. L.; Tiffert, T.; Ginsburg, H. Excess Hemoglobin Digestion and the Osmotic Stability OfPlasmodium Falciparum–Infected Red Blood Cells. *Blood* **2003**, *101* (10), 4189–4194.

(24) Sherman, I. W. Amino Acid Metabolism and Protein Synthesis in Malarial Parasites. *Bull. World Health Organ.* **1977**, *55* (2–3), 265–276.

(25) Egan, T. J.; Combrinck, J. M.; Egan, J.; Hearne, G. R.; Marques, H. M.; Ntenteni, S.; Sewell, B. T.; Smith, P. J.; Taylor, D.; van Schalkwyk, D. A.; Walden, J. C. Fate of Haem Iron in the Malaria Parasite Plasmodium Falciparum. *Biochem. J.* **2002**, *365* (2), 343–347.

(26) Bakar, N. A.; Klonis, N.; Hanssen, E.; Chan, C.; Tilley, L. Digestive-Vacuole Genesis and Endocytic Processes in the Early Intraerythrocytic Stages of Plasmodium Falciparum. *J. Cell Sci.* **2010**, *123* (3), 441–450.

(27) Elliott, D. A.; McIntosh, M. T.; Hosgood, H. D.; Chen, S.; Zhang, G.; Baevova, P.; Joiner, K. A. Four Distinct Pathways of Hemoglobin Uptake in the Malaria Parasite Plasmodium Falciparum. *Proc. Natl. Acad. Sci.* **2008**, *105* (7), 2463–2468.

(28) Ehlgen, F.; Pham, J. S.; de Koning-Ward, T.; Cowman, A. F.; Ralph, S. A. Investigation of the Plasmodium Falciparum Food Vacuole through Inducible Expression of the Chloroquine Resistance Transporter (PfCRT). *PLoS One* **2012**, *7* (6), e38781.

(29) Banerjee, R.; Liu, J.; Beatty, W.; Pelosof, L.; Klemba, M.; Goldberg, D. E. Four Plasmepsins Are Active in the Plasmodium Falciparum Food Vacuole, Including a Protease with an Active-Site Histidine. *Proc. Natl. Acad. Sci.* **2002**, *99* (2), 990–995.

(30) Rosenthal, P. J. Cysteine Proteases of Malaria Parasites. *Int. J. Parasitol.* **2004**, *34* (13–14), 1489–1499.

(31) Tenhunen, R.; Amarver, H. S.; Schmid, R. The Enzymatic Conversion of Heme to Bilirubin by Microsomal Heme Oxygenase*.

(32) Oliveira, M. F.; D'Avila, J. C. .; Torres, C. R.; Oliveira, P. L.; Tempone, A. J.; Rumjanek, F. D.; Braga, C. M. .; Silva, J. R.; Dansa-Petretski, M.; Oliveira, M. A.; de Souza, W.; Ferreira, S. T. Haemozoin in Schistosoma Mansoni. *Mol. Biochem. Parasitol.* **2000**, *111* (1), 217–221.

(33) Chen, M. M.; Shi, L.; Sullivan, D. J. Haemoproteus and Schistosoma Synthesize Heme Polymers Similar to Plasmodium Hemozoin and β-Hematin. *Mol. Biochem. Parasitol.* **2001**, *113* (1), 1–8.

(34) Egan, T. J.; Chen, J. Y.-J.; de Villiers, K. A.; Mabotha, T. E.; Naidoo, K. J.; Ncokazi, K. K.; Langford, S. J.; McNaughton, D.; Pandiancherri, S.; Wood, B. R. Haemozoin (β-Haematin) Biomineralization Occurs by Self-Assembly near the Lipid/Water Interface. *FEBS Lett.* **2006**, *580* (21), 5105–5110.

(35) Slater, A. F.; Swiggard, W. J.; Orton, B. R.; Flitter, W. D.; Goldberg, D. E.; Cerami, A.; Henderson, G. B. An Iron-Carboxylate Bond Links the Heme Units of Malaria Pigment. *Proc. Natl. Acad. Sci.* **1991**, *88* (2), 325–329.

(36) Hematin Compounds and Bile Pigments: Their Constitution, Metabolism, and Function. *J. Am. Med. Assoc.* **1950**, *143* (4), 404.

(37) Sullivan, D. J.; Gluzman, I. Y.; Goldberg, D. E. Plasmodium Hemozoin Formation Mediated by Histidine-Rich Proteins. *Science (80-.).* **1996**, *271* (5246), 219–222.

(38) Ketchum, M. A.; Olafson, K. N.; Petrova, E. V.; Rimer, J. D.; Vekilov, P. G. Hematin Crystallization from Aqueous and Organic Solvents. *J. Chem. Phys.* **2013**, *139* (12), 121911.

(39) Sullivan, D. J. Theories on Malarial Pigment Formation and Quinoline Action. *Int. J. Parasitol.* **2002**, *32* (13), 1645–1653.

(40) Papalexis, V.; Siomos, M.-A.; Campanale, N.; Guo, X.; Kocak, G.; Foley, M.; Tilley, L. Histidine-Rich Protein 2 of the Malaria Parasite, Plasmodium Falciparum, Is Involved in Detoxification of the by-Products of Haemoglobin Degradation. *Mol. Biochem. Parasitol.* **2001**, *115* (1), 77–86.

(41) Slater, A. F. G.; Cerami, A. Inhibition by Chloroquine of a Novel Haem Polymerase Enzyme Activity in Malaria Trophozoites. *Nature* **1992**, *355* (6356), 167–169.

(42) Dorn, A.; Stoffel, R.; Matile, H.; Bubendorf, A.; Ridley, R. G. Malarial Haemozoin/β-Haematin Supports Haem Polymerization in the Absence of Protein. *Nature* **1995**, *374* (6519), 269–271.

(43) Bendrat, K.; Berger, B. J.; Cerami, A. Haem Polymerization in Malaria. *Nature* **1995**, *378* (6553), 138–138.

(44) Fitch, C. D.; Cai, G.; Chen, Y.-F.; Shoemaker, J. D. Involvement of Lipids in Ferriprotoporphyrin IX Polymerization in Malaria. *Biochim. Biophys. Acta - Mol. Basis Dis.* **1999**, *1454* (1), 31–37.

(45) Tripathi, A. K.; Garg, S. K.; Tekwani, B. L. A Physiochemical Mechanism of Hemozoin (β-Hematin) Synthesis by Malaria Parasite. *Biochem. Biophys. Res. Commun.* **2002**, *290* (1), 595–601. https://doi.org/10.1006/bbrc.2001.6231.

(46) Jackson, K. E.; Klonis, N.; Ferguson, D. J. P.; Adisa, A.; Dogovski, C.; Tilley, L. Food Vacuole-Associated Lipid Bodies and Heterogeneous Lipid Environments in the Malaria Parasite, Plasmodium Falciparum. *Mol. Microbiol.* **2004**, *54* (1), 109–122.

(47) Palacpac, N. M. Q.; Hiramine, Y.; Mi-ichi, F.; Torii, M.; Kita, K.; Hiramatsu, R.; Horii, T.; Mitamura, T. Developmental-Stage-Specific Triacylglycerol Biosynthesis, Degradation and Trafficking as Lipid Bodies in Plasmodium Falciparum -Infected Erythrocytes. *J. Cell Sci.* **2004**, *117* (8), 1469–1480.

(48) Vielemeyer, O.; McIntosh, M. T.; Joiner, K. A.; Coppens, I. Neutral Lipid Synthesis and Storage in the Intraerythrocytic Stages of Plasmodium Falciparum. *Mol. Biochem. Parasitol.* **2004**, *135* (2), 197–209.

(49) Pisciotta, J. M.; Coppens, I.; Tripathi, A. K.; Scholl, P. F.; Shuman, J.; Bajad, S.; Shulaev, V.; Sullivan, D. J. The Role of Neutral Lipid Nanospheres in Plasmodium Falciparum Haem Crystallization. *Biochem. J.* **2007**, *402* (1), 197–204.

(50) de Villiers, K. A.; Osipova, M.; Mabotha, T. E.; Solomonov, I.; Feldman, Y.; Kjaer, K.; Weissbuch, I.; Egan, T. J.; Leiserowitz, L. Oriented Nucleation of β-Hematin Crystals Induced at Various Interfaces: Relevance to Hemozoin Formation. *Cryst. Growth Des.* **2009**, *9* (1), 626–632.

(51) Solomonov, I.; Osipova, M.; Feldman, Y.; Baehtz, C.; Kjaer, K.; Robinson, I. K.;

Webster, G. T.; McNaughton, D.; Wood, B. R.; Weissbuch, I.; Leiserowitz, L. Crystal Nucleation, Growth, and Morphology of the Synthetic Malaria Pigment β-Hematin and the Effect Thereon by Quinoline Additives: The Malaria Pigment as a Target of Various Antimalarial Drugs. *J. Am. Chem. Soc.* **2007**, *129* (9), 2615–2627.

(52) Ambele, M. A.; Egan, T. J. Neutral Lipids Associated with Haemozoin Mediate Efficient and Rapid β-Haematin Formation at Physiological PH, Temperature and Ionic Composition. *Malar. J.* **2012**, *11* (1), 337.

(53) Hoang, A. N.; Sandlin, R. D.; Omar, A.; Egan, T. J.; Wright, D. W. The Neutral Lipid Composition Present in the Digestive Vacuole of Plasmodium Falciparum Concentrates Heme and Mediates β-Hematin Formation with an Unusually Low Activation Energy. *Biochemistry* **2010**, *49* (47), 10107–10116.

(54) Kuter, D.; Mohunlal, R.; Fitzroy, S.-M.; Asher, C.; Smith, P. J.; Egan, T. J.; de Villiers, K. A. Insights into the Initial Stages of Lipid-Mediated Haemozoin Nucleation. *CrystEngComm* **2016**, *18* (27), 5177–5187.

(55) Ambele, M. A.; Sewell, B. T.; Cummings, F. R.; Smith, P. J.; Egan, T. J. Synthetic Hemozoin (β-Hematin) Crystals Nucleate at the Surface of Neutral Lipid Droplets That Control Their Sizes. *Cryst. Growth Des.* **2013**, *13* (10), 4442–4452.

(56) Egan, T. J.; Tshivhase, M. G. Kinetics of β-Haematin Formation from Suspensions of Haematin in Aqueous Benzoic Acid. *Dalt. Trans.* **2006**, No. 42, 5024–5032.

(57) Jani, D.; Nagarkatti, R.; Beatty, W.; Angel, R.; Slebodnick, C.; Andersen, J.; Kumar, S.; Rathore, D. HDP—A Novel Heme Detoxification Protein from the Malaria Parasite. *PLoS Pathog.* **2008**, *4* (4), e1000053.

(58) Chugh, M.; Sundararaman, V.; Kumar, S.; Reddy, V. S.; Siddiqui, W. A.; Stuart, K. D.; Malhotra, P. Protein Complex Directs Hemoglobin-to-Hemozoin Formation in Plasmodium Falciparum. *Proc. Natl. Acad. Sci.* **2013**, *110* (14), 5392–5397.

(59) Matz, J. M.; Drepper, B.; Blum, T. B.; van Genderen, E.; Burrell, A.; Martin, P.; Stach, T.; Collinson, L. M.; Abrahams, J. P.; Matuschewski, K.; Blackman, M. J. A Lipocalin Mediates Unidirectional Heme Biomineralization in Malaria Parasites. *Proc. Natl. Acad. Sci.* **2020**, *117* (28), 16546–16556.

(60) Alles, H. K.; Mendis, K. N.; Carter, R. Malaria Mortality Rates in South Asia and in Africa: Implications for Malaria Control. *Parasitol. Today* **1998**, *14* (9), 369–375.

(61) Luxemburger, C.; Ricci, F.; Nosten, F.; Raimond, D.; Bathet, S.; White, N. J. The Epidemiology of Severe Malaria in an Area of Low Transmission in Thailand. *Trans. R. Soc. Trop. Med. Hyg.* **1997**, *91* (3), 256–262.

(62) Meek, S. R. Epidemiology of Malaria in Displaced Khmers on the Thai-Kampuchean Border. *Southeast Asian J. Trop. Med. Public Health* **1988**, *19 2*, 243–252.

(63) Harrison, G.; Kean, B. H.; Mott, K. E.; Russell, A. J. Mosquitoes, Malaria, and Man: A History of the Hostilities since 1880. *J. Hist. Biol.* **1980**, *13* (1).

(64) Breman, J. The Ears of the Hippopotamus: Manifestations, Determinants, and Estimates of the Malaria Burden. *Am. J. Trop. Med. Hyg.* **2001**, *64* (1_suppl), 1–11.

(65) Trigg, P. I.; Kondrachine, A. V. Commentary: Malaria Control in the 1990s. *Bull. World Health Organ.* **1998**, *76* (1), 11–16.

(66) Shiff, C. Integrated Approach to Malaria Control. *Clin. Microbiol. Rev.* **2002**, *15* (2), 278–293.

(67) Wakabi, W. Africa Counts Greater Successes against Malaria. *Lancet* **2007**, *370* (9603), 1895–1896.

(68) Draper, S. J.; Sack, B. K.; King, C. R.; Nielsen, C. M.; Rayner, J. C.; Higgins, M. K.; Long, C. A.; Seder, R. A. Malaria Vaccines: Recent Advances and New Horizons. *Cell Host Microbe* **2018**, *24* (1), 43–56.

(69) Suscovich, T. J.; Fallon, J. K.; Das, J.; Demas, A. R.; Crain, J.; Linde, C. H.; Michell, A.; Natarajan, H.; Arevalo, C.; Broge, T.; Linnekin, T.; Kulkarni, V.; Lu, R.; Slein, M. D.; Luedemann, C.; Marquette, M.; March, S.; Weiner, J.; Gregory, S.; Coccia, M.; Flores-Garcia, Y.; Zavala, F.; Ackerman, M. E.; Bergmann-Leitner, E.; Hendriks, J.; Sadoff, J.; Dutta, S.; Bhatia, S. N.; Lauffenburger, D. A.; Jongert, E.; Wille-Reece, U.; Alter, G. Mapping Functional Humoral Correlates of Protection against Malaria Challenge Following RTS,S/AS01 Vaccination. *Sci. Transl. Med.* **2020**, *12* (553), eabb4757.

(70) Efficacy and Safety of RTS,S/AS01 Malaria Vaccine with or without a Booster Dose in Infants and Children in Africa: Final Results of a Phase 3, Individually Randomised, Controlled Trial. *Lancet* **2015**, *386* (9988), 31–45.

(71) Malaria Vaccine: WHO Position Paper, January 2016 – Recommendations. *Vaccine* **2018**, *36* (25), 3576–3577.

(72) Schwartz, E. Prophylaxis of Malaria. *Mediterr. J. Hematol. Infect. Dis.* **2012**, e2012045.

(73) Malaria Prophylxis Https://www.Malariasite.Com/Prophylaxis/ (Accessed Nov 1, 2019).

(74) Lobel, H. .; Campbell, C. .; Hightower, A. .; Eng, T.; Miani, M.; Eng, T.; Bernard, K. . Long-Term Malaria Prophylaxis with Weekly Mefloquine. *Lancet* **1993**, *341* (8849), 848–851.

(75) Schwartz, E. Prophylaxis of Malaria. *Mediterr. J. Hematol. Infect. Dis.* **2012**, *4* (1), e2012045–e2012045.

(76) Schlagenhauf, P.; Petersen, E. Malaria Chemoprophylaxis: Strategies for Risk Groups. *Clin. Microbiol. Rev.* **2008**, *21* (3), 466–472.

(77) Achan, J.; Talisuna, A. O.; Erhart, A.; Yeka, A.; Tibenderana, J. K.; Baliraine, F. N.; Rosenthal, P. J.; D'Alessandro, U. Quinine, an Old Anti-Malarial Drug in a Modern World: Role in the Treatment of Malaria. *Malar. J.* **2011**, *10* (1), 144.

(78) Peters, W. Antimalarial Drug Resistance: An Increasing Problem. *Br. Med. Bull.* **1982**, *38* (2), 187–192.

(79) Mayxay, M.; Barends, M.; Brockman, A.; Jaidee, A.; Nair, S.; Sudimack, D.; Pongvongsa, T.; Phompida, S.; Phetsouvanh, R.; Anderson, T.; White, N. J.; Newton, P. N. In Vitro Antimalarial Drug Susceptibility and Pfcrt Mutation among Fresh Plasmodium Falciparum Isolates from the Lao PDR (Laos). *Am. J. Trop. Med. Hyg.* **2007**, *76* (2), 245–250.

(80) Legrand, E.; Volney, B.; Meynard, J.-B.; Mercereau-Puijalon, O.; Esterre, P. In Vitro Monitoring of Plasmodium Falciparum Drug Resistance in French Guiana: A

Synopsis of Continuous Assessment from 1994 to 2005. *Antimicrob. Agents Chemother.* **2008**, *52* (1), 288–298.

(81) Tinto, H.; Rwagacondo, C.; Karema, C.; Mupfasoni, D.; Vandoren, W.; Rusanganwa, E.; Erhart, A.; Van Overmeir, C.; Van Marck, E.; D'Alessandro, U. In-Vitro Susceptibility of Plasmodium Falciparum to Monodesethylamodiaquine, Dihydroartemisinin and Quinine in an Area of High Chloroquine Resistance in Rwanda. *Trans. R. Soc. Trop. Med. Hyg.* **2006**, *100* (6), 509–514.

(82) WHO. Malaria Treatment Guidelines.

(83) Greenwood, D. Conflicts of Interest: The Genesis of Synthetic Antimalarial Agents in Peace and War. *J. Antimicrob. Chemother.* **1995**, *36* (5), 857–872.

(84) Edwards, G. Antimalarial Chemotherapy: Mechanisms of Action, Resistance and New Directions in Drug Discovery. *Br. J. Clin. Pharmacol.* **2001**, *52* (4), 464.

(85) H. Wernsdorfer, W.; Payne, D. The Dynamics of Drug Resistance in Plasmodium Falciparum. *Pharmacol. Ther.* **1991**, *50* (1), 95–121.

(86) Young, M. D.; Moore, D. V. Chloroquine Resistance in Plasmodium Falciparum. *Am. J. Trop. Med. Hyg.* **1961**, *10* (3), 317–320.

(87) Wongsrichanalai, C.; Pickard, A. L.; Wernsdorfer, W. H.; Meshnick, S. R. Epidemiology of Drug-Resistant Malaria. *Lancet Infect. Dis.* **2002**, *2* (4), 209–218.

(88) Sanchez, C. P.; Dave, A.; Stein, W. D.; Lanzer, M. Transporters as Mediators of Drug Resistance in Plasmodium Falciparum. *Int. J. Parasitol.* **2010**, *40* (10), 1109–1118.

(89) Martin, R. E.; Ginsburg, H.; Kirk, K. Membrane Transport Proteins of the Malaria Parasite. *Mol. Microbiol.* **2009**, *74* (3), 519–528.

(90) Fidock, D. A.; Nomura, T.; Talley, A. K.; Cooper, R. A.; Dzekunov, S. M.; Ferdig, M. T.; Ursos, L. M. B.; bir Singh Sidhu, A.; Naudé, B.; Deitsch, K. W.; Su, X.; Wootton, J. C.; Roepe, P. D.; Wellems, T. E. Mutations in the P. Falciparum Digestive Vacuole Transmembrane Protein PfCRT and Evidence for Their Role in Chloroquine Resistance. *Mol. Cell* **2000**, *6* (4), 861–871.

(91) Kuhn, Y.; Sanchez, C. P.; Ayoub, D.; Saridaki, T.; van Dorsselaer, A.; Lanzer, M.

Trafficking of the Phosphoprotein PfCRT to the Digestive Vacuolar Membrane in Plasmodium Falciparum. *Traffic* **2010**, *11* (2), 236–249.

(92) World Health Organization. WHO Model Lists of Essential Medicines.

(93) Burgoine, K. L.; Bancone, G.; Nosten, F. The Reality of Using Primaquine. *Malar. J.* **2010**, *9* (1), 376.

(94) N. Burrows, J.; Chibale, K.; N.C. Wells, T. The State of the Art in Anti-Malarial Drug Discovery and Development. *Curr. Top. Med. Chem.* **2011**, *11* (10), 1226–1254.

(95) Na-Bangchang, K.; Karbwang, J. Current Status of Malaria Chemotherapy and the Role of Pharmacology in Antimalarial Drug Research and Development. *Fundam. Clin. Pharmacol.* **2009**, *23* (4), 387–409.

(96) Trenholme, G. M.; Williams, R. L.; Desjardins, R. E.; Frischer, H.; Carson, P. E.; Rieckmann, K. H.; Canfield, C. J. Mefloquine (WR 142,490) in the Treatment of Human Malaria. *Science (80-.).* **1975**, *190* (4216), 792–794.

(97) Nzila, A. The Past, Present and Future of Antifolates in the Treatment of Plasmodium Falciparum Infection. *J. Antimicrob. Chemother.* **2006**, *57* (6), 1043–1054.

(98) Gregson, A.; Plowe, C. V. Mechanisms of Resistance of Malaria Parasites to Antifolates. *Pharmacol. Rev.* **2005**, *57* (1), 117–145.

(99) Plowe, C. V.; Djimde, A.; Bouare, M.; Doumbo, O.; Wellems, T. E. Pyrimethamine and Proguanil Resistance-Conferring Mutations in Plasmodium Falciparum Dihydrofolate Reductase: Polymerase Chain Reaction Methods for Surveillance in Africa. *Am. J. Trop. Med. Hyg.* **1995**, *52* (6), 565–568.

(100) Triglia, T.; Cowman, A. F. Primary Structure and Expression of the Dihydropteroate Synthetase Gene of Plasmodium Falciparum. *Proc. Natl. Acad. Sci.* **1994**, *91* (15), 7149–7153.

(101) Brooks, D. R.; Wang, P.; Read, M.; Watkins, W. M.; Sims, P. F. G.; Hyde, J. E. Sequence Variation of the Hydroxymethyldihydropterin Pyrophosphokinase: Dihydropteroate Synthase Gene in Lines of the Human Malaria Parasite,

Plasmodium Falciparum, with Differing Resistance to Sulfadoxine. *Eur. J. Biochem.* **1994**, *224* (2), 397–405.

(102) Group, Q. A. C. R. Antimalaria Studies on Qinghaosu. *Chin. Med. J. (Engl).* **1979**, *92* (12), 811–816.

(103) Price, R. N.; Douglas, N. M. Artemisinin Combination Therapy for Malaria: Beyond Good Efficacy. *Clin. Infect. Dis.* **2009**, *49* (11), 1638–1640.

(104) Eastman, R. T.; Fidock, D. A. Artemisinin-Based Combination Therapies: A Vital Tool in Efforts to Eliminate Malaria. *Nat. Rev. Microbiol.* **2009**, *7* (12), 864–874.

(105) Shandilya, A.; Chacko, S.; Jayaram, B.; Ghosh, I. A Plausible Mechanism for the Antimalarial Activity of Artemisinin: A Computational Approach. *Sci. Rep.* **2013**, *3* (1), 2513.

(106) Mbengue, A.; Bhattacharjee, S.; Pandharkar, T.; Liu, H.; Estiu, G.; Stahelin, R. V.; Rizk, S. S.; Njimoh, D. L.; Ryan, Y.; Chotivanich, K.; Nguon, C.; Ghorbal, M.; Lopez-Rubio, J.-J.; Pfrender, M.; Emrich, S.; Mohandas, N.; Dondorp, A. M.; Wiest, O.; Haldar, K. A Molecular Mechanism of Artemisinin Resistance in Plasmodium Falciparum Malaria. *Nature* **2015**, *520* (7549), 683–687.

(107) Antony, H.; Parija, S. Antimalarial Drug Resistance: An Overview. *Trop. Parasitol.* **2016**, *6* (1), 30.

(108) Majori, G. Combined Antimalarial Therapy Using Artemisinin. *Parassitologia* **2004**, *46* (1–2), 85–87.

(109) Aweeka, F. T.; German, P. I. Clinical Pharmacology of Artemisinin-Based Combination Therapies. *Clin. Pharmacokinet.* **2008**, *47* (2), 91–102.

(110) Fidock, D. A.; Rosenthal, P. J.; Croft, S. L.; Brun, R.; Nwaka, S. Antimalarial Drug Discovery: Efficacy Models for Compound Screening. *Nat. Rev. Drug Discov.* **2004**, *3* (6), 509–520.

(111) Ashley, E. A.; Dhorda, M.; Fairhurst, R. M.; Amaratunga, C.; Lim, P.; Suon, S.; Sreng, S.; Anderson, J. M.; Mao, S.; Sam, B.; Sopha, C.; Chuor, C. M.; Nguon, C.; Sovannaroth, S.; Pukrittayakamee, S.; Jittamala, P.; Chotivanich, K.; Chutasmit, K.;

Suchatsoonthorn, C.; Runcharoen, R.; Hien, T. T.; Thuy-Nhien, N. T.; Thanh, N. V.; Phu, N. H.; Htut, Y.; Han, K.-T.; Aye, K. H.; Mokuolu, O. A.; Olaosebikan, R. R.; Folaranmi, O. O.; Mayxay, M.; Khanthavong, M.; Hongvanthong, B.; Newton, P. N.; Onyamboko, M. A.; Fanello, C. I.; Tshefu, A. K.; Mishra, N.; Valecha, N.; Phyo, A. P.; Nosten, F.; Yi, P.; Tripura, R.; Borrmann, S.; Bashraheil, M.; Peshu, J.; Faiz, M. A.; Ghose, A.; Hossain, M. A.; Samad, R.; Rahman, M. R.; Hasan, M. M.; Islam, A.; Miotto, O.; Amato, R.; MacInnis, B.; Stalker, J.; Kwiatkowski, D. P.; Bozdech, Z.; Jeeyapant, A.; Cheah, P. Y.; Sakulthaew, T.; Chalk, J.; Intharabut, B.; Silamut, K.; Lee, S. J.; Vihokhern, B.; Kunasol, C.; Imwong, M.; Tarning, J.; Taylor, W. J.; Yeung, S.; Woodrow, C. J.; Flegg, J. A.; Das, D.; Smith, J.; Venkatesan, M.; Plowe, C. V.; Stepniewska, K.; Guerin, P. J.; Dondorp, A. M.; Day, N. P.; White, N. J. Spread of Artemisinin Resistance in Plasmodium Falciparum Malaria. *N. Engl. J. Med.* **2014**, *371* (5), 411–423.

(112) Balikagala, B.; Fukuda, N.; Ikeda, M.; Katuro, O. T.; Tachibana, S.-I.; Yamauchi, M.; Opio, W.; Emoto, S.; Anywar, D. A.; Kimura, E.; Palacpac, N. M. Q.; Odongo-Aginya, E. I.; Ogwang, M.; Horii, T.; Mita, T. Evidence of Artemisinin-Resistant Malaria in Africa. *N. Engl. J. Med.* **2021**, *385* (13), 1163–1171.

(113) Cui, L.; Mharakurwa, S.; Ndiaye, D.; Rathod, P. K.; Rosenthal, P. J. Antimalarial Drug Resistance: Literature Review and Activities and Findings of the ICEMR Network. *Am. J. Trop. Med. Hyg.* **2015**, *93* (3_Suppl), 57–68.

(114) Wells, T. N. C.; Alonso, P. L.; Gutteridge, W. E. New Medicines to Improve Control and Contribute to the Eradication of Malaria. *Nat. Rev. Drug Discov.* **2009**, *8* (11), 879–891.

(115) Olliaro, P.; Nevill, C.; LeBras, J.; Ringwald, P.; Mussano, P.; Garner, P.; Brasseur, P. Systematic Review of Amodiaquine Treatment in Uncomplicated Malaria. *Lancet* **1996**, *348* (9036), 1196–1201.

(116) Lind, D. E.; Levi, J. A.; Vincent, P. C. Amodiaquine-Induced Agranulocytosis: Toxic Effect of Amodiaquine in Bone Marrow Cultures In Vitro. *BMJ* **1973**, *1* (5851), 458–460.

(117) Hatton, C. S. R.; Bunch, C.; Peto, T. E. A.; Pasvol, G.; Russell, S. J.; Singer, C. R. J.;

Edwards, G.; Winstanley, P. Frequency of Severe Neutropenia Associated with Amodiaquine Prophylaxis Against Malaria. *Lancet* **1986**, *327* (8478), 411–414.

(118) Desforges, J. F.; Beutler, E. Glucose-6-Phosphate Dehydrogenase Deficiency. *N. Engl. J. Med.* **1991**, *324* (3), 169–174.

(119) Flannery, E. L.; Chatterjee, A. K.; Winzeler, E. A. Antimalarial Drug Discovery — Approaches and Progress towards New Medicines. *Nat. Rev. Microbiol.* **2013**, *11* (12), 849–862.

(120) Cabrera, D. G.; Horatscheck, A.; Wilson, C. R.; Basarab, G.; Eyermann, C. J.; Chibale, K. Plasmodial Kinase Inhibitors: License to Cure? *J. Med. Chem.* **2018**, *61* (18), 8061–8077.

(121) Srivastava, I. K.; Vaidya, A. B. A Mechanism for the Synergistic Antimalarial Action of Atovaquone and Proguanil. *Antimicrob. Agents Chemother.* **1999**, *43* (6), 1334–1339.

(122) Yuthavong, Y.; Tarnchompoo, B.; Vilaivan, T.; Chitnumsub, P.; Kamchonwongpaisan, S.; Charman, S. A.; McLennan, D. N.; White, K. L.; Vivas, L.; Bongard, E.; Thongphanchang, C.; Taweechai, S.; Vanichtanankul, J.; Rattanajak, R.; Arwon, U.; Fantauzzi, P.; Yuvaniyama, J.; Charman, W. N.; Matthews, D. Malarial Dihydrofolate Reductase as a Paradigm for Drug Development against a Resistance-Compromised Target. *Proc. Natl. Acad. Sci.* **2012**, *109* (42), 16823–16828.

(123) Chughlay, M. F.; Rossignol, E.; Donini, C.; El Gaaloul, M.; Lorch, U.; Coates, S.; Langdon, G.; Hammond, T.; Möhrle, J.; Chalon, S. First-in-human Clinical Trial to Assess the Safety, Tolerability and Pharmacokinetics of P218, a Novel Candidate for Malaria Chemoprotection. *Br. J. Clin. Pharmacol.* **2020**, *86* (6), 1113–1124.

(124) Ittarat, I.; Asawamahasakda, W.; Meshnick, S. R. The Effects of Antimalarials on the Plasmodium Falciparum Dihydroorotate Dehydrogenase. *Exp. Parasitol.* **1994**, *79* (1), 50–56.

(125) Baldwin, J.; Michnoff, C. H.; Malmquist, N. A.; White, J.; Roth, M. G.; Rathod, P. K.; Phillips, M. A. High-Throughput Screening for Potent and Selective Inhibitors of

Plasmodium Falciparum Dihydroorotate Dehydrogenase. *J. Biol. Chem.* **2005**, *280* (23), 21847–21853.

(126) Gujjar, R.; Marwaha, A.; El Mazouni, F.; White, J.; White, K. L.; Creason, S.; Shackleford, D. M.; Baldwin, J.; Charman, W. N.; Buckner, F. S.; Charman, S.; Rathod, P. K.; Phillips, M. A. Identification of a Metabolically Stable Triazolopyrimidine-Based Dihydroorotate Dehydrogenase Inhibitor with Antimalarial Activity in Mice. *J. Med. Chem.* **2009**, *52* (7), 1864–1872.

(127) Gujjar, R.; El Mazouni, F.; White, K. L.; White, J.; Creason, S.; Shackleford, D. M.; Deng, X.; Charman, W. N.; Bathurst, I.; Burrows, J.; Floyd, D. M.; Matthews, D.; Buckner, F. S.; Charman, S. A.; Phillips, M. A.; Rathod, P. K. Lead Optimization of Aryl and Aralkyl Amine-Based Triazolopyrimidine Inhibitors of Plasmodium Falciparum Dihydroorotate Dehydrogenase with Antimalarial Activity in Mice. *J. Med. Chem.* **2011**, *54* (11), 3935–3949.

(128) Coteron, J. M.; Marco, M.; Esquivias, J.; Deng, X.; White, K. L.; White, J.; Koltun, M.; El Mazouni, F.; Kokkonda, S.; Katneni, K.; Bhamidipati, R.; Shackleford, D. M.; Angulo-Barturen, I.; Ferrer, S. B.; Jiménez-Díaz, M. B.; Gamo, F.-J.; Goldsmith, E. J.; Charman, W. N.; Bathurst, I.; Floyd, D.; Matthews, D.; Burrows, J. N.; Rathod, P. K.; Charman, S. A.; Phillips, M. A. Structure-Guided Lead Optimization of Triazolopyrimidine-Ring Substituents Identifies Potent Plasmodium Falciparum Dihydroorotate Dehydrogenase Inhibitors with Clinical Candidate Potential. *J. Med. Chem.* **2011**, *54* (15), 5540–5561.

(129) Swinney, D. C.; Anthony, J. How Were New Medicines Discovered? *Nat. Rev. Drug Discov.* **2011**, *10* (7), 507–519.

(130) Hovlid, M. L.; Winzeler, E. A. Phenotypic Screens in Antimalarial Drug Discovery. *Trends Parasitol.* **2016**, *32* (9), 697–707.

(131) Butera, J. A. Phenotypic Screening as a Strategic Component of Drug Discovery Programs Targeting Novel Antiparasitic and Antimycobacterial Agents: An Editorial. *J. Med. Chem.* **2013**, *56* (20), 7715–7718.

(132) Katsuno, K.; Burrows, J. N.; Duncan, K.; van Huijsduijnen, R. H.; Kaneko, T.; Kita, K.; Mowbray, C. E.; Schmatz, D.; Warner, P.; Slingsby, B. T. Hit and Lead Criteria

in Drug Discovery for Infectious Diseases of the Developing World. *Nat. Rev. Drug Discov.* **2015**, *14* (11), 751–758.

(133) Plouffe, D.; Brinker, A.; McNamara, C.; Henson, K.; Kato, N.; Kuhen, K.; Nagle, A.; Adrián, F.; Matzen, J. T.; Anderson, P.; Nam, T.; Gray, N. S.; Chatterjee, A.; Janes, J.; Yan, S. F.; Trager, R.; Caldwell, J. S.; Schultz, P. G.; Zhou, Y.; Winzeler, E. A. In Silico Activity Profiling Reveals the Mechanism of Action of Antimalarials Discovered in a High-Throughput Screen. *Proc. Natl. Acad. Sci.* **2008**, *105* (26), 9059–9064.

(134) Guiguemde, W. A.; Shelat, A. A.; Bouck, D.; Duffy, S.; Crowther, G. J.; Davis, P. H.; Smithson, D. C.; Connelly, M.; Clark, J.; Zhu, F.; Jiménez-Díaz, M. B.; Martinez, M. S.; Wilson, E. B.; Tripathi, A. K.; Gut, J.; Sharlow, E. R.; Bathurst, I.; Mazouni, F. El; Fowble, J. W.; Forquer, I.; McGinley, P. L.; Castro, S.; Angulo-Barturen, I.; Ferrer, S.; Rosenthal, P. J.; DeRisi, J. L.; Sullivan, D. J.; Lazo, J. S.; Roos, D. S.; Riscoe, M. K.; Phillips, M. A.; Rathod, P. K.; Van Voorhis, W. C.; Avery, V. M.; Guy, R. K. Chemical Genetics of Plasmodium Falciparum. *Nature* **2010**, *465* (7296), 311–315.

(135) Avery, V. M.; Bashyam, S.; Burrows, J. N.; Duffy, S.; Papadatos, G.; Puthukkuti, S.; Sambandan, Y.; Singh, S.; Spangenberg, T.; Waterson, D.; Willis, P. Screening and Hit Evaluation of a Chemical Library against Blood-Stage Plasmodium Falciparum. *Malar. J.* **2014**, *13* (1), 190.

(136) Baragaña, B.; Hallyburton, I.; Lee, M. C. S.; Norcross, N. R.; Grimaldi, R.; Otto, T. D.; Proto, W. R.; Blagborough, A. M.; Meister, S.; Wirjanata, G.; Ruecker, A.; Upton, L. M.; Abraham, T. S.; Almeida, M. J.; Pradhan, A.; Porzelle, A.; Martínez, M. S.; Bolscher, J. M.; Woodland, A.; Luksch, T.; Norval, S.; Zuccotto, F.; Thomas, J.; Simeons, F.; Stojanovski, L.; Osuna-Cabello, M.; Brock, P. M.; Churcher, T. S.; Sala, K. A.; Zakutansky, S. E.; Jiménez-Díaz, M. B.; Sanz, L. M.; Riley, J.; Basak, R.; Campbell, M.; Avery, V. M.; Sauerwein, R. W.; Dechering, K. J.; Noviyanti, R.; Campo, B.; Frearson, J. A.; Angulo-Barturen, I.; Ferrer-Bazaga, S.; Gamo, F. J.; Wyatt, P. G.; Leroy, D.; Siegl, P.; Delves, M. J.; Kyle, D. E.; Wittlin, S.; Marfurt, J.; Price, R. N.; Sinden, R. E.; Winzeler, E. A.; Charman, S. A.; Bebrevska, L.; Gray, D. W.; Campbell, S.; Fairlamb, A. H.; Willis, P. A.; Rayner, J. C.; Fidock, D. A.; Read, K. D.; Gilbert, I. H. A Novel Multiple-Stage Antimalarial Agent That Inhibits Protein

Synthesis. *Nature* **2015**, *522* (7556), 315–320.

(137) Spillman, N. J.; Kirk, K. The Malaria Parasite Cation ATPase PfATP4 and Its Role in the Mechanism of Action of a New Arsenal of Antimalarial Drugs. *Int. J. Parasitol. Drugs Drug Resist.* **2015**, *5* (3), 149–162.

(138) White, N. J.; Pukrittayakamee, S.; Phyo, A. P.; Rueangweerayut, R.; Nosten, F.; Jittamala, P.; Jeeyapant, A.; Jain, J. P.; Lefèvre, G.; Li, R.; Magnusson, B.; Diagana, T. T.; Leong, F. J. Spiroindolone KAE609 for Falciparum and Vivax Malaria. *N. Engl. J. Med.* **2014**, *371* (5), 403–410.

(139) Alonso, P. L.; Brown, G.; Arevalo-Herrera, M.; Binka, F.; Chitnis, C.; Collins, F.; Doumbo, O. K.; Greenwood, B.; Hall, B. F.; Levine, M. M.; Mendis, K.; Newman, R. D.; Plowe, C. V.; Rodríguez, M. H.; Sinden, R.; Slutsker, L.; Tanner, M. A Research Agenda to Underpin Malaria Eradication. *PLoS Med.* **2011**, *8* (1), e1000406.

(140) Schuster, F. L. Cultivation of Plasmodium Spp. *Clin. Microbiol. Rev.* **2002**, *15* (3), 355–364.

(141) Leland, P.; Hollingdale, M. R.; Sigler, C. I. In Vitro Cultivation of the Exoerythrocytic Stage of Plasmodium Berghei in Irradiated Hepatoma Cells. *Am. J. Trop. Med. Hyg.* **1985**, *34* (1), 21–23.

(142) Meister, S.; Plouffe, D. M.; Kuhen, K. L.; Bonamy, G. M. C.; Wu, T.; Barnes, S. W.; Bopp, S. E.; Borboa, R.; Bright, A. T.; Che, J.; Cohen, S.; Dharia, N. V.; Gagaring, K.; Gettayacamin, M.; Gordon, P.; Groessl, T.; Kato, N.; Lee, M. C. S.; McNamara, C. W.; Fidock, D. A.; Nagle, A.; Nam, T.; Richmond, W.; Roland, J.; Rottmann, M.; Zhou, B.; Froissard, P.; Glynne, R. J.; Mazier, D.; Sattabongkot, J.; Schultz, P. G.; Tuntland, T.; Walker, J. R.; Zhou, Y.; Chatterjee, A.; Diagana, T. T.; Winzeler, E. A. Imaging of Plasmodium Liver Stages to Drive Next-Generation Antimalarial Drug Discovery. *Science (80-.).* **2011**, *334* (6061), 1372–1377.

(143) Gego, A.; Silvie, O.; Franetich, J.-F.; Farhati, K.; Hannoun, L.; Luty, A. J. F.; Sauerwein, R. W.; Boucheix, C.; Rubinstein, E.; Mazier, D. New Approach for High-Throughput Screening of Drug Activity on Plasmodium Liver Stages. *Antimicrob. Agents Chemother.* **2006**, *50* (4), 1586–1589.

(144) Wu, T.; Nagle, A.; Kuhen, K.; Gagaring, K.; Borboa, R.; Francek, C.; Chen, Z.; Plouffe, D.; Goh, A.; Lakshminarayana, S. B.; Wu, J.; Ang, H. Q.; Zeng, P.; Kang, M. L.; Tan, W.; Tan, M.; Ye, N.; Lin, X.; Caldwell, C.; Ek, J.; Skolnik, S.; Liu, F.; Wang, J.; Chang, J.; Li, C.; Hollenbeck, T.; Tuntland, T.; Isbell, J.; Fischli, C.; Brun, R.; Rottmann, M.; Dartois, V.; Keller, T.; Diagana, T.; Winzeler, E.; Glynne, R.; Tully, D. C.; Chatterjee, A. K. Imidazolopiperazines: Hit to Lead Optimization of New Antimalarial Agents. *J. Med. Chem.* **2011**, *54* (14), 5116–5130.

(145) Nagle, A.; Wu, T.; Kuhen, K.; Gagaring, K.; Borboa, R.; Francek, C.; Chen, Z.; Plouffe, D.; Lin, X.; Caldwell, C.; Ek, J.; Skolnik, S.; Liu, F.; Wang, J.; Chang, J.; Li, C.; Liu, B.; Hollenbeck, T.; Tuntland, T.; Isbell, J.; Chuan, T.; Alper, P. B.; Fischli, C.; Brun, R.; Lakshminarayana, S. B.; Rottmann, M.; Diagana, T. T.; Winzeler, E. A.; Glynne, R.; Tully, D. C.; Chatterjee, A. K. Imidazolopiperazines: Lead Optimization of the Second-Generation Antimalarial Agents. *J. Med. Chem.* **2012**, *55* (9), 4244–4273.

(146) Kuhen, K. L.; Chatterjee, A. K.; Rottmann, M.; Gagaring, K.; Borboa, R.; Buenviaje, J.; Chen, Z.; Francek, C.; Wu, T.; Nagle, A.; Barnes, S. W.; Plouffe, D.; Lee, M. C. S.; Fidock, D. A.; Graumans, W.; van de Vegte-Bolmer, M.; van Gemert, G. J.; Wirjanata, G.; Sebayang, B.; Marfurt, J.; Russell, B.; Suwanarusk, R.; Price, R. N.; Nosten, F.; Tungtaeng, A.; Gettayacamin, M.; Sattabongkot, J.; Taylor, J.; Walker, J. R.; Tully, D.; Patra, K. P.; Flannery, E. L.; Vinetz, J. M.; Renia, L.; Sauerwein, R. W.; Winzeler, E. A.; Glynne, R. J.; Diagana, T. T. KAF156 Is an Antimalarial Clinical Candidate with Potential for Use in Prophylaxis, Treatment, and Prevention of Disease Transmission. *Antimicrob. Agents Chemother.* **2014**, *58* (9), 5060–5067.

(147) Duffy, S.; Avery, V. M. Identification of Inhibitors of Plasmodium Falciparum Gametocyte Development. *Malar. J.* **2013**, *12* (1), 408.

(148) Almela, M. J.; Lozano, S.; Lelièvre, J.; Colmenarejo, G.; Coterón, J. M.; Rodrigues, J.; Gonzalez, C.; Herreros, E. A New Set of Chemical Starting Points with Plasmodium Falciparum Transmission-Blocking Potential for Antimalarial Drug Discovery. *PLoS One* **2015**, *10* (8), e0135139.

(149) D'Alessandro, S.; Silvestrini, F.; Dechering, K.; Corbett, Y.; Parapini, S.;

Timmerman, M.; Galastri, L.; Basilico, N.; Sauerwein, R.; Alano, P.; Taramelli, D. A Plasmodium Falciparum Screening Assay for Anti-Gametocyte Drugs Based on Parasite Lactate Dehydrogenase Detection. *J. Antimicrob. Chemother.* **2013**, *68* (9), 2048–2058.

(150) Peatey, C. L.; Spicer, T. P.; Hodder, P. S.; Trenholme, K. R.; Gardiner, D. L. A High-Throughput Assay for the Identification of Drugs against Late-Stage Plasmodium Falciparum Gametocytes. *Mol. Biochem. Parasitol.* **2011**, *180* (2), 127–131.

(151) Miguel-Blanco, C.; Lelièvre, J.; Delves, M. J.; Bardera, A. I.; Presa, J. L.; López-Barragán, M. J.; Ruecker, A.; Marques, S.; Sinden, R. E.; Herreros, E. Imaging-Based High-Throughput Screening Assay To Identify New Molecules with Transmission-Blocking Potential against Plasmodium Falciparum Female Gamete Formation. *Antimicrob. Agents Chemother.* **2015**, *59* (6), 3298–3305.

(152) Plouffe, D. M.; Wree, M.; Du, A. Y.; Meister, S.; Li, F.; Patra, K.; Lubar, A.; Okitsu, S. L.; Flannery, E. L.; Kato, N.; Tanaseichuk, O.; Comer, E.; Zhou, B.; Kuhen, K.; Zhou, Y.; Leroy, D.; Schreiber, S. L.; Scherer, C. A.; Vinetz, J.; Winzeler, E. A. High-Throughput Assay and Discovery of Small Molecules That Interrupt Malaria Transmission. *Cell Host Microbe* **2016**, *19* (1), 114–126.

(153) Lucantoni, L.; Silvestrini, F.; Signore, M.; Siciliano, G.; Eldering, M.; Dechering, K. J.; Avery, V. M.; Alano, P. A Simple and Predictive Phenotypic High Content Imaging Assay for Plasmodium Falciparum Mature Gametocytes to Identify Malaria Transmission Blocking Compounds. *Sci. Rep.* **2015**, *5* (1), 16414.

(154) Van Der Kolk, M.; DE Vlas, S. J.; Saul, A.; Van De Vegte-Bolmer, M.; Eling, W. M.; Sauerwein, W. Evaluation of the Standard Membrane Feeding Assay (SMFA) for the Determination of Malaria Transmission-Reducing Activity Using Empirical Data. *Parasitology* **2005**, *130* (1), 13–22.

(155) Terstappen, G. C.; Schlüpen, C.; Raggiaschi, R.; Gaviraghi, G. Target Deconvolution Strategies in Drug Discovery. *Nat. Rev. Drug Discov.* **2007**, *6* (11), 891–903.

(156) Al-Ali, H. The Evolution of Drug Discovery: From Phenotypes to Targets, and Back. *Medchemcomm* **2016**, *7* (5), 788–798.

(157) Chan2, X. F. S. Z. and T.-F. Chemical Genomics: A Systematic Approach in Biological Research and Drug Discovery. **2002**, No. Mol. Biol., 33-43.

(158) Sykes, M. L.; Avery, V. M. Approaches to Protozoan Drug Discovery: Phenotypic Screening. *J. Med. Chem.* **2013**, *56* (20), 7727–7740.

(159) Woodland, J. G. Nsights into the Mechanism of Action of Quinoline Antimalarials against Plasmodium Falciparum Revealed by Novel Fluorescent Analogues and Chemical Proteomics, University of Cape Town.

(160) Prieto, J. H.; Koncarevic, S.; Park, S. K.; Yates, J.; Becker, K. Large-Scale Differential Proteome Analysis in Plasmodium Falciparum under Drug Treatment. *PLoS One* **2008**, *3* (12), e4098.

(161) Yates, J. R. Mass Spectrometry and the Age of the Proteome. *J. Mass Spectrom.* **1998**, *33* (1), 1–19.

(162) Lomenick, B.; Hao, R.; Jonai, N.; Chin, R. M.; Aghajan, M.; Warburton, S.; Wang, J.; Wu, R. P.; Gomez, F.; Loo, J. A.; Wohlschlegel, J. A.; Vondriska, T. M.; Pelletier, J.; Herschman, H. R.; Clardy, J.; Clarke, C. F.; Huang, J. Target Identification Using Drug Affinity Responsive Target Stability (DARTS). *Proc. Natl. Acad. Sci.* **2009**, *106* (51), 21984–21989.

(163) Macgillivray, A. J.; Wood, D. R. The Heterogeneity of Mouse-Chromatin Nonhistone Proteins as Evidenced by Two-Dimensional Polyacrylamide-Gel Electrophoresis and Ion-Exchange Chromatography. *Eur. J. Biochem.* **1974**, *41* (1), 181–190.

(164) Klose, J.; Kobalz, U. Two-Dimensional Electrophoresis of Proteins: An Updated Protocol and Implications for a Functional Analysis of the Genome. *Electrophoresis* **1995**, *16* (1), 1034–1059.

(165) Rabilloud, T. Two-Dimensional Gel Electrophoresis in Proteomics: Old, Old Fashioned, but It Still Climbs up the Mountains. *Proteomics* **2002**, *2* (1), 3–10.

(166) Rabilloud, T.; Blisnick, T.; Heller, M.; Luche, S.; Aebersold, R.; Lunardi, J.; Braun-Breton, C. Analysis of Membrane Proteins by Two-Dimensional Electrophoresis: Comparison of the Proteins Extracted from Normal OrPlasmodium Falciparum -

Infected Erythrocyte Ghosts. *Electrophoresis* **1999**, *20* (18), 3603–3610.

(167) Deitsch, K. W.; Wellems, T. E. Membrane Modifications in Erythrocytes Parasitized by Plasmodium Falciparum. *Mol. Biochem. Parasitol.* **1996**, *76* (1–2), 1–10.

(168) Gero, A.; Dunn, C.; Brown, D.; Pulenthiran, K.; Gorovits, E.; Bakos, T.; Weis, A. New Malaria Chemotherapy Developed by Utilization of a Unique Parasite Transport System. *Curr. Pharm. Des.* **2003**, *9* (11), 867–877.

(169) Antony, H.; Pathak, V.; Ghosh, K.; Parija, S. Comparison of Protein Expression Pattern between the Plasmodium Falciparum Chloroquine-Resistant RKL9 and Chloroquine-Sensitive MRC2 Strains. *Trop. Parasitol.* **2016**, *6* (2), 136.

(170) Rujimongkon, K.; Mungthin, M.; Tummatorn, J.; Ampawong, S.; Adisakwattana, P.; Boonyuen, U.; Reamtong, O. Proteomic Analysis of Plasmodium Falciparum Response to Isocryptolepine Derivative. *PLoS One* **2019**, *14* (8), e0220871.

(171) Carrette, O.; Burkhard, P. R.; Sanchez, J.-C.; Hochstrasser, D. F. State-of-the-Art Two-Dimensional Gel Electrophoresis: A Key Tool of Proteomics Research. *Nat. Protoc.* **2006**, *1* (2), 812–823.

(172) Alban, A.; David, S. O.; Bjorkesten, L.; Andersson, C.; Sloge, E.; Lewis, S.; Currie, I. A Novel Experimental Design for Comparative Two-Dimensional Gel Analysis: Two-Dimensional Difference Gel Electrophoresis Incorporating a Pooled Internal

(173) Graves, P. R.; Haystead, T. A. J. Molecular Biologist's Guide to Proteomics. *Microbiol. Mol. Biol. Rev.* **2002**, *66* (1), 39–63.

(174) Yates, J. R.; Eng, J. K.; McCormack, A. L.; Schieltz, D. Method to Correlate Tandem Mass Spectra of Modified Peptides to Amino Acid Sequences in the Protein Database. *Anal. Chem.* **1995**, *67* (8), 1426–1436.

(175) Huang, F.; Zhang, B.; Zhou, S.; Zhao, X.; Bian, C.; Wei, Y. Chemical Proteomics: Terra Incognita for Novel Drug Target Profiling. *Chin. J. Cancer* **2012**, *31* (11), 507–518.

(176) Rix, U.; Superti-Furga, G. Target Profiling of Small Molecules by Chemical Proteomics. *Nat. Chem. Biol.* **2009**, *5* (9), 616–624.

(177) Powers, J. C.; Asgian, J. L.; Ekici, Ö. D.; James, K. E. Irreversible Inhibitors of Serine, Cysteine, and Threonine Proteases. *Chem. Rev.* **2002**, *102* (12), 4639–4750.

(178) Sadaghiani, A. M.; Verhelst, S. H.; Bogyo, M. Tagging and Detection Strategies for Activity-Based Proteomics. *Curr. Opin. Chem. Biol.* **2007**, *11* (1), 20–28.

(179) Mitsopoulos, G.; Walsh, D. P.; Chang, Y.-T. Tagged Library Approach to Chemical Genomics and Proteomics. *Curr. Opin. Chem. Biol.* **2004**, *8* (1), 26–32.

(180) Miao, Q.; Zhang, C.-C.; Kast, J. Chemical Proteomics and Its Impact on the Drug Discovery Process. *Expert Rev. Proteomics* **2012**, *9* (3), 281–291.

(181) Oda, Y.; Owa, T.; Sato, T.; Boucher, B.; Daniels, S.; Yamanaka, H.; Shinohara, Y.; Yokoi, A.; Kuromitsu, J.; Nagasu, T. Quantitative Chemical Proteomics for Identifying Candidate Drug Targets. *Anal. Chem.* **2003**, *75* (9), 2159–2165.

(182) Wang, G.; Shang, L.; Burgett, A. W. G.; Harran, P. G.; Wang, X. Diazonamide Toxins Reveal an Unexpected Function for Ornithine -Amino Transferase in Mitotic Cell Division. *Proc. Natl. Acad. Sci.* **2007**, *104* (7), 2068–2073.

(183) Shiyama, T.; Furuya, M.; Yamazaki, A.; Terada, T.; Tanaka, A. Design and Synthesis of Novel Hydrophilic Spacers for the Reduction of Nonspecific Binding Proteins on Affinity Resins. *Bioorg. Med. Chem.* **2004**, *12* (11), 2831–2841.

(184) Speers, A. E.; Cravatt, B. F. A Tandem Orthogonal Proteolysis Strategy for High-Content Chemical Proteomics. *J. Am. Chem. Soc.* **2005**, *127* (28), 10018–10019.

(185) Verhelst, S. H. L.; Fonović, M.; Bogyo, M. A Mild Chemically Cleavable Linker System for Functional Proteomic Applications. *Angew. Chemie Int. Ed.* **2007**, *46* (8), 1284–1286.

(186) Yamamoto, K.; Yamazaki, A.; Takeuchi, M.; Tanaka, A. A Versatile Method of Identifying Specific Binding Proteins on Affinity Resins. *Anal. Biochem.* **2006**, *352* (1), 15–23.

(187) Bantscheff, M.; Hopf, C.; Savitski, M. M.; Dittmann, A.; Grandi, P.; Michon, A.-M.; Schlegl, J.; Abraham, Y.; Becher, I.; Bergamini, G.; Boesche, M.; Delling, M.; Dümpelfeld, B.; Eberhard, D.; Huthmacher, C.; Mathieson, T.; Poeckel, D.; Reader,

V.; Strunk, K.; Sweetman, G.; Kruse, U.; Neubauer, G.; Ramsden, N. G.; Drewes, G. Chemoproteomics Profiling of HDAC Inhibitors Reveals Selective Targeting of HDAC Complexes. *Nat. Biotechnol.* **2011**, *29* (3), 255–265.

(188) Bantscheff, M.; Drewes, G. Chemoproteomic Approaches to Drug Target Identification and Drug Profiling. *Bioorg. Med. Chem.* **2012**, *20* (6), 1973–1978.

(189) Greenbaum, D.; Baruch, A.; Hayrapetian, L.; Darula, Z.; Burlingame, A.; Medzihradszky, K. F.; Bogyo, M. Chemical Approaches for Functionally Probing the Proteome. *Mol. Cell. Proteomics* **2002**, *1* (1), 60–68.

(190) Rosenthal, P.; Sijwali, P.; Singh, A.; Shenai, B. Cysteine Proteases of Malaria Parasites: Targets for Chemotherapy. *Curr. Pharm. Des.* **2002**, *8* (18), 1659–1672.

(191) Greenbaum, D.; Medzihradszky, K. F.; Burlingame, A.; Bogyo, M. Epoxide Electrophiles as Activity-Dependent Cysteine Protease Profiling and Discovery Tools. *Chem. Biol.* **2000**, *7* (8), 569–581.

(192) Penarete-Vargas, D. M.; Boisson, A.; Urbach, S.; Chantelauze, H.; Peyrottes, S.; Fraisse, L.; Vial, H. J. A Chemical Proteomics Approach for the Search of Pharmacological Targets of the Antimalarial Clinical Candidate Albitiazolium in Plasmodium Falciparum Using Photocrosslinking and Click Chemistry. *pone* **2014**.

(193) Paquet, T.; Le Manach, C.; Cabrera, D. G.; Younis, Y.; Henrich, P. P.; Abraham, T. S.; Lee, M. C. S.; Basak, R.; Ghidelli-Disse, S.; Lafuente-Monasterio, M. J.; Bantscheff, M.; Ruecker, A.; Blagborough, A. M.; Zakutansky, S. E.; Zeeman, A.-M.; White, K. L.; Shackleford, D. M.; Mannila, J.; Morizzi, J.; Scheurer, C.; Angulo-Barturen, I.; Martínez, M. S.; Ferrer, S.; Sanz, L. M.; Gamo, F. J.; Reader, J.; Botha, M.; Dechering, K. J.; Sauerwein, R. W.; Tungtaeng, A.; Vanachayangkul, P.; Lim, C. S.; Burrows, J.; Witty, M. J.; Marsh, K. C.; Bodenreider, C.; Rochford, R.; Solapure, S. M.; Jiménez-Díaz, M. B.; Wittlin, S.; Charman, S. A.; Donini, C.; Campo, B.; Birkholtz, L.-M.; Hanson, K. K.; Drewes, G.; Kocken, C. H. M.; Delves, M. J.; Leroy, D.; Fidock, D. A.; Waterson, D.; Street, L. J.; Chibale, K. Antimalarial Efficacy of MMV390048, an Inhibitor of Plasmodium Phosphatidylinositol 4-Kinase. *Sci. Transl. Med.* **2017**, *9* (387), eaad9735.

(194) Wang, J.; Zhang, C.-J.; Chia, W. N.; Loh, C. C. Y.; Li, Z.; Lee, Y. M.; He, Y.; Yuan,

L.-X.; Lim, T. K.; Liu, M.; Liew, C. X.; Lee, Y. Q.; Zhang, J.; Lu, N.; Lim, C. T.; Hua, Z.-C.; Liu, B.; Shen, H.-M.; Tan, K. S. W.; Lin, Q. Haem-Activated Promiscuous Targeting of Artemisinin in Plasmodium Falciparum. *Nat. Commun.* **2015**, *6* (1), 10111.

(195) Ismail, H. M.; Barton, V.; Phanchana, M.; Charoensutthivarakul, S.; Wong, M. H. L.; Hemingway, J.; Biagini, G. A.; O'Neill, P. M.; Ward, S. A. Artemisinin Activity-Based Probes Identify Multiple Molecular Targets within the Asexual Stage of the Malaria Parasites Plasmodium Falciparum 3D7. *Proc. Natl. Acad. Sci.* **2016**, *113* (8), 2080–2085.

(196) Siwo, G. H.; Smith, R. S.; Tan, A.; Button-Simons, K. A.; Checkley, L. A.; Ferdig, M. T. An Integrative Analysis of Small Molecule Transcriptional Responses in the Human Malaria Parasite Plasmodium Falciparum. *BMC Genomics* **2015**, *16* (1), 1030.

(197) Yoo, E.; Schulze, C. J.; Stokes, B. H.; Onguka, O.; Yeo, T.; Mok, S.; Gnädig, N. F.; Zhou, Y.; Kurita, K.; Foe, I. T.; Terrell, S. M.; Boucher, M. J.; Cieplak, P.; Kumpornsin, K.; Lee, M. C. S.; Linington, R. G.; Long, J. Z.; Uhlemann, A.-C.; Weerapana, E.; Fidock, D. A.; Bogyo, M. The Antimalarial Natural Product Salinipostin A Identifies Essential α/β Serine Hydrolases Involved in Lipid Metabolism in P. Falciparum Parasites. *Cell Chem. Biol.* **2020**, *27* (2), 143-157.e5.

(198) Chang, J.; Kim, Y.; Kwon, H. J. Advances in Identification and Validation of Protein Targets of Natural Products without Chemical Modification. *Nat. Prod. Rep.* **2016**, *33* (5), 719–730.

(199) Park, C.; Marqusee, S. Pulse Proteolysis: A Simple Method for Quantitative Determination of Protein Stability and Ligand Binding. *Nat. Methods* **2005**, *2* (3), 207–212.

(200) Stankunas, K.; Bayle, J. H.; Gestwicki, J. E.; Lin, Y.-M.; Wandless, T. J.; Crabtree, G. R. Conditional Protein Alleles Using Knockin Mice and a Chemical Inducer of Dimerization. *Mol. Cell* **2003**, *12* (6), 1615–1624.

(201) Sun, W.; Tanaka, T. Q.; Magle, C. T.; Huang, W.; Southall, N.; Huang, R.; Dehdashti, S. J.; McKew, J. C.; Williamson, K. C.; Zheng, W. Chemical Signatures and New

Drug Targets for Gametocytocidal Drug Development. *Sci. Rep.* **2015**, *4* (1), 3743.

(202) Lu, K.; Mansfield, C. R.; Fitzgerald, M. C.; Derbyshire, E. R. Chemoproteomics for Plasmodium Parasite Drug Target Discovery. *ChemBioChem* **2021**, *22* (16), 2591–2599.

(203) Mateus, A.; Määttä, T. A.; Savitski, M. M. Thermal Proteome Profiling: Unbiased Assessment of Protein State through Heat-Induced Stability Changes. *Proteome Sci.* **2016**, *15* (1), 13.

(204) Dziekan, J. M.; Yu, H.; Chen, D.; Dai, L.; Wirjanata, G.; Larsson, A.; Prabhu, N.; Sobota, R. M.; Bozdech, Z.; Nordlund, P. Identifying Purine Nucleoside Phosphorylase as the Target of Quinine Using Cellular Thermal Shift Assay. *Sci. Transl. Med.* **2019**, *11* (473).

(205) Lu, K.-Y.; Quan, B.; Sylvester, K.; Srivastava, T.; Fitzgerald, M. C.; Derbyshire, E. R. Plasmodium Chaperonin TRiC/CCT Identified as a Target of the Antihistamine Clemastine Using Parallel Chemoproteomic Strategy. *Proc. Natl. Acad. Sci.* **2020**, *117* (11), 5810–5817.

(206) Cowell, A. N.; Winzeler, E. A. Advances in Omics-Based Methods to Identify Novel Targets for Malaria and Other Parasitic Protozoan Infections. *Genome Med.* **2019**, *11* (1), 63.

(207) Kloehn, J.; Blume, M.; Cobbold, S.; Saunders, E.; Dagley, M.; McConville, M. Using Metabolomics to Dissect Host–Parasite Interactions. *Curr. Opin. Microbiol.* **2016**, *32*, 59–65.

(208) Flueck, C.; Drought, L. G.; Jones, A.; Patel, A.; Perrin, A. J.; Walker, E. M.; Nofal, S. D.; Snijders, A. P.; Blackman, M. J.; Baker, D. A. Phosphodiesterase Beta Is the Master Regulator of CAMP Signalling during Malaria Parasite Invasion. *PLOS Biol.* **2019**, *17* (2), e3000154.

(209) Lim, M. Y.-X.; LaMonte, G.; Lee, M. C. S.; Reimer, C.; Tan, B. H.; Corey, V.; Tjahjadi, B. F.; Chua, A.; Nachon, M.; Wintjens, R.; Gedeck, P.; Malleret, B.; Renia, L.; Bonamy, G. M. C.; Ho, P. C.-L.; Yeung, B. K. S.; Chow, E. D.; Lim, L.; Fidock, D. A.; Diagana, T. T.; Winzeler, E. A.; Bifani, P. UDP-Galactose and Acetyl-CoA

Transporters as Plasmodium Multidrug Resistance Genes. *Nat. Microbiol.* **2016**, *1* (12), 16166.

(210) Marapana, D. S.; Dagley, L. F.; Sandow, J. J.; Nebl, T.; Triglia, T.; Pasternak, M.; Dickerman, B. K.; Crabb, B. S.; Gilson, P. R.; Webb, A. I.; Boddey, J. A.; Cowman, A. F. Plasmepsin V Cleaves Malaria Effector Proteins in a Distinct Endoplasmic Reticulum Translocation Interactome for Export to the Erythrocyte. *Nat. Microbiol.* **2018**, *3* (9), 1010–1022.

(211) Okombo, J.; Kanai, M.; Deni, I.; Fidock, D. A. Genomic and Genetic Approaches to Studying Antimalarial Drug Resistance and Plasmodium Biology. *Trends Parasitol.* **2021**, *37* (6), 476–492.

(212) Rocamora, F.; Winzeler, E. A. Genomic Approaches to Drug Resistance in Malaria. *Annu. Rev. Microbiol.* **2020**, *74* (1), 761–786.

(213) Luth, M. R.; Gupta, P.; Ottilie, S.; Winzeler, E. A. Using in Vitro Evolution and Whole Genome Analysis To Discover Next Generation Targets for Antimalarial Drug Discovery. *ACS Infect. Dis.* **2018**, *4* (3), 301–314.

(214) Flannery, E. L.; Fidock, D. A.; Winzeler, E. A. Using Genetic Methods To Define the Targets of Compounds with Antimalarial Activity. *J. Med. Chem.* **2013**, *56* (20), 7761–7771.

(215) Kato, N.; Comer, E.; Sakata-Kato, T.; Sharma, A.; Sharma, M.; Maetani, M.; Bastien, J.; Brancucci, N. M.; Bittker, J. A.; Corey, V.; Clarke, D.; Derbyshire, E. R.; Dornan, G. L.; Duffy, S.; Eckley, S.; Itoe, M. A.; Koolen, K. M. J.; Lewis, T. A.; Lui, P. S.; Lukens, A. K.; Lund, E.; March, S.; Meibalan, E.; Meier, B. C.; McPhail, J. A.; Mitasev, B.; Moss, E. L.; Sayes, M.; Van Gessel, Y.; Wawer, M. J.; Yoshinaga, T.; Zeeman, A.-M.; Avery, V. M.; Bhatia, S. N.; Burke, J. E.; Catteruccia, F.; Clardy, J. C.; Clemons, P. A.; Dechering, K. J.; Duvall, J. R.; Foley, M. A.; Gusovsky, F.; Kocken, C. H. M.; Marti, M.; Morningstar, M. L.; Munoz, B.; Neafsey, D. E.; Sharma, A.; Winzeler, E. A.; Wirth, D. F.; Scherer, C. A.; Schreiber, S. L. Diversity-Oriented Synthesis Yields Novel Multistage Antimalarial Inhibitors. *Nature* **2016**, *538* (7625), 344–349.

(216) Sonoiki, E.; Nsanzabana, C.; Legac, J.; Sindhe, K. M. V.; DeRisi, J.; Rosenthal, P. J.

Altered Plasmodium Falciparum Sensitivity to the Antiretroviral Protease Inhibitor Lopinavir Associated with Polymorphisms in Pfmdr1. *Antimicrob. Agents Chemother.* **2017**, *61* (1).

(217) Gilson, P. R.; Kumarasingha, R.; Thompson, J.; Zhang, X.; Penington, J. S.; Kalhor, R.; Bullen, H. E.; Lehane, A. M.; Dans, M. G.; de Koning-Ward, T. F.; Holien, J. K.; Soares da Costa, T. P.; Hulett, M. D.; Buskes, M. J.; Crabb, B. S.; Kirk, K.; Papenfuss, A. T.; Cowman, A. F.; Abbott, B. M. A 4-Cyano-3-Methylisoquinoline Inhibitor of Plasmodium Falciparum Growth Targets the Sodium Efflux Pump PfATP4. *Sci. Rep.* **2019**, *9* (1), 10292.

(218) Vanaerschot, M.; Murithi, J. M.; Pasaje, C. F. A.; Ghidelli-Disse, S.; Dwomoh, L.; Bird, M.; Spottiswoode, N.; Mittal, N.; Arendse, L. B.; Owen, E. S.; Wicht, K. J.; Siciliano, G.; Bösche, M.; Yeo, T.; Kumar, T. R. S.; Mok, S.; Carpenter, E. F.; Giddins, M. J.; Sanz, O.; Ottilie, S.; Alano, P.; Chibale, K.; Llinás, M.; Uhlemann, A.-C.; Delves, M.; Tobin, A. B.; Doerig, C.; Winzeler, E. A.; Lee, M. C. S.; Niles, J. C.; Fidock, D. A. Inhibition of Resistance-Refractory P. Falciparum Kinase PKG Delivers Prophylactic, Blood Stage, and Transmission-Blocking Antiplasmodial Activity. *Cell Chem. Biol.* **2020**, *27* (7), 806-816.e8.

(219) Baker, D. A.; Matralis, A. N.; Osborne, S. A.; Large, J. M.; Penzo, M. Targeting the Malaria Parasite CGMP-Dependent Protein Kinase to Develop New Drugs. *Front. Microbiol.* **2020**, *11*.

(220) Refaat, H. M. Synthesis of Potential Anticancer Derivatives of Pyrido[1,2-a]Benzimidazoles. *Med. Chem. Res.* **2012**, *21* (7), 1253–1260.

(221) Takeshita, H.; Watanabe, J.; Kimura, Y.; Kawakami, K.; Takahashi, H.; Takemura, M.; Kitamura, A.; Someya, K.; Nakajima, R. Novel Pyridobenzimidazole Derivatives Exhibiting Antifungal Activity by the Inhibition of β-1,6-Glucan Synthesis. *Bioorg. Med. Chem. Lett.* **2010**, *20* (13), 3893–3896.

(222) Pieroni, M.; Tipparaju, S. K.; Lun, S.; Song, Y.; Sturm, A. W.; Bishai, W. R.; Kozikowski, A. P. Pyrido[1,2- a]Benzimidazole-Based Agents Active Against Tuberculosis (TB), Multidrug-Resistant (MDR) TB and Extensively Drug-Resistant (XDR) TB. *ChemMedChem* **2011**, *6* (2), 334–342.

(223) Kotovskaya, S. K.; 1; Baskakova, Z. M.; 1; Charushin, V. N.; 2, 4; Chupakhin, O. N.; 2; Belanov, E. F.; 3; Bormotov, N. I.; 3; Balakhnin, S. M.; 3; Serova, and O. A. Synthesis and Antiviral Activity of Fluorinated Pyrido[1,2-a]Benzimidazoles. *Pharm. Chem. J.* **2005**, *39* (Issue 11).

(224) Maryanoff, B. E.; Ho, W.; McComsey, D. F.; Reitz, A. B.; Grous, P. P.; Nortey, S. O.; Shank, R. P.; Dubinsky, B.; Taylor, R. J.; Gardocki, J. F. Potential Anxiolytic Agents. Pyrido[1,2-a]Benzimidazoles: A New Structural Class of Ligands for the Benzodiazepine Binding Site on GABA-A Receptors. *J. Med. Chem.* **1995**, *38* (1), 16–20.

(225) Sandlin, R. D.; Carter, M. D.; Lee, P. J.; Auschwitz, J. M.; Leed, S. E.; Johnson, J. D.; Wright, D. W. Use of the NP-40 Detergent-Mediated Assay in Discovery of Inhibitors of β-Hematin Crystallization. *Antimicrob. Agents Chemother.* **2011**, *55* (7), 3363–3369.

(226) Sandlin, R. D.; Fong, K. Y.; Wicht, K. J.; Carrell, H. M.; Egan, T. J.; Wright, D. W. Identification of β-Hematin Inhibitors in a High-Throughput Screening Effort Reveals Scaffolds with in Vitro Antimalarial Activity. *Int. J. Parasitol. Drugs Drug Resist.* **2014**, *4* (3), 316–325.

(227) Keri, R. S.; Hiremathad, A.; Budagumpi, S.; Nagaraja, B. M. Comprehensive Review in Current Developments of Benzimidazole-Based Medicinal Chemistry. *Chem. Biol. Drug Des.* **2015**, *86* (1), 19–65.

(228) Ramachandran, S.; Hameed P., S.; Srivastava, A.; Shanbhag, G.; Morayya, S.; Rautela, N.; Awasthy, D.; Kavanagh, S.; Bharath, S.; Reddy, J.; Panduga, V.; Prabhakar, K. R.; Saralaya, R.; Nanduri, R.; Raichurkar, A.; Menasinakai, S.; Achar, V.; Jiménez-Díaz, M. B.; Martínez, M. S.; Angulo-Barturen, I.; Ferrer, S.; Sanz, L. M.; Gamo, F. J.; Duffy, S.; Avery, V. M.; Waterson, D.; Lee, M. C. S.; Coburn-Flynn, O.; Fidock, D. A.; Iyer, P. S.; Narayanan, S.; Hosagrahara, V.; Sambandamurthy, V. K. N -Aryl-2-Aminobenzimidazoles: Novel, Efficacious, Antimalarial Lead Compounds. *J. Med. Chem.* **2014**, *57* (15), 6642–6652.

(229) Dziwornu, G.; Coertzen, D.; Leshabane, M.; Korkor, C.; Cloete, C.; Njoroge, M.; Gibhard, L.; Lawrence, N.; Reader, J.; van der Watt, M.; Wittlin, S.; Birkholtz, L.-M.;

Chibale, K. Antimalarial Benzimidazole Derivatives Incorporating Phenolic Mannich Base Side Chains Inhibit Microtubule and Hemozoin Formation: Structure–Activity Relationship and Efficacy Studies. *J. Med. Chem.* *64* (8), 5198–5215.

(230) Ndakala, A. J.; Gessner, R. K.; Gitari, P. W.; October, N.; White, K. L.; Hudson, A.; Fakorede, F.; Shackleford, D. M.; Kaiser, M.; Yeates, C.; Charman, S. A.; Chibale, K. Antimalarial Pyrido[1,2-a]Benzimidazoles. *J. Med. Chem.* **2011**, *54* (13), 4581–4589.

(231) Zhou, Z.; Vorperian, V. R.; Gong, Q.; Zhang, S.; January, C. T. Block of HERG Potassium Channels by the Antihistamine Astemizole and Its Metabolites Desmethylastemizole and Norastemizole. *J. Cardiovasc. Electrophysiol.* **1999**, *10* (6), 836–843.

(232) Suessbrich, H.; Waldegger, S.; Lang, F.; Busch, A. E. Blockade of HERG Channels Expressed in Xenopus Oocytes by the Histamine Receptor Antagonists Terfenadine and Astemizole. *FEBS Lett.* **1996**, *385* (1–2), 77–80.

(233) Chong, C. R.; Chen, X.; Shi, L.; Liu, J. O.; Sullivan, D. J. A Clinical Drug Library Screen Identifies Astemizole as an Antimalarial Agent. *Nat. Chem. Biol.* **2006**, *2* (8), 415–416.

Chapter Two

The Synthesis of Study Compounds and Their Novel Fluorescent Analogues

2.1. Chapter Overview

As earlier mentioned in the introductory chapter, compounds incorporating benzimidazole and pyrido[1,2-a]benzimidazole scaffolds have shown promising pharmacological and physicochemical properties against both CQS and CQR strains of *P. falciparum*. As also already indicated, some analogues from this class of compounds demonstrated pharmacology proof-of-concept by showing efficacy in an *in vivo P. berghei* mouse malaria infection model.[1] However, the details of the mechanism of action of these potential antimalarial drugs against *P. falciparum* remain elusive. Previous work on some

analogues from this class of compounds demonstrated their ability to accumulate in the parasite's acidic DV and this ability might be an important contributor to their efficacy.[1] However, the ability of these compounds to associate with other subcellular compartments is yet to be evaluated. It is hypothesized that an in-depth analysis of their subcellular localization within the parasite would reveal more information about the MOA of these scaffolds and might suggest potential target (s).

Intrinsic and extrinsic fluorescence properties of a compound can be utilized in studying its subcellular distribution within the parasite. If the compound under study has inherent fluorescent properties that are suitable for their direct excitation in live cells, then such a compound could be used without the attachment of an external fluorophore. However, most compounds require the attachment of an external fluorophore, suitable for their subcellular distribution within the parasite for which several considerations must be made when designing fluorescent analogues. For example, SAR studies must guide the decision as to where suitable modifications to the parent compounds must be made to attach a fluorophore. Also, the choice of external fluorophore and the length of the spacer or linker chain between the core of the compound and the extrinsic fluorophore must be considered carefully when designing fluorescent analogues.

This chapter describes the synthesis and characterization of the compounds studied in this work, **KP68**, **KP124** and **DM253**. The design and synthesis aspects relating their novel fluorescent derivatives will also be discussed. The reason behind the choice of fluorophore was discussed. Further, spectroscopic characterization will also be described.

Therefore, the specific objectives with regards to the design, synthesis and characterization described in this chapter were:

i. To resynthesize and characterize the study compounds.
ii. To identify a reporter fluorophore suitable for use in studying their subcellular accumulations in *P. falciparum* live-cells.
iii. To propose and synthesize suitable fluorescent derivatives of the target compounds, **KP68**, **KP124**, and **DM253.** Information from previous SAR studies on the compounds will be used to determine suitable attachment sites to retain the pharmacological activity of the parent molecules.

iv. To characterize the synthesized compounds using high performance liquid chromatography coupled with a mass spectrometer (HPLC-MS) and nuclear magnetic resonance spectroscopy, both proton (^{1}H-NMR) and Carbon (^{13}C-NMR).

2.2. Synthesis of Target PBIs

The synthetic route used to produce the target PBI compounds is outlined in Scheme 2.1. It was adapted from Ndakala *et al.* with slight modifications.[2] The compounds were synthesized through a condensation reaction between ethyl-2-cyanoacetate (**II**) and an appropriate diamine (**I**) to form the substituted benzimidazole intermediate (**III)**. This was followed by a condensation reaction between the benzimidazole intermediates and an appropriate β-keto ester (**IV**) to yield the hydroxy intermediate **V**. The hydroxy intermediates were then reacted with phosphorous oxychloride ($POCl_3$) in a dehydration reaction to obtain the chlorinated intermediate **VI**. Finally, the target compounds were obtained through a nucleophilic substitution reaction of the chlorinated intermediates with an appropriate amine (**VII**). Proton characterization via nuclear magnetic resonance (NMR) spectroscopy is illustrated in the figures that follow.

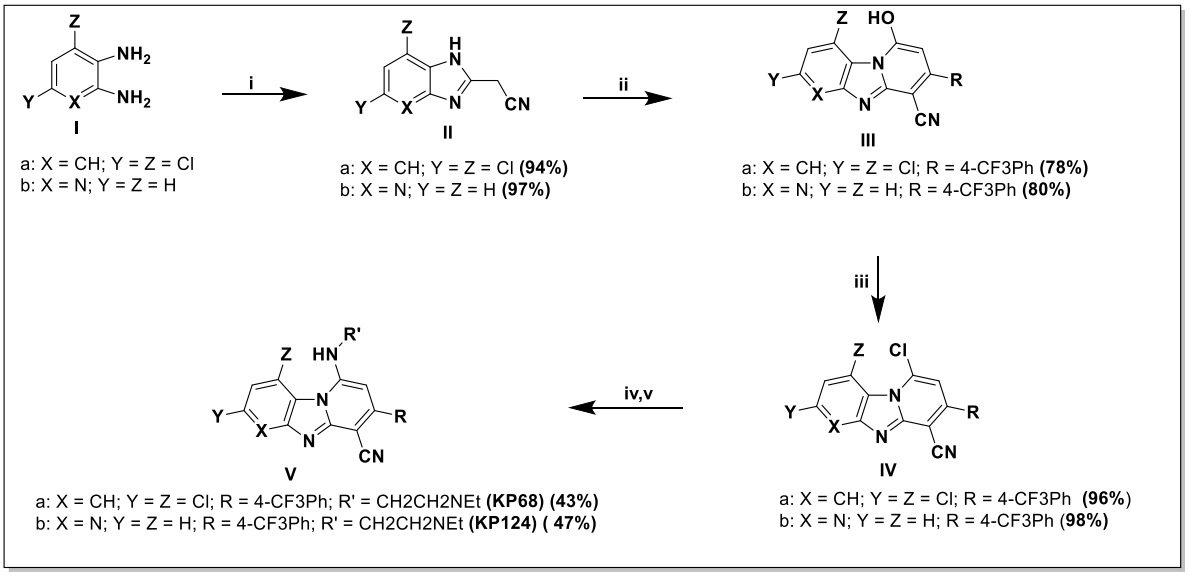

Scheme 2.1. Synthesis of target pyrido[1,2-a]benzimidazoles (PBIs).

Reagents and reaction conditions: (i) Ethyl cyanoacetate, dimethylformamide (DMF), microwave, 150 °C, 1.30 h; (ii) NH_4OAc, appropriate diketoester, 150 °C, 1 h; (iii) $POCl_3$, 130 °C, 2 h; (iv) Amine, Et_3N, tetrahydrofuran (THF), microwave, 80 °C, 40 min (for **KP68** and **KP124).**

2.2.1. Spectroscopic Analysis of the Target Compound KP68

The characteristic ^{1}H-NMR spectrum (600 MHZ, DMSO-d6) of the final target compound shows the appearance of aliphatic signals of the alkyl amine side chain in the region 1.24-5.88 ppm (Figure 2.1). A triplet is observed at 1.24 ppm corresponding to three protons of H-20. A quartet at 3.03 ppm corresponds to the two protons H-19. Two triplets observed at 3.24 and 3.65 ppm correspond to two protons each of H-18 and H-17, respectively. The H-2 proton occurs as a singlet at 5.88 ppm. Characteristic doublets are observed at 8.74 and 7.50 ppm and correspond to the two protons each of H-6 and H-8, respectively. The aromatic protons of the para-substituted benzene ring occur as multiplets and correspond to four protons.

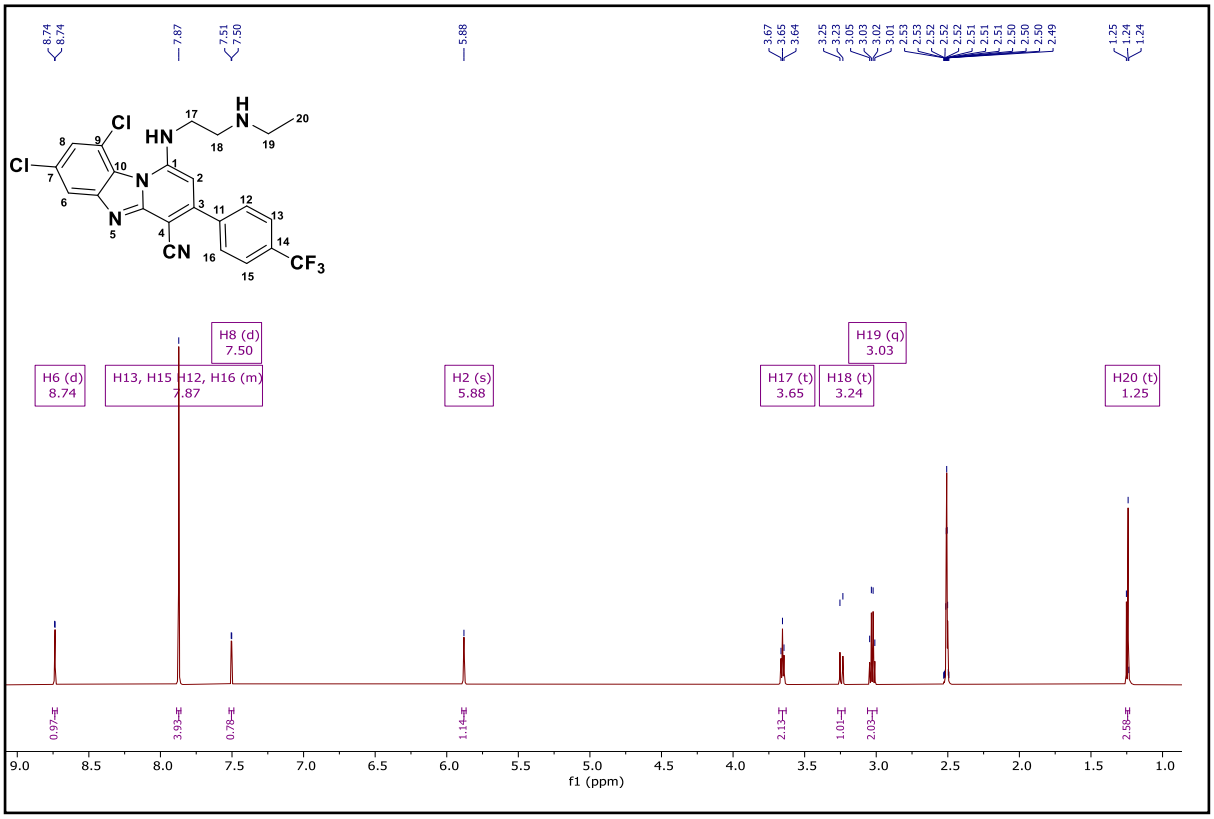

Figure 2.1. ^{1}H-nuclear magnetic resonance spectrum (NMR; 600 MHz DMSO-d_6) of the target compound z (KP68)

2.3. Synthesis of the Benzimidazole lead, DM253

The synthesis of **DM253** commenced with the preparation of a phenethyl bromide intermediate **3** using methods previously described in literature, with slight modifications[3–6] (Scheme 2.2). In a separate reaction, an alkylation of 2-chloro-1H-benzo[d]imidazole at N-1, followed by a coupling reaction with tert-butyl 4-aminopiperidine-1-carboxylate delivered intermediate **4**. Following acidic deprotonation to result in intermediate **5**, coupled with intermediate **3** afforded the target compound **DM253**.

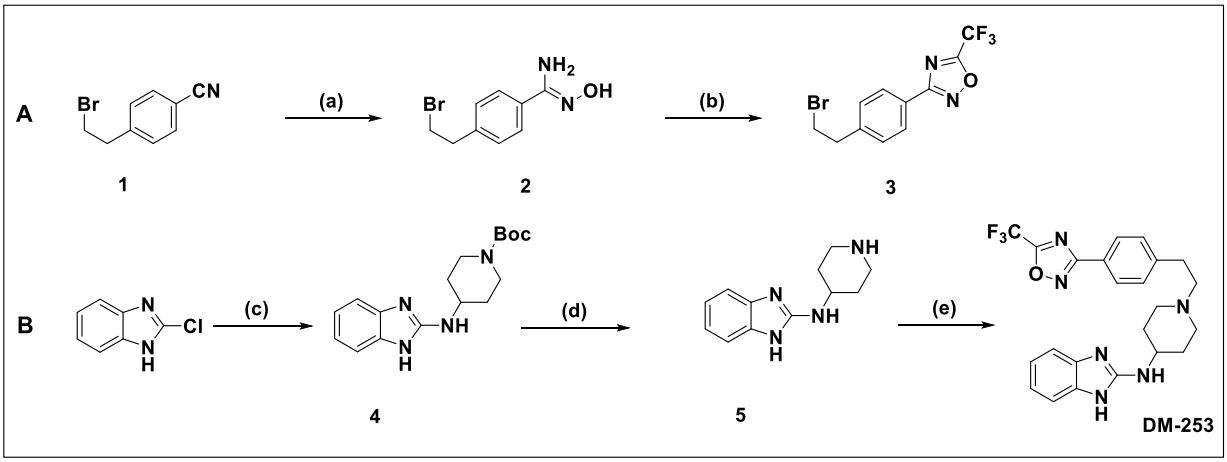

Scheme 2.2. Synthesis of target benzimidazole, **DM253**

Reagents and conditions: (a) *(i)* $NH_2OH{\cdot}HCl$, 8-hydroxyquinolone, Et_2N, EtOH, 79 °C, 1.5 h, *(ii)* 21 °C, 10% HCl, pH 3 (82%); (b) $(CF_3CO)_2O$, DCM, Pyridine, 21 °C, 20 min (76%); (c) alkylating agent, K_2CO_3, acetone, 18-23, °C 2-5 h (98%); (ii) tert-butyl 4-aminopiperidine-1-carboxylate, Et3N,150 °C, 2-12 h, (89%) (d) TFA, DCM, 23 °C, 2 h (85%); (e) **3**, K2CO3, DMF, 70 °C, 12 h (58%).

2.3.1. Characterization of Target Compound, DM253

The formation of **DM253** was confirmed by the presence of two diagnostic methylene proton signals in the ^{1}H-NMR spectrum. All diagnostic signals are assigned in Figure 2.2

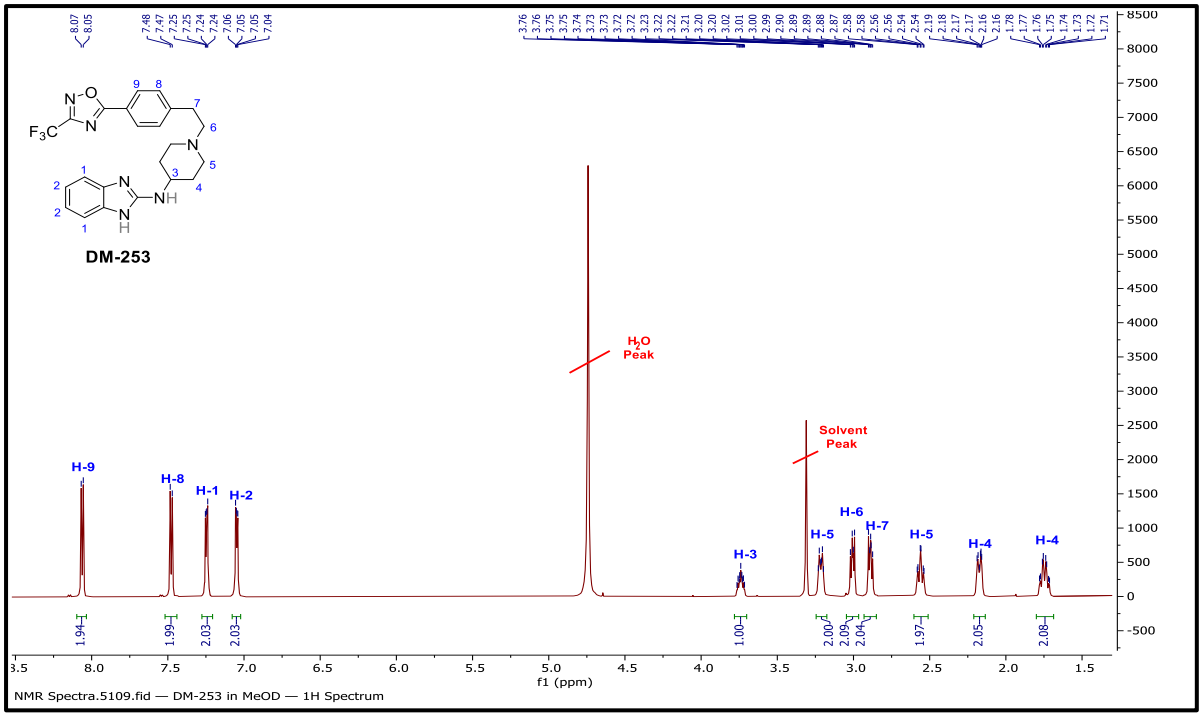

Figure 2.2. [1]H-nuclear magnetic resonance spectrum (NMR; 600 MHz, MeOD) of **DM253**

2.4. Synthesis of Novel Fluorescent Analogues of Target Compounds

2.4.1 Identification of NBD as a Suitable Extrinsic Fluorophore

The native fluorescence of benzimidazoles and pyrido[1,2-a]benzimidazoles have been broadly exploited in their studies in various disease areas.[7] Initial fluorescence studies on the target compounds revealed that **KP68** and **KP124** possess intrinsic fluorescence that would be suitable for their subcellular accumulation within *P. falciparum* live-cells. This is chiefly based on the fact that, the excitation/absorbance maxima of both compounds lie in the ultraviolet-visible (UV-vis) region of the absorption spectrum and could be excited without causing significant damage to the cells. This property of the PBIs and its use in fluorescent colocalization studies is discussed further in Chapter 4. The benzimadole compound **DM253** on the hand did not possess any inherent fluorescence in the various solvents in which it has been studied. From polar solvents such as methanol and water to non-polar solvents such as dichloromethane, **DM253** showed poor fluorescent intensity and an excitation/absortion maxima that lied in the ultraviolet (UV) region instead of the visible region. Further, two-photon excitation microscopy equally failed to cause any significant excitation without photodamage to the cells.

Consequently, a 7-nitrobenz-2-oxa-1,3-diazole (NBD) extrinsic fluorophore was attached to the compounds understudy. NBD was selected as a suitable fluorophore for several reasons. First, it is one of the smallest fluorophores and is therefore expected to cause the least disturbance to biological activity upon conjugation to the compounds.[8] Second, the excitation and emission maxima of the NBD reporter fluorophore in aqueous media are approximately 470 and 540 nm respectively, and hence these bands are expected to overlap minimally with the prominent Soret region of Fe(III)PPIX, should the compounds accumulate in the DV. Third, the fluorescence of NBD is stable over a biologically relevant pH range although the fluorophore is slightly solvatochromic.[8] Furthermore, NBD shows a lower aqueous fluorescence quantum yield compared to hydrophobic environments.[9] This photophysical property was considered in chosing the fluorophore because earlier hypothesis on the action of the target compounds suggested inhibition of the formation of hemozoin as a plausible MOA. Consequently, the modest aqueous quantum yield of NBD will prevent the signal from the DV from overwhelming weaker signals from other organelles in the parasite.

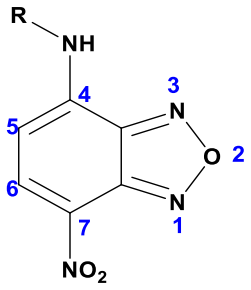

Figure 2.3. The structure and numbering of the 7-nitrobenz-2-oxa-1,3-diazole (NBD) fluorophore when substituted to an amine at the 4-position.

While the photophysical and pharmacological properties of the synthesized fluorescent analogues were evaluated against their parent compounds to ensure they were suitable representatives, there is the concern that attaching an external fluorophore could alter the target (s) and hence the accumulation of the compounds understudy. To study the effect of the NBD external fluorophore on the subcellular accumulation of the target compounds, it was also attached to **KP68** and **KP124**. The colocalization of these fluorescent analogues were studied in comparison to the accumulation observed when the intrinsic fluorescence of the PBIs were used in the colocalization study. NBD is readily available as its 4-chloro derivative and has been attached to biomolecules in

previous studies.[10–12] In terms of synthesis, the presence of an electron withdrawing group para to the chlorine atom makes this NBD derivative susceptible to nucleophilic aromatic substitution which was utilized in the synthesis of the fluorescent analogues. These fluorescent analogues were also designed to retain both pharmacological and key characteristic properties of their parent compounds such as their ability to interact effectively with Fe(III)PPIX.

The three antimalarial leads investigated in this study, **KP68**, **KP124** and **DM253** have been hypothesized to associate significantly with Fe(III)PPIX. This important association was also presumed to be essential to their antimalarial activities. Due to the structural similarities between CQ and the PBIs (Figure 2.4), coupled with the compounds' activity in the cell-free β-hematin inhibition assay, key interactions between CQ and the Fe(III)PPIX were considered when designing novel fluorescent analogues of the PBI.

As described by de Villiers and co-workers, CQ and most aryl methanols that inhibit the formation of hemozoin possess hydrophobic aromatic rings that interacts with the porphyrin ring of Fe(III)PPIX through π–π stacking.[13–15] There is also evidence of hydrogen bonding between the propionate group of Fe(III)PPIX and the protonated nitrogen of the basic side chain of the PBIs investigated in this study.[16] Based on the presence of these groups in PBIs, it was earlier believed that both compounds could be interacting with Fe(III)PPIX in a similar faction as CQ. Consequently, the fluorescent analogues of the PBIs were designed to ensure these interactions were retained. (Figure 2.5)

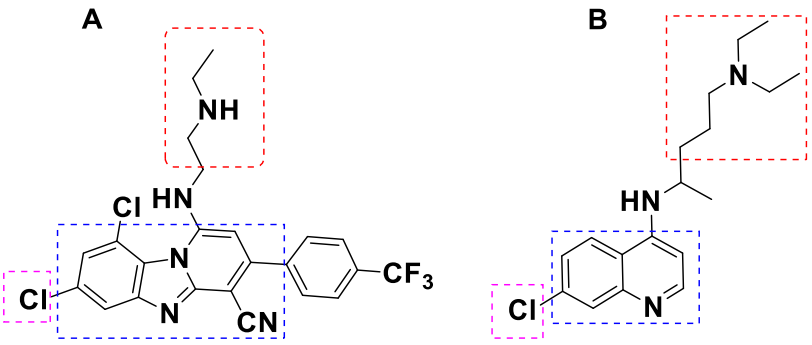

Figure 2.4. Structural similarities between compound **KP68** and CQ, revealing the presence of aromatic hydrophobic rings (Blue), basic amino side chains (Red) and chloro-substituted aromatic rings in both compounds (Purple).

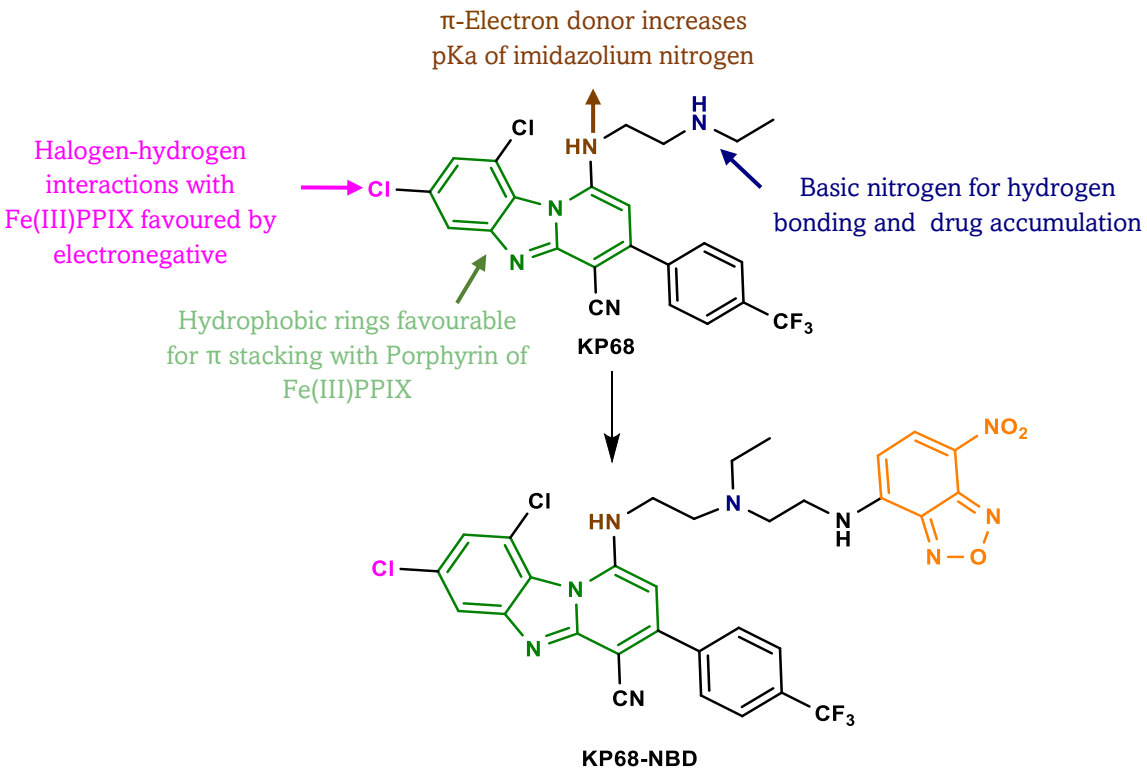

Figure 2.5. Key aspects of the structure-activity relationships between **KP68** and Fe(III)PPIX are shown, leading to the design of a novel NBD-labelled fluorescent derivative **KP68-NBD** to retain the characteristics of the parent molecule.

By comparison, the interaction of **DM253** with Fe(III)PPIX if present, would be fundamentally different. Although the compound has been shown to interact favourably with

Fe(III)PPIX through its *in vitro* β-hematin activity, it is structurally distinct from CQ and its interaction with Fe(III)PPIX would be primarily through hydrophobic interactions between the **DM253** and the porphyrin ring of heme. With credit to the extensive SAR studies from which **DM253** was identified, a suitable point of attachment of the NBD fluorophore through a suitable length linker was identified. The imidazole reactive nitrogen presents the best opportunity to derivatize, without vastly compromising the pharmacological properties of the parent compound. (Figure 2.6)

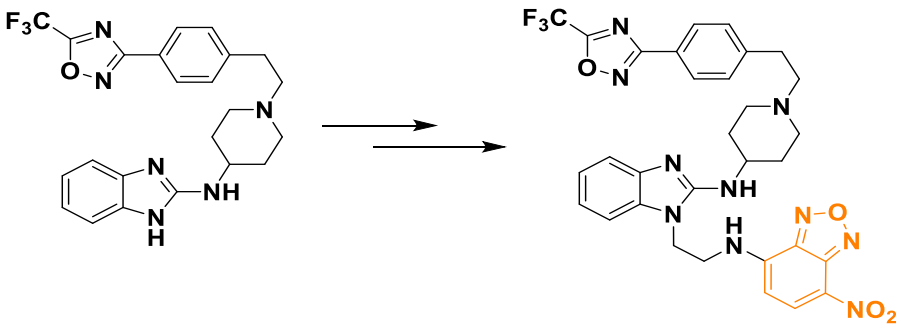

Figure 2.6. Suitable point of attachment of NBD fluorophore on **DM253,** identified by Structure-activity relationship studies

2.5. Synthesis and Characterization of novel Fluorecent Analogues of the PBIs

For the purposes of describing the characterization of the fluorescent analogues of the PBIs depicted in Scheme 2.3, the synthesis of the fluorescent analogues of **KP68** will be used as an illustrative example. Briefly, the fluorescent analogues were synthesized through *N*-alkylation of the target PBIs using *N*-butyloxycarbonyl (Boc)-glycinal, followed by *N*-Boc deprotection using trifluoroacetic acid (TFA), and finally a fluorophore substitution using NBD-Cl.

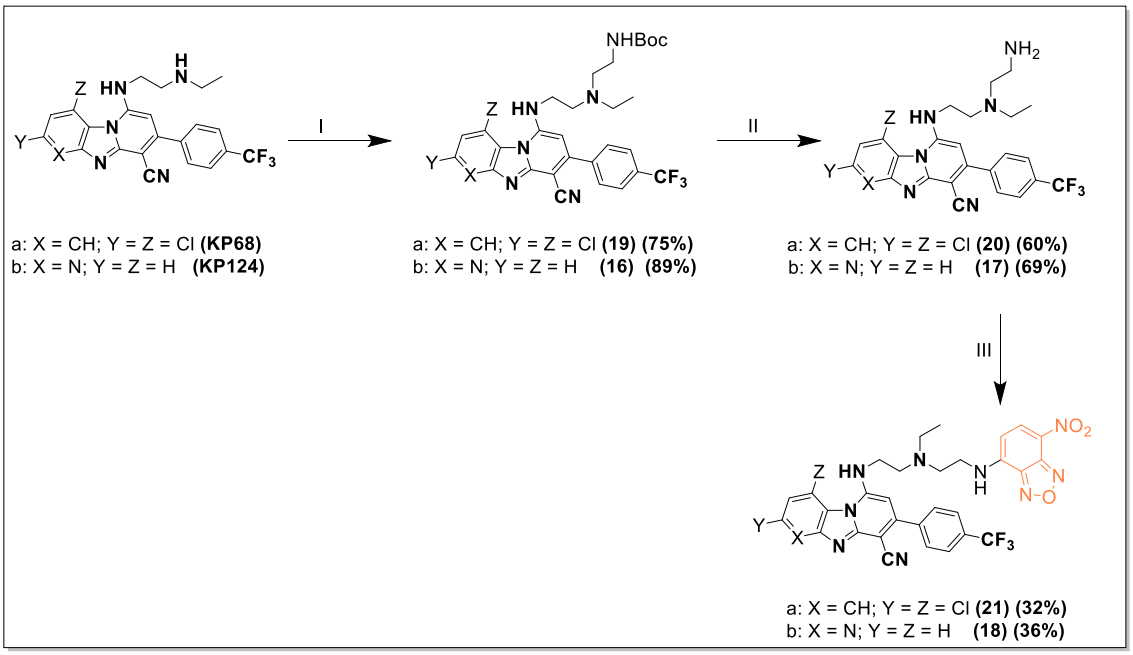

Scheme 2.3. Proposed synthetic scheme for the synthesis of the PBI fluorescent analogues.

Reagents and conditions: (I) $OHCCH_2CH_2NHBoc$, MeOH, 25 °C, 15 min/80 °C, $NaBH_3CN$, 8 h; (II) trifluoroacetic acid (TFA), dichloromethane (DCM), 0-25 °C, 4 h; (III) N,N-Diisopropylethylamine (DIPEA), MeOH, 25 °C, 20 min/NBD-Cl, $NaHCO_3$, MeOH, 75 °C, 2 h.

2.5.1 Characterization of novel Fluorecent Analogues of the PBIs

The ^{1}H-NMR spectrum (600 MHz. DMSO-*d6*) of **KP68-NBD** is shown in Figure 2.7. Characteristic signals relating to the protons on the NBD heterocyclic ring Ha and Hb appear as doublets at 6.21 and 8.15 ppm, respectively (J = 8.9 Hz).

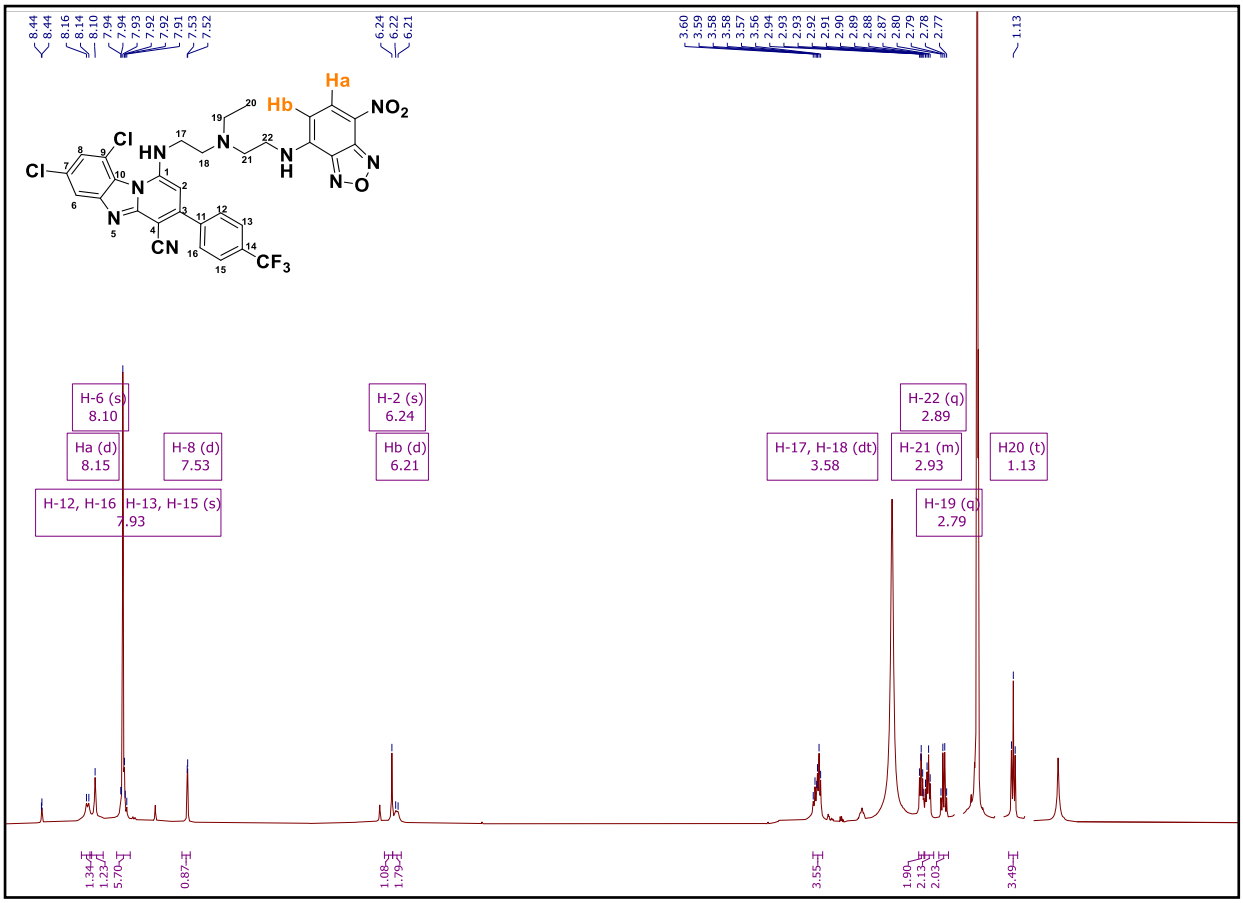

Scheme 2.3. ^{1}H-nuclear magnetic resonance spectrum (NMR; 600 MHz, MeOD) of NBD-labelled **KP68 (21).**

2.6. Synthesis and Characterization of novel Fluorecent Analogue of DM253

The synthesis of **DM253** labelled fluorescent probe utilized a different synthetic route compared to that of the PBIs. Briefly, a nucleophilic aromatic substitution of 2-fluoro nitro benzene by N-Boc ethylenediamine yielded intermediate **4.** Following the S_NAR reaction, the nitro group was reduced under H_2/Pd conditions to yield **5.** Further, intermediate **1** was reacted with **5** through a dicyclohexylcarbodiimide (DCC) cyclocondensation to yield **6.** Following an N-Boc deprotection in acidic media and S_N2 reaction, the final product, NBD-labelled **DM253** is formed (Scheme 2.4)

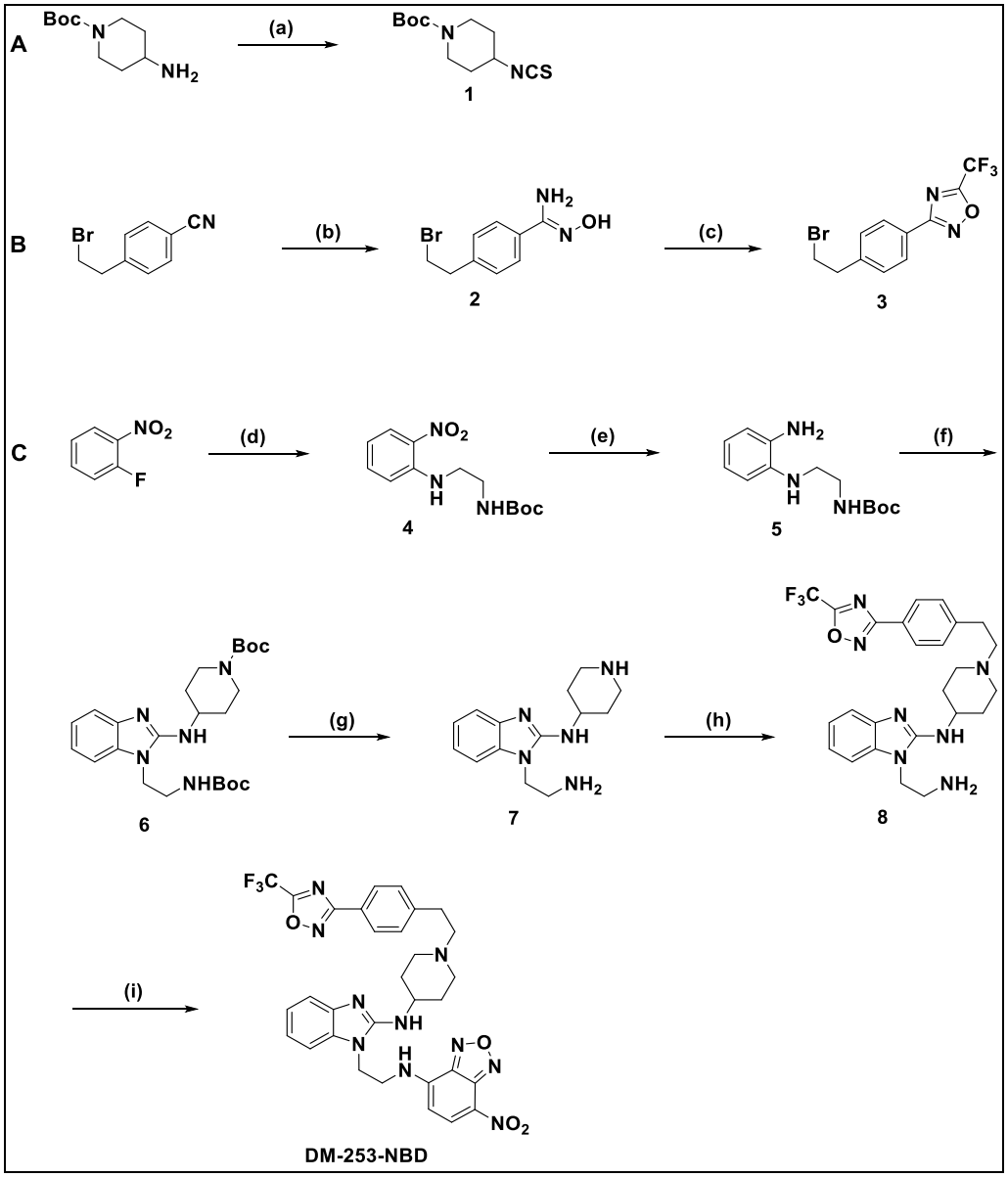

Scheme 2.4. Synthesis of NBD labelled **DM253**

Reagents and conditions: (a) 1,1-Thiocarbonyldiimidazole, DMF, 23 °C, 12 h (78%); (b) *(i)* $NH_2OH{\cdot}HCl$, 8-hydroxyquinolone, Et_3N, EtOH, 79 °C, 1.5 h, *(ii)* 21 °C, 10% HCl, pH 3 (82%); (c) $(CF_3CO)_2O$, DCM, Pyridine, 21 °C, 20 min (76%); (d) *N*-Boc-ethylenediamine, TEA, MeCN, 80 °C, 12 h (96%); (e) H_2 (balloon), 10% Pd/C, 1:1 MeOH/EtOAc, 27 °C, 7 h, (90%); (f) **1**, DCC, TEA, MeCN, 80 °C, 12 h (82%); (g) TFA, DCM, 23 °C, 2 h (85%); (h) **3**, DIPEA, K_2CO_3, MeCN, 26 °C, 5 h (63%); (i) NBD-Cl, $NaHCO_3$, 1:1 MeCN/H_2O, 65 °C, 12 h (73%).

2.6.1. Characterization of novel Fluorecent Analogue of DM253

The formation of NBD labelled **DM253** was confirmed by the appearance of the NBD protons H8 and H9 occurring at 8.21 and 8.47 ppm respectively as shown by the ^{1}H-NMR spectrum in Figure 2.8.

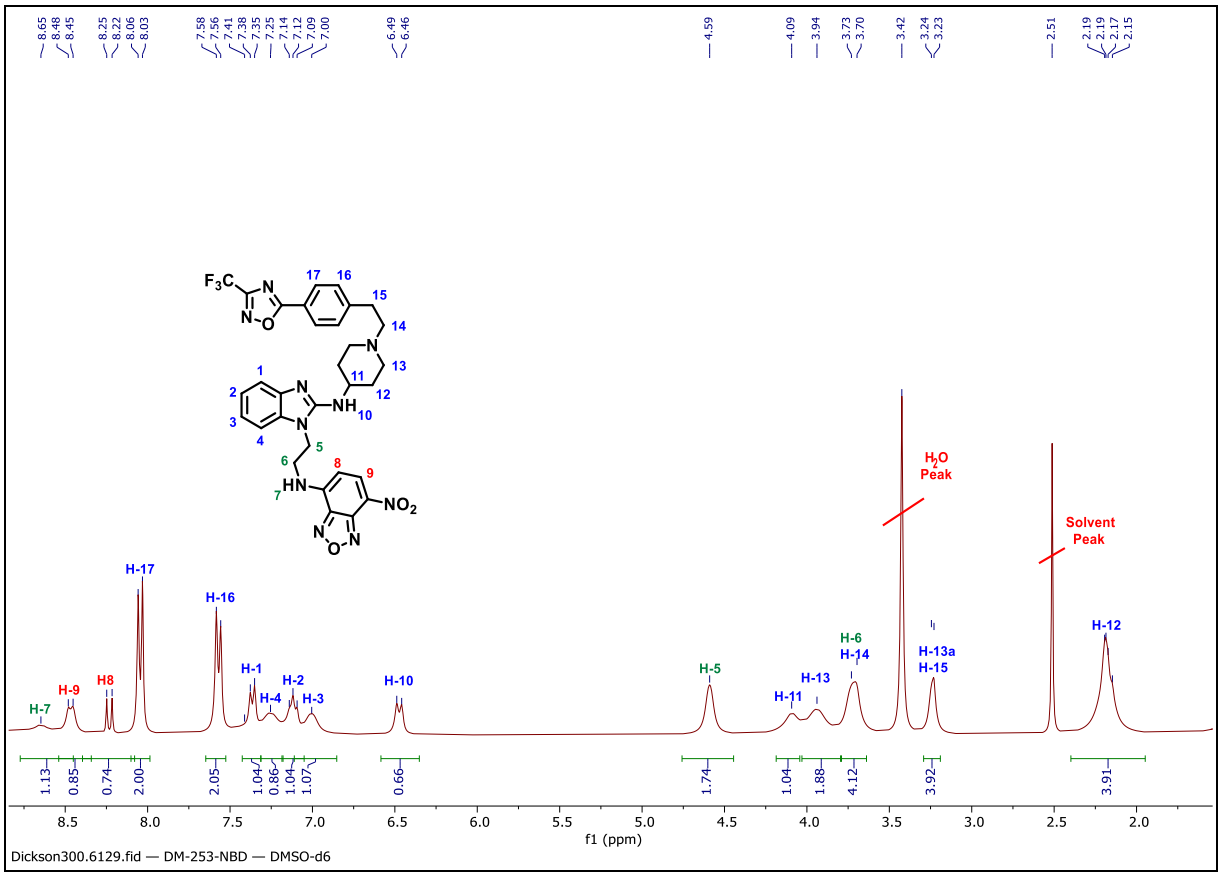

Figure 2.7. ^{1}H-nuclear magnetic resonance spectrum (NMR; 600 MHz, DMSO-*d6*) of NBD-labelled **DM253.**

2.7. Conclusion

In conclusion, this chapter described the rationale, synthesis and characterization of the target PBI and bezimidazole compounds studied in this work. The design process took into consideration the possible interactions between the target PBI compounds and Fe(III)PPIX based on the structural similarities between the compounds and CQ. The final compounds synthesized were fully characterized using spectroscopic techniques such as NMR and chromatography techniques such as TLC and HPLC-MS. Physicochemical parameters such as melting points and solubility were assessed and biological activities in comparison to their parent compounds were evaluated.

2.8. References

(1) Singh, K.; Okombo, J.; Brunschwig, C.; Ndubi, F.; Barnard, L.; Wilkinson, C.; Njogu, P. M.; Njoroge, M.; Laing, L.; Machado, M.; Prudêncio, M.; Reader, J.; Botha, M.; Nondaba, S.; Birkholtz, L.-M.; Lauterbach, S.; Churchyard, A.; Coetzer, T. L.; Burrows, J. N.; Yeates, C.; Denti, P.; Wiesner, L.; Egan, T. J.; Wittlin, S.; Chibale, K. Antimalarial Pyrido[1,2- a]Benzimidazoles: Lead Optimization, Parasite Life Cycle Stage Profile, Mechanistic Evaluation, Killing Kinetics, and in Vivo Oral Efficacy in a Mouse Model. *J. Med. Chem.* **2017**, *60* (4), 1432–1448.

(2) Ndakala, A. J.; Gessner, R. K.; Gitari, P. W.; October, N.; White, K. L.; Hudson, A.; Fakorede, F.; Shackleford, D. M.; Kaiser, M.; Yeates, C.; Charman, S. A.; Chibale, K. Antimalarial Pyrido[1,2-a]Benzimidazoles. *J. Med. Chem.* **2011**, *54* (13), 4581–4589.

(3) Murarka, S.; Martín-Gago, P.; Schultz-Fademrecht, C.; Al Saabi, A.; Baumann, M.; Fansa, E. K.; Ismail, S.; Nussbaumer, P.; Wittinghofer, A.; Waldmann, H. Development of Pyridazinone Chemotypes Targeting the PDEδ Prenyl Binding Site. *Chem. - A Eur. J.* **2017**, *23* (25), 6083–6093.

(4) Maharvi, G. M.; Fauq, A. H. A Synthesis of the γ-Secretase Inhibitor BMS-708163. *Tetrahedron Lett.* **2010**, *51* (50), 6542–6544.

(5) Pankrat'eva, V. E.; Sharonova, T. V.; Tarasenko, M. V.; Baikov, S. V.; Kofanov, E. R. One-Pot Synthesis of 3,5-Disubstituted 1,2,4-Oxadiazoles Using Catalytic System NaOH–DMSO. *Russ. J. Org. Chem.* **2018**, *54* (8), 1250–1255.

(6) Kumar, N. N. B.; Kuznetsov, D. M.; Kutateladze, A. G. Intramolecular Cycloadditions of Photogenerated Azaxylylenes with Oxadiazoles Provide Direct Access to Versatile Polyheterocyclic Ketopiperazines Containing a Spiro-Oxirane Moiety. *Org. Lett.* **2015**, *17* (3), 438–441.

(7) Verdasco, G.; Martín, M. A.; del Castillo, B.; López-Alvarado, P.; Menéndez, J. C. Solvent Effects on the Fluorescent Emission of Some New Benzimidazole Derivatives. *Anal. Chim. Acta* **1995**, *303* (1), 73–78.

(8) Woodland, J. G.; Hunter, R.; Smith, P. J.; Egan, T. J. Shining New Light on Ancient

Drugs: Preparation and Subcellular Localisation of Novel Fluorescent Analogues of Cinchona Alkaloids in Intraerythrocytic Plasmodium f*alciparum*. *Org. Biomol. Chem.* **2017**, *15* (3), 589–597.

(9) Albrecht, C. Joseph R. Lakowicz: Principles of Fluorescence Spectroscopy, 3rd Edition. *Anal. Bioanal. Chem.* **2008**, *390* (5), 1223–1224.

(10) Chattopadhyay, A. Chemistry and Biology of N-(7-Nitrobenz-2-Oxa-1,3-Diazol-4-Yl)-Labeled Lipids: Fluorescent Probes of Biological and Model Membranes. *Chem. Phys. Lipids* **1990**, *53* (1), 1–15..

(11) Maier, O.; Oberle, V.; Hoekstra, D. Fluorescent Lipid Probes: Some Properties and Applications (a Review). *Chem. Phys. Lipids* **2002**, *116* (1–2), 3–18.

(12) Woodland, J. G. Nsights into the Mechanism of Action of Quinoline Antimalarials against Plasmodium Falciparum Revealed by Novel Fluorescent Analogues and Chemical Proteomics, University of Cape Town.

(13) de Villiers, K. A.; Marques, H. M.; Egan, T. J. The Crystal Structure of Halofantrine–Ferriprotoporphyrin IX and the Mechanism of Action of Arylmethanol Antimalarials. *J. Inorg. Biochem.* **2008**, *102* (8), 1660–1667.

(14) Gildenhuys, J.; Sammy, C. J.; Müller, R.; Streltsov, V. A.; le Roex, T.; Kuter, D.; de Villiers, K. A. Alkoxide Coordination of Iron Protoporphyrin IX by Antimalarial Quinoline Methanols: A Key Interaction Observed in the Solid-State and Solution. *Dalt. Trans.* **2015**, *44* (38), 16767–16777.

(15) de Villiers, K. A.; Gildenhuys, J.; le Roex, T. Iron(III) Protoporphyrin IX Complexes of the Antimalarial Cinchona Alkaloids Quinine and Quinidine. *ACS Chem. Biol.* **2012**, *7* (4), 666–671.

(16) Kuter, D.; Benjamin, S. J.; Egan, T. J. Multiple Spectroscopic and Magnetic Techniques Show That Chloroquine Induces Formation of the μ-Oxo Dimer of Ferriprotoporphyrin IX. *J. Inorg. Biochem.* **2014**, *133*, 40–49.

(1) Singh, K.; Okombo, J.; Brunschwig, C.; Ndubi, F.; Barnard, L.; Wilkinson, C.; Njogu, P. M.; Njoroge, M.; Laing, L.; Machado, M.; Prudêncio, M.; Reader, J.; Botha, M.; Nondaba, S.; Birkholtz, L.-M.; Lauterbach, S.; Churchyard, A.; Coetzer, T. L.;

Burrows, J. N.; Yeates, C.; Denti, P.; Wiesner, L.; Egan, T. J.; Wittlin, S.; Chibale, K. Antimalarial Pyrido[1,2- a]Benzimidazoles: Lead Optimization, Parasite Life Cycle Stage Profile, Mechanistic Evaluation, Killing Kinetics, and in Vivo Oral Efficacy in a Mouse Model. *J. Med. Chem.* **2017**, *60* (4), 1432–1448.

(2) Ndakala, A. J.; Gessner, R. K.; Gitari, P. W.; October, N.; White, K. L.; Hudson, A.; Fakorede, F.; Shackleford, D. M.; Kaiser, M.; Yeates, C.; Charman, S. A.; Chibale, K. Antimalarial Pyrido[1,2-a]Benzimidazoles. *J. Med. Chem.* **2011**, *54* (13), 4581–4589.

(3) Murarka, S.; Martín-Gago, P.; Schultz-Fademrecht, C.; Al Saabi, A.; Baumann, M.; Fansa, E. K.; Ismail, S.; Nussbaumer, P.; Wittinghofer, A.; Waldmann, H. Development of Pyridazinone Chemotypes Targeting the PDEδ Prenyl Binding Site. *Chem. - A Eur. J.* **2017**, *23* (25), 6083–6093.

(4) Maharvi, G. M.; Fauq, A. H. A Synthesis of the γ-Secretase Inhibitor BMS-708163. *Tetrahedron Lett.* **2010**, *51* (50), 6542–6544.

(5) Pankrat'eva, V. E.; Sharonova, T. V.; Tarasenko, M. V.; Baikov, S. V.; Kofanov, E. R. One-Pot Synthesis of 3,5-Disubstituted 1,2,4-Oxadiazoles Using Catalytic System NaOH–DMSO. *Russ. J. Org. Chem.* **2018**, *54* (8), 1250–1255.

(6) Kumar, N. N. B.; Kuznetsov, D. M.; Kutateladze, A. G. Intramolecular Cycloadditions of Photogenerated Azaxylylenes with Oxadiazoles Provide Direct Access to Versatile Polyheterocyclic Ketopiperazines Containing a Spiro-Oxirane Moiety. *Org. Lett.* **2015**, *17* (3), 438–441.

(7) Verdasco, G.; Martín, M. A.; del Castillo, B.; López-Alvarado, P.; Menéndez, J. C. Solvent Effects on the Fluorescent Emission of Some New Benzimidazole Derivatives. *Anal. Chim. Acta* **1995**, *303* (1), 73–78.

(8) Woodland, J. G.; Hunter, R.; Smith, P. J.; Egan, T. J. Shining New Light on Ancient Drugs: Preparation and Subcellular Localisation of Novel Fluorescent Analogues of Cinchona Alkaloids in Intraerythrocytic Plasmodium Falciparum. *Org. Biomol. Chem.* **2017**, *15* (3), 589–597.

(9) Albrecht, C. Joseph R. Lakowicz: Principles of Fluorescence Spectroscopy, 3rd

Edition. *Anal. Bioanal. Chem.* **2008**, *390* (5), 1223–1224.

(10) Chattopadhyay, A. Chemistry and Biology of N-(7-Nitrobenz-2-Oxa-1,3-Diazol-4-Yl)-Labeled Lipids: Fluorescent Probes of Biological and Model Membranes. *Chem. Phys. Lipids* **1990**, *53* (1), 1–15.

(11) Maier, O.; Oberle, V.; Hoekstra, D. Fluorescent Lipid Probes: Some Properties and Applications (a Review). *Chem. Phys. Lipids* **2002**, *116* (1–2), 3–18.

(12) Woodland, J. G. Nsights into the Mechanism of Action of Quinoline Antimalarials against Plasmodium Falciparum Revealed by Novel Fluorescent Analogues and Chemical Proteomics, University of Cape Town.

(13) de Villiers, K. A.; Marques, H. M.; Egan, T. J. The Crystal Structure of Halofantrine–Ferriprotoporphyrin IX and the Mechanism of Action of Arylmethanol Antimalarials. *J. Inorg. Biochem.* **2008**, *102* (8), 1660–1667.

(14) Gildenhuys, J.; Sammy, C. J.; Müller, R.; Streltsov, V. A.; le Roex, T.; Kuter, D.; de Villiers, K. A. Alkoxide Coordination of Iron(II) Protoporphyrin IX by Antimalarial Quinoline Methanols: A Key Interaction Observed in the Solid-State and Solution. *Dalt. Trans.* **2015**, *44* (38), 16767–16777.

(15) de Villiers, K. A.; Gildenhuys, J.; le Roex, T. Iron (III) Protoporphyrin IX Complexes of the Antimalarial Cinchona Alkaloids Quinine and Quinidine. *ACS Chem. Biol.* **2012**, *7* (4), 666–671.

(16) Kuter, D.; Benjamin, S. J.; Egan, T. J. Multiple Spectroscopic and Magnetic Techniques Show That Chloroquine Induces Formation of the μ-Oxo Dimer of Ferriprotoporphyrin IX. *J. Inorg. Biochem.* **2014**, *133*, 40–49.

Chapter Three

Principles and Applications Fluorescence in Microscopy

3.1. Chapter Overview

This chapter discusses the theoretical foundations of fluorescence and its application in the mode of action studies. This is because fluorescence spectroscopy and microscopy form the basis of the investigations discussed in Chapter 4.

George Stokes is credited with discovering and coining the term fluorescence, albeit fluorescence-based techniques have been in use long before the 16th Century. This technique has since been developed into the powerful tool it represents today. Recently Fluorescent-based methods have enjoyed increased growth across disciplines. Further, the development of super-resolution fluorescence microscopy in 2014, which earned the scientists; Eric Betzig, Stefan Hell, and William Moerner a Nobel Prize in Chemistry, has contributed to the popularity of this technique. This acknowledgment represents more than a century of development that now allows for the imaging of organelles inside living cells like *P. falciparum* with tremendous precision.

Fluorescence-based techniques are among the popular methods for live-cell imaging and elucidating structures such as organelles and biomolecules in cells and tissues. This technique allows for studying organelles and biomolecules *in situ* without requiring time-intensive staining processes that might be toxic to cells or tissues. It is also characterized by a high degree of specificity, which is attributed to the availability of fluorophore probes that allow biological structures to be highlighted. When combined with confocal microscopy, fluorescence-based techniques provide a clear three-dimensional view of the inner structures of cells without causing undue stress. Technologies that exploit fluorescence equally have high spatial resolution and increased response time, making fluorescence the technique of choice in probing the structure and dynamics of biological systems.

In this chapter, electronic events associated with fluorescence, specifically excitation and emission, will be discussed, followed by the practical use of fluorescence microscopy, focusing on the challenges presented by inner-filter effects. Finally, fluorescence microscopy applications will be described with a focus on the limit of diffraction and

super-resolution structured-illumination microscopy (SR-SIM). Later sections of this chapter will describe the photophysical characterization of the target compounds and their fluorescent derivatives for live-cell imaging.

3.2. Properties of Fluorescence Excitation and Emission

3.2.1. Electronic Spin State

Luminescence is light emission by a substance that has not been heated. Fluorescence and phosphorescence share some similarities, such that they are both characterized by the emission of light from an excited state due to the absorption of protons. Therefore, they are referred to as photoluminescent to distinguish fluorescence and phosphorescence from other types of luminescence.[1,2]

Fluorescence occurs because of light emission from a singlet excited state, while phosphorescence results from emission from a triplet excited state. For fluorescence, excited state orbitals are paired by opposite spins to the ground state orbital electrons. For these electrons to return to the ground state, they should be spin allowed and occur within nanoseconds. Light emission following the triplet excited state is forbidden. However, it could be observed due to spin-orbit coupling. Consequently, transitions to the ground state from the triplet excited state occur slowly and within seconds.[2,3]

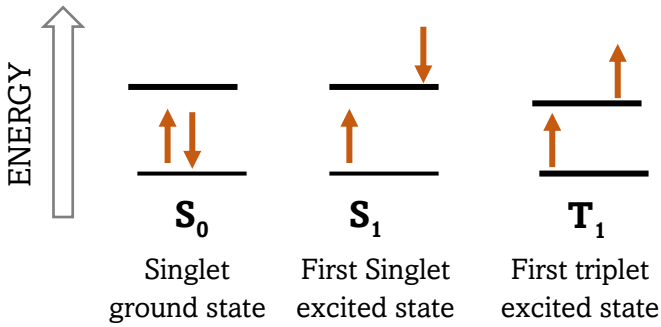

Figure 3.1. A diagram describing the singlet and triplet electronic states.

3.2.2. The Perrin-Jablonski Diagram

The ability of a molecule or atom to emit light after excitation by an outside energy source is referred to as fluorescence, and molecules capable of fluorescence are known as fluorophores or fluorochromes.[4] When excess energy is released by electrons returning to the ground state in the form of photons[5], this phenomenon is described in the

illustration known as the Jablonski diagram. The Perrin-Jablonski diagram illustrates a partial energy-level diagram for a photoluminescent system.[1] It is a valuable demonstration of the photophysical properties that are of use to fluorescence excitation and emission. (Figure 3.2) Fluorescence microscopy is based on the fluorescence of organic molecules rather than atoms. Consequently, molecular fluorescence is used to describe the physical basis of the technique. S_0, S_1, and S_2 are representatives of the singlet ground state and the first and second excited states, respectively. Molecules at each electronic energy level exist in a few vibrational states labelled as 0, 1, 2, and 3 and other rotational energy levels that are not depicted in Figure 3.2. The vertical lines show the transition between energy states. The dotted lines represent the transition between states due to the internal conversion or a non-radiative relaxation process.

Electrons in a steady-state condition are found in the ground state, with the lowest energy level represented as S_0. Following the absorbance of photons with adequate and suitable energy, electrons from S_0 transit to higher energy excited states represented by S_1 and S_2. The conversion from S_0 to S_1 or S_2 (Figure 3.2) typically occurs quickly, taking place within 10^{-15} s.[4] Electrons usually transit from one energy level to the next level down when returning from an excited state, thereby releasing the excess energy. Excited-state electrons take several paths when returning to the ground state. Depending on the molecular configuration of the molecule and the other molecule species present in the solution, it can result in fluorescence, phosphorescence, or radiation-less conversion.[4] Because the energy levels S_2 and S_1 are in proximity, there is a lower probability that an electron in S_2 will bypass S_1 and go directly to S_0. Consequently, fluorescence most often occurs when electrons return from S_1 to S_0.[4] In some instances, the energy difference between S_1 and S_0 is the energy of the photon emitted. In other cases, the energy dissipated by an electron transition from S_1 to S_0 is in the form of heat. In the latter case, fluorescence does not occur.

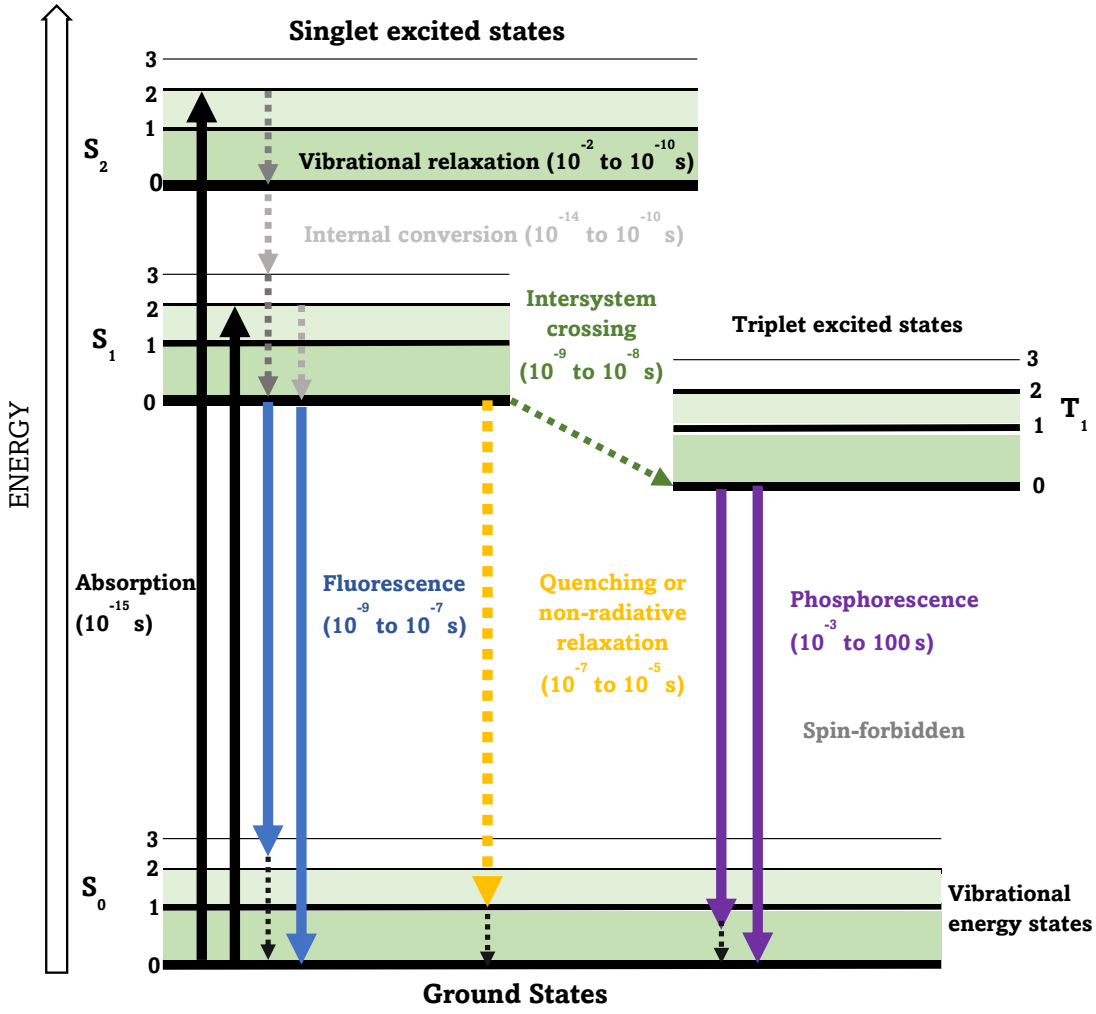

Figure 3.2. Jablonski diagram of a theoretical fluorescent molecule showing most of the possible electronic transitions during excitation and emission.[6]

While the entire fluorescence lifetime, from excitation to emission, occurs in a split second, the interaction between matter and light forms the basis of fluorescence spectroscopy and microscopy. Most fluorophores undergo a series of excitation and emission cycles many times before the excited state of the molecule is photobleached and the fluorophore destroyed.[7]

Further, molecules in the S_1 energy states can equally undergo a spin conversion to the first triplet state (T_1) through an intersystem crossing. Phosphorescence is characterized by emission from the triplet state and occurs at longer wavelengths than fluorescence. Since the transition to the singlet state is forbidden and violates the spin selection rule, a much lower constant rate is observed for these processes than fluorescence. Equally, it occurs quickly between milliseconds to a few seconds. Finally, the transition from T_1 to

S_0 is enhanced in the presence of heavy atoms such as bromine and iodine and is characterized by spin-orbit coupling.

3.3. Properties of Fluorophores

Some fundamental concepts are used to describe and compare fluorophores. These concepts will be alluded to frequently in Chapter 4. They include molar absorption coefficient, the fluorescence lifetime, quantum yield, photobleaching, and quenching. The following subsections will briefly describe these concepts and their effect on fluorescence.

3.3.1. Molar Extinction Coefficient (ε)

Molar extinction, as defined by the Beer-Lambert law, is the measure of the efficiency of a fluorophore in absorbing light at a particular wavelength (λ). Principally, absorption depends on factors such as the molecular structure of the fluorophore, the wavelength of the light being absorbed, and the pH and temperature of the solution in which the fluorophore is prepared.[3] This is mathematically represented below.

$$A = \varepsilon c l \quad \textit{where,}$$

A = absorbance of the homogenous and isotropic sample

ε = molar extinction

c = concentration of the fluorescent dye (mol/L)

l = thickness of the fluorescent solution, in cm

3.3.2. Fluorescence Lifetime

A fluorophore's fluorescence lifetime describes the average time a molecule spends in the excited state before returning to the ground state. As illustrated in the Jablonski diagram (Figure 3.1), molecules transit from the ground state to the excited state following excitation. A two-step process is involved in the deactivation phase, including a non-radiative (internal conversion) and a radiative (fluorescence) process, which results in the depopulation of the excited state. The fluorescence lifetime remains constant for a molecule in a given solvent if there is no energy transfer to the environment. However, it significantly decreases when acceptors such as calcium, oxygen, hydrogen, or magnesium are present. Knowledge of the fluorescence lifetime offers information about

the surrounding environment of a fluorophore. This further allows for mapping cells with space and time resolution.

3.3.3. Fluorescence Quantum Yield

Fluorescent quantum yield represented by QE measures the efficiency of the fluorescence process. It is the ratio between the number of photons absorbed to those emitted. In the case of fluorescein, which has a QE of 90%, it does not mean that the energy of the emitted photons is 90% of the energy of the absorbed photons.[8] It means that, in terms of numbers, there is a 10 to 9 relationship between excitation and emission and the loss in energy due to the non-radiative processes. (Stoke's losses). The non-radiative processes cause the emitted photon to be red-shifted compared to the excitation photon.[8]

Also, the QE of fluorophores varies under different conditions. For example, at a pH of 8, fluorescein has its highest QE of 8; however, at a reduced pH of 6, the compound's QE drops to its lowest at 0.3.[9] In practical terms, this means that the same amount of fluorescein will fluoresce brightly outside the cell and be very dim inside the acidic compartments of the cell. Based on this, fluorescein alone will not be suitable for assessing the acidic digestive vacuole of *P. falciparum,* whose biological pH is around 4.5. However, tagging fluorescein with a pH-insensitive dye will present a powerful method that allows the visualization of the entire cell and simultaneously monitors intracellular pH changes. These considerations must be made when selecting fluorophores for a specific use.

3.3.4. Fluorescence Quenching

When the QE of a fluorophore decreases due to interactions with molecular species nearby, such as proteins or other fluorophores, it is referred to as quenching. The energy transfer is non-radiative, and it results in a weak fluorescence. The spectral characteristics of the emitted light from a quenched fluorophore are identical to that of the non-quenched fluorophore. Commonly, fluorophores are quenched following their conjugation to proteins such as bovine serum albumin or immune globulins due to the high conjugation density of the fluorophore.[8]

Fluorescence quenching is broadly divided into two groups: static and collisional quenching. Static quenching, also known as contact quenching, describes the formation of a non-fluorescent complex between the fluorophore and the molecule that causes

quenching, thereby limiting absorption by reducing the excitable population of molecules.[10] During static quenching, molecules form a complex in the ground state before excitation occurs. The complex formed has specific properties; hence fluorescence emission is reduced without any alteration to the average lifetime of the excited state.[10]

In contrast, collisional quenching occurs because of excited-state deactivation upon interaction with another non-fluorescent molecule in solution. In the collisional quenching process, neither of the molecules is chemically changed. Elevated temperatures and lower viscosities usually accelerate the quenching process as they diminish fluorescence by increasing collisions between molecules. In the excitation state, a fluorophore may be quenched by a dipolar resonance energy transfer mechanism to an acceptor molecule.[3]

3.3.5. Photobleaching

Though similar, quenching and photobleaching have some significant differences. Photobleaching occurs due to the movement of electrons from the singlet to the triplet state.[4] Once in the triplet state, the electrons will interact sufficiently with other species with triplet ground states. This consequently results in an irreversible alteration to the molecular structure of the fluorophore and a permanent loss of fluorescence.[4] This is unlike quenching which can be reversible. A significant drawback of this interaction is the formation of reactive oxygen species in and around the fluorescently labelled cell. These species interact with and damage the cellular structures, resulting in the formation of artifacts. The literature shows that adding an extremely low concentration of ascorbic acid is a non-evasive approach to prevent photobleaching and oxygen-mediated cell damage.[4]

3.3.6. Stoke Shift

The shifted emission of a fluorophore compared to excitation is referred to as stokes shift. (Figure 3.3) When displayed together, the stoke shift represents the distance between the two excitation and emission spectra peaks. The white curve is the excitation spectrum and is, in most cases, identical to the absorption spectrum of the fluorophore, with some exceptions. In cases where the excitation spectrum differs significantly from the emission spectrum, it implies the presence of non-fluorescent species in the solution.[11] A better depiction of the excitation curve is against the molar extinction coefficient, which is the

wavelength-dependent absorptivity of that specific fluorophore in the solvent in which the spectrum was generated. Although, since the excitation and emission spectra are usually plotted on the same graph, fluorescence excitation is observed against varying wavelengths. The shape of a molecule's emission profile depends on the compound's molecular structure rather than on its excitation wavelength.[11]

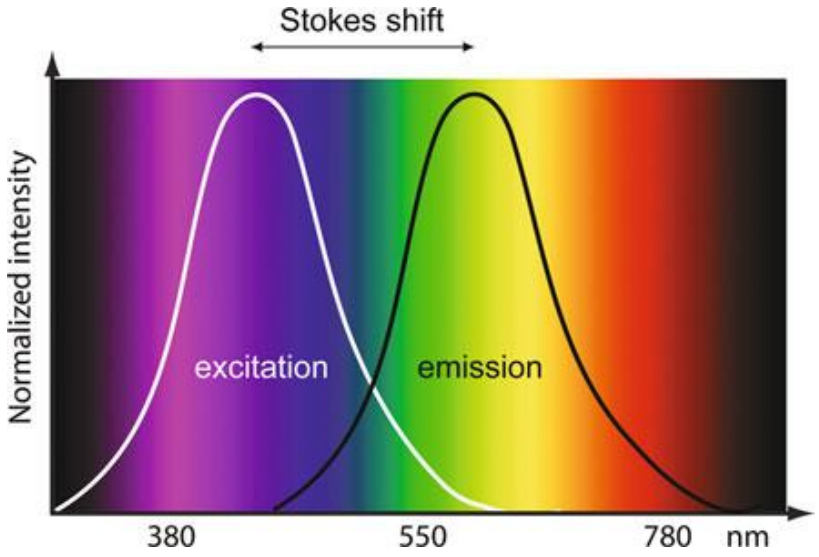

Figure 3.3. Excitation and emission spectra of a hypothetical fluorescent molecule illustrating the red shift (Stokes's shift) of emission wavelength compared to excitation. The degree of the shift depends on the molecule's composition.[4]

3.3.7. Förster Resonance Energy Transfer

Förster or Fluorescence resonance energy transfer (FRET) describes the energy transfer between two fluorophores. It was named after the German scientist Theodor Förster.[12] When a fluorescent donor is excited at its fluorescence excitation wavelength, this excitation energy can be non-radiatively transferred to a second molecule by a long-range dipole-dipole coupling mechanism while the donor fluorophore returns to the ground state.[13]

This energy transfer efficiency depends on the distance between the donor and acceptor molecules. For example, the energy transfer efficiency decreases with the sixth power of the inverse distance between the donor and acceptor molecule. To deduce the distance between the acceptor and the donor molecules, the fluorescence of the acceptor molecule is observed and compared to a referenced intensity, from which the distance between the acceptor and donor can be deduced. The efficiency of the energy transfer (E) can be used

to calculate the distance between a donor and acceptor pair (R) according to equation[13] 3.1 below:

$$E = 1/[1+(R/R_0)^6]$$

Equation 3.1

R_0, referred to as the Förster distance, is the characteristic transfer distance for which $I/I_0 = 0.5$. It can be calculated by equation[13] 3.2:

$$R_0 = 9.79 \times 10^{-5} (J \kappa^2 n^{-4} \Phi_D)^{1/6}$$

Equation 3.2

The J in equation 3.2 measures the spectra overlap between the fluorescence emission from the donor and the acceptor's absorption. The geometric factor, which is dependent on the relative orientations of the energy donor and its acceptor, is represented by κ. Φ_D is the fluorescence quantum yield of the donor, and n is the refractive index of the medium. κ will approach two-thirds if the donor and acceptor molecules tumble rapidly on the timescale of fluorescence emission, and this value is typically used in such calculations. The efficiency of fluorescence resonance energy transfer differs in the degree of spectral overlap, and the value of this degree of spectra overlap is calculated according to equation 3.3.[13]

$$J = \int \varepsilon_A(\lambda)\, I_D(\lambda)\, \lambda^4\, d\lambda / \int I_D(\lambda)\, d\lambda$$

Equation 3.3

Here, the extinction coefficient of the acceptor is represented by $\varepsilon_A(\lambda)$, and the normalized fluorescence intensity is the $I_D(\lambda)$. Wavelengths are expressed in centimeters, and fluorescence intensity is typically measured in arbitrary units (I). This equation ensures a normalized data set.

In addition to the distance between the donor and acceptor molecules, the rate at which energy is transferred depends on other factors such as (i) spectral overlap of the emission spectrum of the donor and the absorption spectrum of the acceptor, (ii) the donor's quantum yield and (iii) the donor's relative orientation and the acceptor's transition dipoles.[10]

3.3.8. Solvatochromism

It has been previously mentioned that the local environment in which a fluorophore is found and factors that affect the environment such as temperature, pH, and the polarity of the solvent have significant effects on a fluorophore's emission spectrum. These effects differ broadly from one fluorophore to the other. The shift observed in fluorescence emission maxima due to the changes in solvent polarity is referred to as solvatochromism.

The solvent molecules surrounding the ground state fluorophore equally possess dipole moments that can interact effectively with the fluorophore's dipole moment. Consequently, an ordered distribution of the solvent molecules is arranged around the fluorophore. After excitation, a change in the fluorophore's dipole moment is observed and causes a rearrangement of the surrounding solvent molecules. However, according to the Franck-Condon principle,[14] upon excitation of a fluorophore, the compound is excited to a higher electronic level quicker than it takes for the solvent and fluorophore to rearrange. Consequently, a delay is observed between the excitation and the rearranging of the solvent molecules around the fluorophore with a much larger dipole moment in the excited state.

Following the fluorophore's excitation to higher vibrational levels of the first excited singlet state (S_1), a loss of excess vibrational energy to the surrounding solvent molecules is observed as the fluorophore relaxes steadily to the lowest vibrational energy level of that state. A more polar solvent induces a more significant reduction in the energy level of the excited state. In contrast, a less polar solvent causes the stabilization effects of the solvent on the excited state. As a result, a more significant stoke shift is observed in polar solvents as opposed to the more minor stokes shifts observed in non-polar solvents. Overall, fluorescence lifetimes are mostly longer than the time needed for solvent relaxation. Therefore, fluorescence emission spectra represent the solvent-relaxed environments in which solvent molecules are oriented around the dipole moment of the fluorophore in the excited state.[4]

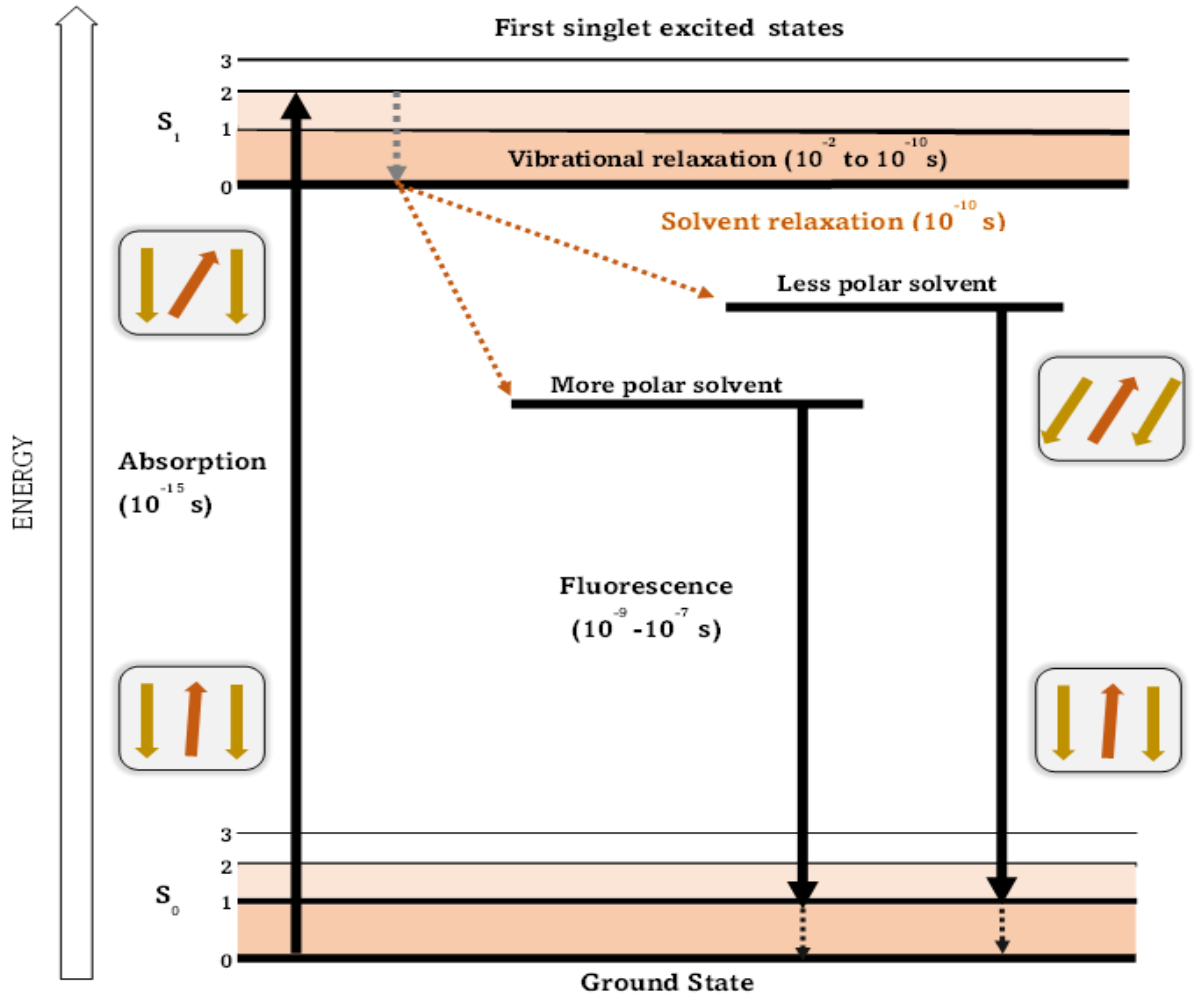

Figure 3.4. Perrin-Jabłoński diagram indicating energy levels and states involved in solvent relaxation. The grey boxes indicate the alignment of the fluorophore (brown) dipole moments and solvent molecules (red) relative to one another in their ground and energetically excited states.[6]

3.4. Fluorescence Spectroscopy

3.4.1 Instrumentation

Fluorescence microscopy is the process of analyzing the fluorescence from a molecule, using its fluorescent properties. This process uses a beam of light as an external energy source to excite electrons in the molecules of a compound and causes them to emit light. The emitted light is directed towards the filter and later onto a detector for measurement and identification of the molecule or any changes in the molecule. This process is also referred to as spectrofluorimetry and is carried out on a spectrofluorimeter. Unlike fluorescence microscopy, spectrofluorimetry is most precise at extremely low fluorophore concentrations. Under ‘’ideal’’ or optically dilute conditions, fluorescence

intensity, represented by F_{ideal} (λ_{ex}, λ_{ex}), which is related to the power of the incident radiation I_0 (λ_{ex}), is defined according to equation 3.4:

$$F_{ideal}\,(\lambda_{ex}, \lambda_{ex}) = 2.3 \times k\,(\lambda_{ex}, \lambda_{ex}) \times I_0\,(\lambda_{ex}) \times \varepsilon(\lambda_{ex}) \times \Phi(\lambda_{em}) \times \Delta_{\chi} \times c$$

Equation 3.4

k(λ_{ex}, λ_{ex}) represents the instrument constant dependent on optical and geometrical factors. This constant is a function of the excitation and emission wavelengths, while $\varepsilon(\lambda_{ex})$ is the molar absorption coefficient of the excitation wavelength of the fluorophore. C represents the fluorophore's concentration, and Δ_{χ} represents the pathlength of the excitation beam. Finally, the fluorescence quantum yield at the emission wavelength is $\Phi(\lambda_{em})$.[15]

The direct proportionality between a fluorophore's concentration and its intensity makes it easy to use simple electronics and optics in a spectrofluorimeter. Xenon lamps are usually used as a light source that illuminates equally in all directions. Two monochromators are typically used in a spectrofluorometer. The first monochromator selects the excitation wavelength, from which the radiation following excitation is split into double paths. Parts of this radiation then pass through to a reference photomultiplier tube and part of it to the sample. Following fluorescence emission from the sample in all directions, the second monochromator is then used to determine the emission wavelengths to be transmitted to the detector. Finally, the light is detected using a second sensitive photocell after dispersion by the emission monochromator.[16,17]

For an accurate spectrofluorometric read, temperature control is required. This is because fluorescence intensity varies with slight temperature changes. Aside from the fluorescence intensity, many other factors affect the fluorescence spectrum. These include the characteristics of the lamp, the transducer, and the monochromators. These factors make it challenging to compare spectra across instruments quantitatively. All the components differ with wavelength and vary from one device to another. There are two main approaches to illuminating a sample on the spectrofluorimeter. The most straightforward and commonly used design involves the excitation and emission from the

center of a cuvette at right angles to each other. The alternative approach is front-face illumination which prevents the inner-filter effect.

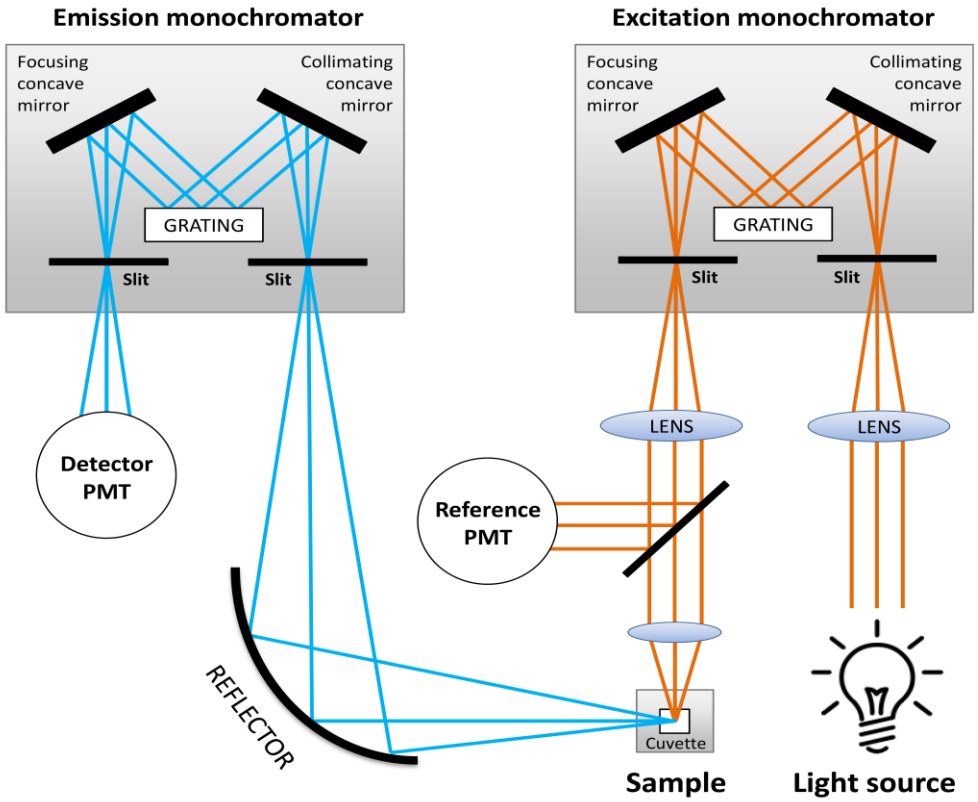

Figure 3.5. Illustration of a typical spectrofluorimeter. The orange rays represent incident radiation, while the blue rays indicate fluorescence rays exiting the sample after excitation[18]

3.4.2. Inner-filter Effect

The inner-filter effect is a phenomenon that occurs because of the optical dispersion of light at the excitation or emission wavelengths by other compounds present in solution. In most commercial spectrofluorimeters, the optics focus on the exciting light and accumulate the emission from the center of the cuvette (Figure 3.6). Consequently, the more absorption at the excitation wavelength, the less light reaches the center of the examined sample, reducing the fluorophore's fluorescence. Meanwhile, the emitted light that reaches the detector is decreased equally due to absorption at the emission wavelength. As described in equation 3.4, ''under ideal'' conditions, fluorescence intensity is a linear function of the fluorophore's concentration. However, these conditions can only be met when light attenuation at excitation and emission wavelengths is insignificant for the desired pathlength. Also, fluorescence intensity is reduced by the absorption of

excitation and emission radiation by a sample, resulting in an inconsistent relationship between the fluorescence intensity observed and the fluorophore's concentration. This further describes the inner-filter effect.

There are two types of inner-filter effects. These include the primary and secondary inner-filter effects. The primary inner-filter effect describes the significant absorption of excitation wavelength, leading to less light reaching the center of the sample and consequently a reduction of the fluorophore's fluorescence. On the other hand, the secondary inner-filter effect refers to the absorption of the emission radiation. It can be averted entirely if emission wavelengths are carefully selected so that no sample components absorb light. However, the primary inner-filter effect can only be minimized but not avoided. This is because the fluorophore's absorption is necessary for excitation to occur.

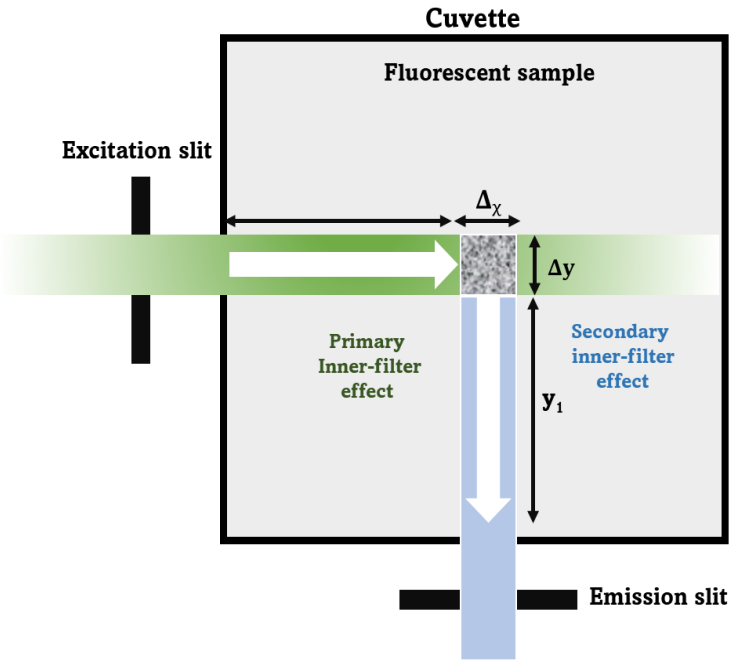

Figure 3.6. Illustration of inner-filter effects in a cuvette showing the attenuation of both the excitation radiation and the emitted fluorescence.[15]

To minimize the impact of the inner-filter effects, various correctional factors have been proposed. The inner-filter effect can be accounted for from equation 3.5 if the instrument's geometry is designed such that the accumulated fluorescence intensity emanates precisely from the center of the cuvette.

$$F_{corr} = F_{obs} \times 10\text{^}(-(A_{ex} \times d_{ex})/2) - (A_{em} \times d_{em})/2$$

Equation 3.5

Here, F_{corr} represents the corrected fluorescence intensity of the fluorophore, which would be measured without the inner-filter effect. F_{obs} is the fluorescence measured in the presence of the inner filter effect. d_{ex} and d_{em} define the pathlengths of the cuvette in the excitation and emission directions, respectively. A_{ex} and A_{em} are the observed changes in absorbance at excitation and emission wavelengths, respectively.[19]

With a focus on the right-angle geometry, where fluorescence begins from the center of the cuvette (Figure 3.6), equation 3.5 above applies. Although this is the case in some spectrofluorometers, it is not the case for all. Hence a more advanced correction technique will equally account for instrument-specific factors. The relationship between F_{ideal} and F_{obs} is described in equation 3.6 below:[15]

$$F_{ideal} = F_{obs} \times 2.3\alpha_{ex}\Delta\chi 10^{\alpha_{ex}\chi_1}/(1 - 10^{-\alpha_{ex}\Delta\chi}) \times 2.3\alpha_{em}\Delta y 10^{\alpha_{em}y1}/(1 - 10^{-\alpha_{em}\Delta y})$$

Equation 3.6

Here, the absorbances of solution per centimeter are represented by a_{ex} and a_{em} and at wavelengths λ_{ex} and λ_{em}, respectively. The distances from the beam edges to the cuvette wall towards the source of light and the detector are depicted by χ_1 and y1, respectively. All geometric parameters Δx, x_1, Δy, y_1, are in units of cm, and α is used to represent the absorbance per cm to differentiate it from the standard A for dimensionless absorbance. The fluorescence signal in this model originates from molecules in the overlap volume of the excitation and emission beams depicted in the shaded region of Figure 3.6. Although these advanced correction methods for inner-filter effects are available, it can still occur, mostly at high absorbance values. Therefore, instead of correcting the inner filter effects, it is sometimes more efficient to reduce its impact by making practical adjustments such as using a smaller cuvette to reduce pathlengths or carefully selecting the excitation and emission wavelength to minimize absorption.[15]

3.5. Fluorescence Microscopy

Fluorescence microscopy has become a rapidly developing scientific research and technological advancement field. Its application has ranged from industrial processes to scientific research and medical diagnosis. More powerful is the application of fluorescence in biological imaging. In this regard, fluorescence microscopy allows the study of the dynamics of living cells with a high spatial resolution that is not invasive to the cells. The availability of a vast number of fluorescent stains allows for the quick and efficient study of subcellular components.

The ability of a fluorescence microscope to suppress out of plane emission when forming an image in the focal plane is an important technical consideration that makes confocal microscopy more advantageous over traditional widefield microscopy. This will be discussed further in the sections below. Also, the resolution of an optical imaging system dictated by the wavelength of the external light source is referred to as the diffraction limit. The term diffraction limit defines the potential of a lens-based optical microscope to capture details that are longer than half the wavelength of the incident light.[8] However, the development of super-resolution techniques has surpassed the diffraction limit and opened a new field of superior imaging techniques.

3.5.1. Widefield Microscopy

Widefield microscopy, also known as epifluorescence, is the most popular fluorescence microscopy technique. Although the method was not applied in this study, it is described briefly here for comparison to other methods. In this technique, the excitation and emission happen above the sample, which is in direct contrast to optical microscopes, where collected light is transmitted through the evaluated sample.[8]

An excitation beam is produced from the light source, dispersing bright white light through a filter reflected by a dichroic mirror. This passes the beam through the objective lens, thereby interacting with the sample. (Figure 3.7) Further, the fluorescence emission from the sample is directed back through the objective lens, where the dichroic mirror transmits only the weaker fluorescence lights. Finally, fluorescence is captured on the detector after passing through the emission filter.[8]

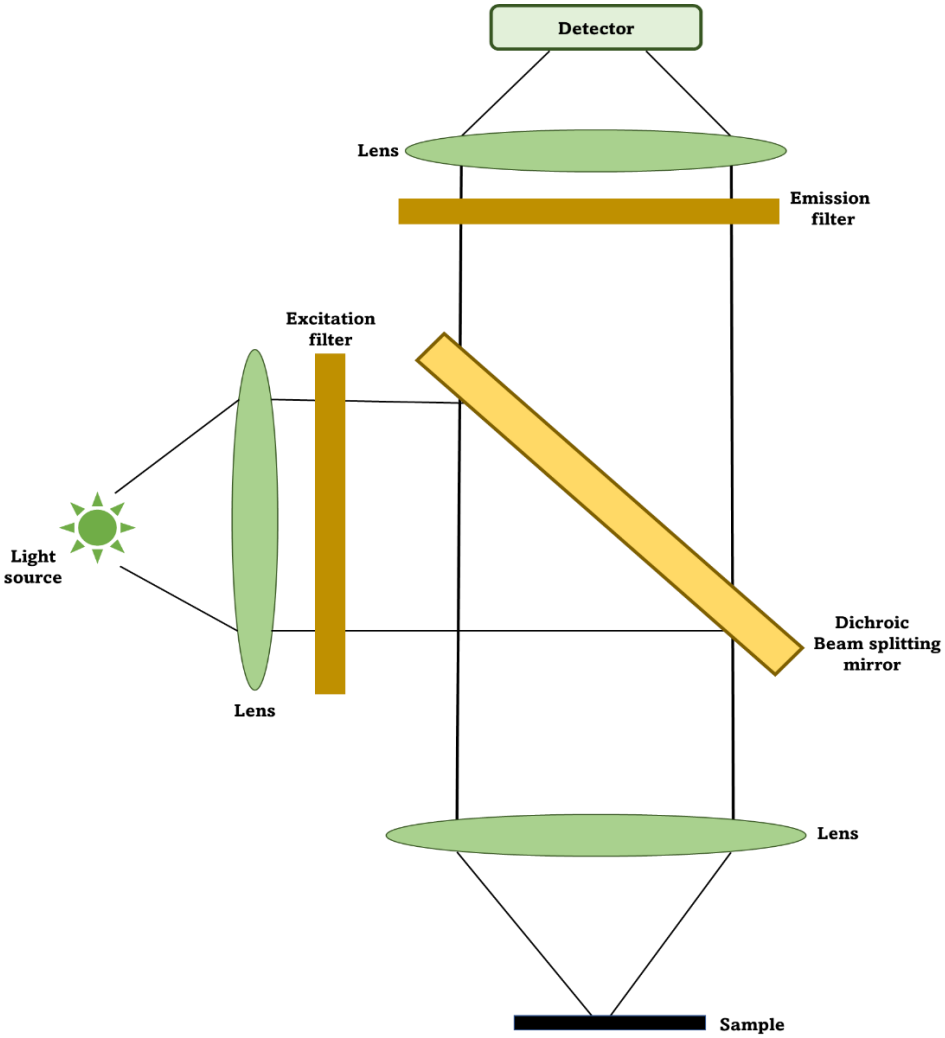

Figure 3.7. An illustration of a widefield microscope. After passing through the first optical filter, the excitation light is focused on the sample under examination from above. Fluorescence is directed to the detector after passing through the emission filter, rejecting reflected and scattered excitation light.[8]

While an epifluorescence microscope is an efficient and powerful tool for collecting fluorescence from a sample being investigated, a significant disadvantage of this type of fluorescence microscopy is that the final image is collected as a two-dimensional image. This image is formed by fluorescence emission both in focus and out-of-focus. Consequently, this results in the loss of spatial information since it is difficult to ascertain what is ''in front'' and what is ''behind''.[8]

3.5.2. Confocal Microscopy

Confocal microscopy forms the basis of the fluorescence live-cell imaging discussed in this thesis work. It presents an alternate approach to developing sharp images using the

standard focusing system described in this section. Here, the excitation of dyes located out-of-focus by the incident beam is not avoided; rather, the instrument is configurated to reject the emission from the out-of-focus excitation. This is achieved through scanning the focal plane with the confocal pinhole, thereby providing geometric restrictions to the out-of-focus emissions.[8] A schematic representation of a typical confocal microscope is depicted in Figured 3.8.

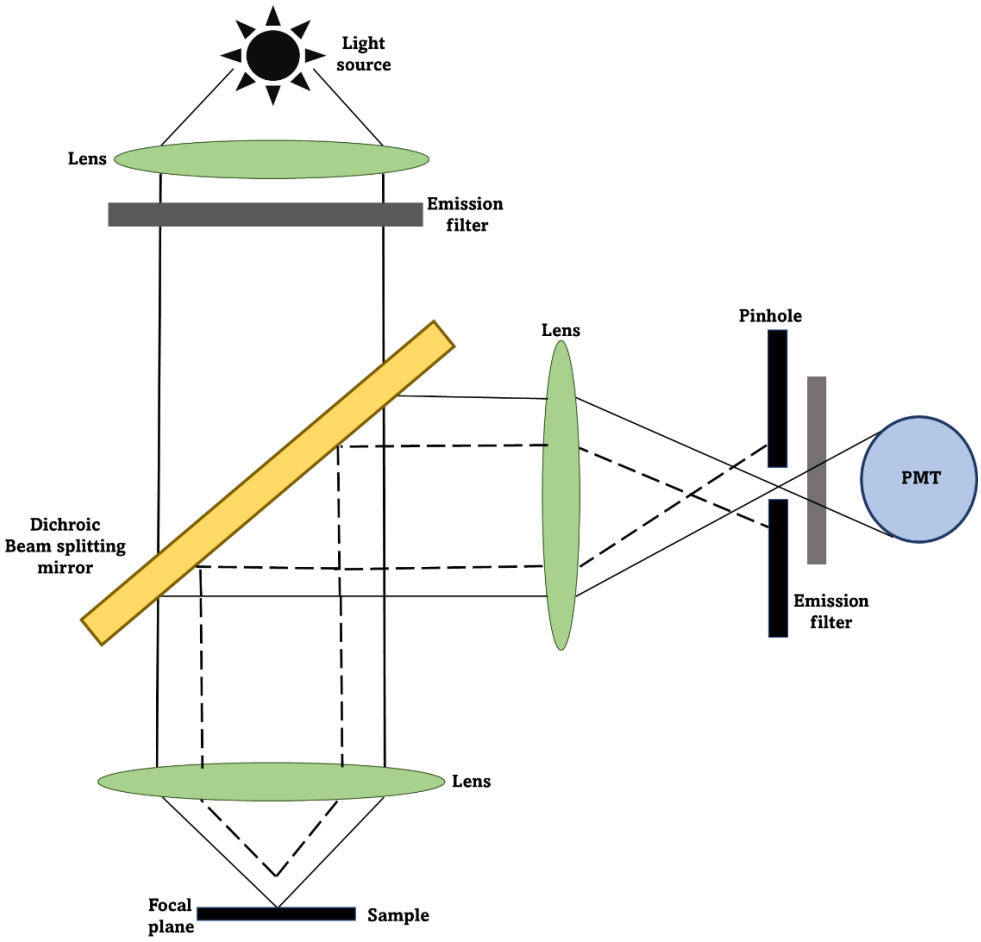

Figure 3. 8. A schematic representation of a typical confocal microscope depicting the beam geometry allows the rejection of photons emitted from outside the focal plane.[8]

Confocal microscopes require a higher intensity of photons for excitation than widefield microscopes. Hence lasers are employed in confocal microscopes. Upon entering the microscope, the laser beams pass through the excitation filter and the dichroic mirror. After which, they are moved in raster by two scanning mirrors across the sample. The fluorescence light then makes its way back through the objective lens, where it is de-scanned by reflecting it off both scanning mirrors. This light is reflected off the dichroic mirror. At this point, only in-focus light proceeds through the pinhole, to the emission

filter, and then to the detector. Notably, the pin-hole rejects all the out-of-focus light and prevents it from reaching the detector.[8]

The resolution along the *z*-axis is by one order of magnitude less than the total internal reflection microscopy. However, the advantage of confocal microscopy is that it allows for adjusting the focal plane. This enables one to scan the object at different *z* levels, so the cross-section at various depts can be obtained. A three-dimensional image of the object can be constructed from these cross-sections by computational means. This technique's major disadvantage is the need to use high intensity lasers for excitation, not only within the focal plane. This is because it increases the chances for photobleaching and phototoxicity, mostly in live cells.[8]

To circumvent this drawback, two-photon excitation sources are used. Two-photon excitation describes the phenomenon that brings an electronic system to an excited state by the absorption of two photons simultaneously. This excitation can only occur at a remarkably high photon density, which can be achieved by trapping the light flux on a spatial and temporal scale. Practically, this can be done by using a short and well-focused laser. In such cases, the focal point of the laser is the only location along the optical path where the density of the photon is high enough to generate two-photon excited species. Thus, two-photon microscopy shows a dramatic difference between the excitation and emission wavelengths. For example, a fluorophore with an average absorption maximum at 520 nm can be excited by two photons of 1050 nm laser and emission detected at 560 nm, thereby easily rejecting the scattered excitation light.[8]

In contrast to single-photon excitation, where fluorescent emission differs linearly with the intensity of the excitation light, fluorescence emission due to two-photon excitation varies with the square of the excitation intensity.[8] High spatial resolution is achieved using this quadratic relationship between excitation and emission. This is because it allows the excitation power to be focused on a small volume without observing emissions outside this volume. Although the photon density is not sufficiently high above and below the focal point for two photons to pass concurrently within the absorption cross-section of a single fluorophore, it is high enough at the focal point such that two photons can be absorbed simultaneously with a good probability.

3.5.3. Super-Resolution Microscopy

Techniques that improve the spatial resolution of microscopic images have been in high demand by researchers. Resolution is described as the ability to resolve one object from another. In optical imaging, the resolution is impacted by the diffraction of light. However, there is a limit to lens-based amplification in light microscopy.

3.5.3.1 Breaking the Diffraction Limit

Ernst Abbe formulated a mathematical expression in 1863 to describe the diffraction limit, which is defined as the point spread functions and their projections. Ernst Abbe[20] and Lord Rayleigh[21] discovered that light travelling at a specific wavelength λ through a medium with refractive index *n* and converged at an angle θ will form a focal spot with radius *d* as described in equation 3.7 below:[22]

$$d = \frac{\lambda}{2\, n\, sin\theta}$$

Equation 3.7

By this equation, the authors showed that this diffraction limit limits widefield and confocal microscopes. Therefore, the diffraction limit must be removed to increase the spatial resolution of images acquired on these microscopes. In confocal and widefield microscopes, the ideal notion that light rays converge into an infinitely sharp focal point does not occur. Instead, the light rays form a blurry focal point due to diffraction.[22]

Since most lenses have a numerical aperture of about 1.5 at an angle of 70°, the theoretical resolution for cell imaging where the wavelength is approaching 400 nm is 150 nm sideways and 500 nm vertically. Currently, the resolution of all confocal and widefield microscopes approaches this limit. For many years, the diffraction limit has remained a technological barrier for cellular imaging in terms of resolution. However, the emergence of modern technologies has resulted in many attempts to lift this barrier and increase the success of obtaining more resolved images. These technologies with the power to break the diffraction limit and significantly increase the resolution of images are collectively known as super-resolution microscopy. An example of a super-resolution technique is stimulated emission depletion (STED).[22]

STED microscopy was developed and demonstrated in the 1990s by Stefan Hell to create super-resolution images by selectively deactivating fluorophores and minimizing the area of illumination of the focal point. This subsequently increases the resolution. STED microscopy utilizes two laser sources: one for exciting the fluorophores and the other for quenching all other fluorophores except those surrounding the region of interest in nanometer ranges. These outer region fluorophores are quenched by forcing them into higher vibrational levels without fluorescence emission (stimulated depletion). The energy of the second laser is usually lower than the excitation energy and is found in the far-red region. However, on the downside, the high intensities needed for STED microscopy results in photobleaching when working with live cells. [22]

Aside from STED microscopy, super-resolution images can also be acquired by randomly alternating between emissions of fluorescent probes that contradict the objects under study and are located at a distance more significant than the diffraction limit. These are referred to as the stochastic methods. The idea here is to excite several sub-populations of these probes consecutively from which composed images are formed. A series of individual long-range probes are imaged at the center of their diffraction limit. These partial fluorescence images are superimposed to obtain a dense, super-resolved image. The two main stochastic methods are photoactivated localization microscopy (PALM) and stochastic optical reconstruction microscopy (STORM).[22]

3.5.3.2 Super-resolution Structured-illumination Microscopy (SR-SIM)

Another type of super-resolution technology, structured-illumination microscopy (SIM), is a lateral resolution technique that overcomes the diffraction limit by a factor of two in a widefield microscope. It is based on a series of excitation light patterns that cause high-resolution images that would typically not be accessible to be encoded into the image observed. Contrary to what is observed in confocal microscopy, a significant improvement in resolution is achieved even without discarding any emitted light. The concept behind SIM is best explained and easily understood in terms of the well-described moiré effect. Here, if two fine patterns are superimposed, a pattern known as moiré fringes will appear (Figure 3.9).[23] These moiré fringes are much coarser than any of the original patterns making them easily noticeable under a microscope even when one or both original patterns are too small to be resolved. One superimposed pattern is usually

the fluorophore's unknown spatial distribution, while the other pattern is structured light intensity.[23]

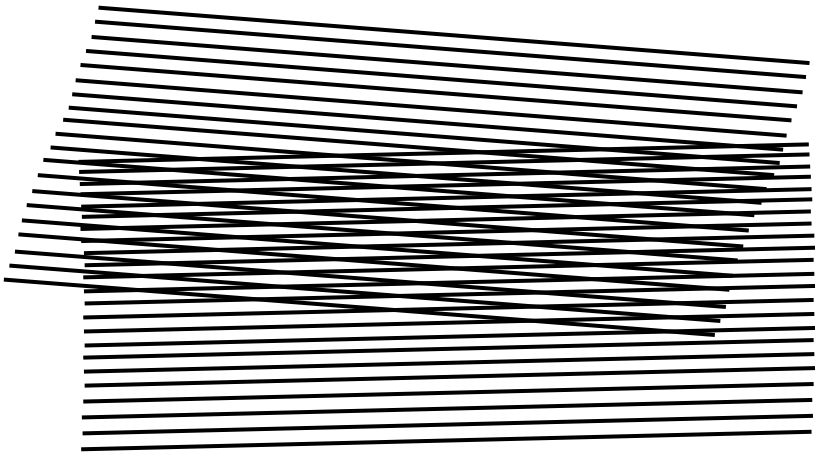

Figure 3. 9. Illustration of moiré fringes formed from the superimposition of two-line patterns. The moiré fringes here are shown as vertical stripes in the overlap regions.[23]

Concerning the quantitative abilities of SIM, it is helpful to think of the sample structure in reciprocal space, that is, its Fourier transform. Three non-zero points are observed here, one at the origin and the other two start circular at the source but are contained in the circle that defines the observable region. (Figure 3.10 a).[23]

Here, low-resolution information exits close to the origin, while higher resolution information exists further away from an observable region of reciprocal space (Figure 3.10 b). With the appearance of a moiré fringe, the visible regions do not only contain the usual information that resides there but also information emanating from the two offset regions as well.[23] (Figure 3.10 c)

At this stage, it is possible to recover information from an area twice the size of the normally observable region from a sequence of images with different orientations and phases. This corresponds to twice the standard resolution (Figure 3.10 d). Since this technique relies solely on the microscope's optics and not the fluorophore's photophysical properties, any fluorophore used in a conventional fluorescence microscope will be compatible. Also, with SIM, the diffraction-limited resolution is doubled to about 100 nm laterally and 300 nm axially, improving image resolution significantly.[23]

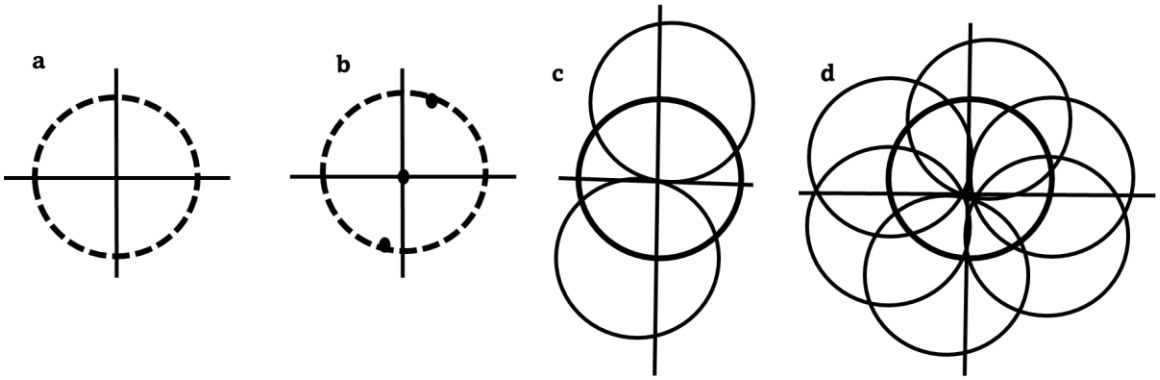

Figure 3.10. Illustrations of a series of diagrams explaining the resolution enhancement possible by SIM.[23]

3.6. Evaluating Fluorescence Colocalization in Biological Microscopy

As earlier described, fluorescence microscopy presents a powerful tool to elucidate the cellular functions of molecules. In most cases, the function of a small molecule can be deduced from its interaction with a particular intracellular compartment (s).[24] These interactions are typically assessed by comparing the fluorescence distribution of a known organelle probe and that of the fluorescently labelled version of the small molecule. Colocalization is a term that was initially used to broadly describe molecular interactions between fluorescently labelled molecules and cellular functions under study. However, there have been criticisms from the scientific community regarding using the term in this manner. It is argued that this approach is not appropriate for detecting the level of detail required to conclude on molecular interactions.[24] The light microscope's resolution is simply insufficient to determine the physical compatibility of two molecules by comparing their fluorescence distributions, even in a super-resolution microscope.

Instead, colocalization is better described as a phenomenon where two fluorescence probes co-distribute with one another. It is more appropriately used to probe whether or not two molecules associate with the same cellular structures. For example, colocalization was successfully used to determine whether CQ interacts with *P. falciparum* organelles such as the lysosomes, mitochondria, nucleus, and lipid bodies.[25] Other studies also used colocalization to probe protein association with endosomes, mitochondria, and microtubules. Fluorescence colocalization is affected by the limits of resolution. While an overlap suggests fluorescence colocalization between two fluorophores, repeated observation of both probes in structures in the cell increases confidence that both probes

occupy the same cellular structures. Colocalization of fluorescence probes can be evaluated visually, quantitatively, and statistically. Visually, the colocalization of two fluorescence probes can be subjectively assessed when the fluorescence emission from both probes is superimposed into what is referred to as ''merged'' images. The cellular structures whose colour reflects the combined colours of both probes depict colocalization. For example, colocalization of 4-chloro-7-nitrobenzofurazan and Lysotracker Red can be evident in the structures that appear yellow. This results from the equal contribution of the green and red emissions from both fluorophores.

3.6.1. Quantitative Image Analysis

Although the visual techniques described above help probe the distribution of fluorescence probes in different cellular compartments, quantitative analyses in terms of scatterplots and statistical analyses are more helpful in providing a quantitative assessment of the degree of colocalization that is not subjective. These statistical analyses are collectively referred to as correlation coefficient-based analyses. These include the Pearson correlation coefficient, Manders overlap, and colocalization coefficients. The statistical analyses of the correlation of the intensity values of the pixels in a dual-channel image are mainly done using correlation coefficients.

3.6.1.1 Scatterplots and the Pearson Correlation Coefficient

The simplest and most common way of assessing the dependency of pixels in images containing two colours where pixel intensity values of the two images are plotted against one another is known as a scatterplot or cytofluorogram. A scatterplot is formed when the intensities of both pixel distributions are proportional to one another and if the detection has been carried out in a linear range. The slope of this line represents the relative stoichiometry of the fluorophores being analyzed. Also, the Pearson correlation coefficient (PCC) can be used to estimate the linear regression by examining the spread of this distribution with respect to a fitted line.

Pearson correlation coefficient is a method of pattern recognition, where an image is matched with another, and the degree of overlap between two patterns is assessed. This technique also provides knowledge regarding the similarity of shapes without regard to the intensity of the signal. For pixel scatterplots, the spread of the dot cloud relative to

the median line can be quantified by the PCC. Complete colocalization is represented by a value of 1, while -1 represents a negative correlation. Zero indicates no colocalization. An illustrative example of positive and negative correlations from a hypothetical data set is presented in Figure 3.11 below.

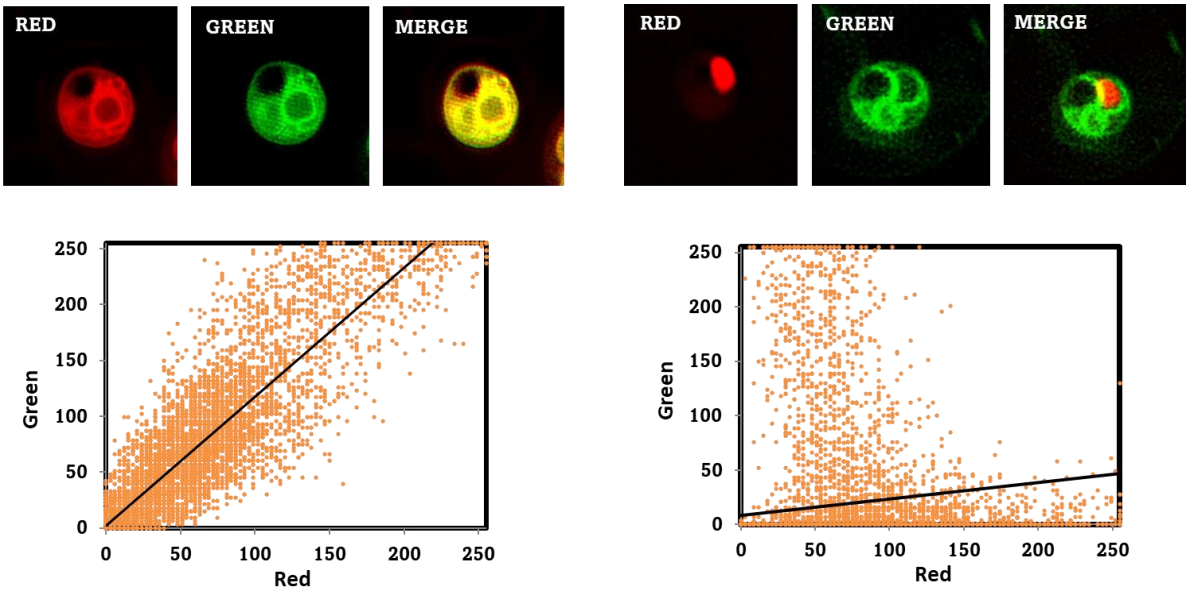

Figure 3. 11. Scatterplots for a hypothetical data set, indicating positive colocalization between the red and green channels (left) and a negative colocalization between the red and green data set (right). Pearson correlation coefficients were calculated and found to be 0.874 and -0.452, respectively.

For a typical image consisting of red and green channels, PCC can be calculated from equation 3.8 below:

$$\text{PCC} = \frac{\sum_i (Ai - a) \times (Bi - b)}{\sqrt{\sum_i (Ai - a)2 \times \sum_i (Bi - b)2}}$$

Equation 3.8

A_i and B_I represent the intensities of pixel i of channels A and B of a two-colour image, respectively. The mean intensities of the two channels are defined by a and b, respectively. The average intensities are deducted from the original intensity values, putting the values of this coefficient between -1 and 1. PCC's success depends on the intensity of the background noise and fluorescence intensity variations between the two channels under analysis. Using PCC alone to evaluate colocalization is not efficient; however, when combined with scatterplots, it is a reasonable estimate of colocalization.

3.6.1.2. Manders Overlap Coefficient

An alternative but closely related assessment metric, the Manders overlap coefficient (MOC), was developed in response to the perceived difficulty in interpreting the negative data set from PCC.[26] This technique of assessing colocalization is described by equation 3.9

$$MOC = (\sum_i (A_i \times B_i)) / \sqrt{(\sum_i A_i^2 \times \sum_i B_i^2)}$$

Equation 3.9

With MOC, the average intensity values of the pixels are not deducted from the original intensity values in equation 3.8, resulting in a new coefficient. This new coefficient varies from zero, which represents no colocalization, to one, which represents complete colocalization. *Ai* and *Bi* belong to a pixel of one of the colocalization objects ($A_i > 0$ and $B_i > 0$) only when the product of the numerators bring in a non-zero value. To put it in context, when one-pixel value is zero, each added product is zero. This signifies no fluorescence and alludes to the fact that the numerator is proportional to the number of colocalizing objects. Similarly, the total number of both the colocalizing and non-colocalizing components of an image is proportional to the denominator.[27]

Manders's overlap coefficient is advantageous over the Pearson correlation coefficient because of its insensitivity to the differences in the intensities of signals between the components of an image resulting from photobleaching, different labelling with fluorophores, or changes made to the gains settings during image acquisition. On the other hand, because the ratio of the number of objects in both components plays a significant role in MOC, a major disadvantage of this technique is that calculations may be ambiguous.[26]

3.6.1.3. The Manders Colocalization Coefficients

The Manders colocalization coefficient (MCC) was developed to cancel out the large effect caused by the number of objects, such that the MCC may be split up into two new coefficients referred to as the split coefficients, developed from equation 3.10.[27]

$$r_M^2 = k_1 \times k_2$$

Equation 3.10

Where the following equations respectively define k1 and k2:

$$k_1 = (\sum\_i (A_i \times B_i)/\sqrt{\sum\_i A_i^2}$$

Equation 3.11

$$K_2 = (\sum\_i (A_i \times B_i)/\sqrt{\sum\_i B_i^2}$$

Equation 3.12

Two parameters are used with these coefficients to express the degree of colocalization. k_1 and k_2 in these equations rely on the sum of the products of the intensities of A and B. Hence, k_1 is affected by the differences in the intensity of the signal from B. Comparably, k_2 is linearly dependent on the intensity of the signals from A.[27] k_1 approaches α in a perfect colocalization while k_2 approaches $1/\alpha$. Here, alpha represents the slope of the mean in the cytofluorogram.[27]

A channel corrupted by the background signal causes an increase in the corresponding coefficient's denominator and consequently decreases the coefficient's value. Both coefficients must be checked carefully to identify the source of the issue if the overlap coefficient approaches zero.[27] Two final coefficients are derived based on the split overlap coefficient independent of the signal intensities. These are known as the Manders colocalization coefficients defined below:[27]

$$M_1 = (\sum\_i (A_{i,\ coloc})/\sqrt{\sum\_i A_i}$$

Equation 3.13

$$M_1 = (\sum\_i (B_{i,\ coloc})/\sqrt{\sum\_i B_i}$$

Equation 3.14

Here, $A_{i,coloc} = A_i$ if $B_i > 0$ and $B_{i,coloc} = B_i$ if $A_i > 0$. Also, M_1 and M_2 can represent any value between zero and one, where one specifies complete colocalization. Further, the sum of the intensities of the colocalizing pixels from one channel is divided by the density such that if a pixel from A has a non-zero intensity counterpart in B, then it is colocalized with B. Consequently, M_1 and M_2 are described so that colocalization can be quantified even with differences in signal intensities between the two components.[28]

In summary, when taken together and compared over several sets of images, the Pearson correlation coefficient and the different Manders coefficients (the overlap, colocalization, and split) present a robust set of tools for analyzing and quantifying colocalizations. The PCC (r_p) helps analyze the correlation between the channels' intensity distributions, while the Manders overlap coefficient (r_M) is better at analyzing the overlap of the signals. When each component of an image under analysis contains an equal number of objects, the overlap coefficient represents the part of the colocalizing objects in the image. The Manders colocalization coefficient M_1 and M_2 are more efficient when the numbers of the objects in the two components vary significantly. The sensitivity of M_1 and M_2 to background signals and cross talk is a significant advantage of this approach to quantifying colocalization.[28]

3.6.1.4. Van Steensel's Cross-correlation coefficient.

Steensel and co-workers developed a different approach to differentiate between positive and partial colocalization. A positive correlation may occur from the sporadic overlap of objects that are randomly distributed.[29]

A cross-correlation analysis was applied by shifting one image pixel-by-pixel in the x-direction compared to the other image (Figure 3.12). The authors calculated the Pearson correlation coefficient for each shifted set (rp) and plotted these values as a function of the pixel shift (δx).[29]

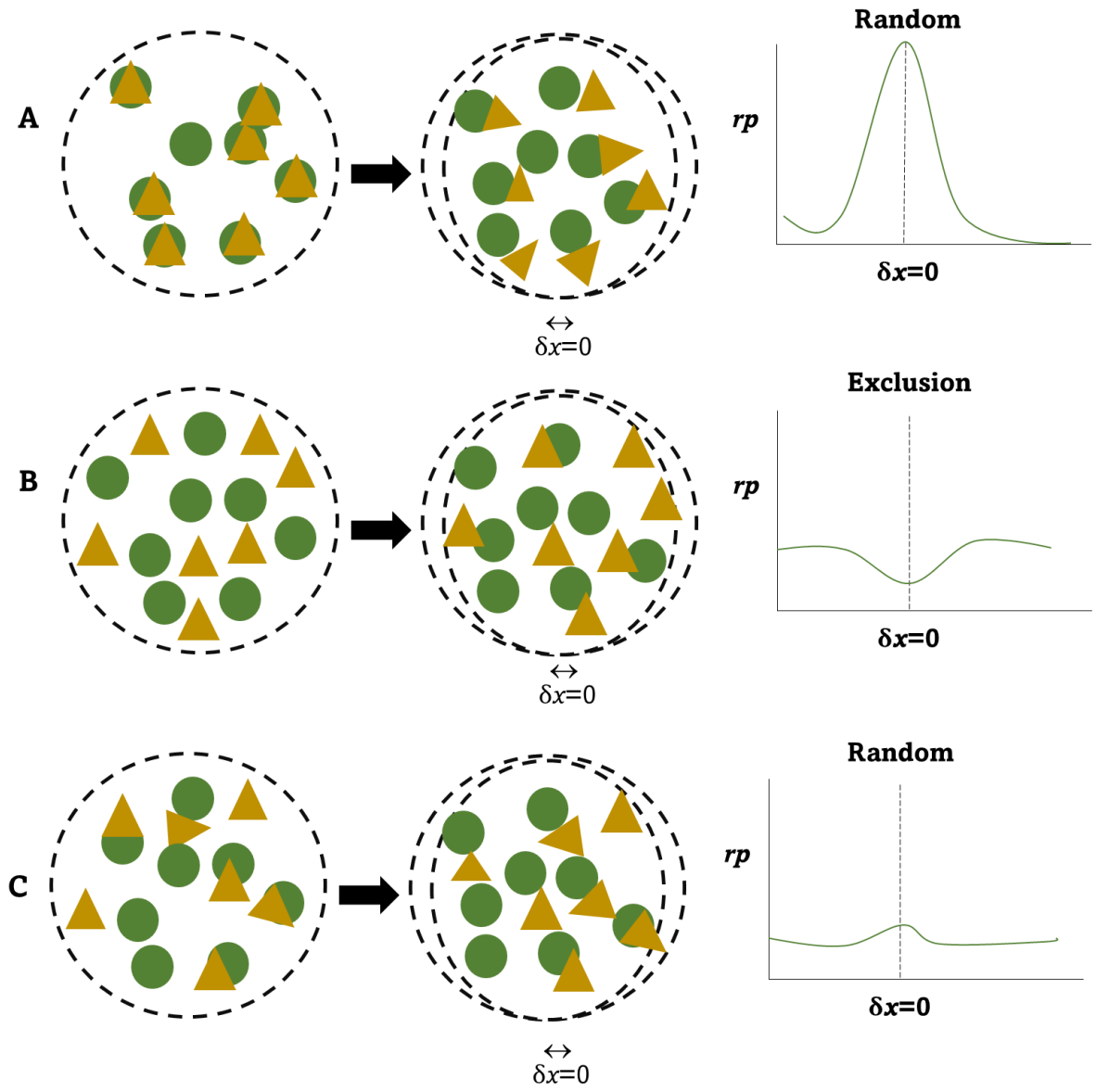

Figure 3.12. An illustration of Van Steensel's cross-correlation analysis, showing three different schemes such as (A) Overlapping, (B) mutually exclusive, and (C) Non-correlated, depicted by the yellow and green elements.[29]

Correlation is usually lost after the displacement in an ideal colocalization situation. Therefore, a peak is observed in the PCC at $\delta x=0$, exhibiting a bell-shaped curve when the objects move further away from each other and the coefficient decreases (Figure 3.12A). A dip is observed at $\delta x=0$, resulting from structures mutually excluded from one another. A shift in either image over a short distance can increase the extent of overlap. (Figure 3.12B) Finally, a slight shift has no effect on the amount of overlap for objects that are partially overlapping or objects that are distributed randomly with regard to each other.[29]

Van Steensel's cross correlation is more efficient in analyzing the signals located in punctuate clusters. Although this technique functions well in discriminating between the different colocalization situations, its limitation is that it is only essential for small isotropic particles. This is because the method varies based on the orientation of the objects compared to the shift axis.[29]

3.7. Intrinsic and Extrinsic Fluorescence

As a starting point toward understanding the MOA of the compounds studied in this thesis work, a fluorescence drug localization study was employed to investigate their subcellular accumulation in *P. falciparum*.

Fluorescence is commonly observed in polycyclic aromatic compounds, which are highly conjugated and capable of undergoing electronic transitions. This accounts for the inherent fluorescence properties of compounds. For compounds without intrinsic fluorescence properties, extrinsic fluorophores are attached to allow their fluorescence imaging. Most small molecules of pharmacological interest to malaria drug discovery are not inherently fluorescent and have required their derivatization by attaching extrinsic fluorophores for fluorescence imaging. However, there have been growing concerns that these extrinsic fluorophores may change the MOA of the studied compound and interfere with their subcellular accumulation in the parasite even when the fluorescent analogues retain antiplasmodium activity. Also, extensive structure-activity relationships are required to ascertain the most appropriate site for the attachment of the external fluorophore, resulting in the need for additional synthetic steps. Furthermore, selecting an appropriate fluorophore suitable for each molecule can be daunting since most fluorophores are either too big, too expensive, or generally not ideal for the molecule under study. Consequently, the intrinsic fluorescence properties of the compounds under investigation would be advantageous in circumventing these drawbacks. For compounds that require the attachment of an extrinsic fluorophore, the fluorescence properties previously described earlier, including the fluorophore's excitation and emission maxima, quantum yield, and quenching, must be considered carefully in selecting an external fluorophore.

Two of the compounds studied in this thesis work, **KP68** and **KP124,** are intrinsically fluorescent and do not require the attachment of an extrinsic. However, **DM253** required

the attachment of NBD extrinsic fluorophore. NBD-labelled analogues of **KP68** and **KP124** were also synthesized to assess the effect of attaching an external fluorophore on the subcellular accumulation of **KP124** and **KP68**. While the fluorescent compounds and the novel fluorescence derivatives were anticipated to have suitable photophysical properties for fluorescence microscopy, it was essential to characterize and evaluate their photophysical, pharmacological, and fundamental physicochemical properties in relation to the parent molecules. The following sections will describe the photophysical characterization of all fluorescent compounds and derivatives earlier prepared in Chapter 2. Here, their absorption and emission spectra will be described together with other photophysical properties such as fluorescence quantum yields, solvatochromism, and stability

Further, the activities of the novel fluorescent derivatives were measured against β-haematin formation using a detergent-mediated assay in comparison to their parent molecules. Most importantly, these derivatives were assessed for their *in vitro* antiplasmodium activities. These measurements, when taken together, have aided in evaluating the suitability of the compounds and fluorescent derivatives for live-cell microscopy studies.

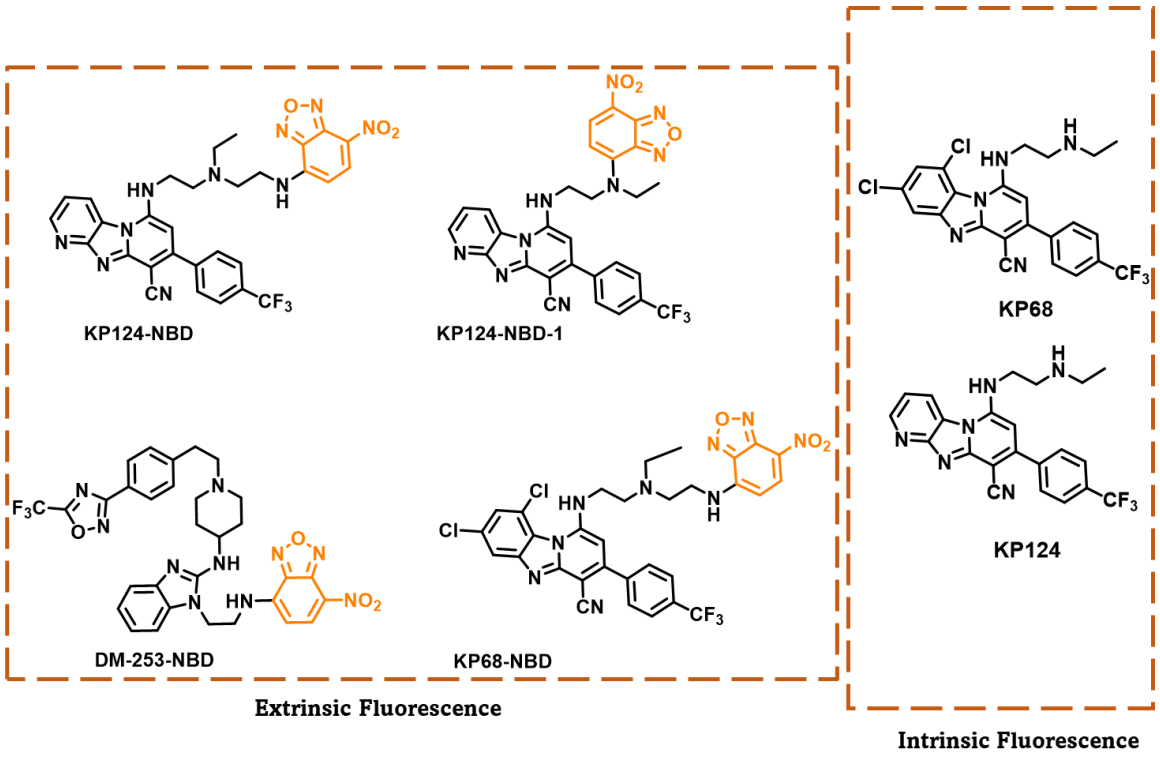

Figure 3.13. Fluorescent compounds and derivatives prepared in this study

3.7.1. Absorption and Fluorescence Emission Spectra

As earlier described in Chapter 2, the target compounds studied in this work and their novel fluorescent derivatives were synthesized and characterized. For the first time, the intrinsic fluorescence properties of the PBIs, **KP68,** and **KP124** were evaluated. Also, NBD reporter fluorophore was identified as a suitable extrinsic fluorophore for probing the subcellular accumulation of the target compounds. Consequently, NBD was attached to the target compounds to form their novel fluorescence derivatives. A single NBD derivative of **KP68** and **DM253** was synthesized while two fluorescence derivatives of **KP124** were prepared, one with NBD directly attached (**KP124-NBD-1**) and the other with NBD two methylene groups away (**KP124-NBD**). All fluorescence compounds studied in this work are listed in Figure 3.13.

Table 3.1. Absorption maxima (λ_{max}) and molar absorption coefficients (ε) at the depicted wavelength of fluorescent compounds and derivatives with their corresponding emission maxima. Measurements were taken in Ethanol.

Fluorescent derivatives	λ_{max}, nm (ε, M^{-1} cm^{-1})	Fluorescence emission maximum at λ_{max}, nm
KP68	300 [15,500], 410 [15,000]	510 (excitation at 300 nm)
KP124	300 [14,000], 410 [17,000]	510 (excitation at 312 nm)
KP68-NBD	312 [15,000], 465 [10,000]	528 (excitation at 465 nm)
KP124-NBD	312 [14,000], 465 [10,500]	520 (excitation at 465 nm)
KP124-NBD-1	297 [16,000], 465 [10,500]	545 (excitation at 465 nm)
DM253-NBD	336 [6,000], 470 [12,500]	530 (excitation at 482 nm)

All the fluorescent compounds generally possess two absorption maxima. A shorter wavelength band at 300-340 nm corresponds to the PBI core in the case of **KP68** and **KP124** and the benzimidazole core in the case of **DM253**. The more extended wavelength band corresponds to the absorption maxima of the NBD extrinsic reporter fluorophore for NBD-labelled derivatives. Strong absorption bands characterize NBD-labelled derivatives, generally around 10,000 M^{-1} cm^{-1}. Regarding the intrinsic fluorescence of **KP124** and **KP68,** both compounds were photophysically identical. This

is expected as both compounds possess similar chemical structures. Primary and secondary absorption bands were observed at around 410 nm and 300 nm, respectively. These correspond to the first and second excited states of the PBIs, respectively.

Fluorescence emission was obtained following excitement at both absorption maxima. The NBD-labelled benzimidazole exhibited a single emission (thus, no fluorescence emission was observed from the benzimidazole core) (Figure 3.14 A). NBD-labelled PBIs showed fluorescence emission between 520 and 545 nm following excitation at 465 nm and absorption due to the NBD fluorophore. Except for NBD-labelled **DM253**, a higher molar extinction coefficient was observed in the absorption from the PBI core, suggesting that the UV absorption band occurring at a wavelength of 312 nm absorbs stronger than the absorption band of the NBD fluorophore ($\boldsymbol{\lambda_{max}}$ 465). Therefore, it was not surprising that primary emission resulted from the excitation of the PBI core, while a weaker fluorescence emission was observed following the excitation of the NBD fluorophore. The fluorescence originating from the PBIs is brighter, possibly quenching the fluorescence of the NBD fluorophore. Also, there is the possibility that an intramolecular arrangement might put the NBD fluorophore near the chlorine atom in **KP68,** which can reduce the intensity of its fluorescence.

The intrinsic fluorescence of the PBIs is demonstrated in the absorption and emission spectra of **KP68** (Figure 3.14 B). Again, two absorption bands were observed. A primary absorption in the UV-region of the electromagnetic spectrum at 300 nm and a secondary absorption band in the ultraviolet-visible region at 410 nm. While both absorptions led to an emission around 520 nm, a brighter emission spectrum was observed due to excitation at the primary absorption band. However, absorption in the UV region is unsuitable for fluorescence live-cell imaging in *P. falciparum*. The secondary absorption band in the UV-vis region at 410 nm can be easily excited with low-energy lasers, making its excitation ideal for *P. falciparum* live-cell imaging.

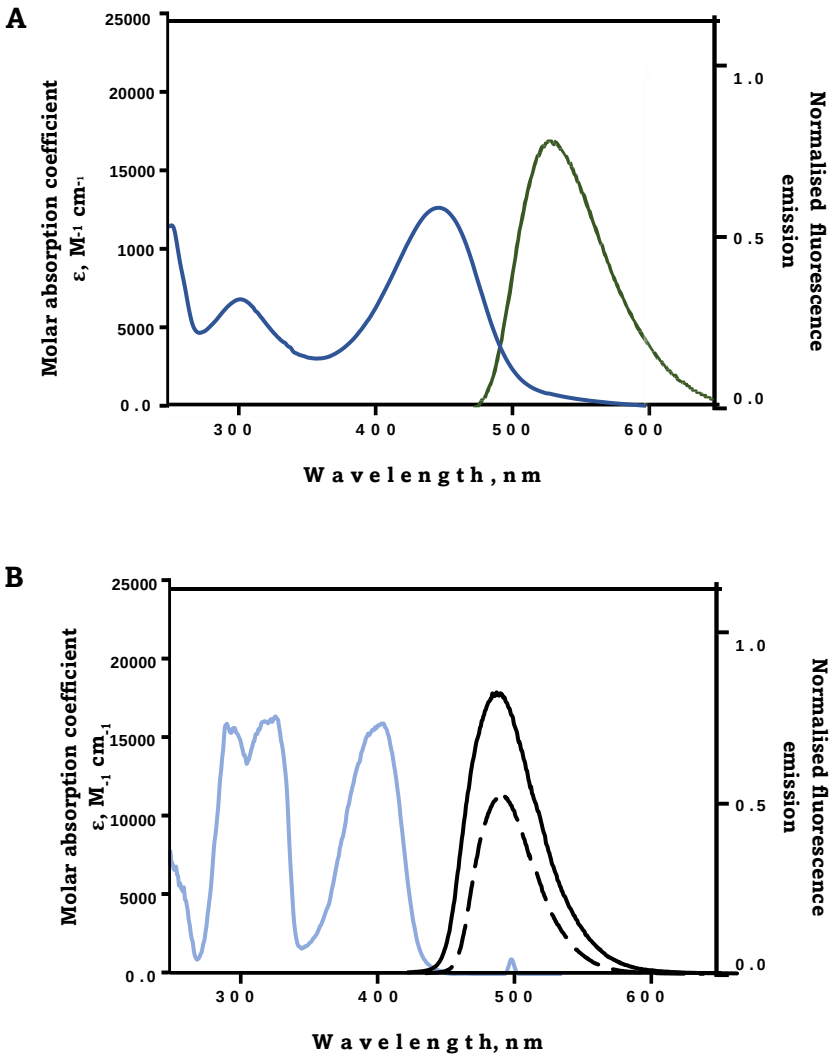

Figure 3.14. The absorption and fluorescence emission spectra of **A)** extrinsically labelled **DM253-NBD** and **B)** intrinsic fluorescence of **KP68**. The absorption spectra (blue) and the emission spectra (black and green) were recorded in ethanol. The solid black line (B) represents an emission spectrum following excitation nm, and the dashed black line indicates emission from excitation at 300nm.

As described in Section 3.3.3 of this chapter, the fluorescence quantum yield (Φ) can be used to assess the brightness of one fluorophore compared to another. Fluorescence quantum yield is the ratio of the number of photons emitted as fluorescence to the number of photons absorbed. The brighter the fluorophore, the more efficiently it emits, and such fluorophores have their quantum yield approaching one. Experimentally, the relative quantum yield of a fluorophore can be determined by comparing it to another fluorophore of known fluorescence quantum yield while keeping all other experimental parameters constant.

In this work, the fluorescence quantum yields of all fluorescent compounds were determined in both organic (ethanol) and mixed solvents (40% (v/v) DMSO in 20 mM Hepes) at pH 7.5 according to the methods previously described.[18] Since the fluorescence quantum yield of quinine has been once found and reported in the literature (Φ = 0.546 in 0.5 M sulfuric acid), it served as a suitable reference compound for determining the fluorescence quantum yield of the fluorescent compounds with unknown quantum yield.[30]

Table 3.2. Fluorescence quantum yields of the fluorescence compounds were evaluated relative to quinine in 0.5 M sulphuric acid (Φ =0.546).[30] Standard errors represent uncertainties from two independent measurements each performed in triplicate.

Compound	Fluorescence quantum yield (Φ) in ethanol	Fluorescence quantum yield (Φ) in 40% (v/v) DMSO in 20 mM Hepes, pH 7.5
KP68	0.470 ± 0.003	0.640 ± 0.002
KP124	0.512 ± 0.009	0.670 ± 0.007
KP68-NBD	0.196 ± 0.015	0.018 ± 0.002
KP124-NBD	0.226 ± 0.006	0.018 ± 0.003
KP124-NBD-1	0.248 ± 0.006	0.035 ± 0.010
DM253-NBD	0.273± 0.006	0.042 ± 0.013

Although the PBIs possess high quantum yields in ethanol (Φ ≈ 0.512) and a higher one still in mixed aqueous solution (Φ ≈ 0.670), the NBD fluorescent derivatives exhibited a weaker fluorescence quantum yield in ethanol and an even weaker quantum yield in the mixed aqueous solvent (Table 3.2). This means that the NBD-labelled derivatives are relatively brighter in ethanol than in a mixed aqueous medium. This is consistent with the fact that the NBD fluorophores are brighter in hydrophobic environments than in hydrophilic ones. As the solvent's polarity increases, the fluorophore's fluorescence intensity reduces. On the other hand, the intrinsic fluorophores are relatively brighter in hydrophilic and hydrophobic media.

3.7.2. Solvent Effects on the Fluorescent Compounds

A fluorophore's absorption and emission profiles can be affected by the solvent in which the spectrum is acquired. The molecules of a solvent can reduce the energy of the excited state by reorganizing the excited-state fluorophore. This process is known as solvent

relaxation. A shift in fluorescence emission maximum caused by the changes in solvent polarity is known as solvatochromism. A higher reduction in the energy level of the excited state is observed in more polar solvents than in less polar solvents, reducing the solvents' stabilization effects. Consequently, this leads to a more significant stoke shift in more polar solvents compared to less polar ones.

The emission spectrum of NBD fluorophore is affected by this solvatochromic shift. A shift in the fluorescence emission maximum is observed for all NBD-labelled analogues from approximately 528 nm to 560 nm, as measured by the solvent polarity parameter E_T (30) (Figure 3.15). A plot of the emission maximum against solvent polarity across ten solvents resulted in a linear correlation (R^2 = 0.974).

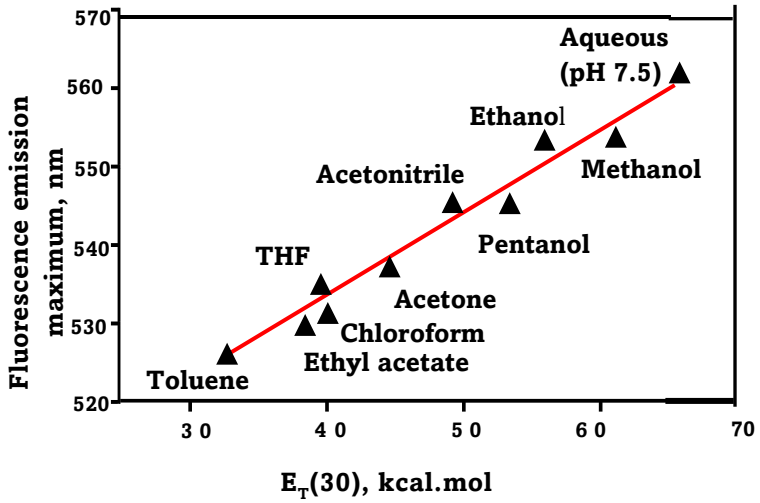

Figure 3.15. A plot of the NBD fluorophore fluorescence emission maximum and solvent polarity in ten common solvents. E_T(30) values were adapted from Reichardt.[31] **KP68-NBD** was excited at 480 nm at a concentration of 10 µM at 25 °C.

Fluorescence intensity following emission was also evaluated across different solvents. (Figure 3.16) As expected, the NBD fluorophore is at its brightest in non-polar solvents and relatively weaker in aqueous environments. Therefore, an association of the NBD-labelled fluorescent derivatives to neutral lipids and phospholipid bilayers should be highly favoured. However, if the compounds accumulate extensively in the DV as hypothesized, their relatively modest aqueous fluorescence quantum yield of the fluorophore means that the signal from the parasite's DV will not overwhelm the microscope's detector at the expense of signals originating from other subcellular

compartments. This trend was equally observed for the intrinsic fluorophores. However, even at their weakest fluorescence intensity, they are brighter than their extrinsically labelled counterparts in the same solvent environment.

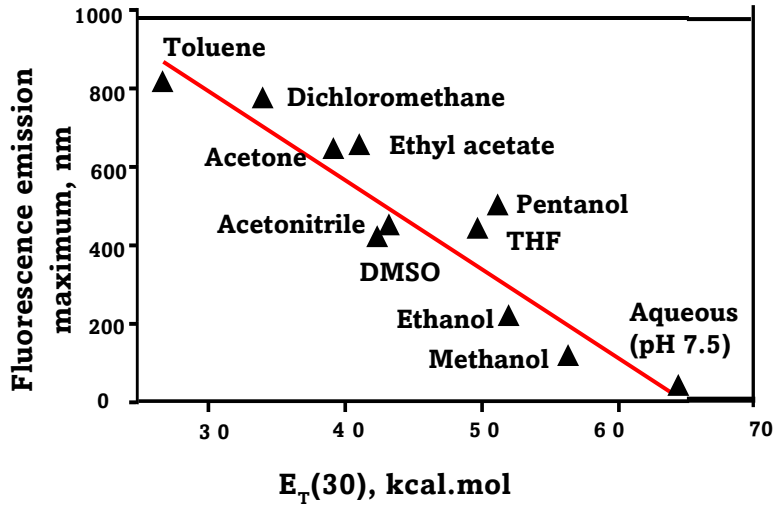

Figure 3.16. A plot of fluorescence emission intensity of the NBD fluorophore and solvent polarity in varying solvents. $E_T(30)$ values were adapted from Reichardt.[31] **KP68-NBD** was excited at 480 nm at a concentration of 10 μM at 25 °C.

3.7.3. Sensitivity of Fluorescence Compounds to Temperature and Light

Exposure of fluorescent compounds to ambient light leads to continuous manipulation of the excited state. This can eventually result in processes such as photobleaching and complete loss of fluorescence. The presence of a solvent and elevated temperatures can speed up the reactivity of the excited state and reactions with the solvent. Therefore, a quantitative stability study was conducted to investigate the fluorescent compounds' ability to degrade under thermal and photo conditions.

For NBD-labelled derivatives, **KP68-NBD** was chosen as a representative molecule, and **KP68** was selected for intrinsic fluorophores. About a milligram of compound material was weighed in different glass vials, representing the various entries in Table 3.3. The samples were either left as solids or dissolved in acetonitrile and subjected to the multiple conditions depicted in table 3.3. These conditions included storage in a fridge, both at 4 °C and -20 °C, in an oven at 70 °C, and on a laboratory benchtop, where temperatures ranged from about 20 °C to 25 °C during the study. For the latter, two sets of samples

were prepared, one which was exposed to ambient light and the other which was not. Quantitative analysis was then performed using HPLC after three months.

The results showed no decomposition in solid-state or solution for samples stored in the fridge at 4 °C and -20 °C. Also, the samples left on the benchtop in the dark showed no decomposition either in the solid-state, but about 4% of this sample in solution was decomposed. Furthermore, about 22% of the compound left in the oven at solid-state decomposed. Finally, the compound showed about 10% degradation when exposed to light at 25 °C in the solid-state and almost completely decomposed in the solution. These observations suggest that the NBD-labelled compounds must be kept from light, especially in solution. Early in the project, it also raised concerns about photobleaching in live cells under the microscope when the NBD fluorophores are exposed to high-energy lights.

On the other hand, the intrinsic fluorophores are generally more stable than their NBD-labelled counterparts. No decomposition was observed at the lower temperatures of 4 °C and -20 °C. Also, at 25 °C with exposure to light, only 4% of the compound decomposed as opposed to 10% in the NBD-labelled counterpart. At 25 °C in the solution state, about 75% of **KP68** decomposed compared to more than 95% observed in NBD-labelled **KP68.** This means that, while decomposition still occurs in the intrinsic fluorophore, it is slower than observed in the NBD-labelled counterpart.

Table 3.3. Stability studies on the NBD-labelled **KP68** in solid and solution states after three months.

Temperature	Exposure to light	Decomposition in the solid-state	Decomposition in the solution state
4 °C	No	0%	0%
-20 °C	No	0%	0%
25 °C	No	0%	4%
25 °C	Yes	10%	95%
70 °C	No	22%	N/A

3.7.4. Evaluation of the Solubility, Antiplasmodium, and β-hematin Inhibition Activities of Fluorescent Compounds

As earlier described in Chapter 1, neutral lipids have been implicated as the site of crystal growth and nucleation in the mechanism of hemozoin formation.[32,33] However, lipids are very expensive, and the time required to prepare the range of lipid blends suitable for initial laboratory screening makes it unamenable with the tools available in the laboratory.[34,35] Instead, an assay was developed to investigate the effects of compounds on β-hematin using the relatively cheaper and commercially available detergent NP-40. The NP-40 detergent is a suitable substitute for neutral lipids, enhancing crystallization under physiologically relevant conditions. By means of quantification, a colorimetric pyridine-iron method, in which the pyridine forms a low-spin complex with Fe(III)PPIX but not with β-hematin, is used.[36] The absorbance at the Soret band of the complex formed from pyridine-Fe(III)PPIX at 405 nm allows for the rapid quantification of β-hematin inhibition.

The target compounds and their fluorescent derivatives were tested in this β-hematin inhibition assay (BHIA), and the results are tabulated below. These are reported as IC_{50}, values representing the compound concentration required to inhibit the formation of β-hematin by 50%. IC_{50} values of 18.4 ± 1.5 μM and 37.2 ± 0.8 μM were obtained for **KP68** and **KP124,** respectively. This is in line with previous studies in which **KP68** was a more potent β-haematin formation inhibitor than **KP124**.[37] All fluorescent derivatives were found to be less potent than their parent compounds in the BHIA except **KP68-NBD**, whose activity is comparable to the parent (Table 3.4). Although most of the NBD-labelled derivatives were less active in the assay than their parent molecules, they all remained potent β-hematin formation inhibitors.

The compounds were also evaluated for their antiplasmodium activity *in vitro* against *P. falciparum* CQS strain (NF54) using the lactate dehydrogenase method previously developed by Makler and co-workers.[38] The results from this are also reported as IC_{50} values in table 3.4. Again, all of the NBD-labelled derivatives of the target compounds showed significant increases in IC_{50} values compared to the parent molecules. **DM253-NBD** showed more than a 10-fold (12 ± 13.9 nM; 140 ± 23 nM) reduction in potency compared to **DM253.** Similarly, **KP68** was found to be more potent than its NBD-labelled

derivative**,** with an about 6-fold shift in IC_{50} (30 ± 2.3 nM; 180 ± 4 nM). Despite the loss in activity observed between **KP68**, **DM253**, and their fluorescently labelled derivatives, the NBD-labelled compounds are active against the parasite and could serve to probe the subcellular accumulation of their parent molecules.

On the other hand, the fluorescent derivatives of **KP124** are not suitable pharmacological representations of the compounds. **KP124-NBD-1** was the least potent, with an IC_{50} of 4453.8 ± 689 nM, while **KP124-NBD** showed more than a 10-fold shift in IC_{50} at 1512.2 ± 55.2. These studies showed that the intrinsic fluorophores are more suitable for probing the subcellular accumulation in *P. falciparum* than their fluorescently labelled derivatives.

Table 3.4. 50% inhibitory concentration (IC_{50}) of the target compounds and their fluorescently labelled derivatives were measured in the NP-40 detergent-mediated assay for β-Hematin inhibition and an in vitro assay against *P. falciparum*. All measurements were taken in triplicates, and uncertainties are reported as mean, standard errors.

Compounds	**β-Hematin inhibition IC_{50}, μM**	***P. falciparum* IC_{50}, nM (NF54 strain)**	**Melting Point** °C
KP68	18.4 ± 1.5	30 ± 2.3	277-279 °C
KP124	37.2 ± 0.8	140 ± 27.7	225-227 °C
DM253	23.8 ± 1.7	12 ± 13.9	100-104 °C
KP68-NBD	15.3 ± 1.2	180 ± 4	187-189 °C
KP124-NBD	43 ± 0.02	1512.2 ± 55.2	117-119 °C
KP124-NBD-1	22.0 ± 2.4	4453.8 ± 689	132-136 °C
DM253-NBD	56.3 ± 2.4	140 ± 23	52-54 °C

The aqueous solubility ranges of all compounds were determined in a turbidimetric solubility assay. This assay measures the absorbance at 620 nm from the scattered light caused by insolubility. As depicted in Table 3.5 below, all compounds were generally insoluble. Except for **DM253** and its NBD-labelled analogue, all the compounds studied in this assay showed solubility below 100 μM. However, the poor solubility of the

compounds is not much of a concern here since tiny amounts of the compounds are required for fluorescence live-cell imaging.

Table 3.5. Aqueous solubility of values of the target compounds and their NBD-labelled derivatives were measured by turbidimetry at pH 7.5.

Compound	Solubility (μM)
KP68	5
KP124	20
KP68-NBD	10
KP124-NBD	20
KP124-NBD-1	10
DM253-NBD	100
DM253-NBD	120

3.8. Summary and Conclusion

Six fluorescent derivatives were synthesized as described in Chapter 2. A list of these compounds is depicted in Figure 3.13. In this chapter, the fundamental principles underlying fluorescence were discussed. The applications of this principle to microscopy form the basis of the work discussed in Chapter 4. Furthermore, the target compounds' photophysical, physicochemical and pharmacological properties were evaluated compared to their fluorescent derivatives.

Photophysical characterization indicated that the NBD-labelled derivatives of the target compound possess two absorption maxima, one due to the PBI and benzimidazole cores and the other due to the NBD fluorophore. The absorption band due to NBD is lower in energy, and emissions due to this absorption band occur around 528-560 nm due to solvatochromism. Similarly, two absorption bands were observed for the intrinsic fluorophores, **KP68** and **KP124.** The primary absorption band, which results in the most intense emission, occurs in the UV region. This requires high energy to excite and is hence

unsuitable for live-cell imaging. The secondary absorption band of these compounds, on the other hand, occurs at 410 nm. This occurs in the visible region of the electromagnetic spectrum and is suitable for live-cell imaging.

Furthermore, results from the detergent-mediated BHIA indicated that all of the fluorescent derivatives retained their abilities to inhibit β-hematin formation, although they are not as potent as their parent molecules. More importantly, NBD-labelled derivatives were significantly less potent against the *P. falciparum* CQS (NF54) strain compared to the parent molecules. **DM253-NBD** showed a more than 12-fold reduction in potency compared to **DM253**. This suggests that the presence of the NBD fluorophore significantly affects the action of the compound. This was the case for **KP68** and **KP124** as well, bringing into question the suitability of these fluorescent derivatives as representatives of the parent molecules. However, the NBD-labelled derivatives of **KP68** and **DM253** retained antiplasmodium activity, albeit reduced, and can be used to probe the subcellular accumulation of the parent compounds. In **KP124**, the activities of the NBD-labelled fluorescent probes are greater than 1 μM (1512.2 ± 55.2, 4453.8 ± 689) and are thus not suitable representatives of **KP124.** Based on this, the intrinsic fluorescence of the compounds is preferred over their fluorescent derivatives. Also, only **DM253-NBD** and **KP68-NBD** are suitable analogues of their respective parent molecules. Therefore, the intrinsic fluorophores, **KP68** and **KP124,** and the NBD-labelled analogues, **DM253-NBD** and **KP68-NBD,** were exploited in live-cell fluorescence microscopy studies of *P. falciparum* as described in Chapter 5**.**

3.9. References

(1) Valeur, B. *Molecular Fluorescence: Priciples and Applications*; Wiley-VCH Verlag GmbH, 2001.

(2) Valeur, B.; Brochon, J.-C. *New Trends in Fluorescence Spectroscopy: Applications to Chemical and Life Sciences*; Springer Science & Business Media, 2012; Vol. 1.

(3) Florida State University. Basic Concepts in Fluorescence micro.magnet.fsu.edu/primer/Atechniques/fluorescence/fluorescenceintro.html.

(4) *Light Microscopy*; Chiarini-Garcia, H., Melo, R. C. N., Eds.; Methods in Molecular Biology; Humana Press: Totowa, NJ, 2011; Vol. 689.

(5) Weller, T. H.; Coons, A. H. Fluorescent Antibody Studies with Agents of Varicella and Herpes Zoster Propagated in Vitro. *Exp. Biol. Med.* **1954**, *86* (4), 789–794.

(6) Jabłoński, A. Über Den Mechanismus Der Photolumineszenz von Farbstoffphosphoren. *Zeitschrift für Phys.* **1935**, *94* (1–2), 38–46.

(7) Janet L Stringer. Basic Concept in Pharmacology https://micro.magnet.fsu.edu/primer/techniques/fluorescence/fluorescenceintro.html.

(8) Demchenko, A. P. *Introduction to Fluorescence Sensing*; Springer International Publishing: Cham, 2015.

(9) Martin, M. M.; Lindqvist, L. The pH Dependence of Fluorescein Fluorescence. *J. Lumin.* **1975**, *10* (6), 381–390.

(10) Lakowicz, J. R. Principles of Fluorescence Spectroscopy. In *Principles of Fluorescence Spectroscopy*; Springer: New York, 2006; pp 1–954.

(11) Murphy, D. B. *Fundamentals of Light Microscopy and Electronic Imaging*; John Wiley & Sons, 2002.

(12) Förster, T. Zwischenmolekulare Energiewanderung Und Fluoreszenz. *Ann. Phys.* **1948**, *437* (1–2), 55–75.

(13) Albrecht, C. Joseph R. Lakowicz: Principles of Fluorescence Spectroscopy, 3rd

Edition. *Anal. Bioanal. Chem.* **2008**, *390* (5), 1223–1224.

(14) Thompson, M. J.; Messina, M. A Quantitative Explanation of the Dynamics Underlying the Franck–Condon Principle: A Mostly Classical Viewpoint. *J. Chem. Educ.* **2019**, *96* (6), 1171–1177.

(15) Gu, Q.; Kenny, J. E. Improvement of Inner Filter Effect Correction Based on Determination of Effective Geometric Parameters Using a Conventional Fluorimeter. *Anal. Chem.* **2009**, *81* (1), 420–426.

(16) K. Wilson and J. Walker. *Principles and Techniques of Biochemistry*; Cambridge University Press: Cambridge, 2004.

(17) Hanlan, J.; Skoog, D. A.; West, D. M. *Principles of Instrumental Analysis*, Sith Editi.; Thomson Brooks / Cole: Canada, 1973; Vol. 18.

(18) Woodland, J. G. Insights into the Mechanism of Action of Quinoline Antimalarials against *Plasmodium falciparum* Revealed by Novel Fluorescent Analogues and Chemical Proteomics, University of Cape Town, 2016.

(19) van de Weert, M.; Stella, L. Fluorescence Quenching and Ligand Binding: A Critical Discussion of a Popular Methodology. *J. Mol. Struct.* **2011**, *998* (1–3), 144–150.

(20) Abbe, E. Beiträge Zur Theorie Des Mikroskops Und Der Mikroskopischen Wahrnehmung. *Arch. für Mikroskopische Anat.* **1873**, *9* (1), 413–468.

(21) Rayleigh. XV. On the Theory of Optical Images, with Special Reference to the Microscope. *London, Edinburgh, Dublin Philos. Mag. J. Sci.* **1896**, *42* (255), 167–195.

(22) Huang, B.; Babcock, H.; Zhuang, X. Breaking the Diffraction Barrier: Super-Resolution Imaging of Cells. *Cell* **2010**, *143* (7), 1047–1058.

(23) Gustafsson, M. G. L. Surpassing the Lateral Resolution Limit by a Factor of Two Using Structured Illumination Microscopy. Short Communication. *J. Microsc.* **2000**, *198* (2), 82–87.

(24) Dunn, K. W.; Kamocka, M. M.; McDonald, J. H. A Practical Guide to Evaluating Colocalization in Biological Microscopy. *Am. J. Physiol. Physiol.* **2011**, *300* (4), C723–C742.

(25) Woodland, J. G.; Hunter, R.; Smith, P. J.; Egan, T. J. Shining New Light on Ancient Drugs: Preparation and Subcellular Localisation of Novel Fluorescent Analogues of Cinchona Alkaloids in Intraerythrocytic *Plasmodium falciparum*. *Org. Biomol. Chem.* **2017**, *15* (3), 589–597.

(26) Manders, E. M. M.; Verbeek, F. J.; Aten, J. A. Measurement of Co-localization of Objects in Dual-colour Confocal Images. *J. Microsc.* **1993**, *169* (3), 375–382.

(27) Manders, E. M. M.; Verbeek, F. J.; Aten, J. A. Measurement of Co-Localization of Objects in Dual-Colour Confocal Images. *J. Microsc.* **1993**, *169* (3), 375–382.

(28) Zinchuk, V.; Grossenbacher-Zinchuk, O. Quantitative Colocalization Analysis of Confocal Fluorescence Microscopy Images. *Curr. Protoc. Cell Biol.* **2011**, *52* (1).

(29) van Steensel, B.; van Binnendijk, E. P.; Hornsby, C. D.; van der Voort, H. T.; Krozowski, Z. S.; de Kloet, E. R.; van Driel, R. Partial Colocalization of Glucocorticoid and Mineralocorticoid Receptors in Discrete Compartments in Nuclei of Rat Hippocampus Neurons. *J. Cell Sci.* **1996**, *109* (4), 787–792.

(30) Melhuish, W. H. Quantum Efficiencies of Fluorescence of Organic Substan Ces: Effect of Solvent and Concentration of the Fluorescent Solute. *J. Phys. Chem.* **1961**, *65* (2), 229–235.

(31) Reichardt, C. Solvatochromic Dyes as Solvent Polarity Indicators. *Chem. Rev.* **1994**, 94 (8), 2319–2358.

(32) Coppens, I.; Vielemeyer, O. Insights into Unique Physiological Features of Neutral Lipids in Apicomplexa: From Storage to Potential Mediation in Parasite Metabolic Activities. *Int. J. Parasitol.* **2005**, *35* (6), 597–615.

(33) Pisciotta, J. M.; Coppens, I.; Tripathi, A. K.; Scholl, P. F.; Shuman, J.; Bajad, S.; Shulaev, V.; Sullivan, D. J. The Role of Neutral Lipid Nanospheres in *Plasmodium falciparum* Haem Crystallization. *Biochem. J.* **2007**, *402* (1), 197–204.

(34) Sandlin, R. D.; Carter, M. D.; Lee, P. J.; Auschwitz, J. M.; Leed, S. E.; Johnson, J. D.; Wright, D. W. Use of the NP-40 Detergent-Mediated Assay in Discovery of Inhibitors of β-Hematin Crystallization. *Antimicrob. Agents Chemother.* **2011**, *55* (7), 3363–3369.

(35) de Villiers, K. A.; Egan, T. J. Heme Detoxification in the Malaria Parasite: A Target for Antimalarial Drug Development. *Acc. Chem. Res.* **2021**, *54* (11), 2649–2659.

(36) Egan, T. J.; Ncokazi, K. K. Quinoline Antimalarials Decrease the Rate of β-Hematin Formation. *J. Inorg. Biochem.* **2005**, *99* (7), 1532–1539.

(37) Singh, K.; Okombo, J.; Brunschwig, C.; Ndubi, F.; Barnard, L.; Wilkinson, C.; Njogu, P. M.; Njoroge, M.; Laing, L.; Machado, M.; Prudêncio, M.; Reader, J.; Botha, M.; Nondaba, S.; Birkholtz, L.-M.; Lauterbach, S.; Churchyard, A.; Coetzer, T. L.; Burrows, J. N.; Yeates, C.; Denti, P.; Wiesner, L.; Egan, T. J.; Wittlin, S.; Chibale, K. Antimalarial Pyrido[1,2- a]Benzimidazoles: Lead Optimization, Parasite Life Cycle Stage Profile, Mechanistic Evaluation, Killing Kinetics, and in Vivo Oral Efficacy in a Mouse Model. *J. Med. Chem.* **2017**, *60* (4), 1432–1448.

(38) Piper, R. C.; Williams, J. A.; Makler, M. T.; Gibbins, B. L.; Hinrichs, D. J.; Ries, J. M.; Bancroft, J. E. Parasite Lactate Dehydrogenase as an Assay for *Plasmodium falciparum* Drug Sensitivity. *Am. J. Trop. Med. Hyg.* **1993**, *48* (6), 739–741.

Chapter Four

Live-Cell Fluorescence Microscopy and Heme Speciation Studies of the Target Compounds and their Novel Fluorescent Analogues

4.1. Chapter Overview

As already alluded to in Section 1.8 of the introductory Chapter 1, benzimidazole and Pyrido[1,2-a]benzimidazole scaffolds have been regarded as privileged because of their ability to interact effectively with different biological systems. This interaction has led to reports of several biological activities, including antimalarial activity, of compounds containing these scaffolds. Three representatives of this class of compounds, **KP68**, **KP124,** and **DM253**, were identified as potent phenotypic whole-cell antimalarial leads. However, the details of their MOA against *P. falciparum* remain unsolved. Previous MOA studies on these compounds have focused on the hemoglobin degradation pathway with respect to inhibition of hemozoin formation. This is due to the structural similarities between some members of this class and chloroquine, which led to their evaluation in a cell-free assay for the inhibition of β-hematin (synthetic heme) formation and subsequently confirmed as bonafide inhibitors of hemozoin formation. However, this might not be the case for other analogues. While inhibiting hemozoin formation may be a contributory mechanism to the action of these compounds, other mechanisms may also be at play.

Investigating the subcellular localization of these antimalarials in *P. falciparum* is the first step in providing deeper insights into the MOA of the compounds. To achieve this, the intrinsic fluorescence of the compounds was exploited in studying their subcellular accumulation in the parasite. Also, novel fluorescent derivatives representing intrinsic fluorophores and **DM253** were designed and synthesized (Chapter 2). These derivatives were evaluated to determine the most suitable analogues of the parent compounds for live-cell imaging (Chapter 3). These experiments identified the intrinsic fluorophores **KP68** and **KP124** as ideal for studying their accumulation in the parasite. Also, NBD-labelled **DM253** and **KP68-NBD** were suitable representatives of their parent compounds, although a reduction of potency was observed for these two compounds.

Imaging the malaria parasite comes with several challenges; amongst them is the parasite's sensitivity to light and issues with resolution posed by the diffraction limit of light. These issues and their solution will be discussed. The commercially available tracker dyes used to co-stain organelles and other subcellular structures in *P. falciparum* are also discussed in this chapter. Furthermore, an in-depth analysis of the compounds' distribution within *P. falciparum*-infected erythrocytes using confocal microscopy is described in this chapter. This also includes colocalization studies following accumulation relative to co-illuminated organelles such as the endoplasmic reticulum, nucleus, mitochondrion, and membrane structures.

Finally, to address the issue of the resolution, due to the parasite's small size, super-resolution structured-illumination microscopy (SR-SIM) and Airyscan microscopy, which doubles the improvement of resolution compared to confocal microscopy, was employed. Based on the observations from live-cell imaging, the compounds were tested in the cellular heme speciation assay to assess their dose-dependent effect on the heme and hemozoin levels in *P. falciparum*.

Therefore, the specific objectives discussed in this chapter are:

i. To describe the basis of earlier hypotheses regarding the action of the study compounds.
ii. To establish suitable conditions for live-cell imaging of *P. falciparum*.
iii. To investigate the accumulation of the target compounds and their novel fluorescent derivatives in organelles and subcellular structures of *P. falciparum* using confocal and super-resolution microscopies.
iv. To assess the dose-dependent effect of these compounds on heme and hemozoin levels in the parasite.

4.2. Earlier Hypothesis on the Action of Target Compounds

As earlier discussed in Section 1.3.1.1 of chapter one, the plasmodium parasite digest's almost all its host's hemoglobin for nutrients it needs to survive and replicate. This process occurs in the parasite's oxygen-rich, lysosome-like acidic digestive vacuole.[1,2] As a result, substantial amounts of heme are released into the DV as by-products. However, heme is toxic to the parasite. As such, the parasite quickly sequesters the

released heme by converting it into an unreactive microcrystalline, hemozoin.[3,4] CQ is the most successful compound to target this pathway by inhibiting the conversion of heme to hemozoin. Since then, the pathway has become an attractive target for malaria drug discovery.[5] CQ is a weak, neutral base accumulating in the parasite's cytoplasm. However, its basic side chain and quinoline nitrogen are protonated in an acidic medium leading to its accumulation in the DV. This occurs through a process known as pH trapping.[6] Also, intermolecular interactions between heme and CQ allow CQ to bind to heme and interfere with its biocrystallization to hemozoin. This results in the build-up of heme to levels that lead to the parasite's death.

de Villiers and co-workers provided an example of a crystal structure of Fe(III)PPIX and halofantrine, an antimalarial compound that inhibits the formation of hemozoin. The authors showed that, like CQ, most aryl compounds inhibiting hemozoin formation have specific properties.[7] They possess hydrophobic aromatic rings that interact through π-π stacking with the porphyrin ring of heme. Also, the propionate group of heme Fe(III)PPIX interacts through hydrogen bonding with the protonated hydrogen of the compounds studied. Finally, coordination of the deprotonated hydroxyl groups of the compound to the iron (III) center of heme was observed.[7–9] Specifically, CQ interacts with heme through hydrogen bonding and π-π stacking interactions.[9] This follows another study that suggested that CQ and other quinoline antimalarials prevent the nucleation and growth of β-hematin crystals by adsorbing to their 001 surfaces through a porphyrin ring to the quinoline amine salt bridge. Furthermore, the intercalation of the quinoline ring between the aromatic groups of β-hematin enhances the adsorption process.[10–12] The 001 face is one of the faces used to describe the morphology of the micrometer-sized β-hematin crystals. These crystals are bounded by 100 and 010 side faces and capped by a 011 and 001. This is equally observed for hemozoin. Consequently, it was hypothesized that **KP68** and **KP124** could be acting through the same pathway as CQ because the compounds possess hydrophobic aromatic groups, a protonatable basic side chain, and a heterocyclic ring nitrogen atom.

To investigate the aforementioned hypothesis, docking studies were employed to predict the structural interactions between the compounds and heme. **KP68** and

KP124 were docked against the β-hematin surface using the 3D crystal structure published by Pagola and co-workers.[13] Intermolecular interactions were observed between **KP68** and the 3D crystal surface of β-hematin. (Figure 4.1) The benzo[4,5]imidazole[1,2-a]pyridine group of the compound interacts through π-π stacking with the porphyrin ring. Its basic amino side chain also forms a hydrogen bond with the propionate group of β-hematin when protonated at pH 4.5. This suggests that it possesses structural features that interact favourably with the surface of the β-hematin crystal structure and is a potential inhibitor of hemozoin formation.

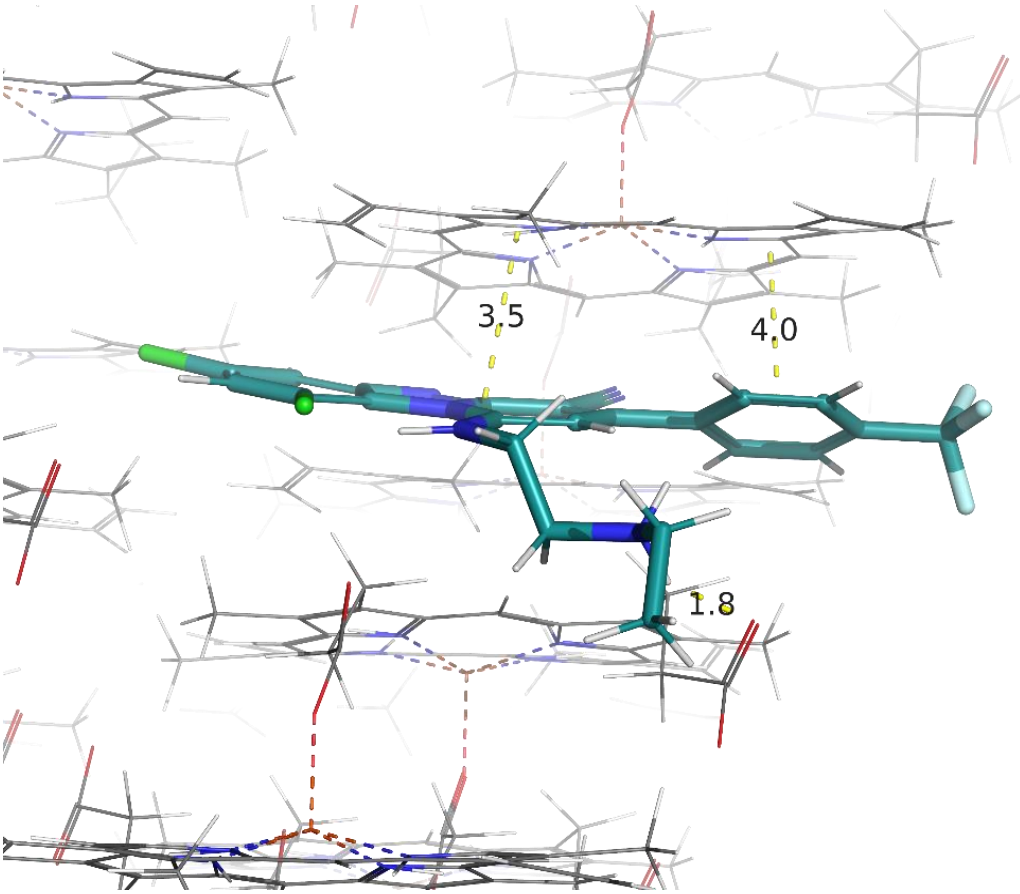

Figure 4.1. Predicted binding mode of **KP68** to the 001 faces of β-hematin showing hydrogen bonding interactions between protonated nitrogen (monoprotonated) on the basic side chain of **KP68** and the propionate group of heme at pH 4.5 (1.8 Å) and π−π-stacking interactions shown between the porphyrin ring of heme and the tricyclic aromatic hydrophobic ring of **KP68** (3.5, 4.0 Å).

The docking pose observed for **KP124** is like the one described for **KP68**. However, the presence of the pyridine nitrogen in this compound affords it a secondary protonation site in an acidic medium (Figure 4.2). The pyridine ring in **KP124** is the main difference between

both compounds. The secondary amine on the side chain and the basic nitrogen in the pyridine ring of **KP124** are protonated at pH 4.5. This means that **KP124** is doubly protonated in an acid medium, where diprotonation occurs in CQ as well.[14] Although in **KP124,** the π −π-stacking interaction between the porphyrin ring of β-hematin and the heteroaromatic ring of the compound is lost because of changes in the orientation of the compound at the active site in the deprotonated state (Figure 2B). Based on these observations, both compounds were tested in the in vitro cell-free β-hematin inhibition assay (BHIA) described in Chapter 3. The tested compounds showed good activities in this assay, represented by values comparable to CQ.[15]

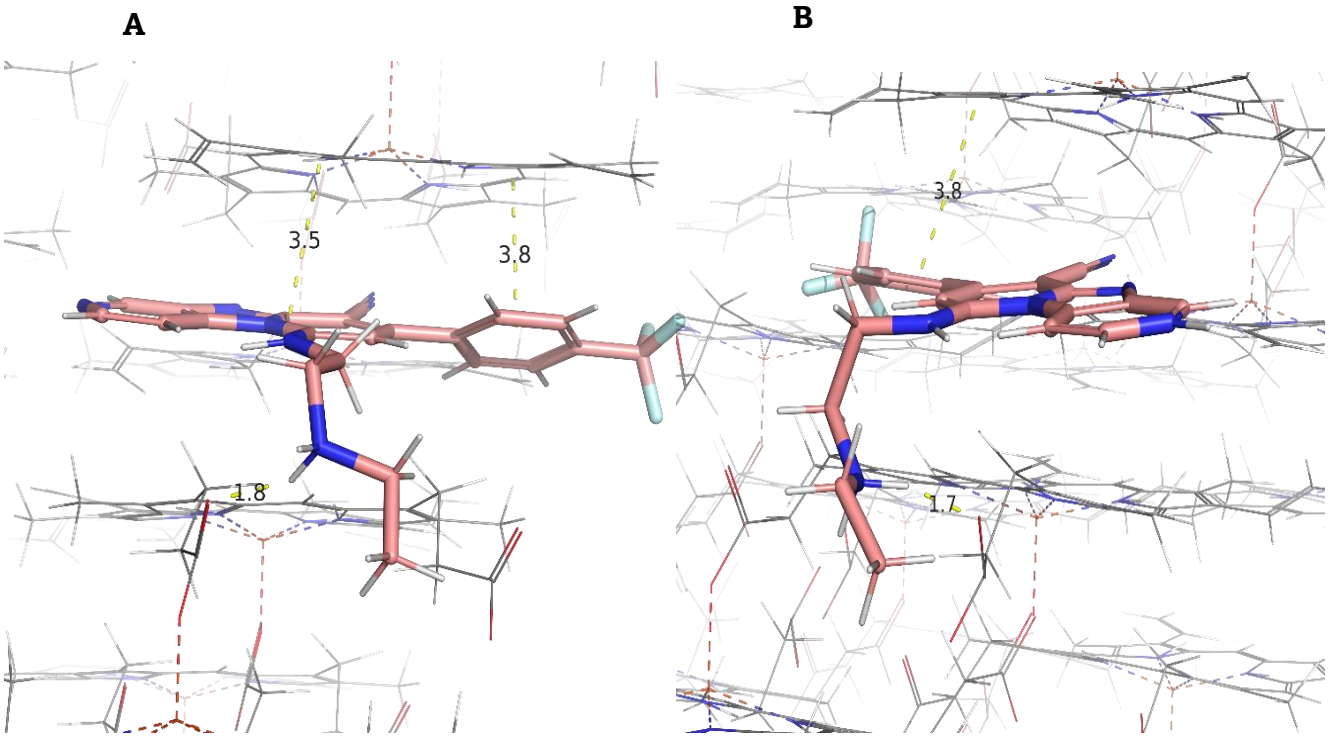

Figure 4.2. Predicted binding mode of **KP124** to the 001 faces of *β*-hematin showing hydrogen bonding interactions between protonated nitrogen (**A** monoprotonated and (**B**) di-protonated on the basic side chain of the compound and the propionate group of heme at pH 4.5 (1.8, 1.7 Å). π−π-stacking interactions are shown between the porphyrin ring of heme and the tricyclic aromatic hydrophobic ring of **KP124** (3.5, 3.8 Å).

Although docking studies and the BHIA provided some insights into the possible MOA of these compounds, these experiments are cell-free and designed to only predict and mimic conditions in the *Plasmodium* parasite. Hence, the compounds were subjected to live-cell confocal microscopy in *P. falciparum*-infected erythrocytes to shed more light on the

accumulation of the compounds *in vitro* using their intrinsic and extrinsic fluorescence properties.

4.3. Consideration for Live-cell Imaging of *P. falciparum*

4.3.1. Photosensitivity and Internal Fluorescence

Important considerations must be made when imaging *P. falciparum*. Although live-cell fluorescence microscopy provides insights into the pertinent details of the malaria parasite, a significant concern for *P. falciparum* imaging is the effect of extreme light sensitivity on the parasite. When exposed to even a moderate amount of light, the parasite undergoes irreversible acidification of the parasite cytosol by a pH unit. This could be due to the disruption of the DV membrane.[16]

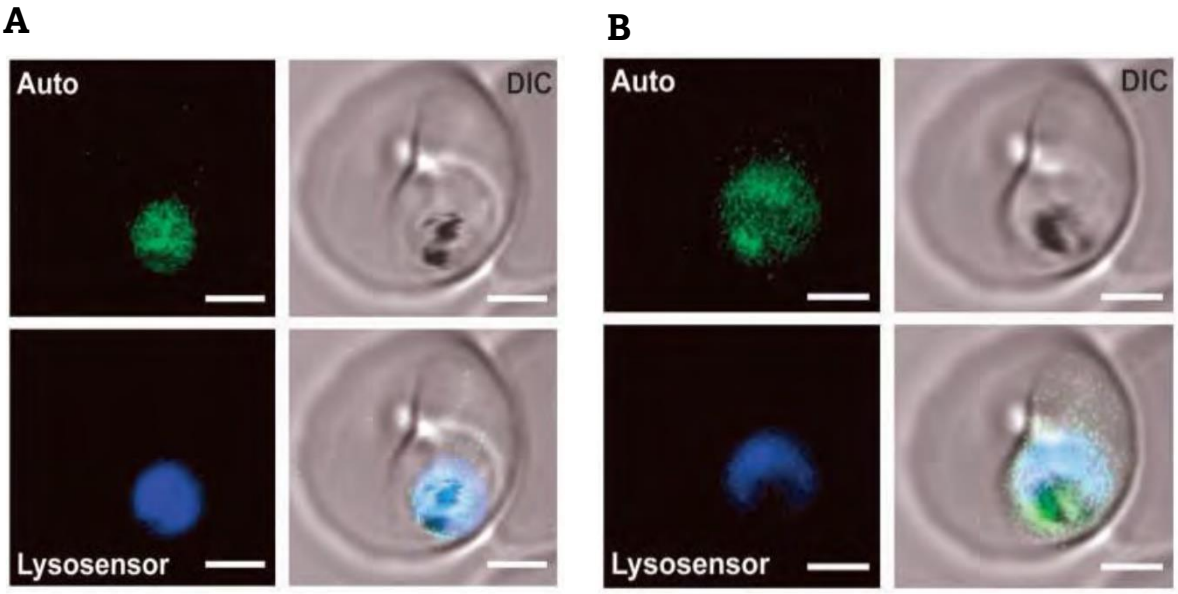

Figure 4.3. Illustration of the susceptibility of *P. falciparum* to photodamage through rupture of the digestive vacuole upon illumination Panel A: infected erythrocyte stained with LysoSensor Blue DND-192, which colocalizes with weak autofluorescence arising from the cell (Auto). Panel B: after 40 exposures at 5 s intervals, autofluorescence and LysoSensor staining are observed throughout the cytosol, indicating its acidification. Scale bar: 2 μm. Adapted from Wissing et al., J. Biol. Chem., 2002, 277, 37747 with permission from the American Society of Biochemistry and Molecular Biology.

The authors suggested that the photosensitive nature of Fe(III)PPIX makes the DV membrane highly susceptible to photodamage by forming an increased amount of hydroxyl

radicals upon irradiation.[16] These radicals are hypothesized to be formed from a Fenton reaction with hydrogen peroxide, formed during the autoxidation of Fe(II)PPIX to Fe(III)PPIX. This reaction is catalyzed by ferrous iron through the equation below:

$$Fe^{2+} + H_2O_2 \longrightarrow Fe^{3+} + \dot{HO} + HO^-$$

The hydrogen peroxide liberated during hemoglobin catabolism directly inhibits the digestive vacuolar H^+-ATPase. This results in the loss of the pH gradient in the parasite.[17] Also, the hydroxyl radicals result in the peroxidation of polyunsaturated fatty acids enriched in the DV, disrupting the membrane and acidifying the parasite's cytosol.[16]

During live-cell imaging in *P. falciparum*, cellular exposure to light must be kept at a minimum to reduce artifacts arising from photodamage. However, high-energy illumination is sometimes unavoidable, especially in confocal microscopy. Therefore, to prevent irreversible acidification during imaging experiments, the autofluorescence of the DV is constantly monitored before and after each acquisition to ensure the integrity of the membrane.

The parasite's autofluorescence arises from the hemozoin pigment in the DV. This is also observed in the synthetic equivalent, β-hematin. Solid-state exciton fluorescence characterized by excitation and emission maxima of 555 nm and 577 nm is observed for both species of crystalline Fe(III)PPIX. The excitation maximum corresponds to the lowest-energy state of the material, represented by the Q-band. Autofluorescence has a low quantum yield, making it unsuitable for in-depth imaging. On the bright side, this also means that the signal from the autofluorescence is unlikely to interfere with the fluorescence of the brighter fluorophores used in this work.

4.3.2. Addressing Issues with Resolution in *P. falciparum* Imaging

RBCs are among the smallest mammalian cells, and *P. falciparum*, embedded in infected RBCs, is even smaller. Depending on the stage of its intraerythrocytic life cycle, the size of the parasite varies from 1 to 6 μm. Consequently, organelles such as the nucleus and digestive vacuole are even smaller, and quantifying these structures using confocal microscopy is particularly challenging. Also, enormous amounts of hemoglobin and free heme are present within the parasite and present further challenges.[18] This is due to the photoreactivity of heme, which may interfere with the fluorescence excitation and

emission signals. Autofluorescence resulting from the uptake of substantial amounts of hemoglobin during the blood-stage of the life cycle may also affect the imaging process. Although this can be addressed by isolating parasites from host cells through detergent lysis, this technique also has disadvantages. Disrupting the parasite's natural metabolic processes may be a significant consequence.

While other microscopic techniques such as electron microscopy might aid in providing high-resolution images, this technique is limited in its investigation of *P. falciparum* for many reasons. Firstly, it is difficult to preserve the parasite's membrane after sample preparation resulting in challenges in identifying organelles in micrograph sections. Also, serial sectioning is labour intensive, making it challenging to analyze the pool of images required to create an overall picture of an organelle. In contrast, live-cell imaging allows one to investigate organelle morphology with little disturbance to cells. However, traditional microscopy is limited in its ability to resolve images because of the diffraction limit earlier described in Chapter 3.

To overcome the limitations above and address the issue of resolution in this work, LSM88, an Airyscan instrument, was used. This technique offers improvement in confocal resolution of up to two-fold without adding special fluorophores or requiring unusual sample preparation. Further, super-resolution structured-illumination microscopy (SR-SIM) was carried out in instances where Airyscan is insufficient.

A comparison between confocal and Airyscan images is shown in Figure 4. The resolution enhancement in the upper panel is evident. Colocalization, in which the fluorescent molecules exhibit spatial overlap due to their interaction with the same organelle structures, is visible between the green and blue images. The region overlap can be seen in the merged images. These channels represent LysoTracker red, which illuminates the membranes of acidic compartments, and **KP124**, respectively.

The reliability of fluorescence imaging and colocalization depends on aligning all channels, especially when using SR-SIM. Consequently, the microscope's software was calibrated with a channel alignment algorithm to correct for lateral and axial shifts between the fluorescent channels. The alignment was achieved using multicolour fluorescent beads provided by the microscope manufacturers. The alignment coefficients obtained from the channel alignment algorithm were then applied to every image set

before acquisition to correct the alignment of the fluorescence channels. All images were acquired at around the range of 2 μm, representing the approximate thickness of a red blood cell. All fluorescent images discussed in this chapter are a maximum intensity projection of the acquired ''z-stack''. Z-stacks are made up of several slices approximately 0.1 μm thick in the vertical direction. Each image stack was evaluated on its own merit to obtain a complete picture of the image taken.

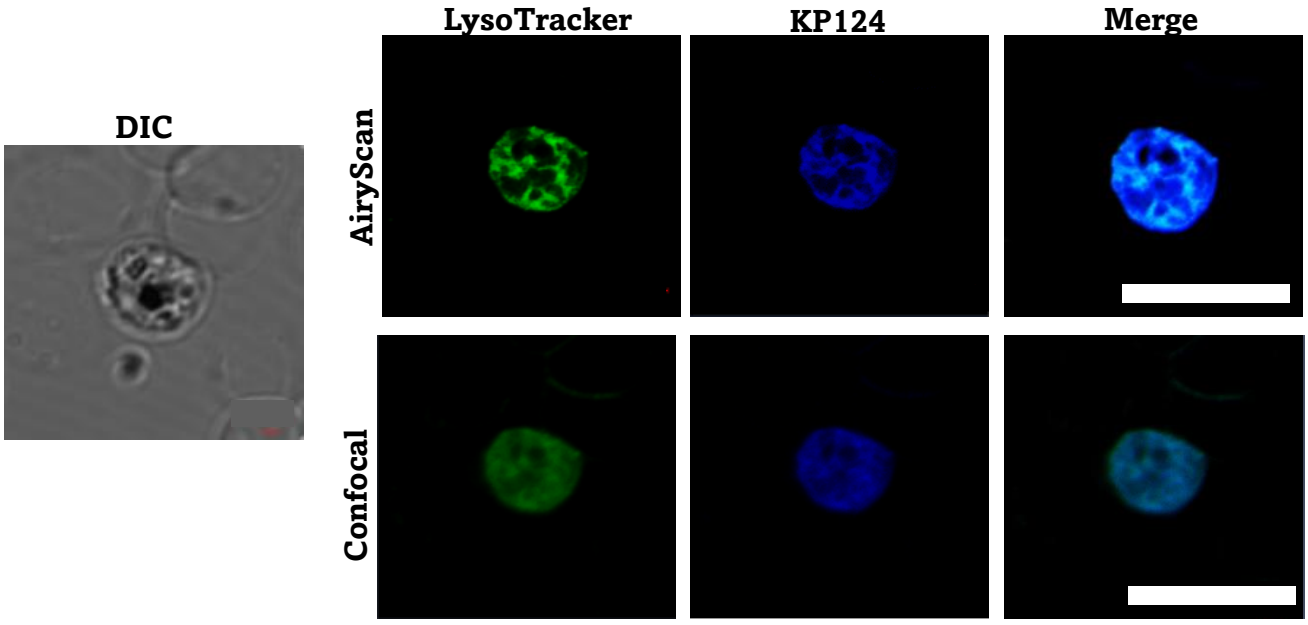

Figure 4.4. A comparison of confocal and Airyscan imaging methods. The lower panel represents an experiment in the confocal mode. The upper panel represents the same experiment visualized using the Airyscan, showing improvement in resolution. Scale bar: 2 μm.

4.3.3. Commercially Available Tracker Dyes Used in this Work

Colocalization studies require using a standardized organelle tracker to co-illuminate cellular compartments or subcellular structures of *P. falciparum*. Several commercially available fluorescent tracker dyes have been previously used in live-cell imaging of *P. falciparum*. Figure 5 illustrates the chemical structures of the trackers used.

MitoTracker Deep Red (Figure 4.5) was identified as a suitable mitochondrion-selective dye to monitor mitochondrial morphology and the functioning of the organelle. It allows for the probing of mitochondrion activity, localization, and abundance.[19–21] While there are other standard fluorescent stains for the mitochondria, such as rhodamine 123 and tetramethylrosamine, which are easily attracted by a functioning mitochondrion, they are

easily quenched with a reduction in mitochondrial membrane potential. Therefore, to overcome this limitation, MitoTracker Deep Red was selected. This is because, once it accumulates in a functioning mitochondrion, this accumulation is retained even if the mitochondrion's membrane potential is lost.[22] The MitoTracker Deep Red is a cell-permeant dye that contains a moderate thiol-reactive chloromethyl moiety.[23] This chloromethyl group is believed to be responsible for keeping the dye associated with the mitochondrion.[23] To label the mitochondrion of *P. falciparum*, the cells are treated and incubated with submicromolar concentrations of the MitoTracker Deep Red. The tracker then diffuses across the plasma membrane and localizes in active mitochondria.

Weakly basic amines localize selectively in a low internal pH cellular environment. These acidotropic probes can be used to investigate the parasite's acidic lysosome.[24,25] These probes have many structural features that result in their selectivity for acidic organelles. They are also efficient at labelling live cells at nanomolar concentrations. The LysoTracker Red (Figure 4.5) comprises a fluorophore linked to a weak base that will lead to its accumulation when protonated at low pH.[26] To achieve selectivity, this probe is used at low concentrations. Their accumulation mechanism is due to protonation and retention in cellular compartments. LysoTracker Red has been previously used to illuminate the parasite's digestive vacuole.[27]

The ER is the proper grouping of lipids and proteins in the cell. Therefore, most fluorescent probes designed for the ER are lipids or chemicals that interfere with protein movement.[28] ER-Tracker is a cell-permeant, live-cell stain highly selected for the ER. The ER-Tracker dye used in this work, ER-Tracker Red, is a fluorescent sulfonylurea antidiabetic drug covalently attached to a boron-dipyrromethane (BODIPY) reporter dye. Glibenclamide binds to the sulfonylurea receptors of ATP-sensitive K^+ channels that are prominent in the ER.[26] However, sulfonylurea receptors may be present on other organelles, leading to unspecific staining. ER-tracker Red exhibits excitation/emission maxima of approximately 504/511 nm and 587/615 nm, respectively. Despite the

mechanistic disadvantage of using this dye, ER-Tracker Red is effective and widely used in marking the ER in live-cell imaging.[29] (Figure 4.5)

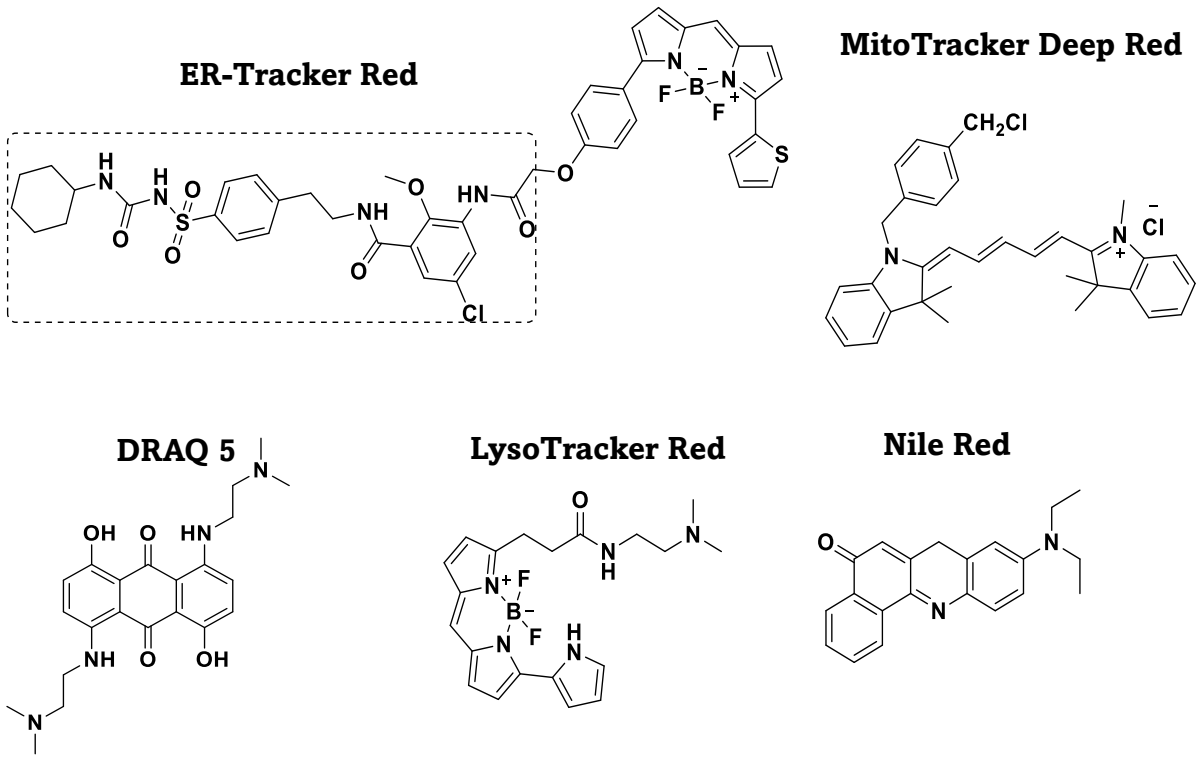

Figure 4.5. Chemical structures of the commercially available tracker dyes used in this study. The sulfonylurea drug glibenclamide is shown in the dashed box in its derivatized amide form.

DRAQ5 (Figure 4.5) is a cell-permeable far-red anthraquinone dye with a high affinity for double-stranded DNA. It is a membrane-permeable dye that can be used to label live cells. It served as a suitable nucleus marker in this study because of its ability to bind DNA stoichiometrically.

Nile Red (Figure 4.5) is a phenoxazine dye employed to localize and quantify lipids, especially neutral lipids droplets and cells.[30–32] Although selective for neutral lipids, it can help quantify phospholipids.[33,34] Nile Red is almost non-fluorescent in aqueous environments, but in a non-polar medium, it undergoes fluorescence enhancement with significant absorption and emission shifts.[35] Fluorescence emission between 650-710 nm identifies phospholipids. However, the signal obtained corresponds to neutral lipids when excited with the same laser but emitted between 575-630 nm. However, the wide window of emission observed with this dye can lead to cross-talk. To circumvent this, narrow filters were created during acquisition to exclude the interfering signal.

4.4. Subcellular Distribution of KP68 and KP124 in *P. falciparum*

4.4.1. Detection of Target Compounds in Infected Red Blood cells

P. falciparum-infected RBCs were resuspended in Ringer's solution and incubated at 37 °C for live-cell imaging.[36] Confocal fluorescence microscopy was used for the initial examination of RBCs infected with the CQS strain of *P. falciparum* (NF54). Infected erythrocytes were easily identified under transmitted light by their hemozoin pigment (Figure 4.6). Detection of **KP68** and **KP124** was also investigated following optimization of drug concentrations.

Cytoplasmic or plasma membrane staining for both compounds was observed in infected host cells (Figure 4.6**,** Panels A and B). However, no signal was detected for either compound in uninfected erythrocytes. This suggests no compound accumulation in uninfected red blood cells and that the compounds are specific for *P. falciparum*. Although there are differences in host plasma membrane composition between infected and uninfected red blood cells,[37] this alone may not be responsible for the compounds' selectivity for infected red blood cells. The tendency of both compounds to accumulate in *P. falciparum* and not uninfected RBCs suggests that the site of action of these compounds is in the parasite and not in the host red blood cell, assuming that the site of accumulation is also the site of action.

Although **KP68** and **KP124** were observed to distribute throughout the parasite's cytosol, **KP68** showed more specific accumulation than **KP124**. Ring-like accumulation was observed in **KP68** (indicated by the white arrow in Figure 4.6, Panel A). Furthermore, there was a discernible structure to these patterns that suggested accumulation within different organelles. Further subcellular accumulation studies were conducted to identify the organelles associated with both compounds.

The ability of these compounds to reverse their accumulation and specific binding was investigated through competition experiments. The minimal signal from the imaging medium containing the fluorescent compounds was removed and replaced with a fresh medium containing no compounds. Images following this treatment suggest that compound accumulation within *P. falciparum* was irreversible.

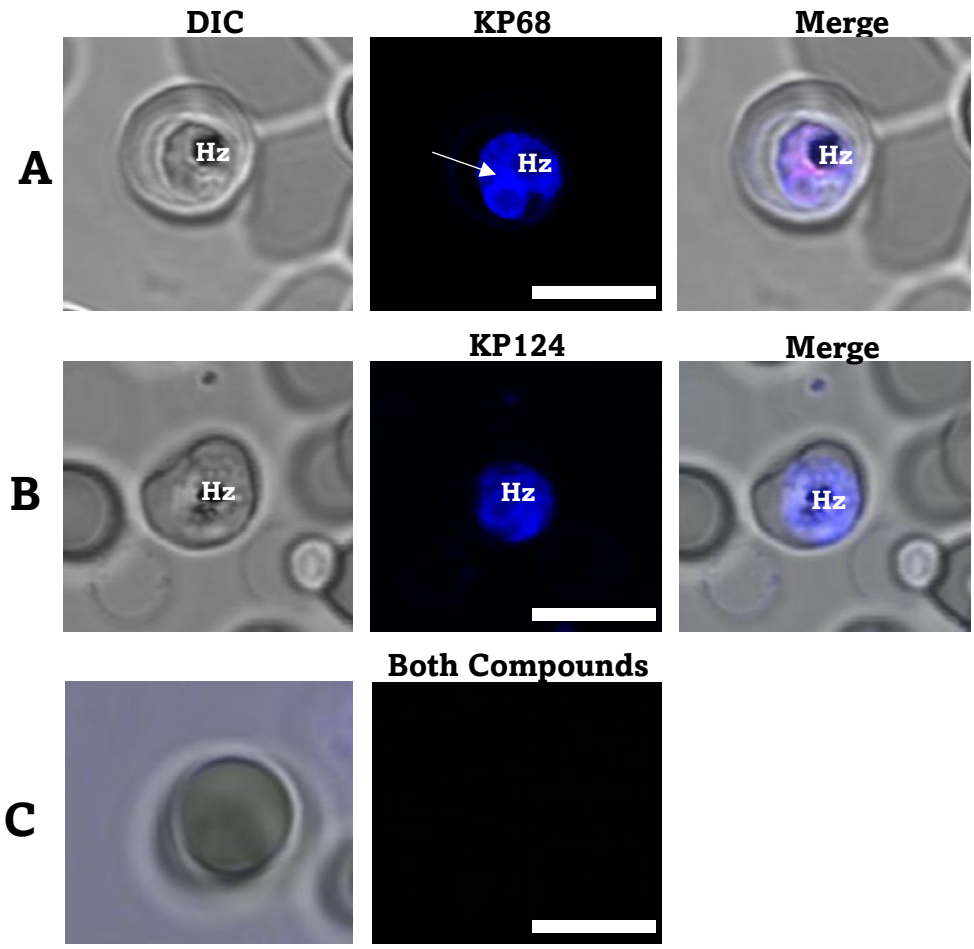

Figure 4.6. Panels **A** and **B** represent *P. falciparum*-infected erythrocytes incubated with **KP68** and **KP124**, respectively. Panel **C** represents an uninfected erythrocyte incubated with both **KP68** and **KP124.** Scale bar: 2 µm.

4.4.2. Preliminary Colocalization Studies Using Confocal Microscopy

Preliminary confocal microscopy showed selective accumulation of **KP124** and **KP68** within the parasite. Compound localization was most intense around hemozoin and consequently in the DV. Hemozoin is represented as ''Hz'' in the images presented.

Confocal microscopy after incubating the cells with LysoTracker Red and **KP68** showed complete colocalization (Figure 4.7A). Since the LysoTracker Red localizes in the low-pH environment, such as the parasite's DV, the dye was expected to localize to the parasite's DV. However, this was not observed. Instead, a more specific localization pattern was observed in the form of two ring-like structures (Figure 4.7A). The most intense localization was observed close to the parasite's membrane and another close to the DV (depicted by white arrows a and b, respectively; Figure 4.7A). It was unclear at this stage

what these structures represented. The inability to observe the LysoTracker Red within the DV may be due to the poor resolution associated with confocal microscopy or the ability of heme to quench fluorescence signals in the parasite's DV. Furthermore, no localization was observed in the nucleus when the parasite was incubated with the nuclear marker DRAQ 5, suggesting no interaction with the nucleus. Finally, MitoTracker Deep Red was incubated with **KP68** in the parasite to investigate the compound's association with the mitochondrion. Following confocal microscopy, the structures shown in the red channel representing the mitochondrion colocalized with the broadly accumulating blue channel of **KP68**. (Figure 4.7C)

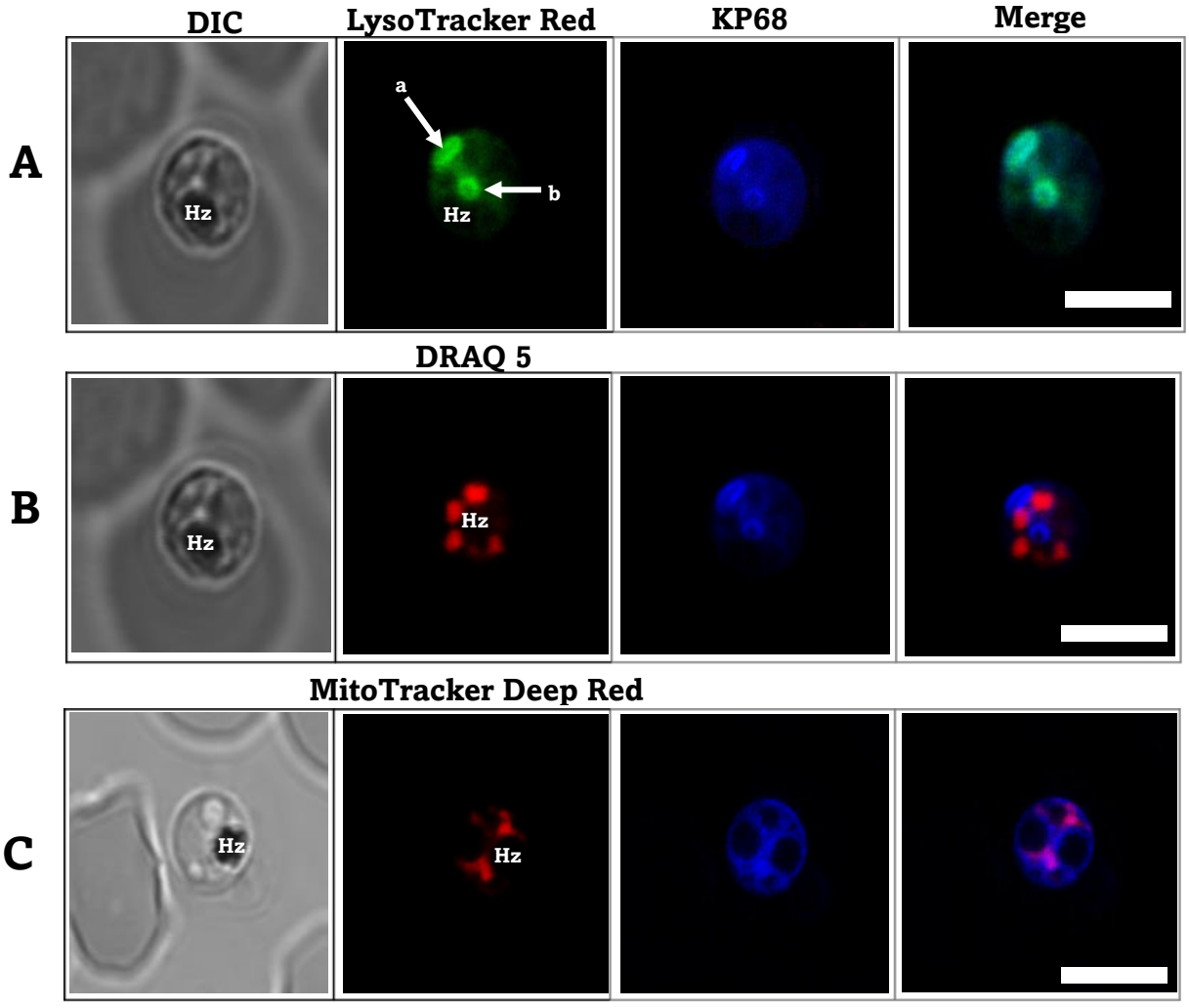

Figure 4.7. Subcellular accumulation of **KP68** with **A**) LysoTracker Red, **B**) Nuclear marker DRAQ5, and **C**) MitoTracker Deep Red in *P. falciparum*. White arrows depict the regions of intense accumulation. Scale bars: 2 μm

Like **KP68, KP124** showed a complete colocalization with the LysoTracker Red. Regions of intense localization of **KP124** were also observed around hemozoin crystals. (Depicted by the white arrow; Figure 4.8). Also, no compound interaction with the nucleus was observed, and a partial colocalization was observed with the MitoTracker Deep Red.

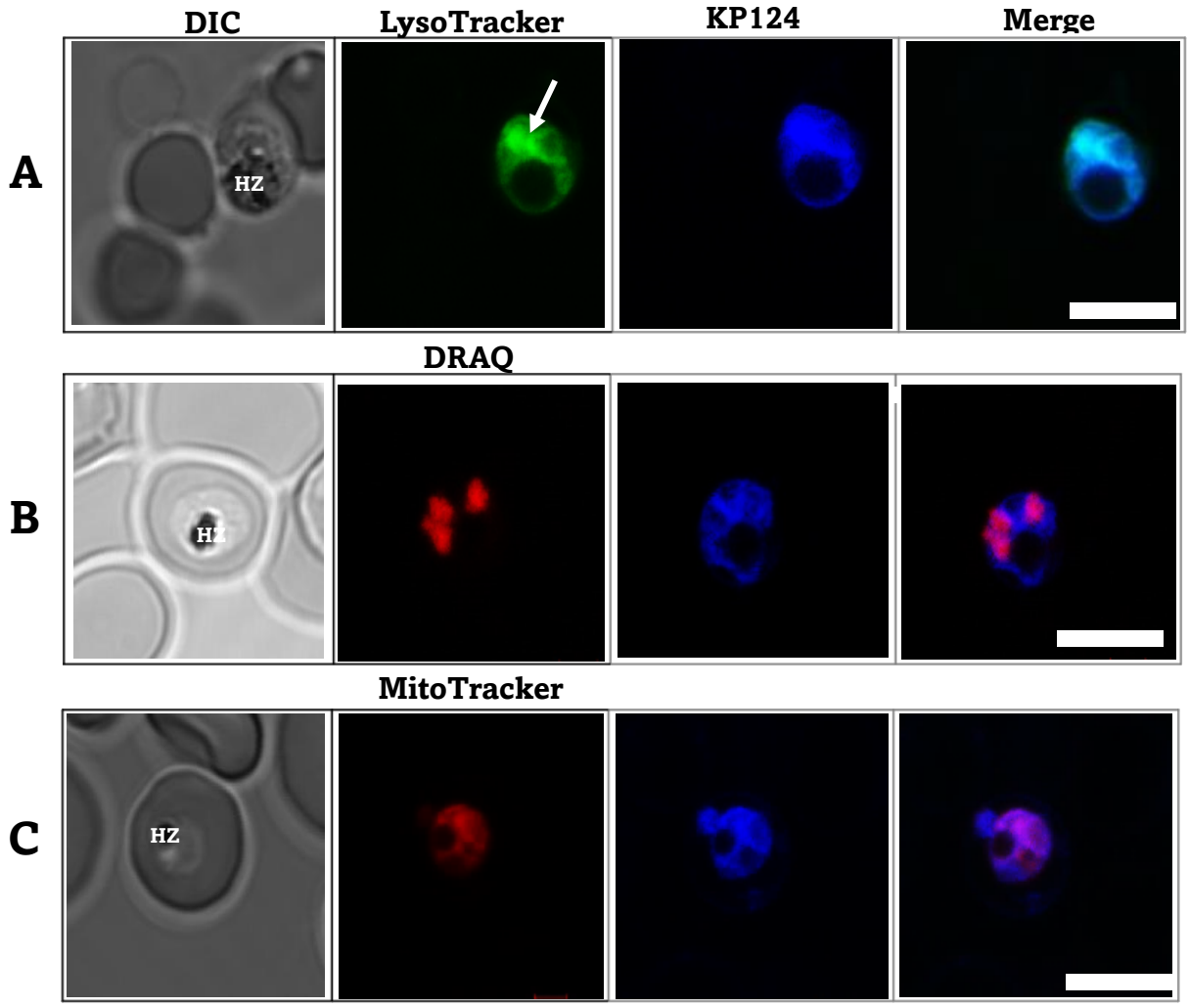

Figure 4.8. Subcellular accumulation of **KP124** with **A**) LysoTracker Red, **B**) Nuclear marker DRAQ5, and **C**) MitoTracker Deep Red in *P. falciparum*. White arrows depict the regions of intense accumulation. Scale bars: 2 μm

While the outcome of this preliminary imaging of **KP68** and **KP124** was the same, a clear difference in the accumulation pattern was observed. This suggested that both compounds interact with different organelles in the parasite and may be acting through other mechanisms. Low resolution remained a significant concern with these images, and conclusions on compound accumulation were challenging. To circumvent this drawback and acquire more resolved images that help in drawing the relevant conclusions regarding

the localization of **KP68** and **KP124**, Airyscan microscopy was employed. It is a near super-resolution technique that increases the resolution of a confocal image two-fold.

4.4.3. Airyscan Fluorescence Microscopy

Airyscan confocal microscopy is a technique based on confocal laser scanning microscopy with the introduction of a detector concept that significantly improves the signal by utilizing light that is otherwise rejected by the confocal pinhole. The increased signal-to-noise ratio may be used to retrieve higher resolution images compared to confocal images. This work applied this technique to assess the colocalization of **KP68** and **KP124** with the organelle trackers.

Using Airyscan microscopy, more details were observed when PBIs were incubated with LysoTracker Red compared to earlier observed via confocal microscopy. In this case, as expected, the LysoTracker Red is localized in the DV and associated with the hemozoin crystals, as depicted in the green channel of Figure 4.9A. Based on the docking studies previously described the potency of **KP68** in the BHIA and the structural similarities between the compound and CQ, **KP68** was expected to localize in the DV when incubated with the parasite. However, no colocalization was observed between **KP68** and the LysoTracker Red. The white arrow in Figure 4.9A shows the Tracker dye accumulated in the DV, but no significant accumulation was observed in the DV by **KP68**. The ability of a compound to interfere with the conversion of heme to hemozoin depends on its ability to localize significantly in the site of action, the DV. Consequently, the inability of **KP68** to localize in the DV suggests that contrary to the earlier hypothesis, the compound's site of accumulation is not in the digestive vacuole, and its primary action is not to inhibit hemozoin formation. It is worth mentioning that the fluorescence emission of **KP68** is at least 2-folds more intense in acidic environments than in basic and neutral environments; hence it is unlikely that the compound could undergo pH quenching in the DV.

On the contrary, **KP124** showed significant colocalization with the LysoTracker Red with regions of intense accumulations around the hemozoin crystals. This suggests that, unlike **KP68**, an enormous amount of **KP124** permeates the DV membrane and accumulates in the acidic digestive vacuole. This may be due to the compound being diprotonated as predicted by the docking studies, allowing it to localize significantly in the DV to

concentrations high enough to be observed through pH trapping. Furthermore, the compound still binds effectively to the surface of hemozoin once protonated. However, the accumulation of **KP124** in the DV is diffused, and the LysoTracker Red does not map out the DV as observed in **KP68.** This could be a result of the ability of **KP124** not only to permeate but also disrupt the DV membrane. Studies have shown that, at specific concentrations, lysosomotropic compounds such as **KP124** break down the parasite's DV membrane upon permeation and interfere with the pH of the environment. This affects the specific accumulation of the acidotrophic dyes in the DV.[38,39]

Although both compounds possess structural features required for interaction with β-hematin to prevent its growth, only **KP124** accumulates in the parasite's DV. Aside from the DV, several organelles play essential roles during the intraerythrocytic stage of the *P. falciparum* life cycle. Unlike the digestive vacuole, organelles such as the ER, mitochondrion, and nucleus occur in all stages of the intraerythrocytic cycle of *P. falciparum* and cannot be formed de novo. Also, these organelles are increasingly becoming potential drug target (s). For instance, the *P. falciparum* mitochondrial electron transporter has been identified as the protein target of the clinically relevant antimalarial atovaquone. Therefore, the ER and mitochondrion were investigated in conjunction with **KP68** and **KP124.** The organelles were illuminated with the ER-Tracker Red and MitoTracker Deep Red, respectively, as described earlier.

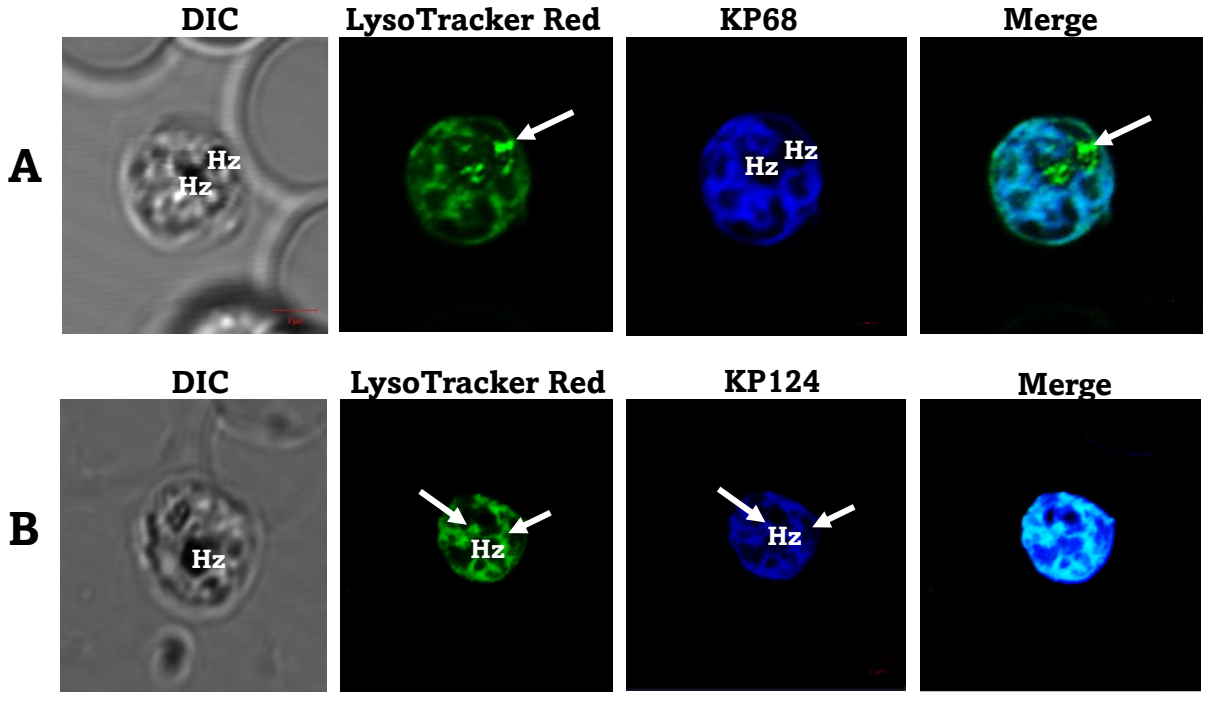

Figure 4.9. Subcellular accumulation of **A**) **KP68** and **B**) **KP124** with LysoTracker Red in *P. falciparum*. The green channels depict signals from the LysoTracker Red, and the blue channels represent the signals from the compounds. White arrows show the regions of most intense accumulation. Scale bars: 2 μm

Parasite incubation with the DRAQ 5 and the target compounds did not reveal any new information compared to what was observed with confocal microscopy. No localization was observed for either compound in the nucleus. The nuclear marker DRAQ 5 corresponds to signals from the red channel, which illuminates the parasite's nucleus. Signals from the compounds correspond to the blue channel. As observed in the "merged" images, no colocalization was observed between either compound or the nuclear marker DRAQ 5, suggesting that these compounds do not act in the parasite's nucleus. (Figure 4.10)

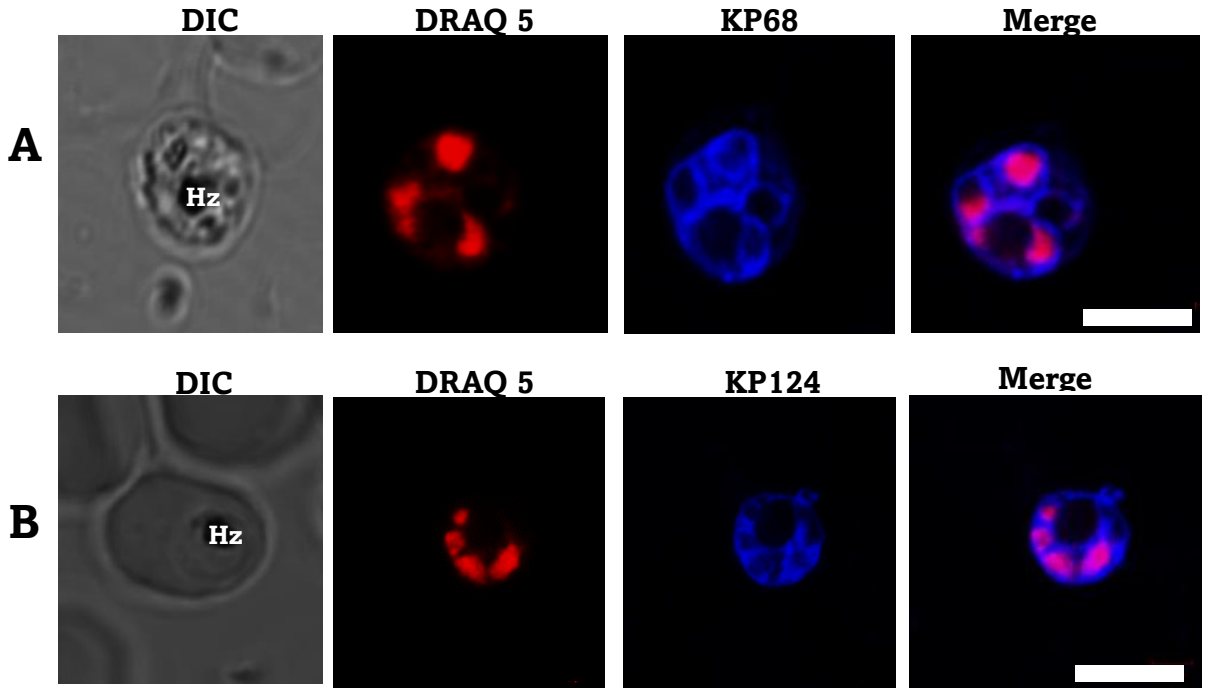

Figure 4.10. Subcellular accumulation of **A**) **KP68** and **B**) **KP124** with DRAQ5 in *P. falciparum*. The red channels depict signals from the DRAQ5, and the blue channels represent the signals from the compounds. Scale bars: 2 μm

When incubated with MitoTracker Deep Red and **KP68,** the infected erythrocytes showed a localized, tube-like structure in the parasite previously described as the morphology of the mitochondrion.[40] (Figure 4.11A). This structure was found close to the parasite plasma membrane. While **KP68** did not colocalize with the MitoTracker Deep

Red, a significant amount of the drug was observed around the mitochondrion. The compound envelops the mitochondrion and strongly associates with the mitochondrial membrane, implicating the mitochondrion in the action of **KP68**.

More diffuse **KP124** accumulation was observed**,** as previously seen with other organelle trackers, as well as strong colocalization with MitoTracker Deep Red (Figure 4.11B). It has been hypothesized that **KP124** may be disrupting the mitochondrion membrane potential, thereby interfering with the accumulation of the MitoTracker Deep Red. However, this hypothesis warrants further investigation. The compound also localized primarily to the parasite's plasma membrane and cytosol, making it difficult to precisely predict the organelles of interest in the action of **KP124.** Aside from the nucleus, the compound seemed to interact significantly with all organelles in the parasite, including lysosomes and mitochondria. This localization pattern continues to implicate hemozoin inhibition.

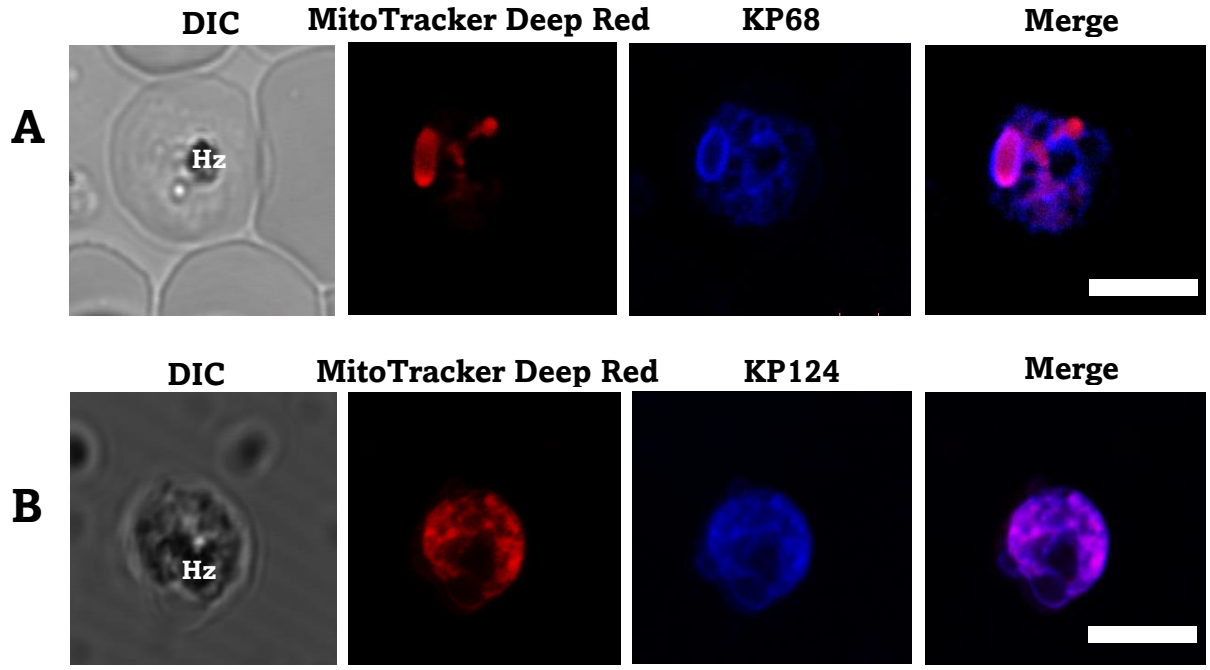

Figure 4.11. Subcellular accumulation of **A**) **KP68** and **B**) **KP124** with MitoTracker Deep Red in *P. falciparum*. The red channels depict signals from the MitoTracker Deep Red, and the blue channels represent the signals from the compounds. Scale bars: 2 μm

Neutral lipids have been shown to carry out essential roles during the ABS of the parasite's life cycle. As described in Section 1.3.1.2 of chapter one, several studies have implicated neutral lipids in the formation of hemozoin. It has been shown that neutral lipid mixtures

enhance heme biocrystallization to hemozoin, and there is ultrastructural evidence of the presence of neutral lipids in the *in vivo* site of hemozoin formation.[41,42] Consequently, the colocalization between the compounds and Nile Red was investigated. Interestingly, two spherical structures are illuminated by Nile Red at a wavelength that only detects neutral lipids. Colocalization with Nile Red was only observed in **KP124** and not **KP68**. The lipid droplets were observed in the cytoplasm close to the DV and the hemozoin crystals, as shown in Figure 4.12B. White arrows point to lipid droplets transported from the cytoplasm to the DV. Colocalization with neutral lipids may be a means by which **KP124** is transported into the DV, where it accumulates and interferes with the hemozoin formation. However, this phenomenon was not observed for **KP68**. The compound showed no colocalization with the neutral lipid bodies, providing another piece of evidence that its site of action is not in the DV. Also, these results suggest that subtle changes in substituents can lead to substantial changes in intracellular localization and possibly a difference in the MOA.

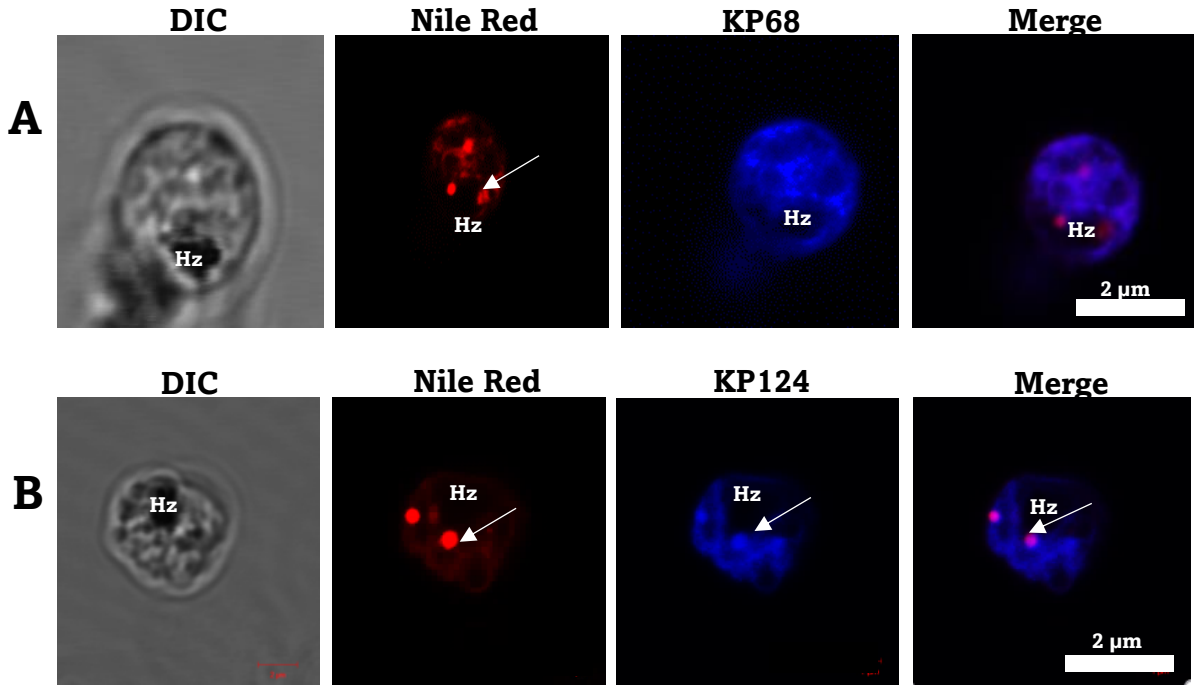

Figure 4.12. Subcellular accumulation of **A**) **KP68**, **B**) **KP124** with Nile Red in *P. falciparum*. The red channel depicts Nile Red, and the blue channels depict the compounds. White arrows depict the regions of intense accumulation. Scale bars: 2 µm

4.5. Quantitative Colocalization Analysis

The spatial colocalization analysis discussed above helps describe patterns of signal distribution in fewer cells, particularly with subcellular structures such as hemozoin or co-illuminated organelles. It is also helpful in giving the first impression of the signal overlap between two or more channels. However, quanlitative analysis is subjective and becomes unsuitable with an increasing number of images. Therefore, a more efficient and less subjective way to analyze images is to assess them quantitatively by measuring the amount of overlap between different signals. As described in Chapter 3, several statistical approaches automatically quantify colocalization in any region of an image without the ambiguity and subjectivity accompanying the bias of visual interpretation. Visual methods may be sufficient for image compartments that are adequately separated spatially. However, if the compartments are not visually distinct, then quantitative tools are required. For this work, the correlation between the intensity values of pixels in a dual-channel image is analyzed using coefficients that measure the relationship between these two values. Just Another Colocalization Plugin" (JACoP) for ImageJ was used for the colocalization analysis described in the following sections.[43]

Pearson's correlation coefficient (r) is the most quantitative estimate of colocalization, which depends on the amount of colocalized signals in both channels. Furthermore, colocalization coefficients M_1 and M_2 remain a meaningful set of coefficients that quantify the colocalized fraction of each channel.[44,45] However, these analytic techniques require a threshold value for each channel analyzed. These values are then used as a cut-off between the specific and non-specific staining, eliminating background noise. Initially, these thresholds are typically based on visual estimations of the images; however, Costes et al. proposed a more powerful way to determine the thresholds.[46]

The expected pixel location on a cytofluorogram representing noise is close to the origin. It takes the shape of a formless cloud; when isolated, this population has a PCC of zero.[46] These values are automatically computed to avoid user inputs. However, automatic thresholding is reserved for images with an improved signal-to-noise ratio. When a poor signal-to-noise ratio is observed, the cloud formed by the pixels due to noise becomes part of the cloud formed by pixels due to the fluorescence signal.[46]

The correlation coefficients computed by quantitative analysis of more than ten different single-cell images for each pair of channels are shown in Table 4.1. All the coefficients discussed here were calculated, considering the automatically generated threshold values, except for the PCC, which was calculated with and without the automatic thresholding algorithm. The signal from the intrinsic fluorophores **KP68** and **KP124** was compared to the LysoTracker Red and the nuclear marker DRAQ5. Since it is unlikely for the LysoTracker Red, which stains the membranes and acidic compartments of the parasite, to colocalize with the DRAQ 5, which represents the nucleus, these correlation coefficients were appropriate negative controls. An exemplary data set for **KP124** and LysoTracker Red is provided in Figure 4.13 to help interpret the result.

Table 4.1. Quantitative colocalization analysis of at least five different single-cell images per dataset resulted in a range of correlation coefficients in the presence or absence of automatic thresholding. Average values are presented with their standard error of the mean.

		No Thresholds	**Automatic thresholds applied**					**Van steensel's CCF**	
Channel 1	Channel 2	*rp*	*rp*	*rm*	*|k1-k2|*	M_1	M_2	Min. δx	Min. δx
KP124	LysoTracker Red	0.812 ± 0.075	0.742± 0.054	0.921± 0.012	0.159± 0.078	0.902± 0.010	0.927± 0.078	-20	0
KP68	LysoTracker Red	0.422 ± 0.021	0.366± 0.075	0.797± 0.014	0.572± 0.070	0.470± 0.009	0.576± 0.008	-20	-2
KP124	DRAQ 5	0.172 ± 0.015	-0.143± 0.028	0.706± 0.019	0.530± 0.068	0.360± 0.168	0.477± 0.128	-20	11
KP68	DRAQ 5	0.222 ± 0.019	-0.140± 0.068	0.724± 0.038	0.780± 0.120	0.297± 0.088	0.298± 0.162	-20	11

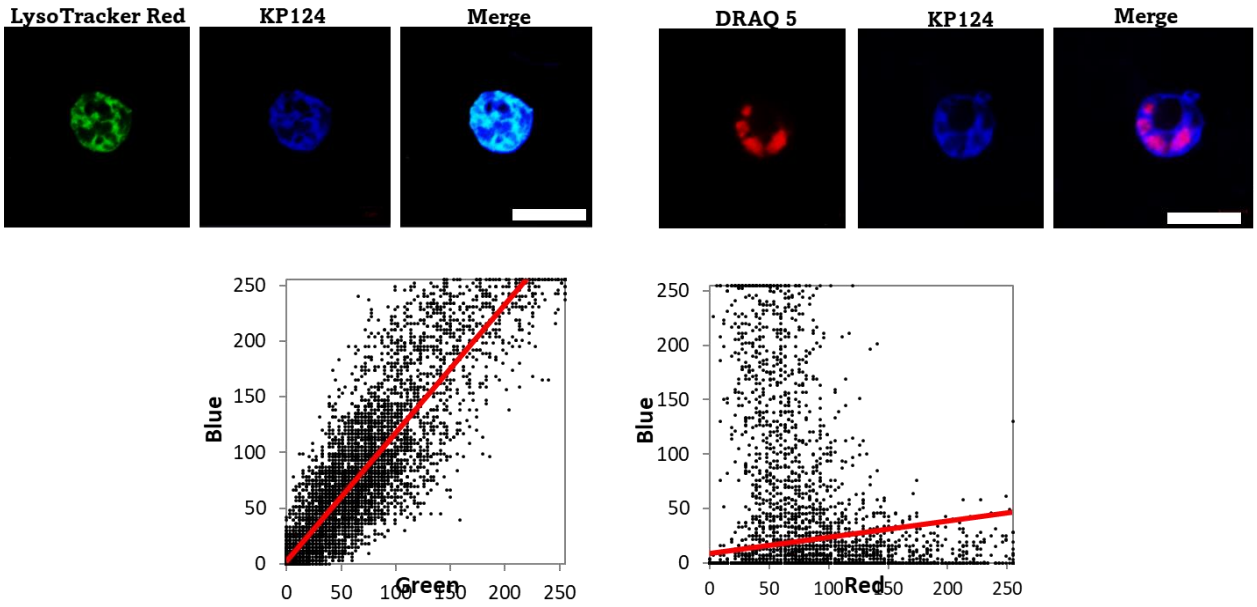

Figure 4.13. Panel A represents an erythrocyte infected with *P. falciparum* and treated with LysoTracker Red (green), **KP124** (blue), and DRAQ 5 (Red). The merged images are depicted as such, and the cytofluorograms show the first estimates of colocalization between blue and green channels and between red and blue channels, respectively. Scale bars represent 5 μm.

Without automatic thresholding, PCC showed that an excellent overlap exists between the signals of **KP124** and LysoTracker Red (r_p > 0.5) and a poor overlap between the compound and DRAQ5 (r_p <0.5). This is reflected in the quantitative impressions of the images; signals from the PBIs share more pixels with the LysoTracker Red than with the nuclear marker DRAQ 5. However, when automatic thresholding is applied, a more substantial negative correlation is observed (r_p < 0), while the positive correlations weaken. This means that the thresholding algorithm eliminated noise pixels in the images.

As previously described in Chapter 3, colocalization can be quantified by splitting the Manders overlap coefficient into two parameters (k) to analyze either signal's contribution to the colocalization. k_1 approaches α when good colocalization is observed, where α is the line of best fit through the cytofluorogram. For the dataset shown in Figure 4.13, k_1 for the green-blue channel combination is estimated at 0.743. This value is close to the mean slope of the cytofluorogram (α), which is 0.756, suggesting a good colocalization between the two channels. k_1 is affected by changes in signal intensity. Therefore, the difference between these split coefficients $|k_1 - k_2|$ indicates colocalization. In the case of the green and blue channels depicted in Figure 4.13, the difference between these splits' coefficients

approaches 0.1. This relationship shows true colocalization and that both channels contribute equally to colocalization.

To conclude, van Steensel's cross-correlation was used as an affirmative approach to differentiate between positive and partial correlation. Here, the images are shifted pixel-by-pixel in the *x*-direction relative to one image. For true colocalization to occur, the correlation is reflected by small δx values for the PBIs compared to the LysoTracker Red. Compared to LysoTracker Red, a larger PCC is observed for colocalization studies with DRAQ 5 after the shifting process ($\delta x = 11$). Using this technique, an improvement in colocalization is achieved after shifting one image relative to the other. This suggests that **KP124** and DRAQ 5 were not colocalized to start with.

These colocalization coefficients led to the general conclusion that colocalization with **KP124** with LysoTracker Red is higher than with **KP68**. A partial colocalization was measured between **KP68** and the LysoTracker Red. This is because, aside from localizing in the acidic compartments of the cell, the dye also associates strongly with the parasite's membrane. Hence although **KP68** does not accumulate in the DV, it colocalizes with the LysoTracker Red in areas associated with the parasite's cytoplasm and membranous structures. The quantitative analysis also supports qualitative observations that both compounds do not localize in the parasite's nucleus. Regarding other organelles, The ER-Tracker showed an unspecific signal throughout the cytoplasm that broadly colocalized with **KP124** but not **KP68**. Due to the diffused nature of this signal, quantitative colocalization analysis was unsuccessful. Furthermore, the colocalization of **KP124** with the MitoTracker Deep Red was confirmed quantitatively and qualitatively. However, in the case of **KP68,** poor colocalization was observed between the compound and MitoTracker Deep Red ($rp < 0.5$). However, since a significant amount of the compound accumulates around the mitochondrion, the mitochondrion was implicated in the action of **KP68**.

4.6. Heme Fractionation Assay of KP124 and KP68

Following the results from live-cell imaging using the intrinsic fluorescence of **KP68** and **KP124,** the ability of both compounds to affect the levels of heme and hemozoin in an *in vitro* parasite culture was investigated according to methods previously described by Combrinck *et al.*[47] When *P. falciparum* was exposed to **KP68**, it did not affect the levels of

heme and hemozoin (Figure 14.4). This observation is consistent with the fact that the compound does not localize in the DV to amounts significant enough to interfere with converting toxic ''free'' heme to hemozoin. It is evident that although **KP68** possesses all the structural properties required to interact with heme and prevent its conversion to hemozoin, this does not translate *in vitro* in erythrocyte-infected *P. falciparum*.

Contrary to **KP68**, significant changes in the levels of heme and hemozoin were observed when the parasite was exposed to an increasing concentration of **KP124.** The heme levels increased steadily with a concomitant decrease in hemozoin levels as a function of concentration, suggesting that exposure to this compound to *P. falciparum* causes the build-up of toxic heme, which leads to the parasite's death. Consequently, unlike **KP68**, **KP124** acts through the inhibition of hemozoin formation. However, when compared to CQ, the effect of **KP124** on the levels of heme and hemozoin was less pronounced at increasing concentrations.[48,49] This implies other contributory mechanisms to the action of **KP124,** which will be investigated through other target identification approaches later discussed in this thesis.

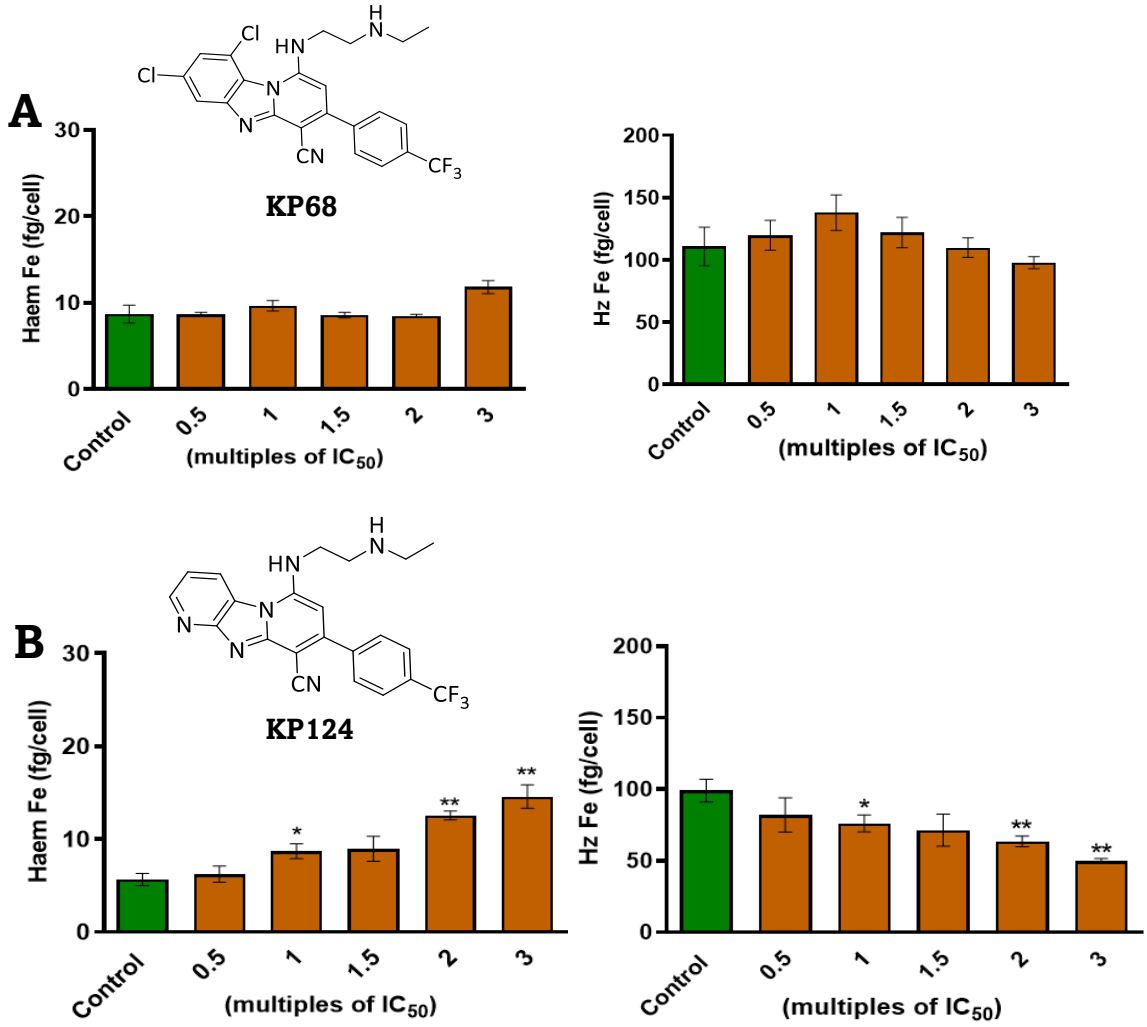

Figure 4.14. Heme Fractionation profiles of **KP68** (A) and **KP124** (B). The amount of ''free'' heme Fe and hemozoin (Hz) Fe at increasing concentrations of both compounds. Significant levels are depicted with asterisks, where * = $p < 0.05$, ** = $p < 0.01$.

As stated earlier, **KP68** is about five times more active against both the CQS and multidrug-resistant strains of *P. falciparum* than **KP124**. Due to this and the results from the hemozoin inhibition, it is evident that the target of **KP68** is outside the parasite's DV. **KP68** acts at lower doses, at which sufficient localization in the DV does not occur, to inhibit the formation of hemozoin. Also, the loss of π–π stacking interactions between the porphyrin ring of β-hematin and the heteroaromatic ring of **KP124** in its diprotonated state could account for the lower activity of the compound compared with known drugs that target this pathway. Interestingly, these two structurally similar compounds have distinct accumulation in the parasite and could have different MOA (s), which will be further explored in this work.

4.7. Exploiting the Extrinsic Fluorescence of DM253

The extrinsic fluorescence of **DM253** was employed to study the subcellular accumulation of the compound**.** As described in Chapter 2, a novel fluorescent derivative of the compound was synthesized by attaching an external NBD fluorophore to the compound. Due to the absence of inherent fluorescence, the NBD fluorophore aids in detecting **DM253** in *P. falciparum*. The fluorescent derivative **DM253-NBD** was evaluated pharmacologically and photophysically to ensure its suitability to represent **DM253** live-cell images, as described in Chapter 3.

Colocalization studies with the fluorescent signals of **DM253-NBD** and LysoTracker Red in *P. falciparum* showed an almost complete colocalization between the two signals. The tracker dye interacted strongly with the LysoTracker, illuminating features that present as spherical objects. These are indicated by white arrows and are believed to be the parasite's lysosome. Also, the regions of intense fluorescence are located around the hemozoin crystals in the DV. (Figure 4.15). An intense fluorescence signal of **DM253-NBD** is also observed in the parasite's cytoplasm. However, this is expected because NBD is most fluorescent in lipophilic environments, making it challenging to deduce if this accumulation is genuinely due to **DM253** or the presence of NBD on the molecule. However, the potent activity of this compound in the BHIA suggests a possible interaction with the hemozoin inhibition pathway.

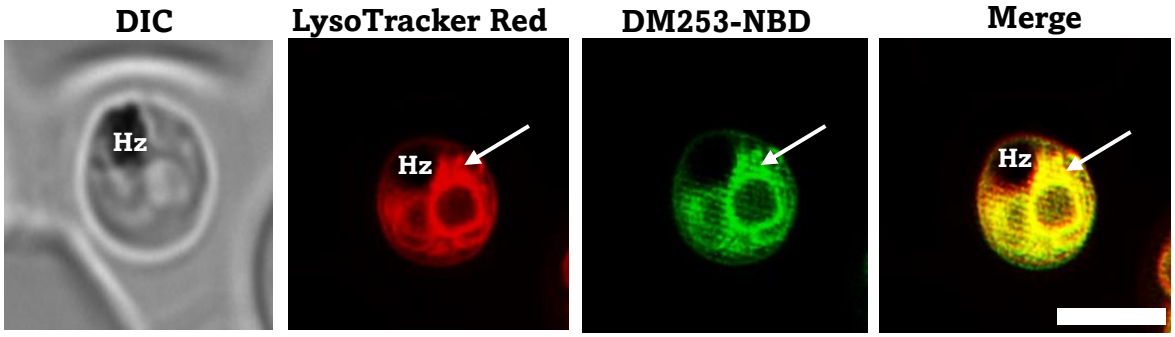

Figure **4.15.** Subcellular accumulation of **DM253** with LysoTracker Red in *P. falciparum*. White arrows depict the regions of intense accumulation. Scale bars: 2 μm

Again, **DM253** showed no colocalization with the nuclear marker DRAQ 5, suggesting that the compound does not accumulate in the nucleus and its action does not involve the parasite's nucleus (Figure 4.16). This is not surprising since only one clinically relevant antimalarial compound, DB75, has been shown to accumulate selectively in the nucleus.

The intrinsic fluorescence property of the antimalarial compound DB75 was used to determine its localization in the parasite's nucleus and implicate it in the compound's action.[50]

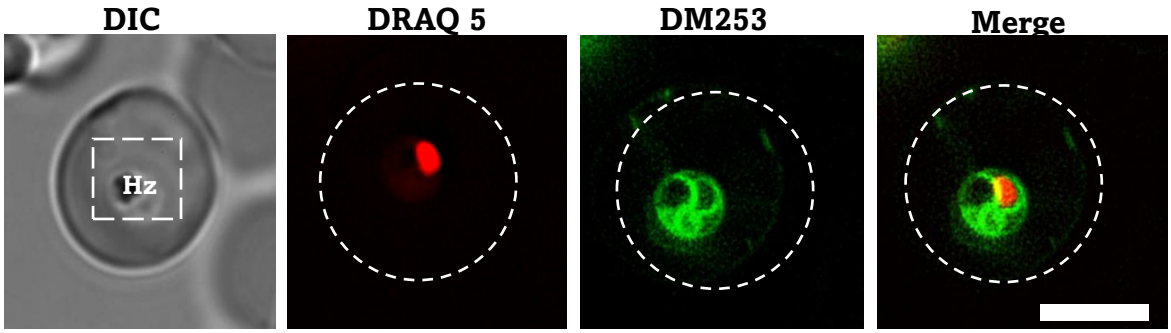

Figure 4.16. Subcellular accumulation of **DM253** with the nuclear marker DRAQ5, in *P. falciparum*. Scale bars: 2 μm

The MitoTracker Deep Red illuminated the parasite's mitochondrion, depicted by signals from the red channel in Figure 4.17. Since late-stage trophozoites were imaged, multiple tube-like structures represented the parasite's mitochondrion. The signal from the MitoTracker Deep Red colocalizes partially with the signal from the **DM253-NBD**. The significant overlap observed between the two channels (rp > 0.5) implicates the mitochondrion in the action of **DM253-NBD**.

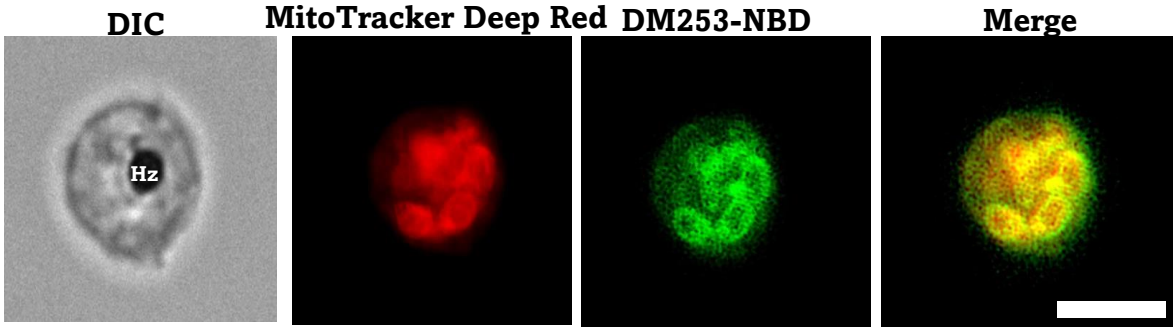

Figure 4.17. Subcellular accumulation of **DM253-NBD** with the MitoTracker Deep Red in *P. falciparum*. Scale bars: 2 μm

Finally, to investigate the association of **DM253-NBD** with the ER and neutral lipids, the ER-Tracker Red and Nile Red were incubated with the compound in *P. falciparum*. SR-SIM revealed an intense accumulation of ER-Tracker Red, which broadly colocalizes with signals from **DM253-NBD** observed as yellow in the "merge" images (Figure 4.18 A). In mature trophozoites, the ER is represented as a punctuate structure illuminated by the

ER-Tracker (Figure 4.18A). This interaction with the ER suggests that ER could play an essential role in the action of **DM253-NBD.**

Similarly, when **DM253-NBD** was incubated with Nile Red to assess the compound's interaction with neutral lipids, quantitative colocalization analysis indicated a strong colocalization correlation between the red and green channels with rp >0.5. Neutral lipids can be observed in the DIC image shown by the white arrows in Figure 4.18B and further illuminated by the Nile Red.

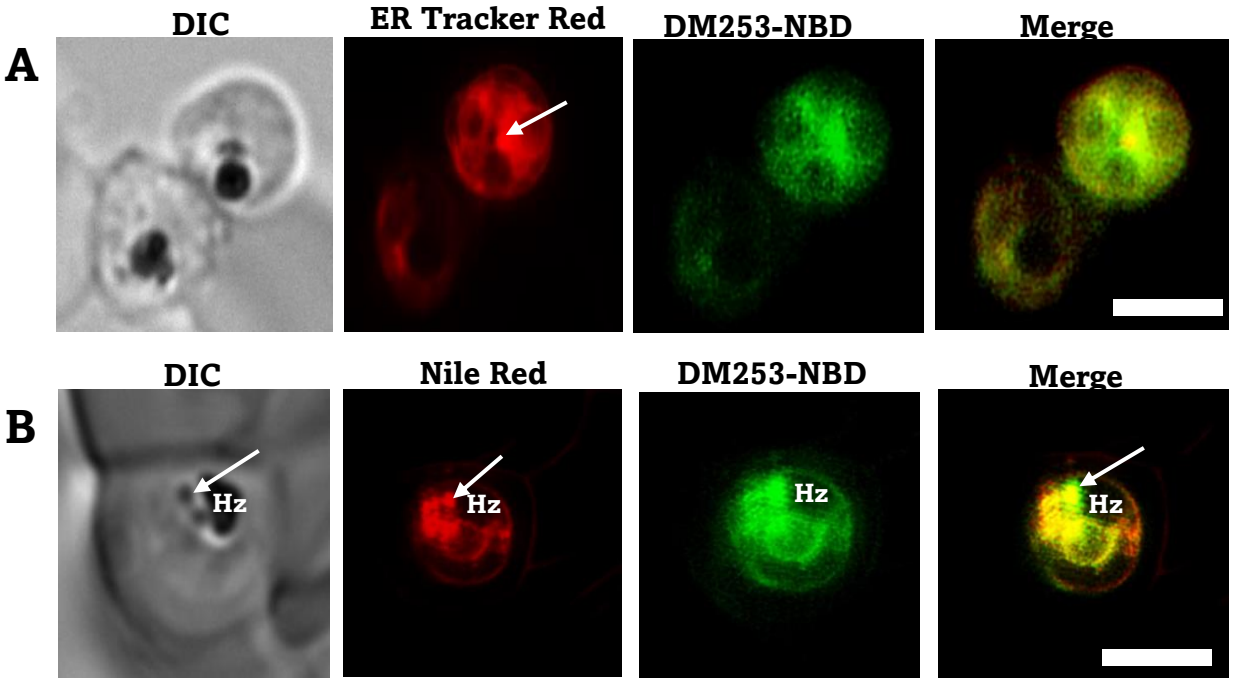

Figure 4.18. Subcellular accumulation of **DM253-NBD** with **A**) ER-Tracker Red and **B**) Nile Red in *P. falciparum*. White arrows depict the regions of intense accumulation. Scale bars: 2 μm

The results from the live-cell imaging employing SR-SIM implicated all the organelles in *P. falciparum* except the nucleus. This, coupled with the compound's β-hematin inhibition activity, suggests hemozoin inhibition as a contributory mechanism of **DM253**. Consequently, a heme fraction assay was carried out to analyze further the compound's effect on the levels of heme and hemozoin at increasing concentrations. The assay results indicate that with increasing concentration of **DM253**, no significant impact on the levels of heme and hemozoin is observed. (Figure 4.19) This either suggests that

DM253 does not act through hemozoin inhibition, and the accumulation observed in the live-cell imaging is due to the influence of the NBD reporter fluorophore attached to a

molecule or that the compound acts on other pathways in the DV aside from directly inhibiting the formation of hemozoin.

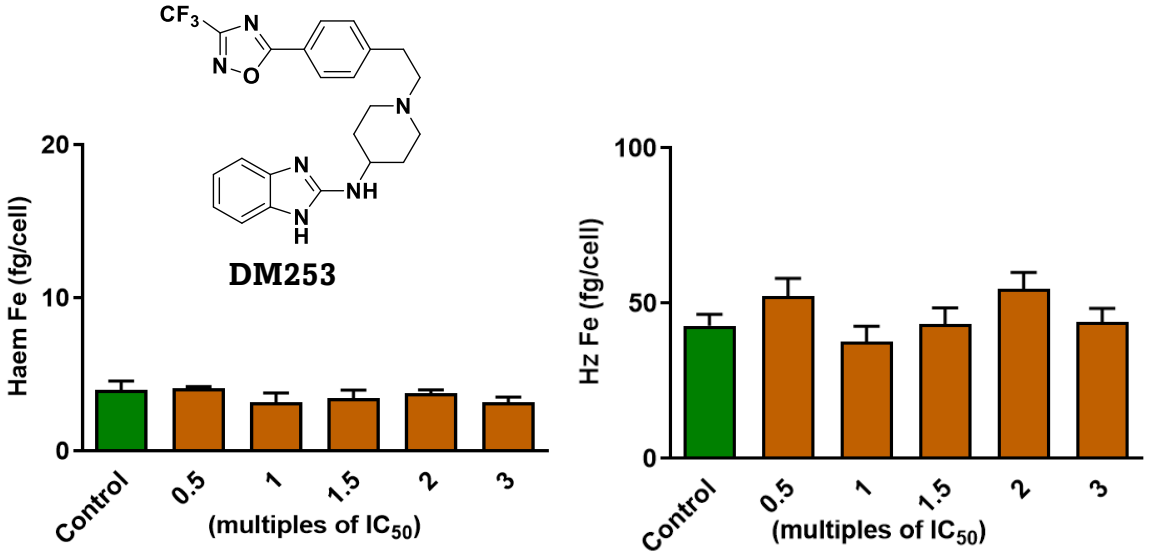

Figure 4.19. Heme Fractionation profiles of **DM253**. The amount of ''free'' heme Fe and hemozoin (Hz) Fe at increasing concentrations of both compounds. Significant levels are depicted with asterisks, where * = $p < 0.05$, ** = $p < 0.01$

4.7.1 Effect of NBD on the Accumulation of KP68

There are some limitations to the fluorescence microscopy approach discussed in this work. Although fluorescence live-cell imaging is carried out under less evasive conditions and imaged with reduced disturbance to the parasite's natural metabolic processes, there are still some limitations to the technique. Colocalization studies depend on the ability of the commercially available tracker dyes to selectively accumulate in the organelles that they represent. For example, the nuclear marker DRAQ 5 must illuminate the nucleus selectively for successful colocalization studies with a compound under investigation. However, most tracker dyes available are lipophilic and interact with the cytoplasm and hydrophobic regions of the parasite. This results in very diffused signals with a lot of background noise, making quantitative colocalization studies challenging.

Furthermore, **DM253** was labelled with a hydrophobic external fluorophore (NBD) that is structurally different from the parent molecule. Although this fluorophore was selected due to its small size and ability to cause the least perturbation to the cell, it increases the hydrophobicity of the compounds, reduces solubility in some instances, and can cause a

preference for the fluorescent analogue for membranous and lipid components. This is observed in the accumulation pattern of **DM253-NBD**. Also, these NBD-labelled probes are quenched after complexation with Fe(III)PPIX and hemozoin. A similar accumulation pattern was observed when the localization pattern of **DM253-NBD** was compared with the localization of other NBD-labelled probes reported in the literature.[51] This begs the question as to whether the accumulation observed was due to the compounds under study or the NBD fluorescent probe.

Therefore, to investigate the effect of attaching an NBD extrinsic fluorophore to the compounds under study, an NBD-labelled **KP68** was employed. Accumulation due to the inherent fluorescence properties of **KP68** was compared to the localization due to its fluorescent derivative **KP68-NBD**. As discussed in Chapter 3, despite the loss in antiplasmodium activity compared to the parent compound, **KP68-NBD** still retained its overall antiplasmodium activity suitable for its use in probing the subcellular accumulation of **KP68**.

The accumulation of **KP68** and **KP68-NBD** was compared to ascertain the effect of the reporter fluorophore on the localization of the **KP68**. Overall, **KP68** and its fluorescent derivative showed a distinct accumulation pattern. As previously observed for NBD-labelled fluorescent derivatives, a complete colocalization was observed between NBD-labelled **KP68** and the LysoTracker Red. Signals from **KP68-NBD** interacted with the hydrophobic regions of the parasite, as shown by its colocalization with the LysoTracker Red (Figure 4.20, Panel A). On the other hand, a more specific colocalization was observed for **KP68**. As earlier described, no significant colocalization was observed between **KP68** and the LysoTracker Red. It is evident from this observation that, as suspected, the presence of NBD results in the preference of the fluorescent derivative for the parasite's hydrophobic regions and membranous structures.

Also, while no colocalization was observed between **KP68** and the ER-Tracker Red (Figure 4.21, Panel B), a complete colocalization was observed between the tracker dye and **KP68-NBD**, shown as yellow in the merged image in Figure 4.21, Panel A. The effect of NBD on the accumulation of **KP68** is significant, and in some instances, it affects the overall conclusion in terms of whether or not **KP68** accumulates in a specific organelle. Therefore, even for fluorescent derivatives that retain biological activity, the presence of

an external fluorophore can alter its accumulation in the parasite depending on the physical property of the fluorophore and consequently change the MOA. Hence the intrinsic fluorescence properties of compounds are preferred in probing their subcellular localization in *P. falciparum*.

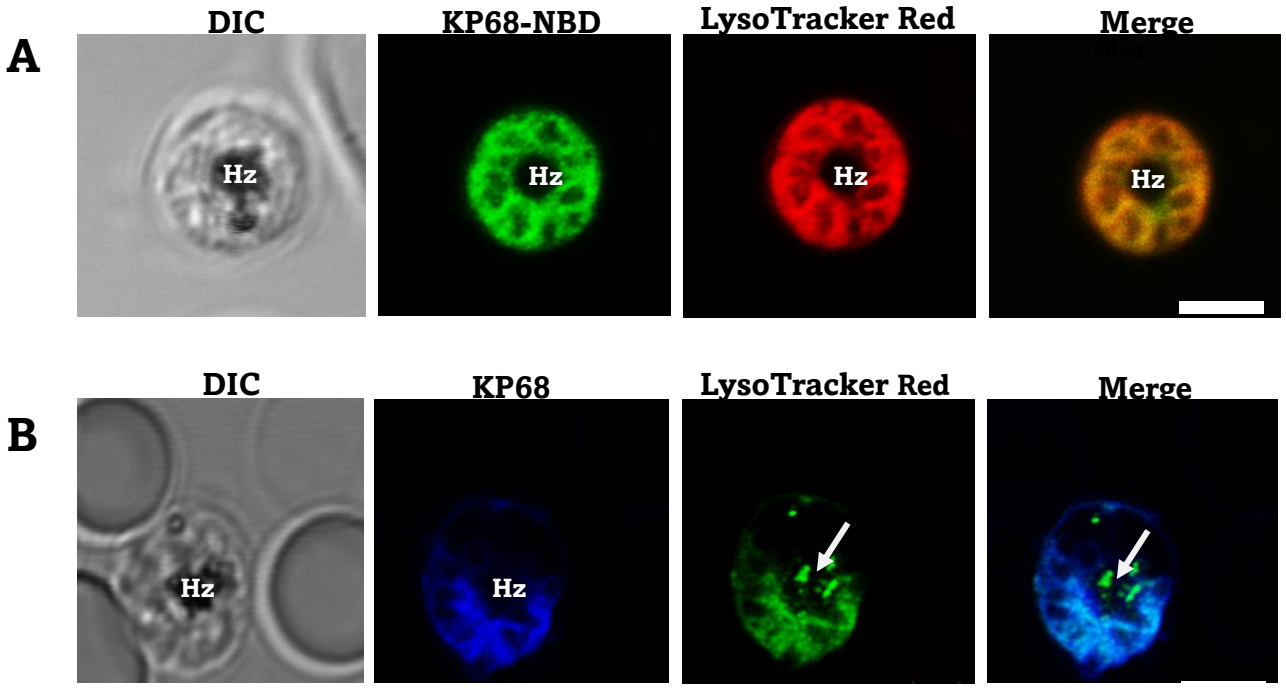

Figure 4.20. Subcellular accumulation of **A**) **KP68-NBD** and **B**) **KP68** with LysoTracker Red in *P. falciparum*. White arrows show the regions of most intense accumulation. Scale bars:2 μm

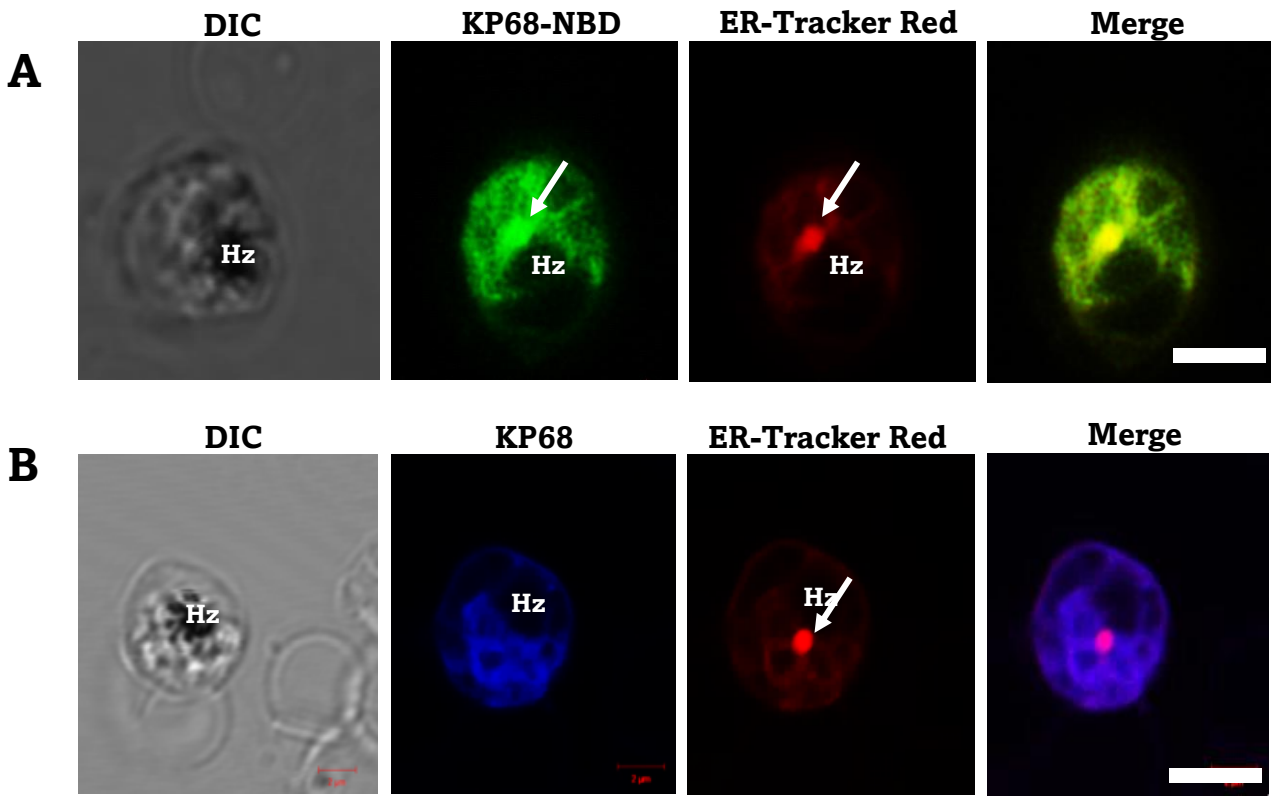

Figure 4.21. Subcellular accumulation of **A**) **KP68-NBD** and **B**) **KP68** with ER-Tracker Red in *P. falciparum*. The green channels depict signals from the **KP68-NBD**, and the blue channels represent the signals from the compounds. Signals from the ER-Tracker Red are represented by the red channels. White arrows show the regions of most intense accumulation. Scale bars: 2 μm

4.8. Summary and Conclusion

Fluorescence provides a unique view of structural and functional details of intraerythrocytic *P. falciparum*. Although other techniques such as ultrastructural studies can provide exceptional resolution, they are limited by poor contrast and extensive sample preparation. To circumvent these drawbacks, light microscopy offers live-cell imaging techniques that require reduced sample preparation and allow for the acquisition of reliable information about the accumulation of drugs and drug candidates in biological systems.

In this chapter, the intrinsically fluorescent antimalarial PBIs, **KP68, KP124,** and the NBD-labelled **DM253** prepared in Chapter 2 and subsequently validated in Chapter 3 were probed using live-cell imaging techniques. Despite the many challenges presented by light microscopy in imaging *P. falciparum*, chiefly regarding the photosensitivity of cells and the small size of the parasite, overcoming them results in imaging that generates valuable insights into the action of the study compounds. Commercially available tracker dyes used in this work were carefully selected to co-stain the organelles in the parasite without crosstalk with the compounds under study.

All fluorescent compounds were found to accumulate selectively in *P. falciparum*-infected erythrocytes. No accumulation was observed in uninfected erythrocytes. **KP124** and **DM253-NBD** were observed in proximity to the hemozoin pigment and subsequently in the parasite's DV. In addition to the DV, these compounds were observed to localize diffusely throughout the cell and associate intensely with the parasite's plasma membrane. **KP68,** on the other hand, showed no accumulation in the parasite' DV, although significant amounts of the compound are observed in the cytoplasm and plasma membranes.

Quantitative colocalization analysis showed an excellent correlation between the signal distribution of **KP124** and **DM253-NBD** and LysoTracker Red. This confirms the qualitative observations that these compounds accumulate within acid and membranous structures in the parasite. A negative correlation was observed for **KP68** and the LysoTracker Red, again confirming the quantitative observation that this compound does not accumulate in the parasite acidic compartments. Also, a negative correlation was

observed between all fluorescent compounds and the nuclear marker DRAQ 5, indicating that it is unlikely these compounds act by interfering with processes in the nucleus.

KP124 and **DM253-NBD** exhibited a broad colocalization with the ER and the mitochondrion following co-staining with the ER-Tracker Red and MitoTracker Deep Red. However, no colocalization was observed between **KP68** and the ER-Tracker Red, while a significant amount of the compound accumulates in the mitochondrion membrane, implicating the mitochondrion in the action of **KP68.**

Aside from **KP68,** all fluorescent compounds accumulated significantly with the hemozoin-associated neutral lipid bodies. Furthermore, when tested in the cell fractionation assay, only **KP124** showed a significant effect on the levels of heme and hemozoin. The compound causes a dose-dependent increase in the levels of free heme and a decrease in hemozoin. Taken together, these results support hemozoin inhibition through accumulation in the digestive vacuole as a MOA of **KP124** with contributions from the compound's interaction with the ER and mitochondrion. While this is not the case for **KP68**, its interaction with the parasite's membranous structures and the mitochondrion serves as a starting point toward understanding the MOA of the compound in *P. falciparum*.

Fluorescence live-cell imaging alone is not enough to elucidate the MOA of these compounds. However, it serves as a starting point in understanding their action, and other approaches to target identification will contribute more information on their MOA.

4.9. References

(1) Sullivan, D. J. Theories on Malarial Pigment Formation and Quinoline Action. *Int. J. Parasitol.* **2002**, *32* (13), 1645–1653.

(2) Francis, S. E.; Sullivan, D. J.; Goldberg, and D. E. Hemoglobin Metabolism in the Malaria Parasite *Plasmodium falciparum*. *Annu. Rev. Microbiol.* **1997**, *51* (1), 97–123.

(3) Pagola, S.; Stephens, P. W.; Bohle, D. S.; Kosar, A. D.; Madsen, S. K. The Structure of Malaria Pigment β-Hematin. *Nature* **2000**, *404* (6775), 307–310.

(4) Ncokazi, K. K.; Egan, T. J. A Colorimetric High-Throughput β-Hematin Inhibition Screening Assay for Use in the Search for Antimalarial Compounds. *Anal. Biochem.* **2005**, *338* (2), 306–319.

(5) Egan, T. J.; Ross, D. C.; Adams, P. A. Quinoline Anti-Malarial Drugs Inhibit Spontaneous Formation of β-Haematin (Malaria Pigment). *FEBS Lett.* **1994**, *352* (1), 54–57.

(6) Wongsrichanalai, C.; Pickard, A. L.; Wernsdorfer, W. H.; Meshnick, S. R. Epidemiology of Drug-Resistant Malaria. *Lancet Infect. Dis.* **2002**, *2* (4), 209–218.

(7) de Villiers, K. A.; Marques, H. M.; Egan, T. J. The Crystal Structure of Halofantrine–Ferriprotoporphyrin IX and the Mechanism of Action of Arylmethanol Antimalarials. *J. Inorg. Biochem.* **2008**, *102* (8), 1660–1667.

(8) de Villiers, K. A.; Gildenhuys, J.; Roux, Le, T. Iron(III) Protoporphyrin IX Complexes of the Antimalarial Cinchona Alkaloids Quinine and Quinidine. *ACS Chem. Biol.* **2012**, *7* (4), 666–671.

(9) Gildenhuys, J.; Sammy, C. J.; Müller, R.; Streltsov, V. A.; le Roex, T.; Kuter, D.; de Villiers, K. A. Alkoxide Coordination of Iron Protoporphyrin IX by Antimalarial Quinoline Methanols: A Key Interaction Observed in the Solid-State and Solution. *Dalt. Trans.* **2015**, *44* (38), 16767–16777.

(10) Buller, R.; Peterson, M. L.; Almarsson, Ö.; Leiserowitz, L. Quinoline Binding Site on Malaria Pigment Crystal: A Rational Pathway for Antimalaria Drug Design. *Cryst. Growth Des.* **2002**, *2* (6), 553–562.

(11) Solomonov, I.; Osipova, M.; Feldman, Y.; Baehtz, C.; Kjaer, K.; Robinson, I. K.; Webster, G. T.; McNaughton, D.; Wood, B. R.; Weissbuch, I.; Leiserowitz, L. Crystal Nucleation, Growth, and Morphology of the Synthetic Malaria Pigment β-Hematin and the Effect Thereon by Quinoline Additives: The Malaria Pigment as a Target of Various Antimalarial Drugs. *J. Am. Chem. Soc.* **2007**, *129* (9), 2615–2627.

(12) L'abbate, F. P.; Müller, R.; Openshaw, R.; Combrinck, J. M.; de Villiers, K. A.; Hunter, R.; Egan, T. J. Hemozoin Inhibiting 2-Phenylbenzimidazoles Active against Malaria Parasites. *Eur. J. Med. Chem.* **2018**, *159*, 243–254.

(13) Pagola, S.; Stephens, P. W.; Bohle, D. S.; Kosar, A. D.; Madsen, S. K. The Structure of Malaria Pigment β-Haematin. *Nature* **2000**, *404* (6775), 307–310.

(14) Chinappi, M.; Via, A.; Marcatili, P.; Tramontano, A. On the Mechanism of Chloroquine Resistance in Plasmodium Falciparum. *PLoS One* **2010**, *5* (11), e14064.

(15) Singh, K.; Okombo, J.; Brunschwig, C.; Ndubi, F.; Barnard, L.; Wilkinson, C.; Njogu, P. M.; Njoroge, M.; Laing, L.; Machado, M.; Prudêncio, M.; Reader, J.; Botha, M.; Nondaba, S.; Birkholtz, L.-M.; Lauterbach, S.; Churchyard, A.; Coetzer, T. L.; Burrows, J. N.; Yeates, C.; Denti, P.; Wiesner, L.; Egan, T. J.; Wittlin, S.; Chibale, K. Antimalarial Pyrido[1,2- a]Benzimidazoles: Lead Optimization, Parasite Life Cycle Stage Profile, Mechanistic Evaluation, Killing Kinetics, and in Vivo Oral Efficacy in a Mouse Model. *J. Med. Chem.* **2017**, *60* (4), 1432–1448.

(16) Wissing, F.; Sanchez, C. P.; Rohrbach, P.; Ricken, S.; Lanzer, M. Illumination of the Malaria Parasite Plasmodium Falciparum Alters Intracellular PH. *J. Biol. Chem.* **2002**, *277* (40), 37747–37755.

(17) van Schalkwyk, D. A.; Saliba, K. J.; Biagini, G. A.; Bray, P. G.; Kirk, K. Loss of PH Control in Plasmodium Falciparum Parasites Subjected to Oxidative Stress. *PLoS One* **2013**, *8* (3), e58933.

(18) Lanzer, M.; Rohrbach, P. Subcellular PH, and Ca^{2+} in Plasmodium Falciparum: Implications for Understanding Drug Resistance Mechanisms. *Curr. Sci.* **2007**, *92* (11), 1561–1570.

(19) Abramov, A. Y.; Smulders-Srinivasan, T. K.; Kirby, D. M.; Acin-Perez, R.; Enriquez,

J. A.; Lightowlers, R. N.; Duchen, M. R.; Turnbull, D. M. Mechanism of Neurodegeneration of Neurons with Mitochondrial DNA Mutations. *Brain* **2010**, *133* (3), 797–807.

(20) Rubio, F. J.; Liu, Q.-R.; Li, X.; Cruz, F. C.; Leao, R. M.; Warren, B. L.; Kambhampati, S.; Babin, K. R.; McPherson, K. B.; Cimbro, R.; Bossert, J. M.; Shaham, Y.; Hope, B. T. Context-Induced Reinstatement of Methamphetamine Seeking Is Associated with Unique Molecular Alterations in Fos-Expressing Dorsolateral Striatum Neurons. *J. Neurosci.* **2015**, *35* (14), 5625–5639.

(21) Csiszar, A.; Labinskyy, N.; Pinto, J. T.; Ballabh, P.; Zhang, H.; Losonczy, G.; Pearson, K.; de Cabo, R.; Pacher, P.; Zhang, C.; Ungvari, Z. Resveratrol Induces Mitochondrial Biogenesis in Endothelial Cells. *Am. J. Physiol. Circ. Physiol.* **2009**, *297* (1), H13–H20.

(22) Poot, M.; Zhang, Y. Z.; Krämer, J. A.; Wells, K. S.; Jones, L. J.; Hanzel, D. K.; Lugade, A. G.; Singer, V. L.; Haugland, R. P. Analysis of Mitochondrial Morphology and Function with Novel Fixable Fluorescent Stains. *J. Histochem. Cytochem.* **1996**, *44* (12), 1363–1372.

(23) Presley, A. D.; Fuller, K. M.; Arriaga, E. A. MitoTracker Green Labeling of Mitochondrial Proteins and Their Subsequent Analysis by Capillary Electrophoresis with Laser-Induced Fluorescence Detection. *J. Chromatogr. B* **2003**, *793* (1), 141–150.

(24) Griffiths, G.; Hoflack, B.; Simons, K.; Mellman, I.; Kornfeld, S. The Mannose 6-Phosphate Receptor and the Biogenesis of Lysosomes. *Cell* **1988**, *52* (3), 329–341.

(25) Lagunoff, D. Lysosomes in Biology and Pathology. *JAMA J. Am. Med. Assoc.* **1974**, *227* (3), 331.

(26) Spence Johnson, Iain D., M. T. Z. *The Molecular Probes Handbook : A Guide to Fluorescent Probes and Labeling Technologies*; Life Technologies Corporation: [Carlsbad, CA], 2010.

(27) Bohórquez, E. B.; Chua, M.; Meshnick, S. R. Quinine Localizes to a Non-Acidic Compartment within the Food Vacuole of the Malaria Parasite *Plasmodium*

falciparum. *Malar. J.* **2012**, *11* (1), 350.

(28) Gerdes, H.-H.; Rudolf, R. Green Light for the Secretory Pathway. *Protoplasma* **1999**, *209* (1–2), 1–8.

(29) Gratraud, P.; Huws, E.; Falkard, B.; Adjalley, S.; Fidock, D. A.; Berry, L.; Jacobs, W. R.; Baird, M. S.; Vial, H.; Kremer, L. Oleic Acid Biosynthesis in Plasmodium Falciparum: Characterization of the Stearoyl-CoA Desaturase and Investigation as a Potential Therapeutic Target. *PLoS One* **2009**, *4* (9), e6889.

(30) Gocze, P. M.; Freeman, D. A. Factors Underlying the Variability of Lipid Droplet Fluorescence in MA-10 Leydig Tumor Cells. *Cytometry* **1994**, *17* (2), 151–158.

(31) Johnson, M. E.; Berk, D. A.; Blankschtein, D.; Golan, D. E.; Jain, R. K.; Langer, R. S. Lateral Diffusion of Small Compounds in Human Stratum Corneum and Model Lipid Bilayer Systems. *Biophys. J.* **1996**, *71* (5), 2656–2668.

(32) Song, S.; Lee, K. Y. Polymers for Microfluidic Chips. *Macromol. Res.* **2006**, *14* (2), 121–128.

(33) Hasan, M. T.; Chang, C. C. Y.; Chang, T. Y. Somatic Cell Genetic and Biochemical Characterization of Cell Lines Resulting from Human Genomic DNA Transfections of Chinese Hamster Ovary Cell Mutants Defective in Sterol-Dependent Activation of Sterol Synthesis and LDL Receptor Expression. *Somat. Cell Mol. Genet.* **1994**, *20* (3), 183–194.

(34) Woestenborghs, R.; Lorreyne, W.; Heykants, J. Determination of Itraconazole in Plasma and Animal Tissues by High-Performance Liquid Chromatography. *J. Chromatogr. B Biomed. Sci. Appl.* **1987**, *413*, 332–337.

(35) Brown, W. J.; Sullivan, T. R.; Greenspan, P. Nile Red Staining of Lysosomal Phospholipid Inclusions. *Histochemistry* **1992**, *97* (4), 349–354.

(36) Fitch, C. D.; Chevli, R.; Banyal, H. S.; Phillips, G.; Pfaller, M. A.; Krogstad, D. J. Lysis of Plasmodium Falciparum by Ferriprotoporphyrin IX and a Chloroquine-Ferriprotoporphyrin IX Complex. *Antimicrob. Agents Chemother.* **1982**, *21* (5), 819–822.

(37) Chou, A. C.; Fitch, C. D. Mechanism of Hemolysis Induced by Ferriprotoporphyrin IX. *J. Clin. Invest.* **1981**, *68* (3), 672–677.

(38) Ch'ng, J.-H.; Kotturi, S. R.; Chong, A. G.-L.; Lear, M. J.; Tan, K. S.-W. A Programmed Cell Death Pathway in the Malaria Parasite Plasmodium Falciparum Has General Features of Mammalian Apoptosis but Is Mediated by Clan CA Cysteine Proteases. *Cell Death Dis.* **2010**, *1* (2), e26–e26.

(39) Ch'ng, J.-H.; Liew, K.; Goh, A. S.-P.; Sidhartha, E.; Tan, K. S.-W. Drug-Induced Permeabilization of Parasite's Digestive Vacuole Is a Key Trigger of Programmed Cell Death in Plasmodium Falciparum. *Cell Death Dis.* **2011**, *2* (10), e216–e216.

(40) Melhuish, W. H. Quantum Efficiencies of Fluorescence of Organic Substan Ces: Effect of Solvent and Concentration of the Fluorescent Solute. *J. Phys. Chem.* **1961**, *65* (2), 229–235.

(41) Fitch, C. D.; Cai, G.; Chen, Y.-F.; Shoemaker, J. D. Involvement of Lipids in Ferriprotoporphyrin IX Polymerization in Malaria. *Biochim. Biophys. Acta - Mol. Basis Dis.* **1999**, *1454* (1), 31–37.

(42) Pisciotta, J. M.; Coppens, I.; Tripathi, A. K.; Scholl, P. F.; Shuman, J.; Bajad, S.; Shulaev, V.; Sullivan, D. J. The Role of Neutral Lipid Nanospheres in Plasmodium Falciparum Haem Crystallization. *Biochem. J.* **2007**, *402* (1), 197–204.

(43) Bolte, S.; Cordelières, F. P. A Guided Tour into Subcellular Colocalization Analysis in Light Microscopy. *J. Microsc.* **2006**, *224* (3), 213–232.

(44) Manders, E. M. M.; Verbeek, F. J.; Aten, J. A. Measurement of Co-localization of Objects in Dual-colour Confocal Images. *J. Microsc.* **1993**, *169* (3), 375–382.

(45) Manders, E. M.; Stap, J.; Brakenhoff, G. J.; van Driel, R.; Aten, J. A. Dynamics of Three-Dimensional Replication Patterns during the S-Phase, Analysed by Double Labelling of DNA and Confocal Microscopy. *J. Cell Sci.* **1992**, *103* (3), 857–862.

(46) Costes, S. V.; Daelemans, D.; Cho, E. H.; Dobbin, Z.; Pavlakis, G.; Lockett, S. Automatic and Quantitative Measurement of Protein-Protein Colocalization in Live Cells. *Biophys. J.* **2004**, *86* (6), 3993–4003.

(47) Combrinck, J. M.; Fong, K. Y.; Gibhard, L.; Smith, P. J.; Wright, D. W.; Egan, T. J. Optimization of a Multi-Well Colorimetric Assay to Determine Haem Species in Plasmodium Falciparum in the Presence of Anti-Malarials. *Malar. J.* **2015**, *14* (1), 253.

(48) Combrinck, J. M.; Fong, K. Y.; Gibhard, L.; Smith, P. J.; Wright, D. W.; Egan, T. J. Optimization of a Multi-Well Colorimetric Assay to Determine Haem Species in Plasmodium Falciparum in the Presence of Anti-Malarials. *Malar. J.* **2015**, *14* (1), 253.

(49) Fong, K. Y.; Wright, D. W. Hemozoin and Antimalarial Drug Discovery. *Future Med. Chem.* **2013**, *5* (12), 1437–1450.

(50) Purfield, A. E.; Tidwell, R. R.; Meshnick, S. R. The Diamidine DB75 Targets the Nucleus of *Plasmodium falciparum*. *Malar. J.* **2009**, *8* (1), 104.

(51) Woodland, J. G. Nsights into the Mechanism of Action of Quinoline Antimalarials against *Plasmodium falciparum* Revealed by Novel Fluorescent Analogues and Chemical Proteomics, University of Cape Town.

Chapter Five

Genomic Approaches to Target Deconvolution and Elucidation of Mechanism of Resistance of PBIs

5.1. Chapter Overview

It has been almost two decades since the first reference genome assemblies were published for the most virulent species of the *Plasmodium* genus, *P. falciparum*.[1–3] Since then, reference genomic data has been reported for all human-infecting malaria parasites.[4,5] The availability of sequenced reference genomes has aided in advancing our understanding of the disease biology, MOA of drugs candidates and the mode of parasite resistance to available drugs and drug leads. *Plasmodium* species that affect humans possess close-packed genomes of about 23-24 Mb.[6] In *P. falciparum*, this genome encodes about 5400 protein-coding genes together with a varying number of subtelomeric multigene families stretching across 14 chromosomes.[6] These genomics data have facilitated the identification of genes implicated in the various parasite traits, specifically those related to antimalarial drug responses. Genetics and genomics tools have also been employed to study other parasitic processes such as intracellular protein trafficking and red blood cell egress and invasion.[7–10] Whole-genome sequencing approaches such as genome-wide association studies, experimental genetic crosses and *in vitro* resistance selections constitute powerful genome-based techniques to deconvolute the genetic determinants of parasite resistance to antimalarial drug leads thereby inferring relevant information on their action (s).[6] While all these techniques are valuable in studying the genome of the parasite, *in vitro* resistance selections followed by whole-genome sequencing is particularly relevant in predicting the determinants of resistance at a low cost.

This chapter describes the use of resistance selection techniques to determine the mechanism of resistance (MoR) and potential target (s) of the compounds under study. Resistant mutant selection, followed by whole-genome sequencing raised parasite mutant strains that are resistant to **KP68** and identified genes that might be implicated in the parasite's resistance to the compound. Cross resistance studies between the **KP68**-mutant line and **KP124,** as well as further profiling of both compounds against over 40

barcoded parasite lines covering a range of resistance mechanisms and targets, provided important insights into the action of the target compounds.

5.2. Key Concepts of Relevance to *In Vitro* Resistance Selection

Following the development of an *in vitro* system for continuous culture of *P. falciparum by* Trager and Jenson in 1979,[11] the parasite has remained amenable to long term culture. The success of this development aided Nguyen-Dinh and Trager to perform what is now known as the first insight into how resistance selection could be performed *in vitro* using the Petri dish method. Key concepts such as fitness cost of the parasite, resistance selection frequency and accelerated resistance to multiple drugs phenomenon are pertinent to *in vitro* resistance selection and must be discussed.[12]

5.2.1. Resistance-Associated Fitness Cost of the Parasite

There are several physiological changes associated with parasite mutations under drug pressure. Parasite resistance to antimalarial chemotypes is generally achieved by the alteration of gene expression, mostly in transporters and by mutations that change the structure protein targets.[13] Consequently, in response to these physiological changes there is a general reduction in the fitness of parasite lines carrying mutations due to natural selection.[13] Fitness is measured *in vitro* by comparing the growth rates of resistant and sensitive strains at a given ratio in competitive growth experiments.[14,15] The spread of resistance to known antimalarials on the market from Asia to Africa have been strongly linked to the cost of fitness. For example, parasite resistance to antimalarial drugs on the market tend to originate from Southeast Asia, where malaria transmissions are relatively low, and patients have reduced immunity to the disease.[16] However, in areas of high malaria transmission, such as the WHO African region, where people are sometimes co-infected with up to seven genetically different parasite clones, a greater natural selection pressure results in the propensity of the less fit parasites to be outcompeted by sensitive strains.[17]

The scenario of CQ resistance better describes the impact of fitness on resistance. In the 1980s the first-line treatment of malaria was changed from CQ to sulfadoxine-pyrimethamine due to the worldwide prevalence of the CQ resistance strains of *P. falciparum*. Following the withdrawal of CQ from many countries, several field isolates

were screened for the K76T mutation in P*f*CRT.[15] The removal of CQ as selection pressure aided in the re-emergence of the of CQS strains of the parasite, thereby demonstrating the fitness advantage of CQS over resistant strains.[15] In the case of mefloquine, parasite resistance to the drug has been attributed to a higher copy number variation (CNV) of *pfmdr1*, resulting in a decreased susceptibility of the parasite to mefloquine and a higher fitness cost.[18] Indeed, the deamplification of the *pfmdr1* gene has been shown to increase *P. falciparum's* sensitivity to mefloquine.[19] However, in the absence of mefloquine drug pressure, parasites with multiple copies of *pfmdr1* were outcompeted by those with a single copy of *pfmdr1*.[18] Evidently, fitness cost plays an essential role in the spread of parasites resistant to antimalarials.

5.2.2. Frequency of Resistance Selection

Most often, resistance to clinically approved antimalarials takes about 10-15 years to develop after a drug has been introduced onto the market.[16] For example, resistance to CQ emerged 12 years after it had been introduced into the clinic.[20] However, in some cases the parasite develops resistance to some drugs within the same year they were introduced into the clinic such as was seen for atovaquone and antifolates.[21–23] This can be primarily due to the difference in the resistance selection frequencies of the antimalarials. Mutant parasites can be selected either by *in vivo* or *in vitro* application of drug pressure.[24] However, spontaneous mutations or naturally occurring resistance does occur, which is independent of drug treatment and is facilitated solely by the background mutation rate of the parasite.[25–27]

The ease with which parasite mutants are generated for a drug candidate *in vitro* in the laboratory can, in some cases, predict how fast resistance will emerge in the clinic.[28] Among the current clinically approved antimalarial drugs, atovaquone has the highest frequency of naturally occurring resistance, measured *in vitro*.[25] The compound has since been used as a standard to compare the frequency of spontaneous resistance through the minimum inoculum for resistance (MIR) studies.[17] MIR studies indirectly measure the potential of a resistant genotype to occur and be selected for, *in vitro*.[29] Experiments that measure the MIR should be considered when progressing antimalarial compounds or compound series through selection criteria.

5.2.3. Accelerated Resistance to Multiple Drugs (ARMD) Phenomenon

The accelerated resistance to multiple drugs (ARMD) phenomenon is described as the higher ability of Asian parasite clones to develop resistance *in vitro*. Repeatedly, resistance to newly introduced antimalarial drugs has been reported to originate from the Thai-Cambodian border.[25] In comparison to other resistant strains, ARMD strains can develop resistance to antimalarial drugs at an increased rate. While the exact mechanism of this is still unknown, it has been hypothesized that this resistant phenotype is because of a defective DNA repair system.[30,31]

Some parasite strains such as Dd2, a clone from the multidrug resistant parent W2 strain,[30] suffer a more extensive loss of repair mechanism than others. In ARMD, spontaneous mutations occur at a rate of 10^{-6},[30] implying that a parasite population of 10^{8} will with certainty include resistance cells. For this reason, the Dd2 strain is ideal for the *in vitro* mutant selection with practical limits of culture volumes.

5.3. In Vitro Resistance Selection and Whole-Genome Sequencing

In vitro drug selection followed by whole-genome sequencing (WGS) of parasite clones, takes advantage of the genomic data available on the *Plasmodium* parasite to identify the genetic determinants underlying antimalarial drug resistance.[32] Information on the genetics of antimalarial resistance is important in a bid to monitor the emergence and spread of parasite resistance to drugs through molecular surveillance efforts. Such knowledge also provides insight into developing therapeutic strategies to overcome or delay resistance in the clinic. Drug discovery also benefits from the timely identification of genetic determinants underlying the resistance to lead compounds in the pipeline to assess the resistance liabilities or MoR of the compounds before further progression. Finally, the MoR can in some instances, correlate with the MOA and the molecular targets(s) of antiplasmodium compounds.[32]

Previous reports show that, to simulate parasite mutations that occur in the clinic following drug pressure as well as to investigate the MoR of the compounds under study and subsequently their MOA, parasites were pressured with sublethal doses of drugs, enriching for recrudescent parasites that have mutated to survive drug pressure.[33–35] *In*

vitro resistance selection experiments can be performed in a single step, stepwise or pulse manner.

5.3.1. Single-Step, Stepwise and Pulse Manner Selection of Mutants

There are well established techniques for evolving resistant parasites *in vitro* although there is yet to be a standardized protocol between various laboratories.[17,25] The most used techniques are the single-step and stepwise selection of mutants. In some cases, the pulse method is applied. In single-step selections, large numbers of parasites are pressured at a single drug concentration throughout the experiment, usually about 3-5x IC_{50} of the drug evaluated. The IC_{50} is calculated as the concentration which induces half-maximal growth inhibition of parasite growth dosed with the drug at either 48 or 72 h. The single-step method is useful in raising resistant mutants quickly, usually within 60 days and the mutants generated by this method provide useful insight into the mechanism of resistance and drug target deconvolution studies. However, this technique is laborious and requires handling enormous amounts of bulk culture at a time, typically multiple flasks of 100-200 mL each. It is also material intensive necessitating the use of massive quantities of red blood cells and culture media.

An alternative to single-step selection is the stepwise method. Here, parasite materials are incubated with the drug of interest at a starting concentration of 1x IC_{50} with the concentration of the drug exposure being increased over time. The incremental exposure of drug pressure may lead to the selection of resistant mutants over time. In the stepwise selections, parasites must be observed closely, and the selection process can be lengthy, spanning over several months of continuous culture. Finally, in cases where resistant mutants could not be raised with either the single step or stepwise method, the pulse method is applied. In this method, parasites are exposed to the drug for 1-2 days, followed by a drug wash off, after which the parasites are left to recover. Upon successful selection, resistant mutants are cloned by limiting dilution and resistance is confirmed by comparing the IC_{50} shift between the mutant line and parent parasite line. Genes implicated in parasite resistance to the drug under study are identified by WGS or Sanger sequencing in the case of known candidates. *P. falciparum* genetic manipulation tools such as the zinc-finger nucleases or clustered regularly interspaced short palindromic repeats (CRISPR) or

CRISPR-associated gene 9 (Cas9) are used to validate the role of the mutated genes in the resistance phenotype observed.[36]

5.4. *In Vitro* Selection of KP68-Resistance Mutants

As earlier described, **KP68** was identified from a phenotypic screen as a whole cell active antimalarial lead, with potency against both drug sensitive and multidrug resistant strains of *P. falciparum*. The focus of this work, as stated in the first chapter, is to pull together information from orthogonal approaches such as fluorescent localization, proteomics, and genomics studies to increase the possibility of successfully defining the MOA of **KP68**, **KP124** and **DM253** and more importantly identifying their molecular target.

The selection of **KP68** performed according to the procedure summarized in Figure 5.1 Two flasks each containing 2 x 10^9 Dd2 parasites were cultured under 5x IC_{50} of **KP68** (300 nM). Parasites appeared to die slowly and form gametocytes but all healthy trophozoites and rings were cleared by day 12. Recrudescence was observed on day 42 in one flask only. No parasites recrudesced in the other flasks.

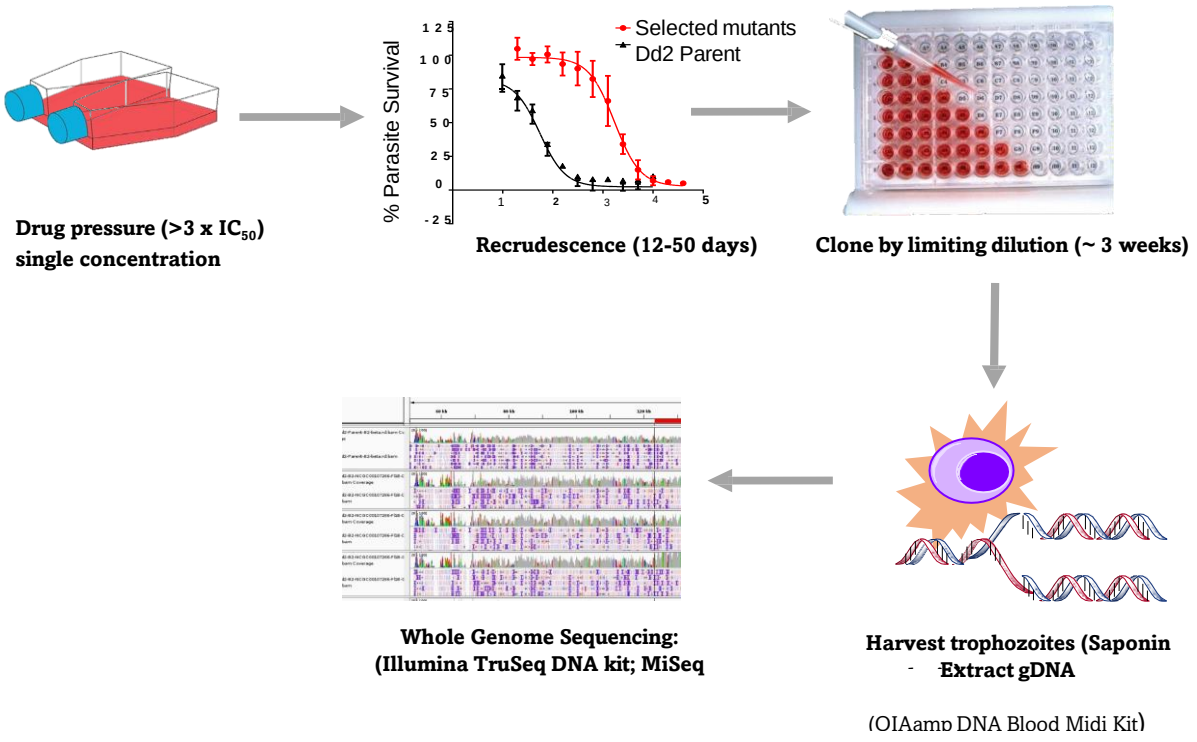

Figure 5.1. Single-step strategy for the selection of **KP68**-resistance mutants

KP68 was tested against the recrudesced bulk mutants and the parent Dd2 to confirm mutants were successfully raised. A growth inhibition assay was performed by incubating parasites for 72 h and 37 °C across a range of drug concentrations with two-fold dilutions in 96-well plates, at 0.2 - 0.4% starting parasitemia and 1% hematocrit. Parasite growth in each well was assessed on an Accuri C6 flow cytometer after staining with 100 nM MitoTracker Deep Red and 1x SYBR green in 1x phosphate-buffered saline (PBS pH 7.4) and incubating at 37 °C for at least 20 min in the dark. The IC_{50} values were determined by non-linear regression in the case of normal dose response curves and by linear extrapolation for those with biphasic curves. The bulk mutants showed a 4x IC_{50} (*Pf* Dd2 IC_{50} = 158 nM) shift compared to the Dd2 parental line, although both lines displayed signs of a biphasic dose response curve. (Figure 5.2)

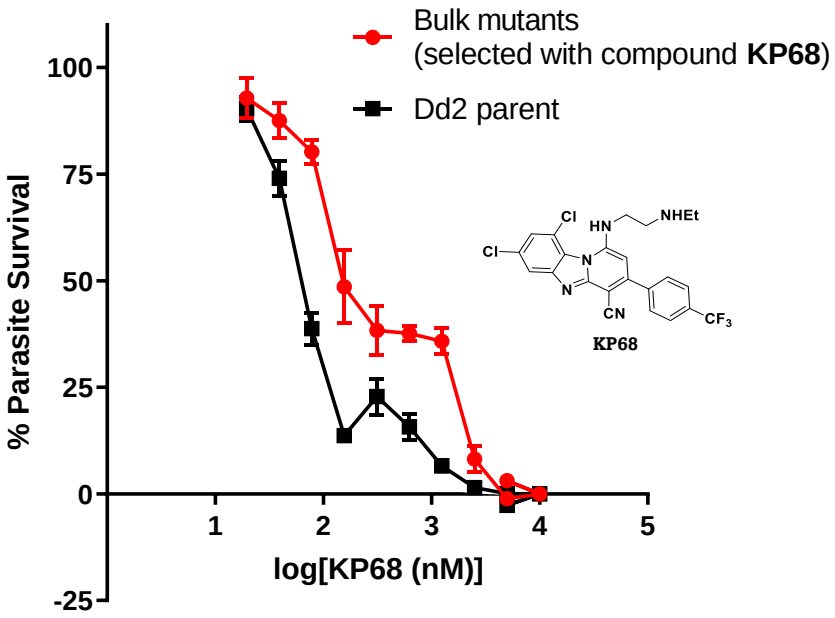

Figure 5.2. Cross-resistance between the **KP68**-resistant selected bulk mutants compared with the Dd2 parental line. Error bars represent the standard error of the mean (SEM) over 3 independent repeats with two or three technical replicates (N, n = 3, 2-3).

5.4.1. Generating KP68-Mutant Clones by Limiting Dilution

Dilution cloning, also known as cloning by limiting dilution is a method used to obtain a monoclonal cell population from a polyclonal mass of cells. This method has become a standard means of cloning *P. falciparum* isolates *in vitro*.[37] It involves the culture of bulk mutant culture in a 96-well microtiter plate at dilutions that are below one parasite per

well. To achieve this, a series of increasing dilutions of the bulk parent culture is undertaken and at the right dilution, individual clones grow in a single well.[38] The **KP68**-recrudesced bulk mutants were cloned by limiting dilution and the individual clones were profiled (Figure 5.3). Clones showed a range of IC_{50} shifts from 0.6-5x IC_{50} and all showed more pronounced biphasic dose responses compared to the Dd2 parent. Three clones with diverse profiles were selected for sequencing (A7, E10 and H9), whereby parasitized RBCs were lysed with saponin to harvest the trophozoites and their gDNA extracted with the QIAamp DNA Blood Midi Kit.

Clone	IC_{50} (nM)	IC_{50} fold shift	Whole genome sequencing
A7	**37**	**0.6x**	**Yes**
E5	104	1.7x	
E10	**315**	**5x**	**Yes**
H9	**ND**	**ND**	**Yes**

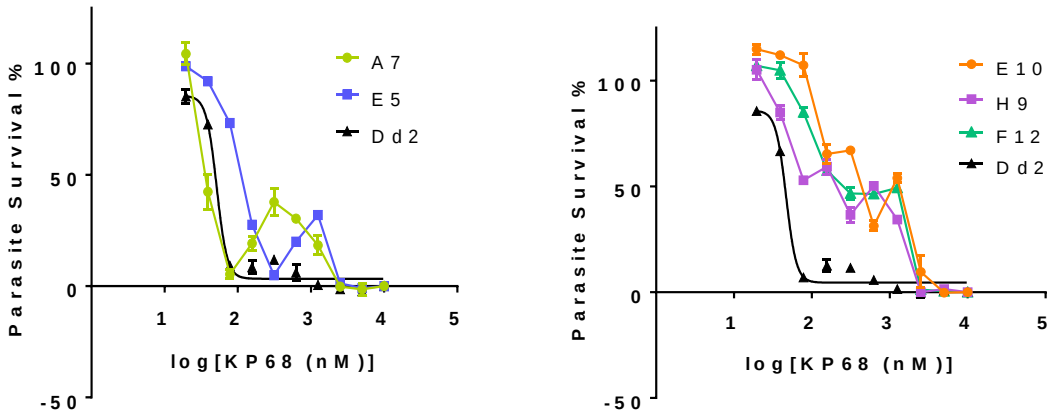

Figure 5.3. Profiles of the selected clones from the **KP68** resistance selection, measured just prior to saponin lysis. Clones A7, E10 and H9 were harvested and sequenced. Error bars represent the standard deviation for the assay where N,n = 1,2).

5.4.2. Illumina-Based Whole Genome Sequencing of KP68-Mutant Clones

Illumina-based whole-genome sequencing revealed a single nucleotide polymorphism (SNP) stop codon E28* (Gaa to Taa) in the mitochondrial carrier protein (putative) on

chromosome Pf3D7_09_v3 in all three clones (Table 5.1). Furthermore, copy number variations (CNVs) were observed, including a deamplification of the mitochondrial-processing peptidase on chromosome 5, next to the *P. falciparum* multidrug resistance protein 1 (P*f*MDR1) as well as the deamplification of the P*f*MDR1 itself. Clones E10 and H9 contained similar CNVs to each other while A7 only showed CNVs in a subset of these genes (see Table 5.1). For example, a variation in the copy number of an ABC transporter I family member (known as ABCI1) was identified in clones E10 and H9 but not in A7. This might be because A7 was less resistant than the other two clones (Figure 5.3).

The SNP observed in the mitochondrial carrier protein (MCP) in all three clones implicates them in the action of **KP68.** This is compounded by the fact that the parasite mitochondrion was earlier shown to be a site of accumulation of the drug. A significant amount of the **KP68** was seen around what appears to be a membrane enveloping the mitochondrion as discussed in Chapter 4. The parasite's mitochondrion has long been suggested as a potential drug target in the discovery of antimalarial drugs. Parasite metabolic processes such as the citric acid cycle and the urea cycle all take place in the mitochondrion and some antimalarial drugs in the clinic, including atovaquone, have been shown to act on the parasite's mitochondrion.[39,40] The mitochondrion carriers are made up of a family of inner membrane transporters and are responsible for the effective translocation of essential metabolites across the inner membrane of the mitochondrion. MCPs are essential for parasitic function and are a potential drug target.[41]

To assess the role of the E28* stop codon on the resistance phenotype for representative clones A7 and E10, the lines were assessed for their degree of resistance while cultured on or off drug pressure. Since SNPs are more stable than CNVs in the culture, a lack of drug pressure can influence the CNVs faster than influencing the SNPs. The two cultures were profiled against **KP68** while being cultured with and without 300nM **KP68** (5 x Dd2 IC_{50}). Polymerase chain reaction (PCR) amplification was carried out on the mitochondrial carrier protein (MCP) to confirm the presence of the stop codon E28* in both clones whilst culturing without drug pressure. A difference in the resistance phenotype was observed between those cultured on and off drug pressure (Figure 5.4) revealing the instability of this phenotype and the influence of the CNVs on the degree of resistance. This result suggests that the SNP stop codon in the MCP is not the sole driver of resistance. Instead,

the several CNVs observed, including an interesting deamplification of a mitochondrial-processing peptidase, the deamplification of the P*f*MDR1 and the ABC transporter family member 1 could contribute to the mediation of drug resistance and may play a role in the MOA of **KP68**

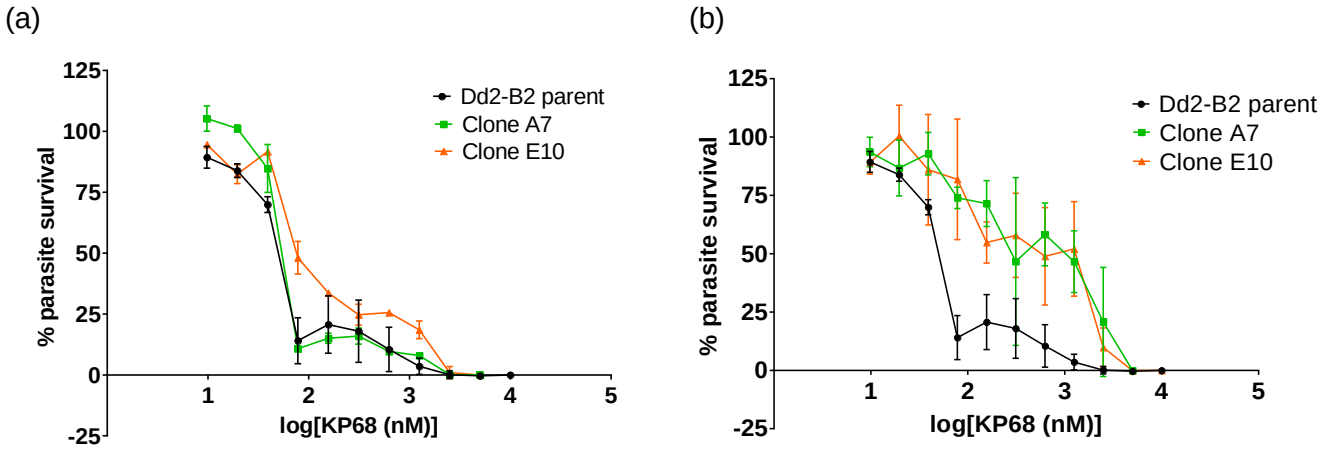

Figure 5.4. Dose-response profiles of **KP68**-selected mutant clones A7 (green) and E10 (orange) relative to the Dd2 parental line (black) against **KP68,** while culturing (a) in the absence of drug pressure or (b) in the presence of 300 nM **KP68**. Error bars represent the standard deviation of the mean where N, n = 2, 2.

Previously, polymorphisms in the P*f*MDR1 gene, encoding for a trans-membrane homologue of PGH1 protein was implicated in multidrug resistance to *P. falciparum*. Amodiaquine, lumefantrine, mefloquine and chloroquine have been affected by the SNP in P*f*MDR1.[42,43] Aside from P*f*MDR1, several other ABC transporters are encoded in the *Plasmodium* genome including the ABCI1 and a similar *P. falciparum* transporter ABCI3 which has recently been found to confer a parasite strain-dependent pleiotropic antimalarial drug resistance of some chemically diverse antimalarial compounds.[44] CNVs observed in other genes in the mitochondrion such as the mitochondrial-processing peptidase subunit alpha, putative and the 50S ribosomal protein reiterate the significance of the parasite's mitochondrion in the action of **KP68**.

Table 5. 1. Results of the whole-genome sequencing for **KP68**-resistant clones

SNPs:

CHROM	POS	REF	ALT	mutation in	EFFECT	IMPACT	AMINO_ACID_CHANGE	CODON_CHANGE	EXON_ID	GENE_NAME	description
Pf3D7_09_v3	404393	G	T	FI2-A7, FI2-E10, FI2-H9	STOP_GAINED	HIGH	E28*	Gaa/Taa	1	PF3D7_0908800	mitochondrial carrier protein, putative

CNVs: Factors indicate amplification or deamplification of the designated gene, in absolute numbers. NA represents no change in the amplification relative to Dd2.

gid	chr	annotation	count	FI2-A7.factor	FI2-E10.factor	FI2-H9.factor	mean.factor
PF3D7_0318100	Pf3D7_03_v3	stomatin-like protein	2	NA	2.026232885	2.050392348	2.038312617
PF3D7_0318200	Pf3D7_03_v3	DNA-directed RNA polymerase II subunit RPB1	2	NA	2.026232885	2.050392348	2.038312617
PF3D7_0318300	Pf3D7_03_v3	conserved Plasmodium protein, unknown function	2	NA	2.026232885	2.050392348	2.038312617
PF3D7_0318400	Pf3D7_03_v3	conserved Plasmodium protein, unknown function	2	NA	2.026232885	2.050392348	2.038312617
PF3D7_0318500	Pf3D7_03_v3	conserved Plasmodium protein, unknown function	2	NA	2.026232885	2.050392348	2.038312617
PF3D7_0318600	Pf3D7_03_v3	cleavage and polyadenylation specificity factor, putative	2	NA	2.026232885	2.050392348	2.038312617
PF3D7_0318700	Pf3D7_03_v3	conserved Plasmodium protein, unknown function	2	NA	2.026232885	2.050392348	2.038312617
PF3D7_0318800	Pf3D7_03_v3	triosephosphate isomerase, putative	2	NA	2.026232885	2.050392348	2.038312617
PF3D7_0318900	Pf3D7_03_v3	conserved protein, unknown function	2	NA	2.026232885	2.050392348	2.038312617
PF3D7_0319000	Pf3D7_03_v3	P-type ATPase, putative	2	NA	2.026232885	2.050392348	2.038312617
PF3D7_0319100	Pf3D7_03_v3	E3 ubiquitin-protein ligase RBX1, putative	2	NA	2.026232885	2.050392348	2.038312617
PF3D7_0319200	Pf3D7_03_v3	endonuclease/exonuclease/phosphatase family protein, putative	2	NA	2.026232885	2.050392348	2.038312617
PF3D7_0319300	Pf3D7_03_v3	ubiquitin-conjugating enzyme E2, putative	2	NA	2.026232885	2.050392348	2.038312617
PF3D7_0319400	Pf3D7_03_v3	kinesin-8, putative	2	NA	2.026232885	2.050392348	2.038312617
PF3D7_0319500	Pf3D7_03_v3	RNA-binding protein, putative	2	NA	2.026232885	2.050392348	2.038312617
PF3D7_0319600	Pf3D7_03_v3	elongation factor 1-delta, putative	2	NA	2.026232885	2.050392348	2.038312617
PF3D7_0319700	Pf3D7_03_v3	ABC transporter I family member 1, putative	2	NA	2.026232885	2.050392348	2.038312617
PF3D7_0319800	Pf3D7_03_v3	conserved Plasmodium protein, unknown function	2	NA	2.026232885	2.050392348	2.038312617
PF3D7_0319900	Pf3D7_03_v3	conserved Plasmodium protein, unknown function	2	NA	2.026232885	2.050392348	2.038312617
PF3D7_0521900	Pf3D7_05_v3	conserved Plasmodium protein, unknown function	3	-1.998475657	-1.984946331	-1.987699959	-1.990373982
PF3D7_0522000	Pf3D7_05_v3	conserved Plasmodium protein, unknown function	3	-1.998475657	-1.984946331	-1.987699959	-1.990373982
PF3D7_0522100	Pf3D7_05_v3	conserved Plasmodium protein, unknown function	3	-1.998475657	-1.984946331	-1.987699959	-1.990373982
PF3D7_0522200	Pf3D7_05_v3	transcription initiation factor TFIID subunit 10, putative	3	-1.998475657	-1.984946331	-1.987699959	-1.990373982
PF3D7_0522300	Pf3D7_05_v3	18S rRNA (guanine-N(7))-methyltransferase, putative	3	-1.998475657	-1.984946331	-1.987699959	-1.990373982
PF3D7_0522400	Pf3D7_05_v3	conserved Plasmodium protein, unknown function	3	-1.998475657	-1.984946331	-1.987699959	-1.990373982
PF3D7_0522500	Pf3D7_05_v3	50S ribosomal protein L17, apicoplast, putative	3	-1.998475657	-1.984946331	-1.987699959	-1.990373982
PF3D7_0522600	Pf3D7_05_v3	inner membrane complex protein	3	-1.998475657	-1.984946331	-1.987699959	-1.990373982
PF3D7_0522700	Pf3D7_05_v3	iron-sulfur assembly protein	3	-1.998475657	-1.984946331	-1.987699959	-1.990373982
PF3D7_0522800	Pf3D7_05_v3	pre-mRNA-splicing factor BUD31, putative	3	-1.998475657	-1.984946331	-1.987699959	-1.990373982
PF3D7_0522900	Pf3D7_05_v3	zinc finger protein, putative	3	-1.998475657	-1.984946331	-1.987699959	-1.990373982
PF3D7_0523000	Pf3D7_05_v3	multidrug resistance protein 1	3	-1.998475657	-1.984946331	-1.987699959	-1.990373982
PF3D7_0523100	Pf3D7_05_v3	mitochondrial-processing peptidase subunit alpha, putative	3	-1.998475657	-1.984946331	-1.987699959	-1.990373982
PF3D7_0523200	Pf3D7_05_v3	conserved Plasmodium protein, unknown function	3	-1.998475657	-1.984946331	-1.987699959	-1.990373982
mal_mito_1	Pf_M76611	cytochrome c oxidase subunit 3	3	-1.969323334	-1.606365289	-2.564539869	-2.04674283
mal_mito_2	Pf_M76611	cytochrome c oxidase subunit 1	3	-1.969323334	-1.606365289	-2.564539869	-2.04674283
mal_mito_3	Pf_M76611	cytochrome b	3	-1.969323334	-1.606365289	-2.564539869	-2.04674283

5.4.3. Cross-Resistance Studies Employing KP68-Generated Clones

CQ resistance has been attributed to a point mutation in the *P. falciparum* chloroquine resistance transporter (P*f*CRT). The **KP68** bulk mutant line was tested against CQ to assess the possibility of cross-resistance between both compounds. However, there was no significant cross resistance observed when the bulk mutants were tested against CQ in the comparison to the Dd2 parent line. This suggests that both compounds are acting through a different MoR and could also be acting through a different MOA. (Figure 5.5)

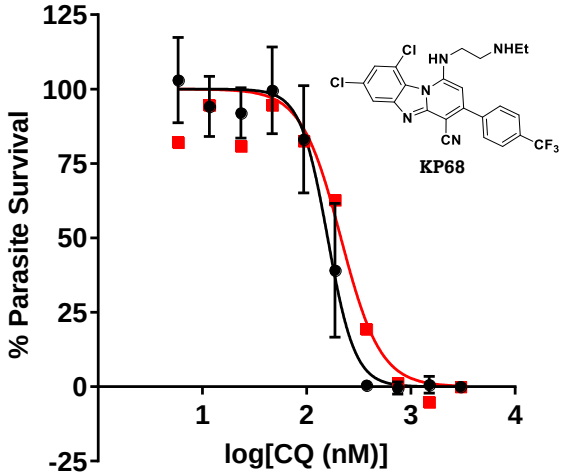

Figure 5.5. Cross-resistance between the **KP68**-resistant selected bulk mutants (red) compared with the Dd2 parental line (black) for CQ. Error bars represent one repeat, carried out for CQ cross resistance with **KP68** bulk mutants (N, n = 1,1).

Furthermore, variation in the copy number of ABCI1, identified in two out of the three prompted a cross resistance study between the **KP68**-mediated clones and **MMV675939** from the University of Cape Town's Holistic Drug discovery and Development (H3D) Centre. This is because, a CNV of a similar transporter, ABCI3, was previously observed in parasites selected with **MMV675939,** which confirmed that the ATP-binding cassette transporter conveys *P. falciparum* resistance to **MMV675939.**[44] Also, the unusual biphasic dose-response curves observed for **KP68** against its resistant clones was equally observed in with **MMV675939** against a 3D7-A10-based ABCI3 CNV line and a Dd2-B2 line. However, no significance cross resistance was observed, thereby supporting the specificity of ABCI3 for mediating resistance to **MMV675939** and not **KP68.** (Figure 5.6)

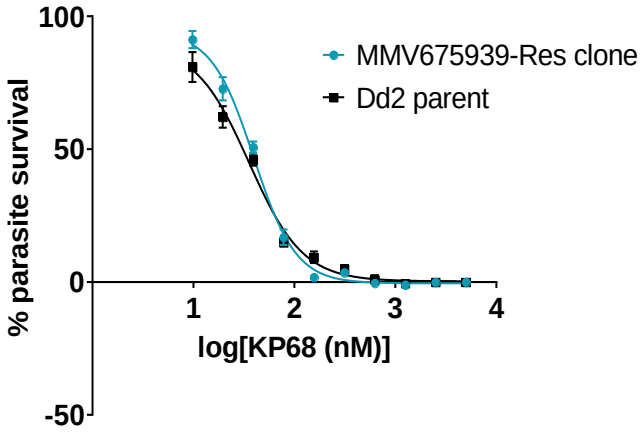

Figure 5.6. No significant-cross resistance was observed between **KP68**, and **MMV675939**-resistant mutant (clone containing ABCI 3 CNV) compared with the Dd2 parental line (IC_{50} = 40 ± 2 nM vs 36 ± 3 nM respectively). Error bars represent the standard deviation where N,n = 1,4

Finally, cross resistance between the **KP68**-resistant clones A7 and E10 and the other PBI compound under study, **KP124** was also tested. The structural distinction between **KP124** is the replacement of the 1,3-dichlorobenzene ring in **KP68** with a pyridine ring on the benzimidazole core in **KP124.** Compound **KP124** showed a shallow dose response curve against the Dd2 parent and the **KP68**-generated clones with an insignificant shift in dose response curves. This suggests that there is no cross resistance between **KP68** and **KP124** and that the analogues have different MoRs. It may also suggest that the compounds act through different MOAs. Earlier, fluorescent localization and haem fractionation studies discussed in Chapter 4 revealed the inhibition of hemozoin formation as a major contributor to the action of **KP124** but not **KP68.** The cross-resistance studies between **KP124** and the **KP68-**generated clones further reiterates this observation from the localization studies. (Figure 5.7)

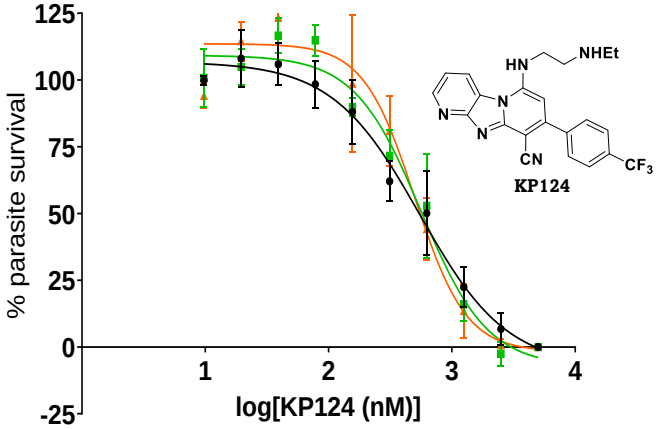

Figure 5.7. No significant cross-resistance was observed between **KP68-**resitant mutant clones and **KP124.** Error bars represent the standard deviation where N,n = 1,4

5.4.4. *In Vitro* Barcoded Cross-Resistance Studies Against *P. falciparum* Strains

As technology advances, new techniques with improved methodologies are developed in the quest to identify novel drug targets or resistance mechanisms. Advances in genetic manipulation of organisms have equally advanced significantly over the last decade through the development of site-specific nucleases such as the Cas9.[45] These nucleases are useful in the effective and specific modification of organisms. However, genetic validation of gene function in *P. falciparum* has been challenging due to the difficulty in generating large stable plasmids in *E. coli.* Also, the potential targets for Cas9 are limited because it requires an NGG protospacer adjacent motif sequence (PAM) which is much more uncommon in the genomic data of *P. falciparum* than other eukaryotes.[46] Although, there have been various efforts in the past to develop effective protocols,[47,48] these restrictions have slowed progress in studying the parasite's genome uncovering new targets and the functions of many uncharacterized genes.

To address these drawbacks, researchers from the Wellcome Sanger Institute developed DNA barcoded parasite lines covering a variety of drug targets and resistance mechanisms. They utilized CRISPR/Cas9 as a genome editing tool to insert a short barcode cassette into a non-essential locus of each parasite line.[49] This allowed a head-to-head competition experiment in the presence of the compounds under study, in this case, **KP68** and **KP124.** Parasite growth over an assay period of 14 days is monitored by flow cytometry after an *in vitro* selective pressure of 3x the IC_{50} is applied. (Figure 5.8)

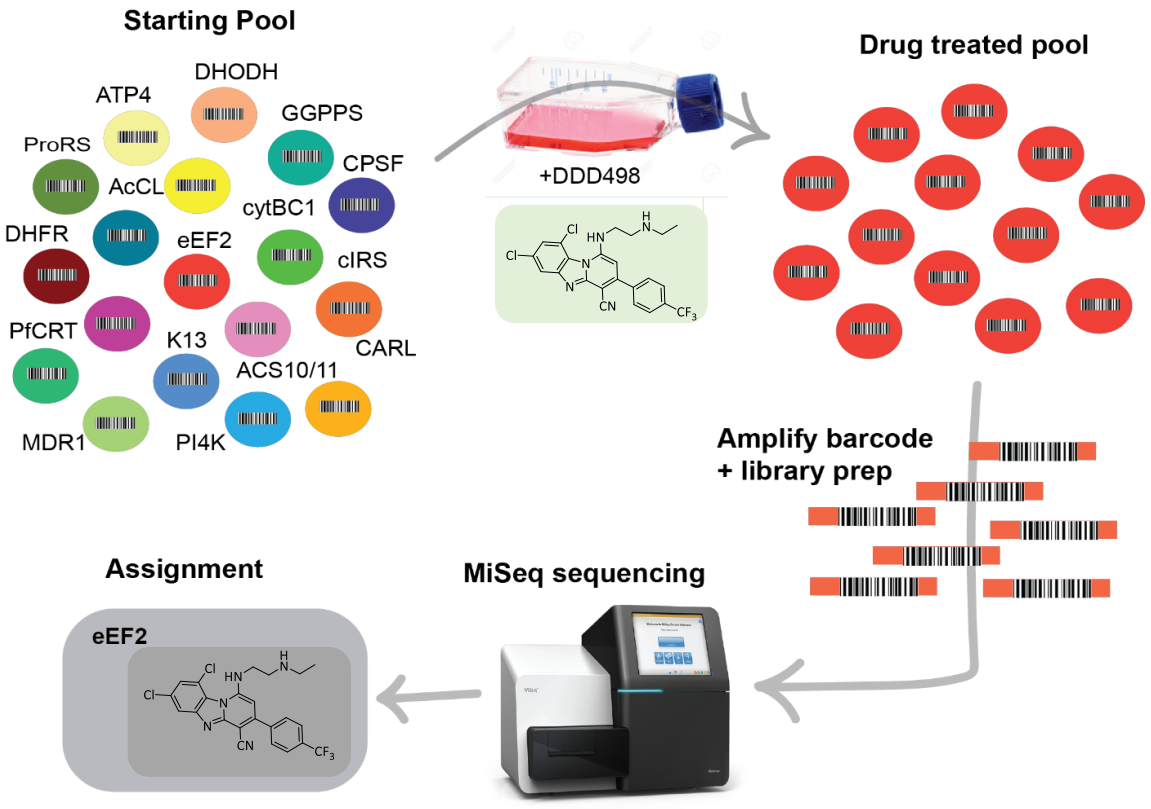

Figure 5.8. Cross resistance profiling using barcoded pool of parasite lines covering a range of targets and resistance mechanisms.

The absence of parasite growth suggests that the compound has insignificant cross resistance with any of the over 40 DNA barcoded lines carrying specific mutations in both the Dd2 and 3D7 background, representing a variety of resistance mechanisms. The absence of cross resistance suggests that the compound under study does not share the same resistance mechanism or binding mode to the resistance-mediating target as those compounds used to derive the mutant lines present in the pool. Outgrowth on the other hand indicates one or more surviving lines and subsequent barcode sequencing using next generation sequencing of barcode amplicons provides a count of barcode representation before and after compound exposure. This allows the identification of the cross resistant lines and knowledge of the potential proteins involved in the MoR or MOA. Both compounds studied, **KP68** and **KP124**, (Figure 5.9, A and B) showed no cross resistance with any of the barcoded lines in the pool indicating that both compounds could be acting through a mechanism or binding mode not represented in the pool of barcoded lines. This is evident from the absence of a significant log fold change between the treated and untreated lines. Since data from fluorescent localization and hemozoin

fractionation studies implicated the inhibition of hemozoin formation as a contributory mechanism to the MOA of **KP124**, it was earlier hypothesized that the parasite's MoR to **KP124** could be linked to P*f*CRT. However, the absence of cross resistance between the compound and P*f*CRT mutant line represented in the pool suggests that parasite resistance to **KP124** maybe through a different mechanism.

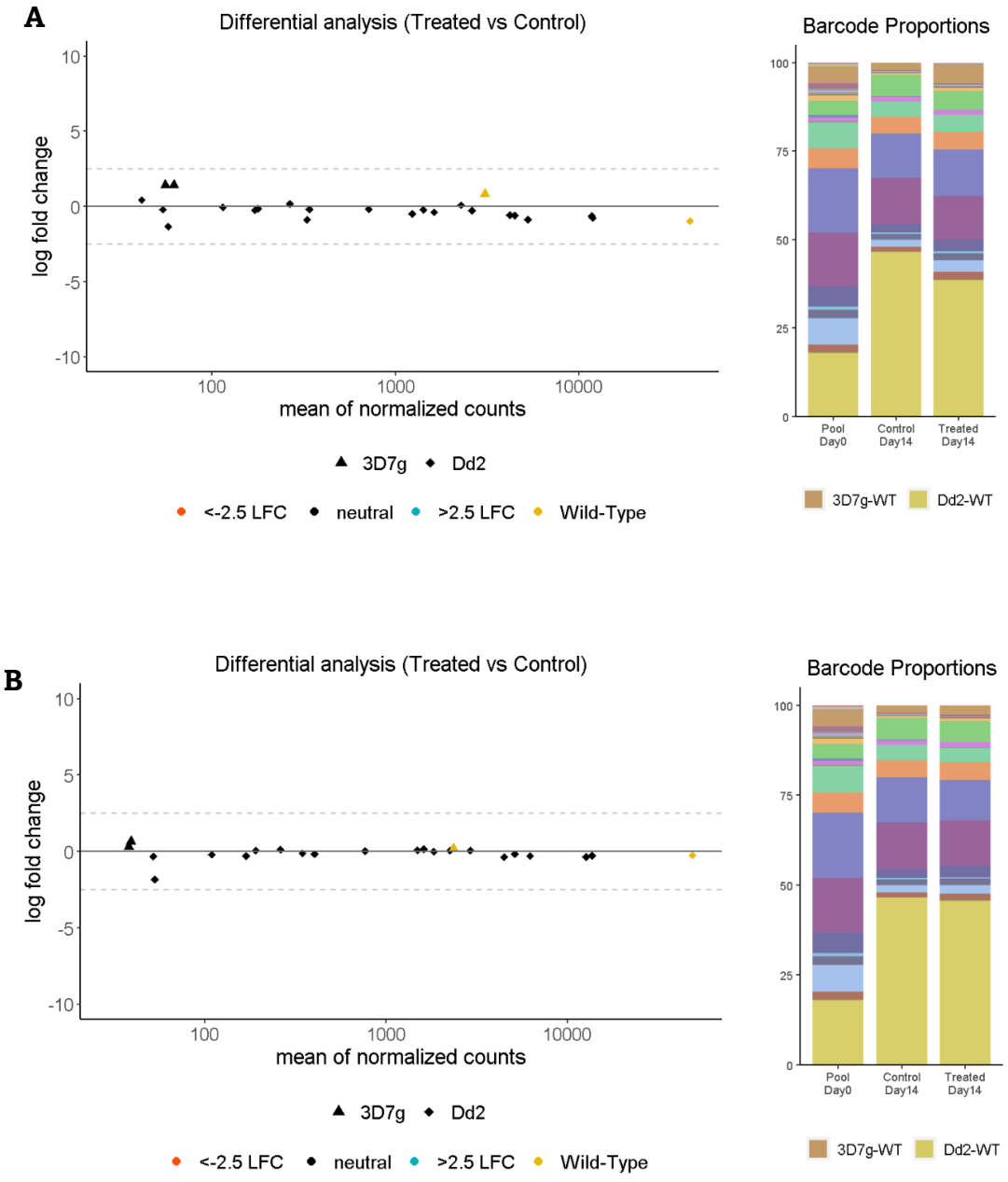

Figure 5.9. Cross resistance profiling using a barcoded pool of parasite lines covering a range of targets and resistance mechanisms. **A** and **B** shows no log-fold change between treated **KP68** and **KP124** treated and untreated lines, respectively.

5.5. Conclusion

Efforts to identify novel antimalarial targets and deconvolute the molecular markers of antimalarial resistance have been aided by the powerful tools provided by the recent advances in *P. falciparum* genomics. A well-known genomics approach to elucidating the MoR of phenotypic whole cell antimalarial leads with unknown MOA is to employ *in vitro* selections with *P. falciparum* ABS parasites. The MoR and the potential MOA of previously reported PBI antimalarials were investigated via resistance selection of Dd2 parasites with the lead compound **KP68**. WGS of resistant mutant clones revealed a SNP stop codon in a mitochondrion carrier protein. Members of the mitochondrial carrier family of membrane transporters play vital roles in the parasite's cellular metabolism. However, it was observed that this resistance phenotype was unstable and dependent on growth under drug pressure, showing that this mutation is not solely responsible for this resistance phenotype. Instead, the several CNVs observed, including an interesting deamplification of a mitochondrial-processing peptidase as well as the multidrug resistance transporter PfMDR1 could contribute to the mediation of drug resistance and may play a role in the MOA of **KP68.** Indeed, with significant amounts of **KP68** accumulating around the mitochondrion, the parasite's mitochondrion remains an organelle of interest in the mode of action of the compound**.** Through cross resistance studies with clones generated for **KP68**, it was shown that resistance to **KP124** could be mediated through a different mechanism from **KP68**. This confirms earlier information deduced from the drug accumulation and hemozoin inhibition studies previously carried out on these compounds. Similarly, no cross resistance was observed between the mutant clones generated for **KP68** and **CQ**. This again suggests that both compounds are acting through a different MoR and possibly through a different MOA. Finally, efforts to raise resistant mutants for **DM253** using single step mutant selection have been unsuccessful as no parasites recrudesced after 60 days. The next chapter will describe the use of chemical proteomics tools to contribute more information to the MOA of these compounds with focus on identifying their protein binding partners.

5.6. References

(1) Gardner, M. J.; Tettelin, H.; Carucci, D. J.; Cummings, L. M.; Aravind, L.; Koonin, E. V.; Shallom, S.; Mason, T.; Yu, K.; Fujii, C.; Pederson, J.; Shen, K.; Jing, J.; Aston, C.; Lai, Z.; Schwartz, D. C.; Pertea, M.; Salzberg, S.; Zhou, L.; Sutton, G. G.; Clayton, R.; White, O.; Smith, H. O.; Fraser, C. M.; Adams, M. D.; Venter, J. C.; Hoffman, S. L. Chromosome 2 Sequence of the Human Malaria Parasite *Plasmodium falciparum*. *Science (80-.).* **1998**, *282* (5391), 1126–1132.

(2) Bowman, S.; Lawson, D.; Basham, D.; Brown, D.; Chillingworth, T.; Churcher, C. M.; Craig, A.; Davies, R. M.; Devlin, K.; Feltwell, T.; Gentles, S.; Gwilliam, R.; Hamlin, N.; Harris, D.; Holroyd, S.; Hornsby, T.; Horrocks, P.; Jagels, K.; Jassal, B.; Kyes, S.; McLean, J.; Moule, S.; Mungall, K.; Murphy, L.; Oliver, K.; Quail, M. A.; Rajandream, M.-A.; Rutter, S.; Skelton, J.; Squares, R.; Squares, S.; Sulston, J. E.; Whitehead, S.; Woodward, J. R.; Newbold, C.; Barrell, B. G. The Complete Nucleotide Sequence of Chromosome 3 of *Plasmodium falciparum*. *Nature* **1999**, *400* (6744), 532–538.

(3) Carucci, D. J.; Gardner, M. J.; Tettelin, H.; Cummings, L. M.; Smith, H. O.; Adams, M. D.; Hoffman, S. L.; Venter, J. C. The Malaria Genome Sequencing Project. *Expert Rev. Mol. Med.* **1998**, *1* (03).

(4) Shen, H.-M.; Chen, S.-B.; Wang, Y.; Chen, J.-H. Whole-Genome Sequencing of a Plasmodium Vivax Isolate from the China-Myanmar Border Area. *Mem. Inst. Oswaldo Cruz* **2015**, *110* (6), 814–816.

(5) Rutledge, G. G.; Böhme, U.; Sanders, M.; Reid, A. J.; Cotton, J. A.; Maiga-Ascofare, O.; Djimdé, A. A.; Apinjoh, T. O.; Amenga-Etego, L.; Manske, M.; Barnwell, J. W.; Renaud, F.; Ollomo, B.; Prugnolle, F.; Anstey, N. M.; Auburn, S.; Price, R. N.; McCarthy, J. S.; Kwiatkowski, D. P.; Newbold, C. I.; Berriman, M.; Otto, T. D. Plasmodium Malariae and P. Ovale Genomes Provide Insights into

(6) Okombo, J.; Kanai, M.; Deni, I.; Fidock, D. A. Genomic and Genetic Approaches to Studying Antimalarial Drug Resistance and Plasmodium Biology. *Trends Parasitol.* **2021**, *37* (6), 476–492.

(7) Flueck, C.; Drought, L. G.; Jones, A.; Patel, A.; Perrin, A. J.; Walker, E. M.; Nofal, S.

D.; Snijders, A. P.; Blackman, M. J.; Baker, D. A. Phosphodiesterase Beta Is the Master Regulator of CAMP Signalling during Malaria Parasite Invasion. *PLOS Biol.* **2019**, *17* (2), e3000154.

(8) Lim, M. Y.-X.; LaMonte, G.; Lee, M. C. S.; Reimer, C.; Tan, B. H.; Corey, V.; Tjahjadi, B. F.; Chua, A.; Nachon, M.; Wintjens, R.; Gedeck, P.; Malleret, B.; Renia, L.; Bonamy, G. M. C.; Ho, P. C.-L.; Yeung, B. K. S.; Chow, E. D.; Lim, L.; Fidock, D. A.; Diagana, T. T.; Winzeler, E. A.; Bifani, P. UDP-Galactose and Acetyl-CoA Transporters as Plasmodium Multidrug Resistance Genes. *Nat. Microbiol.* **2016**, *1* (12), 16166.

(9) Marapana, D. S.; Dagley, L. F.; Sandow, J. J.; Nebl, T.; Triglia, T.; Pasternak, M.; Dickerman, B. K.; Crabb, B. S.; Gilson, P. R.; Webb, A. I.; Boddey, J. A.; Cowman, A. F. Plasmepsin V Cleaves Malaria Effector Proteins in a Distinct Endoplasmic Reticulum Translocation Interactome for Export to the Erythrocyte. *Nat. Microbiol.* **2018**, *3* (9), 1010–1022.

(10) Ross, L. S.; Dhingra, S. K.; Mok, S.; Yeo, T.; Wicht, K. J.; Kümpornsin, K.; Takala-Harrison, S.; Witkowski, B.; Fairhurst, R. M.; Ariey, F.; Menard, D.; Fidock, D. A. Emerging Southeast Asian P*f*CRT Mutations Confer *Plasmodium falciparum* Resistance to the First-Line Antimalarial Piperaquine. *Nat. Commun.* **2018**, *9* (1), 3314.

(11) Trager, W.; Jensen, J. Human Malaria Parasites in Continuous Culture. *Science (80-.).* **1976**, *193* (4254), 673–675.

(12) Nguyen-Dinh, P.; Trager, W. Chloroquine Resistance Produced in Vitro in an African Strain of Human Malaria. *Science (80-.).* **1978**, *200* (4348), 1397–1398.

(13) Hastings, I.; Donnelly, M. The Impact of Antimalarial Drug Resistance Mutations on Parasite Fitness, and Its Implications for the Evolution of Resistance. *Drug Resist. Updat.* **2005**, *8* (1–2), 43–50.

(14) Huijben, S.; Nelson, W. A.; Wargo, A. R.; Sim, D. G.; Drew, D. R.; Read, A. F. Chemotherapy, Within-Host Ecology and the Fitness of Drug-Resistance Malaria Parasites. *Evolution (N. Y).* **2010**,.

(15) Rosenthal, P. J. The Interplay between Drug Resistance and Fitness in Malaria Parasites. *Mol. Microbiol.* **2013**, *89* (6), 1025–1038.

(16) Wongsrichanalai, C.; Pickard, A. L.; Wernsdorfer, W. H.; Meshnick, S. R. Epidemiology of Drug-Resistant Malaria. *Lancet Infect. Dis.* **2002**, *2* (4), 209–218.

(17) Garcia-Bustos, J. F.; Gamo, F.-J. Antimalarial Drug Resistance and Early Drug Discovery. *Curr. Pharm. Des.* **2013**, *19* (2), 270–281.

(18) Preechapornkul, P.; Imwong, M.; Chotivanich, K.; Pongtavornpinyo, W.; Dondorp, A. M.; Day, N. P. J.; White, N. J.; Pukrittayakamee, S. *Plasmodium falciparum* Pfmdr1 Amplification, Mefloquine Resistance, and Parasite Fitness. *Antimicrob. Agents Chemother.* **2009**, *53* (4), 1509–1515.

(19) Lim, P.; Dek, D.; Try, V.; Sreng, S.; Suon, S.; Fairhurst, R. M. Decreasing Pfmdr1 Copy Number Suggests That Plasmodium Falciparum in Western Cambodia Is Regaining In Vitro Susceptibility to Mefloquine. *Antimicrob. Agents Chemother.* **2015**, *59* (5), 2934–2937.

(20) H. Wernsdorfer, W.; Payne, D. The Dynamics of Drug Resistance in *Plasmodium falciparum*. *Pharmacol. Ther.* **1991**, *50* (1), 95–121.

(21) Peters, W.; Robinson, B. L. Malaria. In *Handbook of Animal Models of Infection*; Elsevier, 1999; pp 757–773.

(22) Björkman, A.; Phillips-Howard, P. A. The Epidemiology of Drug-Resistant Malaria. *Trans. R. Soc. Trop. Med. Hyg.* **1990**, *84* (2), 177–180.

(23) Hutchinson, D. B.; Viravan, C.; Kyle, D. E.; Looareesuwan, S.; Canfield, C. J.; Webster, H. K. Clinical Studies of Atovaquone, Alone or in Combination with Other Antimalarial Drugs, for Treatment of Acute Uncomplicated Malaria in Thailand. *Am. J. Trop. Med. Hyg.* **1996**, *54* (1), 62–66.

(24) Witkowski, B.; Berry, A.; Benoit-Vical, F. Resistance to Antimalarial Compounds: Methods and Applications. *Drug Resist. Updat.* **2009**, *12* (1–2), 42–50.

(25) Rathod, P. K.; McErlean, T.; Lee, P.-C. Variations in Frequencies of Drug Resistance in Plasmodium Falciparum. *Proc. Natl. Acad. Sci.* **1997**, *94* (17), 9389–9393.

(26) Paget-Mcnicol, S.; Saul, A. Mutation Rates in the Dihydrofolate Reductase Gene of *Plasmodium falciparum*. *Parasitology* **2001**, *122* (5), 497–505.

(27) Conrad, D. F.; Hurles, M. E. The Population Genetics of Structural Variation. *Nat. Genet.* **2007**, *39* (S7), S30–S36.

(28) Paget-Mcnicol, S.; Saul, A. Mutation Rates in the Dihydrofolate Reductase Gene of *Plasmodium falciparum*. *Parasitology* **2001**, *122* (5), 497–505.

(29) Ding, X. C.; Ubben, D.; Wells, T. N. A Framework for Assessing the Risk of Resistance for Anti-Malarials in Development. *Malar. J.* **2012**, *11* (1), 292.

(30) Castellini, M. A.; Buguliskis, J. S.; Casta, L. J.; Butz, C. E.; Clark, A. B.; Kunkel, T. A.; Taraschi, T. F. Malaria Drug Resistance Is Associated with Defective DNA Mismatch Repair. *Mol. Biochem. Parasitol.* **2011**, *177* (2), 143–147.

(31) Trotta, R. F.; Brown, M. L.; Terrell, J. C.; Geyer, J. A. Defective DNA Repair as a Potential Mechanism for the Rapid Development of Drug Resistance in *Plasmodium falciparum*. *Biochemistry* **2004**, *43* (17), 4885–4891.

(32) Rocamora, F.; Winzeler, E. A. Genomic Approaches to Drug Resistance in Malaria. *Annu. Rev. Microbiol.* **2020**, *74* (1), 761–786.

(33) Sonoiki, E.; Ng, C. L.; Lee, M. C. S.; Guo, D.; Zhang, Y.-K.; Zhou, Y.; Alley, M. R. K.; Ahyong, V.; Sanz, L. M.; Lafuente-Monasterio, M. J.; Dong, C.; Schupp, P. G.; Gut, J.; Legac, J.; Cooper, R. A.; Gamo, F.-J.; DeRisi, J.; Freund, Y. R.; Fidock, D. A.; Rosenthal, P. J. A Potent Antimalarial Benzoxaborole Targets a *Plasmodium falciparum* Cleavage and Polyadenylation Specificity Factor Homologue. *Nat. Commun.* **2017**, *8* (1), 14574.

(34) Vanaerschot, M.; Lucantoni, L.; Li, T.; Combrinck, J. M.; Ruecker, A.; Kumar, T. R. S.; Rubiano, K.; Ferreira, P. E.; Siciliano, G.; Gulati, S.; Henrich, P. P.; Ng, C. L.; Murithi, J. M.; Corey, V. C.; Duffy, S.; Lieberman, O. J.; Veiga, M. I.; Sinden, R. E.; Alano, P.; Delves, M. J.; Lee Sim, K.; Winzeler, E. A.; Egan, T. J.; Hoffman, S. L.; Avery, V. M.; Fidock, D. A. Hexahydroquinolines Are Antimalarial Candidates with Potent Blood-Stage and Transmission-Blocking Activity. *Nat. Microbiol.* **2017**, *2* (10), 1403–1414.

(35) Cowell, A. N.; Istvan, E. S.; Lukens, A. K.; Gomez-Lorenzo, M. G.; Vanaerschot, M.; Sakata-Kato, T.; Flannery, E. L.; Magistrado, P.; Owen, E.; Abraham, M.; LaMonte, G.; Painter, H. J.; Williams, R. M.; Franco, V.; Linares, M.; Arriaga, I.; Bopp, S.; Corey, V. C.; Gnädig, N. F.; Coburn-Flynn, O.; Reimer, C.; Gupta, P.; Murithi, J. M.; Moura, P. A.; Fuchs, O.; Sasaki, E.; Kim, S. W.; Teng, C. H.; Wang, L. T.; Akidil, A.; Adjalley, S.; Willis, P. A.; Siegel, D.; Tanaseichuk, O.; Zhong, Y.; Zhou, Y.; Llinás, M.; Ottilie, S.; Gamo, F.-J.; Lee, M. C. S.; Goldberg, D. E.; Fidock, D. A.; Wirth, D. F.; Winzeler, E. A. Mapping the Malaria Parasite Druggable Genome by Using in Vitro Evolution and Chemogenomics. *Science (80-.).* **2018**, *359* (6372), 191–199.

(36) Ng, C. L.; Fidock, D. A. *Plasmodium falciparum In Vitro* Drug Resistance Selections and Gene Editing; 2019; pp 123–140.

(37) Butterworth, A. S.; Robertson, A. J.; Ho, M.-F.; Gatton, M. L.; McCarthy, J. S.; Trenholme, K. R. An Improved Method for Undertaking Limiting Dilution Assays for in Vitro Cloning of *Plasmodium falciparum* Parasites. *Malar. J.* **2011**, *10* (1), 95.

(38) Rosario, V. Cloning of Naturally Occurring Mixed Infections of Malaria Parasites. *Science (80-.).* **1981**, *212* (4498), 1037–1038.

(39) Nixon, G. L.; Moss, D. M.; Shone, A. E.; Lalloo, D. G.; Fisher, N.; O'Neill, P. M.; Ward, S. A.; Biagini, G. A. Antimalarial Pharmacology and Therapeutics of Atovaquone. *J. Antimicrob. Chemother.* **2013**, *68* (5), 977–985.

(40) Siregar, J. E.; Kurisu, G.; Kobayashi, T.; Matsuzaki, M.; Sakamoto, K.; Mi-ichi, F.; Watanabe, Y.; Hirai, M.; Matsuoka, H.; Syafruddin, D.; Marzuki, S.; Kita, K. Direct Evidence for the Atovaquone Action on the Plasmodium Cytochrome Bc 1 Complex. *Parasitol. Int.* **2015**, *64* (3), 295–300.

(41) Palmieri, F.; Pierri, C. L.; De Grassi, A.; Nunes-Nesi, A.; Fernie, A. R. Evolution, Structure and Function of Mitochondrial Carriers: A Review with New Insights. *Plant J.* **2011**, *66* (1), 161–181.

(42) Holmgren, G.; Hamrin, J.; Svärd, J.; Mårtensson, A.; Gil, J. P.; Björkman, A. Selection of Pfmdr1 Mutations after Amodiaquine Monotherapy and Amodiaquine plus Artemisinin Combination Therapy in East Africa. *Infect. Genet. Evol.* **2007**, *7* (5), 562–569.

(43) Foote, S. J.; Kyle, D. E.; Martin, R. K.; Oduola, A. M. J.; Forsyth, K.; Kemp, D. J.; Cowman, A. F. Several Alleles of the Multidrug-Resistance Gene Are Closely Linked to Chloroquine Resistance in *Plasmodium falciparum*. *Nature* **1990**, *345* (6272), 255–258.

(44) Murithi, J. M.; Deni, I.; Pasaje, C. F. A.; Okombo, J.; Bridgford, J. L.; Gnädig, N. F.; Edwards, R. L.; Yeo, T.; Mok, S.; Burkhard, A. Y.; Coburn-Flynn, O.; Istvan, E. S.; Sakata-Kato, T.; Gomez-Lorenzo, M. G.; Cowell, A. N.; Wicht, K. J.; Le Manach, C.; Kalantarov, G. F.; Dey, S.; Duffey, M.; Laleu, B.; Lukens, A. K.; Ottilie, S.; Vanaerschot, M.; Trakht, I. N.; Gamo, F.-J.; Wirth, D. F.; Goldberg, D. E.; Odom John, A. R.; Chibale, K.; Winzeler, E. A.; Niles, J. C.; Fidock, D. A. The *Plasmodium falciparum* ABC Transporter ABCI3 Confers Parasite Strain-Dependent Pleiotropic Antimalarial Drug Resistance. *Cell Chem. Biol.* **2021**.

(45) Ran, F. A.; Hsu, P. D.; Wright, J.; Agarwala, V.; Scott, D. A.; Zhang, F. Genome Engineering Using the CRISPR-Cas9 System. *Nat. Protoc.* **2013**, *8* (11), 2281–2308.

(46) Bushell, E.; Gomes, A. R.; Sanderson, T.; Anar, B.; Girling, G.; Herd, C.; Metcalf, T.; Modrzynska, K.; Schwach, F.; Martin, R. E.; Mather, M. W.; McFadden, G. I.; Parts, L.; Rutledge, G. G.; Vaidya, A. B.; Wengelnik, K.; Rayner, J. C.; Billker, O. Functional Profiling of a Plasmodium Genome Reveals an Abundance of Essential Genes. *Cell* **2017**, *170* (2), 260-272.e8.

(47) Skinner-Adams, T. S.; Lawrie, P. M.; Hawthorne, P. L.; Gardiner, D. L.; Trenholme, K. R. Comparison of *Plasmodium falciparum* Transfection Methods. *Malar. J.* **2003**, *2* (1), 19.

(48) Caro, F.; Miller, M. G.; DeRisi, J. L. Plate-Based Transfection and Culturing Technique for Genetic Manipulation of *Plasmodium falciparum*. *Malar. J.* **2012**, *11* (1), 22.

(49) Carrasquilla, M.; Adjalley, S.; Sanderson, T.; Marin-Menendez, A.; Coyle, R.; Montandon, R.; Rayner, J. C.; Pance, A.; Lee, M. C. S. Defining Multiplicity of Vector Uptake in Transfected Plasmodium Parasites. *Sci. Rep.* **2020**, *10* (1), 10894.

Chapter Six

Chemical Proteomics Approach to Identifying Protein Binding Partners of Pyrido[1,2-a]benzimidazoles

6.1. Chapter Overview

Evidence suggests that the PBI antimalarials interact with the hemozoin biocrystallisation pathway in *P. falciparum* by inhibiting the dimerization of Fe(III)PPIX into the growing crystal.[1,2] Notwithstanding, previous investigations discussed in Chapters 4 and 5 suggested that organelles other than the parasite's digestive vacuole may be playing significant roles in the MOA of this class of antimalarials. The single point mutation observed in the mitochondrial carrier protein when a **KP68** parasite mutant was raised, alongside the CNVs explicitly observed in the parasite's mitochondrion processing peptidase and its multidrug resistance transporter, suggests that while hemozoin inhibition might be a contributory mechanism to the action of some of these compound, other analogues in this class may be acting through mechanisms that might be novel. Although *in vitro* evolution followed by WGS has helped identify resistant mechanisms and MOA of phenotypic whole-cell active leads, a significant drawback in using this approach is that, in an identifiable resistant gene, mutations in that gene may repeatedly appear in resistant parasites, concealing the real target and the MOA of the compound.[3] For example, *in vitro* resistance selection has failed to identify the MoR and molecular target (s) of **KAF156,** a phenotypic whole-cell antimalarial compound that has progressed in the drug development pipeline. Resistant mutants generated for **KAF156** repeatedly reveal membrane transporters such as P*f*CARL, which is non-essential and mediates resistance in many compounds.[4] Consequently, employing multiple non-biased target deconvolution approaches that result in the same conclusion regarding an identified target when studying the MOA of a compound is imperative.

Chemical proteomics provides a unique opportunity to directly study the protein binding partners of **KP68** and **KP124.** This approach has been successful in identifying protein targets for antimalarial drug candidates.[5] However, no work has been done in using this approach to identify the binding partners for the PBIs.

Hence this chapter investigates the binding partners of the PBIs understudy in *P. falciparum* using a chemical proteomics approach. This approach uses matrix-based affinity methods, linking agarose beads to the compounds of interest and finally using these matrices to probe the *P. falciparum* proteome for the binding target(s) to these antimalarials.

Therefore, the specific objectives described in this chapter include to:

I. Prepare cell lysate from *P. falciparum* trophozoites in a suitable manner for use in these experiments.
II. Prepare PBI-labelled agarose beads as a stationary phase to pull down protein binding partners.
III. Use the drug-labelled beads prepared to capture drug-binding sub-proteomes of the PBI antimalarial binding partners from *P. falciparum* and identify protein targets using SDS-Page and MS.

6.2. Background to Techniques Described in this Chapter

Despite the essential roles the knowledge of molecular targets and mode of action plays in malaria therapy, the MOA of several promising antimalarial drug candidates remains unclear. It was reported that 7% of all approved drugs are purported to have an unknown primary target (s), and about 18% do not have well-defined MOA (s).[6] Despite the long and extensive use of CQ, quinine, and quinidine for the treatment of malaria, their MOA is still not completely understood. However, hemozoin inhibition has been implicated in their MOA.[7] More recently, the Malaria Drug Accelerator (MalDA) consortium, comprised of leading research laboratories worldwide, has been working to change the status quo by accelerating and improving the early malaria drug discovery process by identifying essential and druggable targets.[8] In conjunction with other approaches previously described in this work, such as drug localization studies, *in vitro* evolution, and WGS, the chemical proteomics approach to target deconvolution provides another route to identify the molecular target (s) of whole-cell active antimalarial compounds. If successful, this approach provides direct evidence of on-target engagement that is not provided by the other methods previously described.

One common proteomics strategy involves immobilizing the compound of interest onto magnetic beads. The drug labelled beads are then used to ‘’pull down’’ interacting proteins from *P. falciparum* cell lysates. (Figure 6.1) These experiments are carried out in the presence of competing for the free compound to discriminate between specific and non-specific bound proteins. Proteins that bound specifically to the drug-labelled beads are then identified and quantified by MS as possible putative target (s).

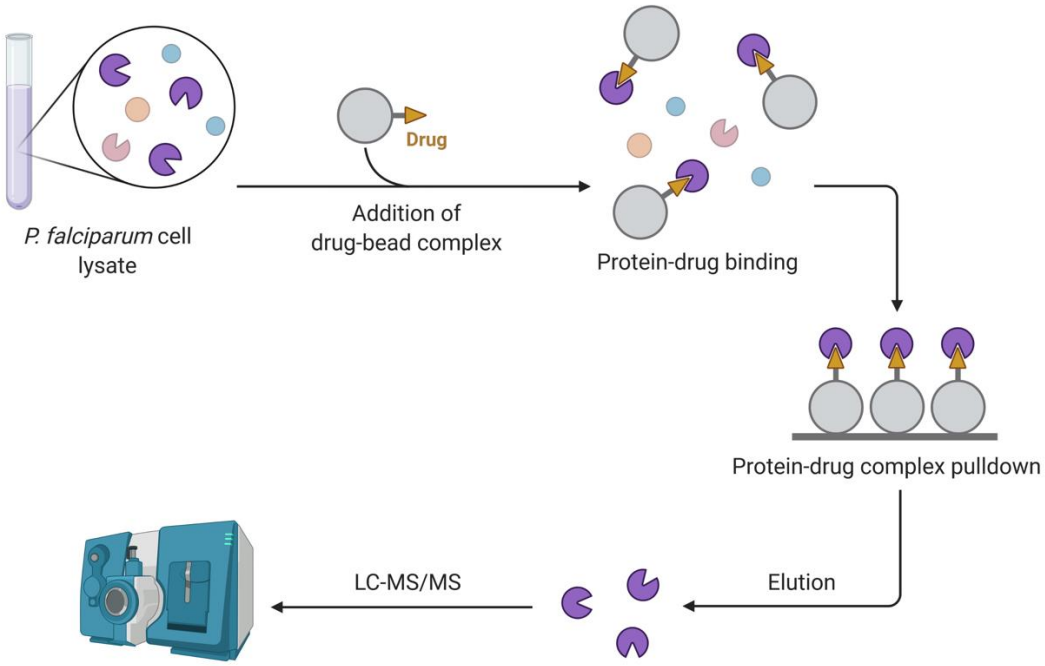

Figure 6.1. Workflow of matrix-based affinity chromatography as a chemoproteomics technique. Created by BioRender.com.

6.2.1. Matrix-based Affinity Chromatography

As described earlier, affinity chromatography has successfully separated complex protein mixtures by exploiting specific receptor and ligand interactions. This strategy requires the compound of interest to contain a reactive functionality amenable to synthetic derivatization. Also, the binding molecule of interest should be derivatized such that its biological activity and binding specificity would not be negatively impacted. Finally, the matrix must not interfere with the binding of the target to the drug. A significant drawback to this approach is the difficulty in some cases to find a suitable synthetic chemistry route required to derivatize the molecule to make it amenable for covalent linking to the stationary phase without compromising its antiplasmodium activity or altering its target.

After exposure to all possible binding targets in the form of a complex parasite lysate mixture, the matrix is followed by several wash steps to elute non-specific protein binding partners. Bound proteins remaining after the wash step are eluted under denaturing conditions (solid-phase elution, Figure 6.2A) or with excess free drug (competition elution, Figure 6.2B). SDS-Page and MS then identify the proteins. There are mostly more non-specific protein binders than the target (s). For this reason, negative control experiments are set up using either an inactive analogue or a non-specific binding matrix (Comparison variant, Figure 6.2C).[9]

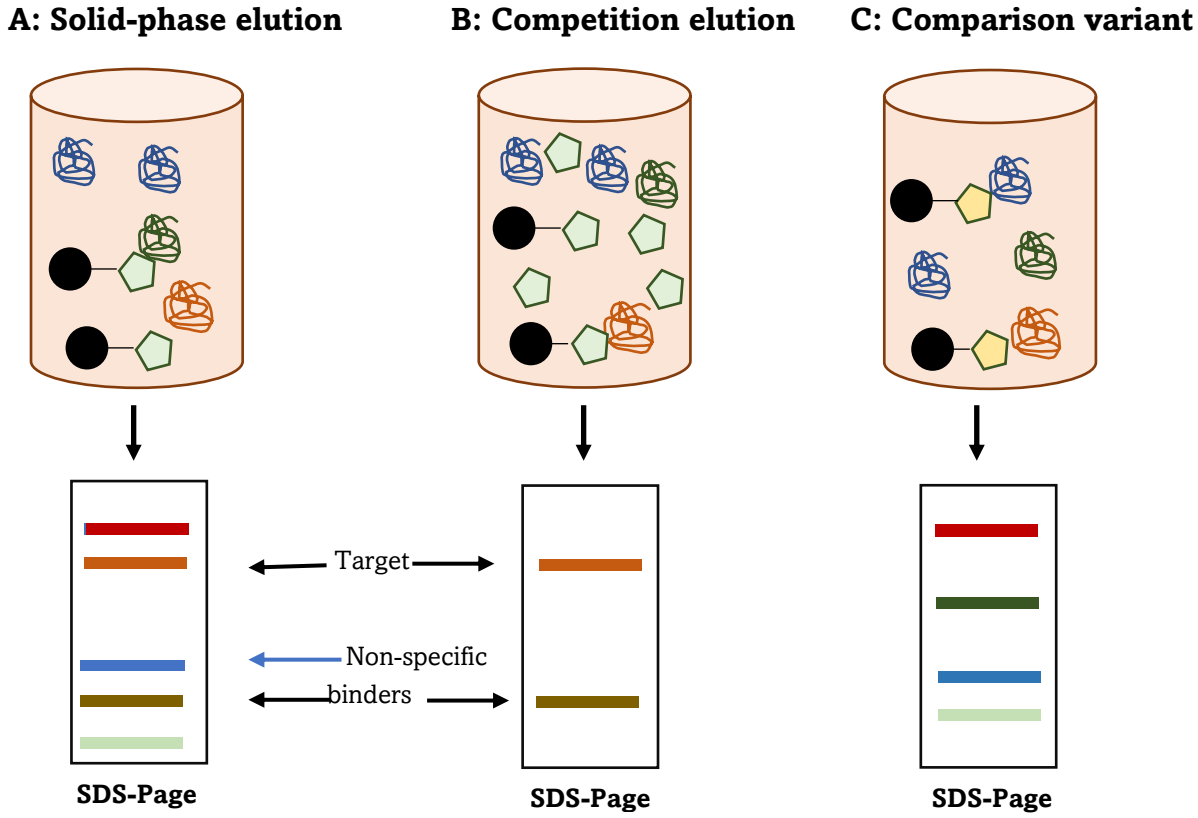

Figure 6.2. Detection of protein targets using matrix-based affinity chromatography. A ligand (green pentagon) is tethered to a matrix (black circle) and incubated with protein extract. After a series of washing steps have removed non-binding proteins, any ligand-bound proteins are eluted using (A) denaturing buffer conditions or (B) an excess of free ligand and then investigated by SDS-Page. To minimize the identification of non-specific binders, the proteins obtained with an inactive ligand analogue or non-specific matrix are also determined (C), and the two outcomes are compared.[9]

6.2.2. Preparation of Biological Material for Affinity Experiments

P. falciparum lysate was prepared from mature trophozoites using freeze-thaw and sonication methods. The parasite's trophozoite embodies 80% of its genomic data.[10] That, coupled with the fact that the hemoglobin degradation pathway is well developed at this life cycle stage, makes it suitable for this study.[11] Hence matured trophozoites were harvested for this work. In the freeze-thaw method, trophozoites from erythrocytes were lysed using saponin. The resultant pellets were washed extensively to remove all unwanted RBCs and, more importantly, excess hemoglobin, which could interfere with detecting proteins with lower abundance. Once saponin-lysed, parasite pellets were stored at -80°C for three days and subsequently thawed. This process results in rupturing the parasitophorous vacuolar and plasma membranes of the parasite. However, the tougher DV membrane remained intact (Figure 6.3). To lyse this membrane, a freeze-thaw cycle was performed over several days. Lysis of the DV was judged to be complete when no distinct shapes were observed under the microscope. During cell lysis, samples were placed on ice to maintain their integrity, protease inhibitors were used to prevent premature proteolysis, and gentle mixing was performed to help minimize protein aggregation. Fractions from each lysis step was collected and pulled together.

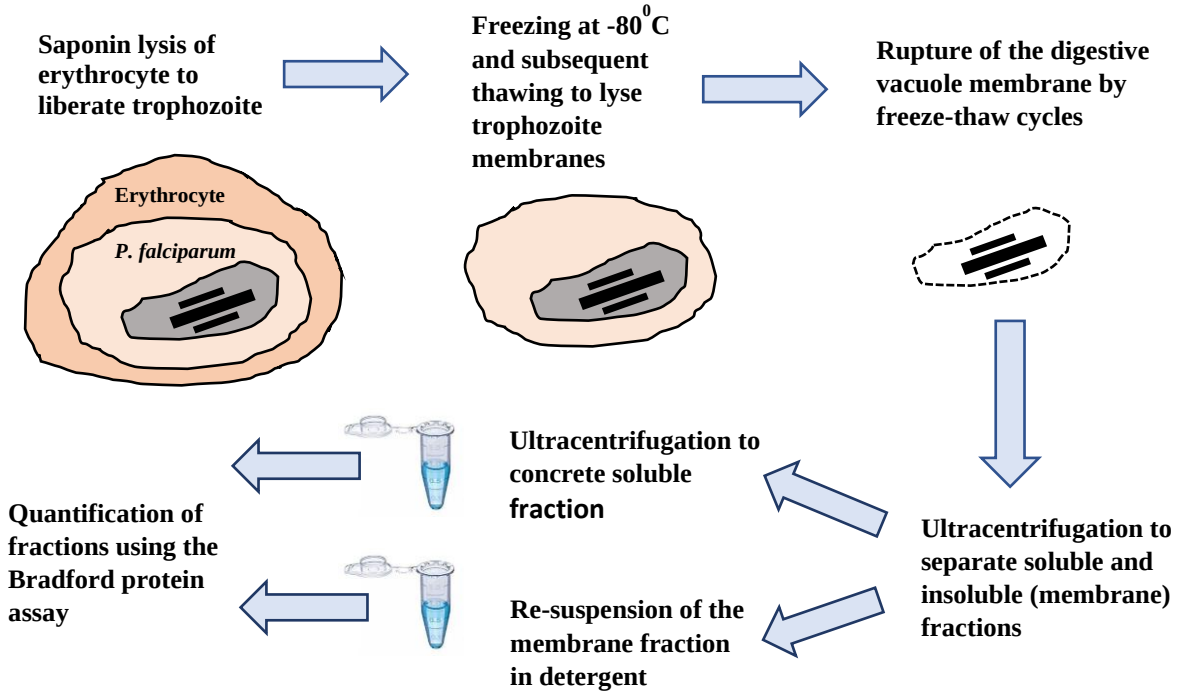

Figure 6.3. Freeze-thaw method to prepare *P. falciparum* lysate for proteomics.

Ultracentrifugation was performed to separate soluble proteins from the membrane-associated insoluble fraction. Afterward, the soluble fraction was concentrated via ultrafiltration using 10 kDa molecular weight cut-off tubes. The membrane fraction was resuspended with a minimum volume of 0.2 % Triton X-100 detergent and triturated to increase solubility. Finally, the protein concentrations of all fractions were quantified using the Bradford assay. This assay measures the binding of Coomassie Brilliant Blue G-250 dye to proteins.[12] Under acidic conditions, the dye is in the doubly protonated red cationic form (max 470 nm); however, when the dye binds to a protein, it is converted to a stable unprotonated blue format (max 595 nm). Therefore, using a standard curve, measuring the absorbance at this latter wavelength determines the protein concentration.[13] In this assay, bovine serum albumin was used for calibration purposes. Although successful in preparing lysates for proteomics, the freeze-thaw method is time-intensive as it could take weeks to prepare. Also, freezing, and thawing lysates could interfere with the integrity of unstable proteins. Therefore, an alternate cell lysis technique known as sonication was employed to circumvent these drawbacks. This technique physically lyses cells using pulsed, high-frequency sound waves to perturb the cells. The sound waves are conveyed using a sonicator with a vibrating probe submerged in the liquid suspension containing the *P. falciparum* saponin lysed cells. The mechanical energy from the probe results in the formation of microscopic vapor bubbles that form temporarily and implode. This causes shock waves to radiate through the sample and results in cell lysis. Lysates prepared from the sonication and freeze-thaw methods were compared on SDS-Page and found to be similar. (Figure 6.4) Therefore, subsequent lysates were prepared using the sonication method.

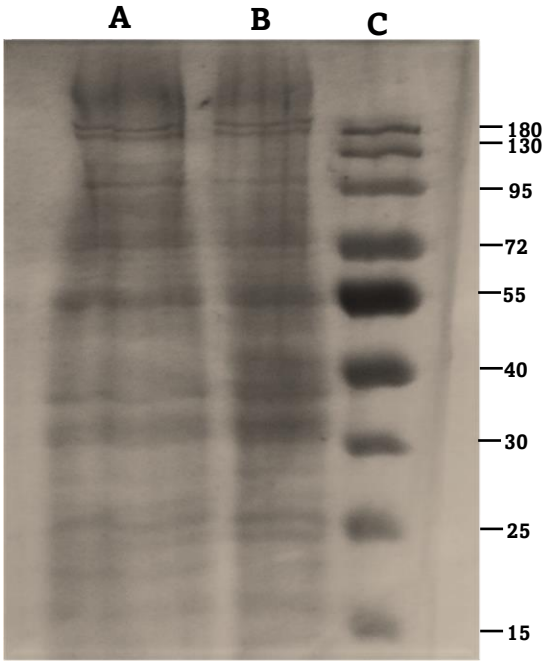

Figure 6.4. SDS-Page (12% acrylamide) treated with Coomassie Brilliant Blue. **A** and **B** represent lysates prepared from the freeze-thaw and sonication methods, respectively. C represents the molecular weight marker.

6.2.3. Separation of Bound Proteins By SDS-Page and Detection by Staining

Electrophoresis explores the separation of a charged molecule due to the presence of an electric field, resulting in separation.[14] The rate at which the charged molecules, such as proteins, migrate towards the electrode of opposite charge depends on a number of factors. These include the electric field's strength, the system's temperature, the concentration of the buffer used, and the charge of the proteins.[14] When electrophoresis is performed in polyacrylamide, the gel acts as a sieve, allowing smaller proteins to move faster than larger ones. In the context of this work, a discontinuous buffer system was used in which the gel is divided into a large-pore "stacking gel" above a smaller-pore "resolving gel." Proteins are initially expected to move quickly through the stacking gel and more slowly as they progress to the resolving gel. Proteins approaching the resolving gel stack on top of each other, forming a tight band which subsequently improves their resolution.[15] Further, the presence of glycinate and chloride ions in the electrophoresis buffer intercalates the proteins as they migrate through the gel. SDS-Page, the most popular form of electrophoresis, includes SDS in the discontinuous buffer system. In the presence of SDS, the separated proteins are completely denatured and dissociate from

each other. SDS binds noncovalently to proteins in a manner that confers (I) an overall negative charge on the proteins, (II) a similar mass-to-charge ratio for all proteins, and (III) a long rod-like shape on the proteins instead of their complex tertiary conformations.[15] Consequently, the rate at which SDS-bound proteins migrate in a gel is dependent on their sizes, which aids in estimating their molecular weight. The detection of individual protein bands following electrophoresis is achieved by staining the gel. Coomassie brilliant Blue series of anionic dyes and silver-based stains are some of the most popular stains.[15–17]It has also been shown in the literature that staining first with Coomassie Brilliant Blue, de-staining, and subsequent staining with silver stain enhances the sensitivity and aids in the identification of low abundance proteins.[17]

6.2.4. Protein Identification by Mass Spectrometry

Samples identified for mass spectrometric analysis are enzymatically cleaved into smaller fragments. This is achieved either by “in-solution” or “in-gel” digestions depending on whether the source is a protein mixture or a band from a protein electrophoresis gel. Before digestion, several modifications are made to the protein in in-gel and in-solution digestions. These modifications include reducing the proteins and thiomethylating of cysteine residues, after which the modified proteins are digested by an appropriate protease such as trypsin.[18]. Following the removal of residual components from the digestion, liquid chromatography separates the trypsin-digested peptides by hydrophobicity. These peptides are then delivered to a tandem mass spectrometer. In this work, mass spectra were obtained on a Q Exactive mass spectrometer operating in positive mode. The peptides were ionized by electrospray ionization, and the first spectrometer separated peptides according to their mass-to-charge ratio (m/z). Ions of a particular m/z ratio are then selected and fragmented. The resulting fragments ions are separated and detected on the second spectrometer. The resulting fragment ions from this second stage of MS are compared to the database to identify the proteins that initially correspond to the observed fragment ions.[19]

6.3. Affinity Chromatography and Identification of Protein Binding Partners

6.3.1 Preparation of the PBI Antimalarial-Labelled Stationary Phase

As mentioned earlier in this chapter, affinity chromatography requires the attachment of the molecules understudy to a stationary phase. *N*-hydroxysuccinimide-activated Sepharose 4 Fast Flow (GE Health care) was identified as an appropriate stationary phase. (Figure 6.5) This highly cross-linked agarose matrix contains pre-activated NHS end groups. These groups form stable amide bonds when reacted with small molecules of interest, containing amine groups. Due to the presence of a secondary amine on the side chain of both PBI compounds described in this chapter, this agarose bead was predicted to be compatible with the compounds. Its NHS end groups would enable the compounds to be immobilized on the stationary phase without any further derivatizations that could compromise their interactions with their putative target (s).

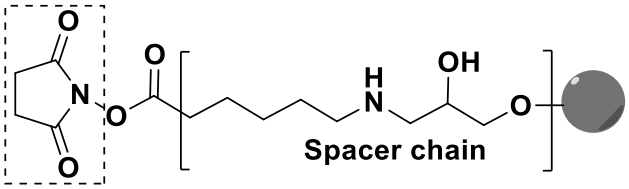

Figure 6.5. Sepharose 4 Fast Flow beads activated with an N-hydroxysuccinimide (NHS) leaving group indicated in the dashed box. The spacer chain is shown in brackets.[19]

The choice of the spacer chain between the bead and the activated end-group is equally essential. The spacer chain should be long enough for binding to the target and not too long to allow for promiscuous binding to many other off-targets. A short spacer chain may generate steric hindrance, obstructing the ligand-target interaction. On the other hand, if the spacer chain is too hydrophobic, different linkers may interact with one another or promote unspecific target binding with proteins. Consequently, an appropriate chemical spacer should be moderately hydrophilic and lengthy enough to avoid steric hindrance. The spacer chain in the NHS-activated Sepharose bead met the above-stated criteria and was found to be appropriate for this study. The ligands under investigation in this work, **KP68,** and **KP124,** are secondary amine-containing molecules capable of undergoing coupling reactions with NHS-activated beads through nucleophilic acyl substitution

(S_NAc), as shown in Figure 6.6. This results in the loss of the NHS group and the formation of an amide bond between the compounds and the affinity matrix.

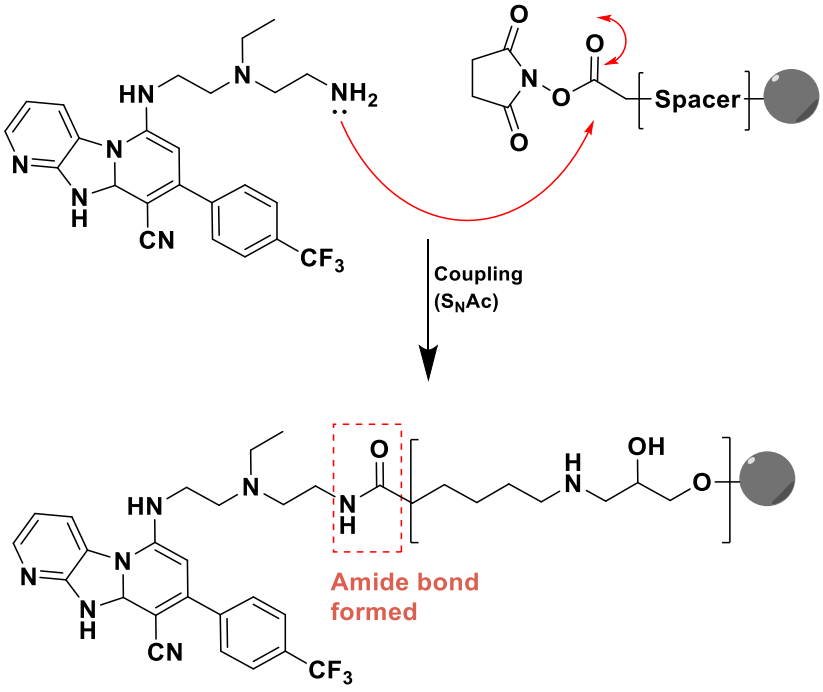

Figure 6.6. The coupling reaction to the beads via nucleophilic acyl substitution (S_NAc) of the N-hydroxysuccinimidyl ester is exemplified by **KP124**.

A workflow for preparing the drug-labelled beads is described in Figure 6.7. Briefly, the beads were washed with 1 mM HCl to remove the isopropanol solution in which they were supplied. Afterward, they were incubated in a solution made of the required moles of the derivatized drug necessary for the desired loading capacity of the beads. The drug solution was made up of 100 Mm Hepes at pH 8.4. However, since both compounds are not completely soluble in an aqueous medium, about 10% DMSO was added to aid dissolution. This was rotated at 25°C for one hour, after which the beads were washed with a fresh ligand-free buffer three times. The washings of unbound drugs were collected, made to a specific volume, and quantified by the spectrometry to assess the amount of ligand immobilized on the bead (Figure 6.8). The drug-labelled beads were further incubated in a "blocking solution" of 100 mM Tris at pH 8.5. This is to allow the primary amine-containing Tris molecule to react with the NHS-activated end groups of the Sepharose beads to produce a Tris-blocked end group that is hydrophilic. Finally, the

beads were washed with low and high pH buffers and stored in 20% aqueous ethanol to prevent microbial contamination.

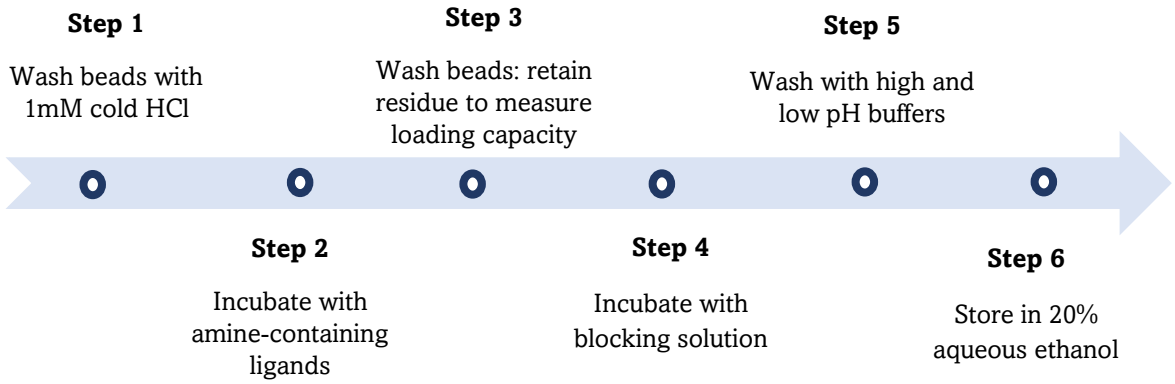

Figure 6.7. Workflow for the preparation of drug-labelled beads for this study.

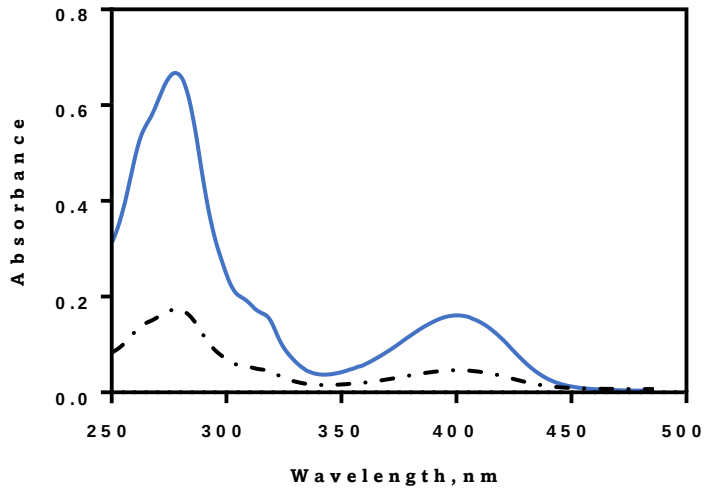

Figure 6.8. The UV-visible spectrum of **KP68** before immobilization on the NHS-activated Sepharose beads (blue) and of the wash-off after immobilization (Black dashed) shows the successful labelling of the beads.

The ligand required to derivatize a specific amount of the beads depends on the ligand's size and the putative target (s). According to previous studies, 3 µmol ligand/mL matrix was an ideal concentration for a pull-down study.[20] However, the manufacturers indicated that to load the beads to 100%, 19.5 µmol ligand/mL of ligand to bead is required.[21] To assess the effect of the loading capacity on the experiment, *P. falciparum* soluble lysate was incubated with beads labelled with 3 µmol of **KP68** per mL and those labelled with 19 µmol per mL of beads. It was observed that loading the beads with 19 µmol/mL of

ligand overloaded the matrix. An overloaded matrix encourages non-specific binding due to proteins' auto-aggregation. On the other hand, when the beads were loaded to about 15% of their capacity (3 µmol/mL), almost all the ligand in the solution was linked to the matrix within an hour. This lane also showed a better elution profile where presumably only proteins of interest to the ligand are retained. (Figure 6.9.A) The washings after immobilization showed almost no signal on the spectrophotometer.

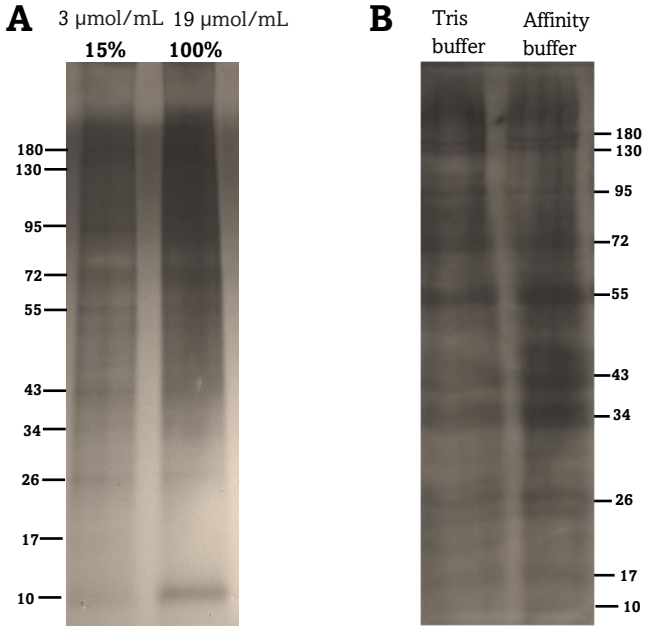

Figure 6.9. SDS-page (12% acrylamide) stained with silver stain. Panel **A** depicts the difference between two loading capacities of **KP86-**labelled beads, where 19 µmol/mL represents 100% loading and 3 µmol/mL represents 15% loading. Panel **B** showed similar elution profiles when **KP68**-labelled beads were washed in tris and affinity buffers. In both panels, labelled beads were incubated with *P. falciparum* soluble fraction and eluted by solid-phase elution.

The choice of a buffer system was based on a Hepes-based buffer previously described by graves and co-workers at pH 7.5[22], which contained 0.1% CHAPS detergent known as the "affinity buffer''. However, other buffer systems such as Tris-based buffer at pH 8.3 have been previously used. To ascertain the effect of these buffer systems on protein binding, **KP68**-labelled beads were exposed to soluble *P. falciparum* lysate fraction in the presence of both Tris and Hepes-based buffers. No significant difference was observed in the elution profiles in both cases (Figure 6.9.B). This implies that a small amount of detergent does not affect protein binding to the matrix. Consequently, affinity buffer was maintained with a slight modification of replacing the 0.1% CHAPS with 0.1% triton.

6.4. Matrix-based Affinity Chromatography of *P. falciparum*

KP68 and **KP124** labelled beads equilibrated in the affinity buffer in which the experiment was conducted. The beads were then incubated with soluble and insoluble lysates from *P. falciparum* mature trophozoite cultures at 4 °C for an hour. After that, the mixture was centrifuged to separate the beads from non-binders in the supernatant. The beads were resuspended in fresh affinity buffer and washed several times to ensure that all unbound proteins were removed. Solid-phase elution was performed to compare and identify the binding proteome of interest to the drug-labelled beads and the ''blocked'' Tris-labelled beads. The blocked tris labelled beads serve as unlabelled bead negative control. Proteins binding to these beads were identified as non-specific protein binders of no interest to either compound. Proteins bound to the drug-labelled and blocked beads were boiled in sample application buffer, centrifuged, and their supernatants separated on the SDS page. The protein bands were subsequently visualized by Coomassie Blue stain followed by silver stain.

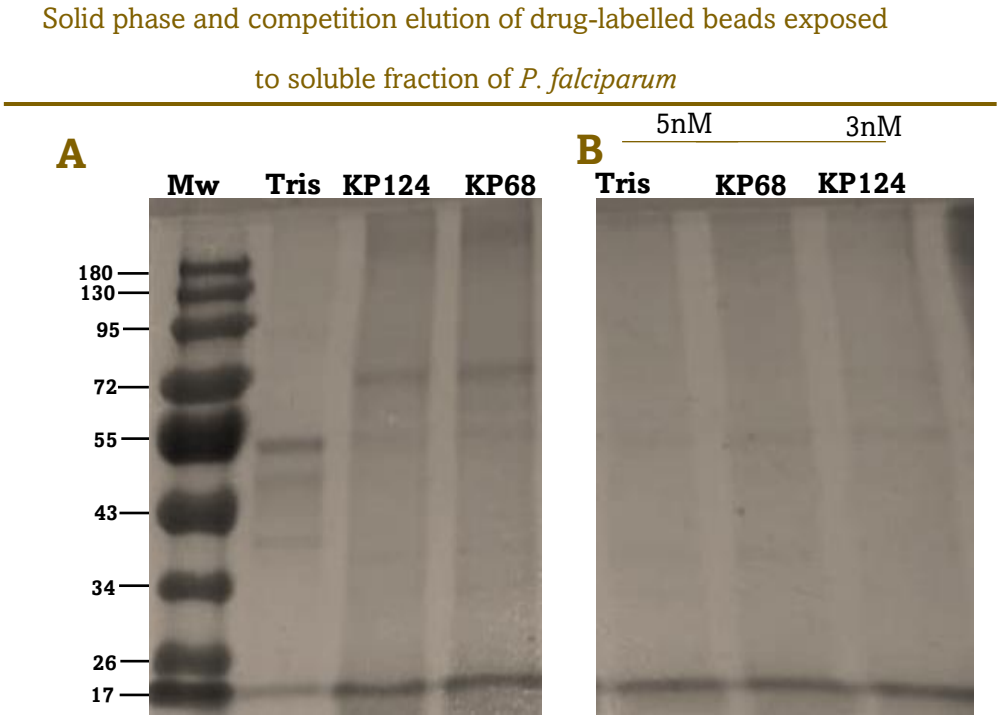

Figure 6.10. SDS-page (12% acrylamide) stained with silver stain. Beads were exposed to a soluble fraction of *P. falciparum*. Gel **A** depicts solid-phase elution after incubation with **KP68**, **KP124,** and Tris labelled beads. MW represents the molecular weight ladder. Gel **B** depicts successive competition eluents with excess free ligand after concentration.

The average protein abundance in *P. falciparum* has been estimated at 200 ppm. Therefore, if all the available potential protein target is retained on the bead and subsequently eluted, it is estimated that 8 ng of the protein will be recovered. Assuming this protein is spread over a gel band of 0.5 mm x 10 mm on SDS-Page, the band representing this protein will have a concentration of 1.6 ng protein/mm^2. The protein detection limit of the silver stain is 0.1 ng/mm^2. This suggests that proteins with abundances 3 ppm and above can be detected on the gel by double staining. More than 80% of the over 5000 proteins in the plasmodium proteome have abundances above 3 ppm. Based on this, 40 µg of lysate was used for these experiments, representing about 5x the limit of P. *falciparum* protein detection on a gel.

After exposing labelled beads to soluble and membrane fractions of the *P. falciparum* cell lysates, they were eluted through solid-phase and competition elution. The competition eluents were pooled and concentrated by ultrafiltration. A silver-stained gel of samples after both solid-phase and competition elution of both **KP68** and **KP124** labelled beads is depicted in Figure 6.10. Several bands were observed in the lanes corresponding to the drug labelled beads between 95-34 kDa and a higher molecular weight band occurring above 180 kDa. The lane corresponding to the Tris-labelled beads showed bands between 55-43 kDa depicting non-specific protein binders since the same bands were observed in the lanes corresponding to the drug labelled beads. Further competition elution revealed lighter bands, equally observed around 72-43 kDa. Although the gel aided in identifying the molecular weight range of the proteins eluted, a more precise MS analysis was required to identify the eluted proteins accurately.

Therefore, the competition eluents were analyzed using MS-based proteomics techniques described in Section 6.2.4. Samples were digested both in-gel and in-solution. For in-gel digestion, the samples were run 1.5 cm in a 12% acrylamide gel and stained with Coomassie Brilliant Blue stain, after which the entire band was cut out and digested using trypsin. Samples were equally digested in solution and compared to those obtained from in-gel digestion. Following digestion, separation, and tandem MS, the peptide fragments obtained were screened against the *P. falciparum* protein database for identification.

6.4.1. Identified Protein Binding Partners of KP68 Using Mass Spectrometry

Ornithine aminotransferase is a highly abundant protein found in the parasite's cytoplasm. MS identified this protein as the most probable binding partner of **KP68**. (Table 6.1) It is involved in the first step of the sub-pathway that synthesizes L-glutamate-5-semialdehyde from L-ornithine. This sub-pathway is part of the L-proline biosynthesis, which is in turn, part of the amino acid biosynthesis pathway. Polyamine biosynthesis is essential for the replication of cells.[23] Various experimental studies have suggested compounds that inhibit different aspects of the polyamine biosynthesis, such as the aminotransferase inhibitor canaline,[24] an ornithine decarboxylase inhibitor difluoromethylornithine,,[25] the S-adenosylmethionine decarboxylate inhibitor MDL75311,[26] and the methylthioadenosine phosphorylase antimetabolite hydroxyethylthioadenosine,[27] all inhibit the growth of *P. falciparum in vitro*. Ornithine aminotransferase from *P. falciparum* 3D7 has been previously cloned, functionally expressed, and characterized. In the *plasmodium falciparum* genome, it exists as a single copy and on chromosomes 6/7/8. The amino acid sequence of ornithine aminotransferase, deduced from the *P. falciparum* 3d7 strain, was 80-85% similar to those observed in *P. yoelii* and *P. vivax*. Aminooxy compounds have been found to inhibit ornithine aminotransferases.[28–30]

In particular, canaline, an aminooxy present in legumes[31], inhibits this enzyme such that large doses of the compound are needed to cause toxicity in mammalian cells (Figure 6.11).[32] For this reason, canaline was previously investigated as an anticancer agent based on its ability to interfere with polyamine synthesis and other biochemical processes in tumour cells.[32] Canaline was later identified as a potent antimalarial compound with the whole-cell activity of 297 ± 23.6 nM and uncompetitively inhibiting the enzyme with a Ki of 492 ± 98 nM.[24] This makes ornithine aminotransferase a viable antimalarial drug target.

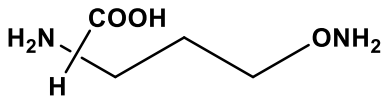

Canaline

P*f*Ki = 492 ± 98 nM
P*f*3D7 = 297 ± 23.6 nM

Figure 6.11. Chemical structure of Canaline with activity in the CQ-sensitive 3D7 strain and an enzymatic activity against ornithine aminotransferase.

S-adenosylmethionine synthase protein, also identified as a binding partner of **KP68,** catalyzes the formation of S-adenosylmethionine from methionine and adenosine triphosphate (ATP). This pathway is used in amino acid biosynthesis as well.

Table 6.1. List of *P. falciparum* proteins identified with **KP68**-labelled beads, in order of decreasing probability.

Protein ID	Protein name	Abundance	Molecular weight (kDa)
PFF0435w	Ornithine aminotransferase	11265 ppm	46
PF3D7_0730900	EMP1-trafficking protein	22 ppm	244
PF3D7_0922200	S-adenosylmethionine synthase	188 ppm	44.8
PF3D7_1466100	Serine/threonine-protein phosphate	72 ppm	101
PF3D7_1462800	Glyceraldehyde-3-phosphate dehydrogenase	20141 ppm	37
PF3D7_0501300	Skeleton-binding protein	451 ppm	36
PF3D7_0501600	Rhoptry-associated protein 2	31 ppm	48
PF3D7_0818900	Heat shock protein 70	8798 ppm	74
PF3D7_1325400	Uncharacterized protein OS	20 ppm	419

The glyceraldehyde-3-phosphate dehydrogenase is essential to the glycolytic pathway, ultimately contributing to carbohydrate degradation.[33] Previously, the gene for *P. falciparum* glyceraldehyde-3-phosphate dehydrogenase (P*f*GAPDH) was cloned, and the protein expressed as histidine-tagged recombinant protein from *Escherichia coli*.[34] The protein's three-dimensional structure was determined from the crystallized recombinant protein.[34,35] Although the RBCs protect the parasite from the host's immune system, it makes the acquisition of relevant nutrients for its growth challenging. For instance, the intraerythrocytic parasites require enormous energy for rapid growth and division. However, many of the biosynthetic pathways necessary to produce the needed energy are absent in the parasite.[33,36] Consequently, Roth and co-workers earlier demonstrated increased levels of glycolysis in parasite-infected RBCs in comparison to unparasitized

RBCs, resulting from parasite-derived glycolytic enzymes.[33] Their findings stirred interest in developing glycolytic enzymes such as P*f*GAPDH as targets for antimalarial drug discovery.[37] There are ten catalytic pathways available in the glycolytic pathway to convert glucose to pyruvate with the release of ATP, and GAPDH catalyzes the sixth of those in the host. Interrupting the process of glycolysis would block ATP production.[34,35] There have been efforts to identify inhibitors that selectively inhibit P*f*GAPDH over the human ortholog by exploring structural differences in both enzymes.[38] P*f*GAPDH was equally identified as a binding partner for **KP124**.

Another protein identified to be of interest to **KP68** is the *Plasmodium falciparum* skeleton binding protein 1 (P*f*SBP1). This protein is an extracellular protein, also found in the integral components of the parasite's membrane and the Maurer's cleft.[39] Studies have shown that P*f*SBP1 is required to transport the *Plasmodium falciparum* erythrocyte membrane protein 1 (P*f*EMP1).[40] Upon the parasite's invasion of the host erythrocytes, it alters the host cells by exporting parasite-encoded proteins across the parasitophorous vacuole membrane (PVM) into the cytosol of the erythrocyte and some transported into the membrane of the host membrane.[41,42] This completely alters the infected host erythrocyte to aid in acquiring nutrients and evading the host's immune system. Many processes are involved in transporting proteins to the surface and cytoskeleton of parasitized RBCs. These include trafficking across the parasite membrane, erythrocyte cytosol, and PVM.[43,44] Before reaching their destination, transported proteins interact with structures such as the Maurer clefts and the knobs.[45,46] These structures provide a template for P*f*EMP1.[47] The role of P*f*EMP1 is to mediate adhesion by binding to host receptors, including chondroitin sulfate A and to import mitochondrial protein.[48] In addition to being essentially required for the transport of P*f*EMP1, P*f*SBP1 is believed to be responsible for anchoring Maurer clefts to the erythrocyte cytoplasm and also interacts with host proteins to prevent the early rupture of the RBCs.[49]

Rhoptry associated protein 2 (RAP2), also found to interact with **KP68,** is located in the parasite's rhoptries. Together with RAP1 and RAP3, these proteins are thought to play significant roles in the invasion of erythrocytes by extracellular merozoites and the overall maintenance of the intraerythrocytic cycle.[50] Other proteins such as the *Plasmodium falciparum* heat shock protein and the uncharacterized protein OS were equally identified

as protein binding partners. Out of all the proteins identified as binding partners of **KP68**, ornithine aminotransferase is the only chemically validated target in *P. falciparum* and the most probable binding partner identified by MS. However, this protein is highly abundant in the cell, which could increase its probability of interacting with **KP68**. What is more interesting is the P*f*EMP1 which localizes in the lumen-facing lipid bilayer of the mitochondrial envelope.[51] In the mitochondrion, it serves as mitochondrial adenosine diphosphate (ADP) and ATP transmembrane transporter.[51] However, a few hours post the intraerythrocytic stage of infection, P*f*EMP1 is transported with the help of other proteins such as P*f*SBP1 onto the host cell's surface.[52] There, the protein is anchored by electron-dense protrusions on the surface of the RBCs known as knobs.[53] The P*f*EMP1-knobs complex at the surface of parasite-infected RBCs are responsible for the virulent adhesion-related pathologies such as cerebral and placental malaria.[54] More recently, Chen and co-workers utilized combined transcriptome and proteome profiling to implicate P*f*EMP1 in the antimalarial action of dihydroartemisinin (DHA).[55] They showed, via optical and scanning electron microscopy, morphological differences in the membrane of infected RBCs due to DHA. Also, artemisinin sensitivity was significantly increased when P*f*EMP1 was knocked out, suggesting that the protein might be involved in the action of DHA.[55] Consequently, P*f*EMP1 can be exploited as a target in antimalarial drug design. Besides the fact that P*f*EMP1 is essential for the survival of the parasites, significant amounts of **KP68** were observed to envelop the parasite's mitochondrial membrane. Also, the mitochondrial carrier proteins mediate resistance in the compound. Consequently, inhibition of the high molecular weight mitochondrial protein P*f*EMP1 could contribute significantly to the compounds MOA. All proteins identified as binding partners of **KP68** are absent in the Tris-labelled beads competed off by **KP68**. Hence these proteins are specific to **KP68.**

6.4.2. Identified Protein Binding Partners of KP124 Using Mass Spectrometry

KP124 has been previously identified as an inhibitor of the conversion of heme to hemozoin through the heme speciation assay and fluorescent localization studies. The direct conversion of heme to hemozoin is not a protein-mediated process. There have been varying theories about how hemozoin is formed, including it being lipid-mediated, as earlier discussed in Section 1.3.1.2. However, protein inhibition is not required by a

drug to inhibit the conversion of heme to hemozoin. Inhibition of hemozoin formation is has been shown in Chapter 4 as a MOA of **KP124**, and it is believed that other targets or mechanism (s) might be involved in the compound's action. MS identified the elongation factor 1-alpha protein, serine/threonine protein, GTPase-activating protein, putative, Glyceraldehyde-3-phosphate dehydrogenase, ribosomal protein S3 OS and Exported protein 2 OS proteins. Of these, the serine/threonine protein and the Glyceraldehyde-3-phosphate dehydrogenase protein were equally identified as protein binding partners for **KP68** (Table 6.2).

Table 6.2. List of *P. falciparum* proteins identified with **KP124**-labelled beads, in order of decreasing probability.

Protein ID	Protein name	Abundance	Molecular weight (kDa)
PF3D7_1357000	Elongation factor 1-alpha	6558 ppm	46
PF3D7_1466100	Serine/threonine-protein phosphatase	72 ppm	100
PF3D7_0907200	GTPase-activating protein, putative	17 ppm	134
PF3D7_1466100	Glyceraldehyde-3-phosphate dehydrogenase	20141 ppm	101
PF3D7_1465900	ribosomal protein S3 OS	3303 ppm	25
PF3D7_1471100	Exported protein 2 OS	864.7 ppm	33

The *P. falciparum* elongation factor-1-alpha protein is an abundance cytoplasmic protein which enhances the guanosine triphosphate (GTP)-dependent binding of aminoacyl-transfer RNA to the A-site of ribosomes during protein biosynthesis.[56] Also identified is the *P. falciparum GTPase*-activating protein, putative. The main functions of this protein are intracellular transport and activation of the parasite's GTPase activity.[51] In conjunction with other factors and proteins, it also plays a vital role in initiating protein synthesis in eukaryotes, including *P. falciparum*.[57] Further, the ribosomal protein S3, found in the parasite's cytosolic small ribosomal subunit and the nucleus, was identified as a protein-binding partner of **KP124**. It is a structural constituent of the ribosome and is actively

involved in RNA binding.[51] Finally, the Serine/threonine-protein phosphatase was identified as a binding partner for both **KP124** and **KP68** labelled beads after competition elution. This protein is localized in the parasite's nucleus, and its function is not clearly defined. It is thought to be involved in the dephosphorylation of proteins.[51] It is uncertain how essential this protein is to parasite survival. However, its function is linked to protein biosynthesis and transport. It is also interesting to note that almost all the proteins identified in relation to **KP124** directly or indirectly affect protein biosynthesis in the parasite. This implicates this pathway in the action of the compound, with a significant contribution from hemozoin inhibition.

6.5. Conclusion

Although benzimidazoles and PBIs have been earlier identified as privileged scaffolds that can be exploited for antimalarial drug discovery, there is no literature regarding their MOA. Inhibition of the formation of hemozoin inhibition is a contributory MOA of these scaffolds. However, there are no reports of studies that assess a direct engagement of analogues of these scaffolds with their protein binding partners in *P. falciparum*. Chemical proteomics strategies have successfully identified protein targets of compounds and deconvoluted their MOA. In this regard, biological materials in the form of cell lysates from *P. falciparum* trophozoites were prepared appropriately for use in these experiments. **KP68** and **KP124** labelled matrices were prepared by reacting *N*-hydroxysuccinimide-activated beads with the primary amine derivatives prepared in chapter 2 of this thesis. The coupling capacity of the matrix was reduced from 19.5 to 3 µmol/mL to prevent the overloading of the beads. The drug-labelled matrices were used to capture **KP68** and **KP124** protein binding partners in *P. falciparum-infected* RBCs. The binding sub-proteomes were separated and visualized on SDS-Page and identified via MS.

After competing off relevant proteins associated with **KP68,** several faint bands were observed between the molecular weights of 55-180 kDa with a higher molecular weight band above 180kDa. This band was later identified as the P*f*EMP1 with a molecular weight of 244 kDa. This protein is essential to the survival of the parasite, such that inhibiting it could lead to parasite death. Other proteins were also identified, including ornithine aminotransferase, P*f*GAPDH, and RAP2. They could all be inhibited synergistically by **KP68** to cause overall stress and the ultimate death of the parasite.

The proteins identified as binding partners of **KP124** include the elongation factor 1-alpha, GTPase-activating protein, putative, and the ribosomal protein S3 OS, all of which directly function to support protein biosynthesis in the parasite.

The proteins identified as binding partners of **KP68** are not representative of the genes implicated in the compound's resistance mechanism described in Chapter 5. It was anticipated that the results from the proteomics experiment would complement that of the resistance selection experiment. However, no correlation can be drawn from the results obtained from the two approaches

6.6. References

(1) Korkor, C. M.; Garnie, L. F.; Amod, L.; Egan, T. J.; Chibale, K. Intrinsic Fluorescence Properties of Antimalarial Pyrido[1,2- a]Benzimidazoles Facilitate Subcellular Accumulation and Mechanistic Studies in the Human Malaria Parasite *Plasmodium falciparum*. *Org. Biomol. Chem.* **2020**, *18* (42), 8668–8676.

(2) Singh, K.; Okombo, J.; Brunschwig, C.; Ndubi, F.; Barnard, L.; Wilkinson, C.; Njogu, P. M.; Njoroge, M.; Laing, L.; Machado, M.; Prudêncio, M.; Reader, J.; Botha, M.; Nondaba, S.; Birkholtz, L.-M.; Lauterbach, S.; Churchyard, A.; Coetzer, T. L.; Burrows, J. N.; Yeates, C.; Denti, P.; Wiesner, L.; Egan, T. J.; Wittlin, S.; Chibale, K. Antimalarial Pyrido[1,2- a]Benzimidazoles: Lead Optimization, Parasite Life Cycle Stage Profile, Mechanistic Evaluation, Killing Kinetics, and in Vivo Oral Efficacy in a Mouse Model. *J. Med. Chem.* **2017**, *60* (4), 1432–1448. 1.

(3) Cowell, A. N.; Winzeler, E. A. Advances in Omics-Based Methods to Identify Novel Targets for Malaria and Other Parasitic Protozoan Infections. *Genome Med.* **2019**, *11* (1), 63.

(4) Magistrado, P. A.; Corey, V. C.; Lukens, A. K.; LaMonte, G.; Sasaki, E.; Meister, S.; Wree, M.; Winzeler, E.; Wirth, D. F. *Plasmodium falciparum* Cyclic Amine Resistance Locus (P*f*CARL), a Resistance Mechanism for Two Distinct Compound Classes. *ACS Infect. Dis.* **2016**, *2* (11), 816–826.

(5) Paquet, T.; Le Manach, C.; Cabrera, D. G.; Younis, Y.; Henrich, P. P.; Abraham, T. S.; Lee, M. C. S.; Basak, R.; Ghidelli-Disse, S.; Lafuente-Monasterio, M. J.; Bantscheff, M.; Ruecker, A.; Blagborough, A. M.; Zakutansky, S. E.; Zeeman, A.-M.; White, K. L.; Shackleford, D. M.; Mannila, J.; Morizzi, J.; Scheurer, C.; Angulo-Barturen, I.; Martínez, M. S.; Ferrer, S.; Sanz, L. M.; Gamo, F. J.; Reader, J.; Botha, M.; Dechering, K. J.; Sauerwein, R. W.; Tungtaeng, A.; Vanachayangkul, P.; Lim, C. S.; Burrows, J.; Witty, M. J.; Marsh, K. C.; Bodenreider, C.; Rochford, R.; Solapure, S. M.; Jiménez-Díaz, M. B.; Wittlin, S.; Charman, S. A.; Donini, C.; Campo, B.; Birkholtz, L.-M.; Hanson, K. K.; Drewes, G.; Kocken, C. H. M.; Delves, M. J.; Leroy, D.; Fidock, D. A.; Waterson, D.; Street, L. J.; Chibale, K. Antimalarial Efficacy of MMV390048, an Inhibitor of Plasmodium Phosphatidylinositol 4-Kinase. *Sci.*

Transl. Med. **2017**, *9* (387).

(6) Gregori-Puigjané, E.; Setola, V.; Hert, J.; Crews, B. A.; Irwin, J. J.; Lounkine, E.; Marnett, L.; Roth, B. L.; Shoichet, B. K. Identifying Mechanism of Action Targets for Drugs and Probes. *Proc. Natl. Acad. Sci.* **2012**, *109* (28), 11178–11183.

(7) Loh, C. C. Y.; Suwanarusk, R.; Lee, Y. Q.; Chan, K. W. K.; Choy, K.-Y.; Rénia, L.; Russell, B.; Lear, M. J.; Nosten, F. H.; Tan, K. S. W.; Chow, L. M. C. Characterization of the Commercially-Available Fluorescent Chloroquine-BODIPY Conjugate, LynxTag-CQ green, as a Marker for Chloroquine Resistance and Uptake in a 96-Well Plate Assay. *PLoS One* **2014**, *9* (10), e110800.

(8) Yang, T.; Ottilie, S.; Istvan, E. S.; Godinez-Macias, K. P.; Lukens, A. K.; Baragaña, B.; Campo, B.; Walpole, C.; Niles, J. C.; Chibale, K.; Dechering, K. J.; Llinás, M.; Lee, M. C. S.; Kato, N.; Wyllie, S.; McNamara, C. W.; Gamo, F. J.; Burrows, J.; Fidock, D. A.; Goldberg, D. E.; Gilbert, I. H.; Wirth, D. F.; Winzeler, E. A. MalDA, Accelerating Malaria Drug Discovery. *Trends Parasitol.* **2021**, *37* (6), 493–507.

(9) Terstappen, G. C.; Schlüpen, C.; Raggiaschi, R.; Gaviraghi, G. Target Deconvolution Strategies in Drug Discovery. *Nat. Rev. Drug Discov.* **2007**, *6* (11), 891–903.

(10) Gardner, M. J.; Hall, N.; Fung, E.; White, O.; Berriman, M.; Hyman, R. W.; Carlton, J. M.; Pain, A.; Nelson, K. E.; Bowman, S.; Paulsen, I. T.; James, K.; Eisen, J. A.; Rutherford, K.; Salzberg, S. L.; Craig, A.; Kyes, S.; Chan, M.-S.; Nene, V.; Shallom, S. J.; Suh, B.; Peterson, J.; Angiuoli, S.; Pertea, M.; Allen, J.; Selengut, J.; Haft, D.; Mather, M. W.; Vaidya, A. B.; Martin, D. M. A.; Fairlamb, A. H.; Fraunholz, M. J.; Roos, D. S.; Ralph, S. A.; McFadden, G. I.; Cummings, L. M.; Subramanian, G. M.; Mungall, C.; Venter, J. C.; Carucci, D. J.; Hoffman, S. L.; Newbold, C.; Davis, R. W.; Fraser, C. M.; Barrell, B. Genome Sequence of the Human Malaria Parasite *Plasmodium falciparum*. *Nature* **2002**, *419* (6906), 498–511.

(11) Fong, K. Y.; Wright, D. W. Hemozoin and Antimalarial Drug Discovery. *Future Med. Chem.* **2013**, *5* (12), 1437–1450.

(12) Egan, T. J.; Mavuso, W. W.; Ross, D. C.; Marques, H. M. Thermodynamic Factors Controlling the Interaction of Quinoline Antimalarial Drugs with Ferriprotoporphyrin IX. *J. Inorg. Biochem.* **1997**, *68* (2), 137–145.

(13) Comper, W. D.; Zamparo, O. Hydraulic Conductivity of Polymer Matrices. *Biophys. Chem.* **1989**, *34* (2), 127–135.

(14) Garfin, D. E. One-Dimensional Gel Electrophoresis; 1990; pp 425–441.

(15) A Guide to Polyacrylamide Gel Electrophoresis and Detection.

(16) de Villiers, K. A.; Gildenhuys, J.; Roux, Le, T. Iron(III) Protoporphyrin IX Complexes of the Antimalarial Cinchona Alkaloids Quinine and Quinidine. *ACS Chem. Biol.* **2012**, *7* (4), 666–671.

(17) Sigma-Aldrich. ProteoSilver Plus Silver Stain Kit Technical Bulletin.

(18) Aebersold, R.; Mann, M. Mass Spectrometry-Based Proteomics. *Nature* **2003**, *422* (6928), 198–207.

(19) Rix, U.; Superti-Furga, G. Target Profiling of Small Molecules by Chemical Proteomics. *Nat. Chem. Biol.* **2009**, *5* (9), 616–624.

(20) Guiffant, D.; Tribouillard, D.; Gug, F.; Galons, H.; Meijer, L.; Blondel, M.; Bach, S. Identification of Intracellular Targets of Small Molecular Weight Chemical Compounds Using Affinity Chromatography. *Biotechnol. J.* **2007**, *2* (1), 68–75.

(21) Amersham Biosciences. *Affinity Chromatography: Principles and Methods*; 2002.

(22) Graves, P. R.; Kwiek, J. J.; Fadden, P.; Ray, R.; Hardeman, K.; Coley, A. M.; Foley, M.; Haystead, T. A. J. Discovery of Novel Targets of Quinoline Drugs in the Human Purine Binding Proteome. *Mol. Pharmacol.* **2002**, *62* (6), 1364–1372.

(23) Marton, L. J.; Pegg, A. E. Polyamines as Targets for Therapeutic Intervention. *Annu. Rev. Pharmacol. Toxicol.* **1995**, *35* (1), 55–91.

(24) Berger, B. J. Antimalarial Activities of Aminooxy Compounds. *Antimicrob. Agents Chemother.* **2000**, *44* (9), 2540–2542.

(25) Assaraf, Y. G.; Golenser, J.; Spira, D. T.; Messer, G.; Bachrach, U. Cytostatic Effect of Difluoromethylornithine against *Plasmodium falciparum* and Its Reversal by Diamines and Spermidine. *Parasitol. Res.* **1987**, *73* (4), 313–318.

(26) Wright, P. S.; Byers, T. L.; Cross-Doersen, D. E.; McCann, P. P.; Bitonti, A. J.

Irreversible Inhibition of S-Adenosylmethionine Decarboxylase in *Plasmodium falciparum*-Infected Erythrocytes: Growth Inhibition in Vitro. *Biochem. Pharmacol.* **1991**, *41* (11), 1713–1718.

(27) Sufrin, J. R.; Meshnick, S. R.; Spiess, A. J.; Garofalo-Hannan, J.; Pan, X. Q.; Bacchi, C. J. Methionine Recycling Pathways and Antimalarial Drug Design. *Antimicrob. Agents Chemother.* **1995**, *39* (11), 2511–2515.

(28) Baskaran, N.; Prakash, V.; Savithri, H. S.; Radhakrishnan, A. N.; Rao, N. A. Mode of Interaction of Aminooxy Compounds with Sheep Liver Serine Hydroxymethyltransferase. *Biochemistry* **1989**, *28* (25), 9613–9617.

(29) Beeler, T.; Churchich, J. E. Reactivity of the Phosphopyridoxal Groups of Cystathionase. *J. Biol. Chem.* **1976**, *251* (17), 5267–5271.

(30) Rosenthal, G. A. L-Canaline: A Potent Antimetabolite and Anti-Cancer Agent from Leguminous Plants. *Life Sci.* **1997**, *60* (19), 1635–1641.

(31) Rosenthal, G. A.; Hughes, C. G.; Janzen, D. H. L-Canavanine, a Dietary Nitrogen Source for the Seed Predator Caryedes Brasiliensis (Bruchidae). *Science (80-.).* **1982**, *217* (4557), 353–355.

(32) Bolkenius, F. N.; Knödgen, B.; Seiler, N. DL-Canaline and 5-Fluoromethylornithine. Comparison of Two Inactivators of Ornithine Aminotransferase. *Biochem. J.* **1990**, *268* (2), 409–414.

(33) Roth, E. J.; Calvin, M.; Max-Audit, I.; Rosa, J.; Rosa, R. The Enzymes of the Glycolytic Pathway in Erythrocytes Infected with *Plasmodium falciparum* Malaria Parasites. *Blood* **1988**, *72* (6), 1922–1925.

(34) Satchell, J. F.; Malby, R. L.; Luo, C. S.; Adisa, A.; Alpyurek, A. E.; Klonis, N.; Smith, B. J.; Tilley, L.; Colman, P. M. Structure of Glyceraldehyde-3-Phosphate Dehydrogenase from *Plasmodium falciparum*. *Acta Crystallogr. Sect. D Biol. Crystallogr.* **2005**, *61* (9), 1213–1221.

(35) Daubenberger, C. A.; Pöltl-Frank, F.; Jiang, G.; Lipp, J.; Certa, U.; Pluschke, G. Identification and Recombinant Expression of Glyceraldehyde-3-Phosphate Dehydrogenase of *Plasmodium falciparum*. *Gene* **2000**, *246* (1–2), 255–264.

(36) Roth Jr, E. Plasmodium Falciparum Carbohydrate Metabolism: A Connection between Host Cell and Parasite. *Blood Cells* **1990**, *16* (2–3), 453–460.

(37) Brady, R.; Cameron, A. Structure-Based Approaches to the Development of Novel Anti-Malarials. *Curr. Drug Targets* **2004**, *5* (2), 137–149.

(38) Ladame, S.; Fauré, R.; Denier, C.; Lakhdar-Ghazal, F.; Willson, M. Selective Inhibition of Trypanosoma Cruzi GAPDH by "Bi-Substrate" Analogues. *Org. Biomol. Chem.* **2005**, *3* (11), 2070.

(39) Blisnick, T.; Betoulle, M. E. M.; Barale, J.-C.; Uzureau, P.; Berry, L.; Desroses, S.; Fujioka, H.; Mattei, D.; Breton, C. B. Pfsbp1, a Maurer's Cleft *Plasmodium falciparum* Protein, Is Associated with the Erythrocyte Skeleton. *Mol. Biochem. Parasitol.* **2000**, *111* (1), 107–121.

(40) Maier, A. G.; Rug, M.; O'Neill, M. T.; Beeson, J. G.; Marti, M.; Reeder, J.; Cowman, A. F. Skeleton-Binding Protein 1 Functions at the Parasitophorous Vacuole Membrane to Traffic P*f*EMP1 to the *Plasmodium falciparum*–Infected Erythrocyte Surface. *Blood* **2007**, *109* (3), 1289–1297.

(41) Marti, M.; Good, R. T.; Rug, M.; Knuepfer, E.; Cowman, A. F. Targeting Malaria Virulence and Remodeling Proteins to the Host Erythrocyte. *Science (80-.).* **2004**, *306* (5703), 1930–1933.

(42) Hiller, N. L.; Bhattacharjee, S.; van Ooij, C.; Liolios, K.; Harrison, T.; Lopez-Estrano, C.; Haldar, K. A Host-Targeting Signal in Virulence Proteins Reveals a Secretome in Malarial Infection. *Science (80-.).* **2004**, *306* (5703), 1934–1937.

(43) Wickham, M. E.; Rug, M.; Ralph, S. A.; Klonis, N.; McFadden, G. I.; Tilley, L.; Cowman, A. F. Trafficking and Assembly of the Cytoadherence Complex in *Plasmodium falciparum*-Infected Human Erythrocytes. *EMBO J.* **2001**, *20* (20), 5636–5649.

(44) Lopez-Estraño, C.; Bhattacharjee, S.; Harrison, T.; Haldar, K. Cooperative Domains Define a Unique Host Cell-Targeting Signal in *Plasmodium falciparum*-Infected Erythrocytes. *Proc. Natl. Acad. Sci.* **2003**, *100* (21), 12402–12407.

(45) Kilejian, A.; Abati, A.; Trager, W. *Plasmodium falciparum* and Plasmodium Coatneyi:

Immunogenicity of “Knob-like Protrusions” on Infected Erythrocyte Membranes. *Exp. Parasitol.* **1977**, *42* (1), 157–164.

(46) Kilejian, A.; Jensen, J. B. A Histidine-Rich Protein from *Plasmodium falciparum* and Its Interaction with Membranes. *Bull. World Health Organ.* **1977**, *55* (2–3), 191.

(47) Su, X.; Heatwole, V. M.; Wertheimer, S. P.; Guinet, F.; Herrfeldt, J. A.; Peterson, D. S.; Ravetch, J. A.; Wellems, T. E. The Large Diverse Gene Family Var Encodes Proteins Involved in Cytoadherence and Antigenic Variation of *Plasmodium falciparum*-Infected Erythrocytes. *Cell* **1995**, *82* (1), 89–100.

(48) Baruch, D. I.; Ma, X. C.; Singh, H. B.; Bi, X.; Pasloske, B. L.; Howard, R. J. Identification of a Region of P*f*EMP1 That Mediates Adherence of *Plasmodium falciparum* Infected Erythrocytes to CD36: Conserved Function with Variant Sequence. *Blood, J. Am. Soc. Hematol.* **1997**, *90* (9), 3766–3775.

(49) Blisnick, T.; Vincensini, L.; Barale, J. C.; Namane, A.; Breton, C. B. LANCL1, an Erythrocyte Protein Recruited to the Maurer’s Clefts during *Plasmodium falciparum* Development. *Mol. Biochem. Parasitol.* **2005**, *141* (1), 39–47.

(50) Perrin, L. H.; Merkli, B.; Gabra, M. S.; Stocker, J. W.; Chizzolini, C.; Richle, R. Immunization with a *Plasmodium falciparum* Merozoite Surface Antigen Induces a Partial Immunity in Monkeys. *J. Clin. Invest.* **1985**, *75* (5), 1718–1721.

(51) https://www.uniprot.org/.

(52) McHugh, E.; Carmo, O. M. S.; Blanch, A.; Looker, O.; Liu, B.; Tiash, S.; Andrew, D.; Batinovic, S.; Low, A. J. Y.; Cho, H.-J.; McMillan, P.; Tilley, L.; Dixon, M. W. A. Role of *Plasmodium falciparum* Protein GEXP07 in Maurer’s Cleft Morphology, Knob Architecture, and *P. falciparum* EMP1 Trafficking. *MBio* **2020**, *11* (2).

(53) Looker, O.; Blanch, A. J.; Liu, B.; Nunez-Iglesias, J.; McMillan, P. J.; Tilley, L.; Dixon, M. W. A. The Knob Protein KAHRP Assembles into a Ring-Shaped Structure That Underpins Virulence Complex Assembly. *PLOS Pathog.* **2019**, *15* (5), e1007761.

(54) Rowe, J. A.; Claessens, A.; Corrigan, R. A.; Arman, M. Adhesion of *Plasmodium falciparum*-Infected Erythrocytes to Human Cells: Molecular Mechanisms and Therapeutic Implications. *Expert Rev. Mol. Med.* **2009**, *11*.

(55) Chen, L.; Zheng, Z.; Liu, H.; Wang, X.; Qu, S.; Yang, Y.; Deng, S.; Zhang, Y.; Tuo, L.; Zhao, Y.; Li, Y. Combined Transcriptome and Proteome Profiling for Role of P*f*EMP1 in Antimalarial Mechanism of Action of Dihydroartemisinin. *Microbiol. Spectr.* **2021**, *9* (3).

(56) Riis, B.; Rattan, S. I. S.; Clark, B. F. C.; Merrick, W. C. Eukaryotic Protein Elongation Factors. *Trends Biochem. Sci.* **1990**, *15* (11), 420–424.

(57) Das, S.; Ghosh, R.; Maitra, U. Eukaryotic Translation Initiation Factor 5 Functions as a GTPase-Activating Protein. *J. Biol. Chem.* **2001**, *276* (9), 6720–6726.

Chapter Seven

Overall Conclusions and Recommendations for Future Work

7.1. Overall Conclusions

Malaria remains a daunting global problem that is characterized by intermittent high fevers. Further neurological complications such as brain injury and coma may occur in the case of cerebral malaria.[1] The disease primarily affects pregnant women and children under five years old. In most West African countries such as Ghana, a child dies of malaria every minute.[2] Over the years, chemotherapy has been the mainstay of malaria control and treatment. However, the challenges posed by the emergence of resistance to all available antimalarial chemotypes, including the current first-line treatment, Artemisinin-based combination therapies, have required the need to develop new, safe, and potent antimalarial compounds with novel modes of action. A phenotypic whole-cell screening approach to drug discovery was employed to fuel the antimalarial drug discovery pipeline with new molecule entities. This approach delivered two pyrido[1,2-a]benzimidazole compounds, **KP68**, **KP124**, and a benzimidazole compound **DM253,** as potent antimalarial leads. However, the mechanistic details of these compounds' action against the intraerythrocytic cycle of *P. falciparum* remain unsolved. Consequently, the broad aim of this work was to use multiple non-biased target deconvolution approaches that aid in studying the MOA of the compounds.

Previous studies on these compounds supported the inhibition of hemozoin formation as a plausible MOA for these compounds.[3,4] This was based on the potency of the compounds in the cell-free β-hematin inhibition assay and the ability of some compounds in the series to cause a dose-dependent increase in the levels of heme and an accompanying decrease in hemozoin levels in the cell fractionation assay. However, it was unclear if these compounds, in particular, act through this mechanism and if that is the primary or sole mechanism through which these compounds act. Therefore, to conduct a detailed investigation into the mode of action of these compounds, their intrinsic and extrinsic fluorescence properties were employed to systematically investigate their localization within *P. falciparum*. Furthermore, a chemical proteomics approach, where agarose beads were functionalized with the compounds studied, was

used to identify protein binding targets in *P. falciparum*. Finally, a genomics approach was employed through *in vitro* resistance selection followed by whole-genome sequencing. Resistant mutant parasite lines are raised by continuous exposure of the parasite to high compound concentrations, after which whole-genome sequencing of this mutant line compared to the parent line reveals genes that mediate resistance. While this approach aids in studying the compounds' resistance mechanism, in some cases, it provides insights into their mode of action. These approaches are summarised in Figure 7.1.

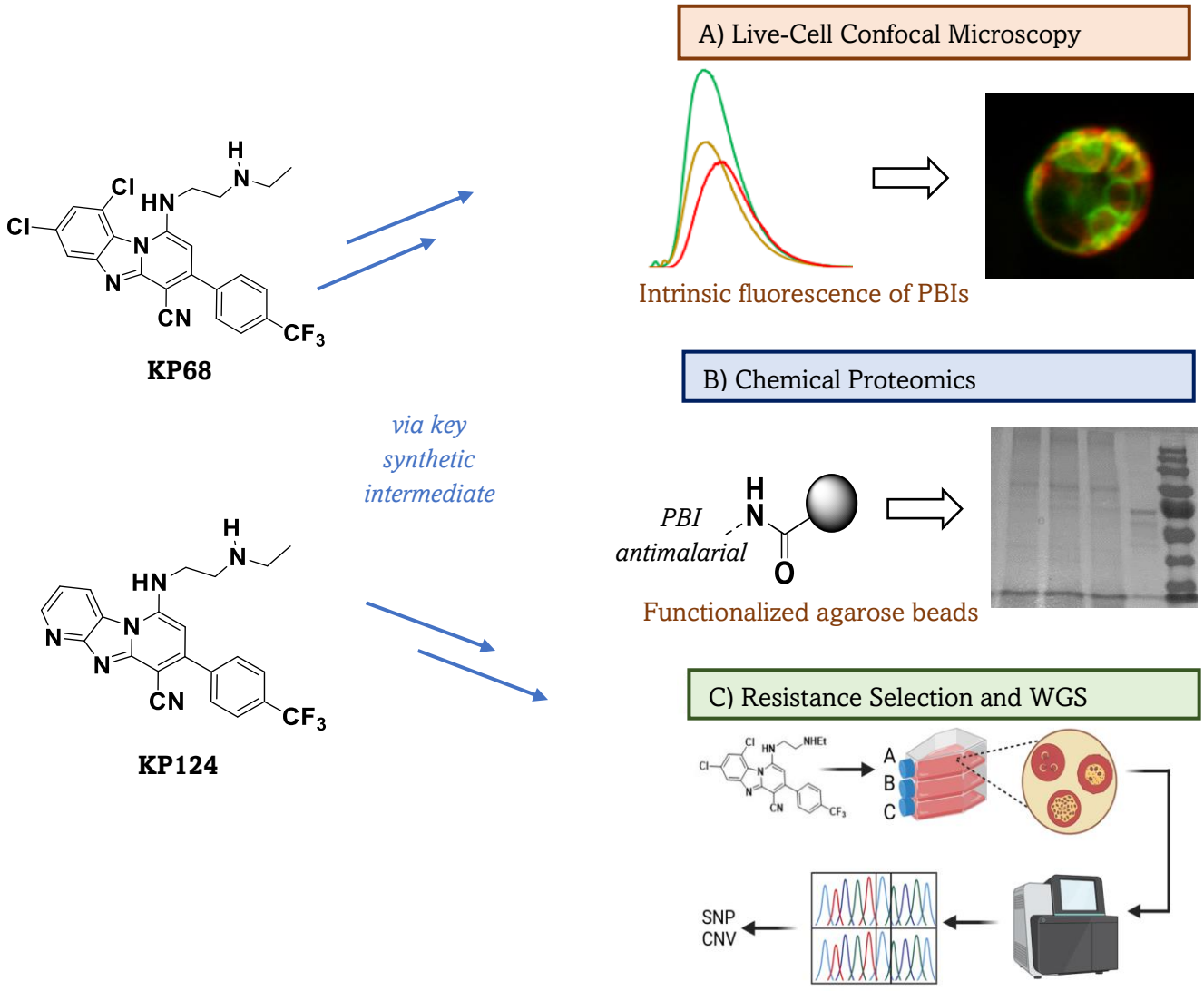

Figure 7.1. A summary of the major approaches employed in this work.

The pyrido[1,2- a]benzimidazole compounds **KP68** and **KP124** possess inherent fluorescence abilities suitable for studying their subcellular accumulation in the parasite. However, the benzimidazole compound **DM253** required the derivatization and attachment of an external fluorophore. For the preparation of the fluorescent derivatives

of **DM253**, NBD was selected as a suitable reporter due to its small size and appropriate photophysical properties. Structure-activity relationship studies were used to identify a suitable site for structural modification. Although **KP68** and **KP124** possess inherence fluorescence, NBD was attached to compare fluorescence accumulation due to their intrinsic and extrinsic fluorescence. A general strategy for synthetically attaching the NBD fluorophore to the target compounds included introducing an additional amino group for attachment through a nucleophilic aromatic substitution reaction.

The fluorescent compounds' photophysical, physicochemical and pharmacological properties were evaluated. Their novel NBD-labelled derivatives were also evaluated to determine if they were suitable representatives of the parent molecules for live-cell imaging. Absorption and emission maxima of the study compounds were measured and found to be ideal for live-cell imaging without causing undue stress on the cells. All fluorescent derivatives retained activity in the β-hematin inhibition assay compared to the parent compounds. More importantly, all derivatives exhibited low to moderate nanomolar activities against the chloroquine-sensitive strain of *P. falciparum*, except for **KP124-NBD**.

Fluorescence live-cell imaging revealed the selective accumulation of all fluorescent compounds within *P. falciparum*-infected erythrocytes. **KP124** and **DM253-NBD** were found near the hemozoin crystals, hence the region corresponding to the parasite's acidic digestive vacuole. In this region, the parasite converts its toxic ''free'' heme to an inert, less harmful hemozoin. It is speculated that once accumulated in the digestive vacuole; the compounds interfere with the conversion of heme to hemozoin. This is in line with the potency of these compounds in the cell-free β-hematin inhibition assay (BHIA) and previous studies that confirm inhibiting the formation of hemozoin as a contributory mode of action for some compounds in the series.[3] Interestingly, **KP68**, which is structurally related to **KP124**, has a different accumulation pattern. Despite possessing the structural properties required to interfere with the conversion of heme to hemozoin and its potency in the BHIA, this compound does not accumulate in the digestive vacuole to a concentration significant enough to prevent the conversion of heme to hemozoin. These conclusions were drawn from the excellent colocalization observed between the LysoTracker Red and **KP124** and **DM253-NBD** but not **KP68**, using the quantitative

analysis of cells co-stained with the LysoTracker Red and the compounds. Furthermore, qualitative and quantitative analysis indicated that none of the compounds accumulate in the nucleus, and any notion that these compounds interfere with processes in the nucleus is unlikely.

Super-resolution technique (SR-SIM) and Airyscan microscopy were employed to overcome the resolution challenges in this work. Extensive colocalization was observed between the ER and the **KP124** and **DM253-NBD.** Furthermore, a broad colocalization was observed between these compounds and the MitoTracker Deep Red. This implicates both organelles in the action of **KP124** and **DM253-NBD**. On the contrary, **KP68** showed no localization of the ER; however, significant amounts of the compound are observed around the mitochondrion, making it an organelle of interest in the action of **KP124.** Based on the results from the live-cell images, the compounds were tested in the cellular heme fractionation assay. The results showed a dose-dependent increase in heme levels and a concomitant decrease in hemozoin levels when chloroquine-sensitive strain parasites were incubated with **KP124.** This confirms inhibition of hemozoin formation as a MOA of **KP124.** On the other, **KP68** and **DM253** showed no effect on the levels of heme and hemozoin. This confirmed the live-cell imaging results, which show no accumulation of **KP68** in the digestive vacuole where hemozoin inhibition occurs. However, it was somewhat surprising that **DM253** showed no effect on the levels of heme and hemozoin; this is because the fluorescent derivative associates strongly with the digestive vacuole and hemozoin-associated neutral lipids. It later became apparent that the lipophilic NBD fluorophore may have influenced the accumulation of the compound, giving rise to its preference for the parasite's hydrophobic environments and its strong interaction with the LysoTracker Red. While fluorescence live-cell imaging sheds light on these compounds' mode of action, this approach alone cannot fully deconvolute the mode of action of molecules. Consequently, genomics and proteomics approaches were employed to further investigate the mode of action of these compounds.

In vitro resistance selection of **KP68** parasite mutant lines, followed by whole-genome sequencing, revealed a single nucleotide polymorphism (SNP) in the mitochondrion carrier protein (MCP). MCPs are membrane proteins found in the mitochondrial membrane of the parasite and are responsible for the efficient transport of essential

metabolites across the inner membrane of the mitochondrion. The parasite's mitochondrion has earlier been identified via fluorescence live-cell imaging as a site of significant accumulation of **KP68**. In fact, the compound was observed to envelop the mitochondrion with a strong affinity for its membrane. Therefore, observing a SNP, the mitochondrion carrier protein further implicates the mitochondrion in the action of **KP68**. Furthermore, a number of copy number variations were also observed, including a deamplification of a mitochondrial-processing peptidase, the deamplification of the *Plasmodium falciparum* multidrug resistance 1 (P*f*MDR1), and the ABC transporter family member 1. Due to the instability of the resistance phenotype due to the SNP in the MCP, it is speculated that this stop codon in the MCP is not the sole driver of resistance. Rather, the observed CNVs could contribute to the compound's resistance mechanism and may play a role in its mode of action. Cross-resistance studies with clones generated for **KP68** showed no cross-resistance with **KP124,** suggesting that resistance to **KP124** could be mediated through a different mechanism compared to **KP68.** Similarly, no cross-resistance was observed between the mutant clones generated for **KP68** and **CQ**, suggesting that both compounds act through a different MoR and possibly through a different MOA.

Finally, chemical proteomics was employed to identify protein binding partners within the parasite. To achieve this, drug-labelled matrices were prepared to capture the PBI antimalarial-binding proteins in *P. falciparum*. In *P. falciparum*, SDS-Page identified several bands between the molecular weights 180-34 kDa for **KP68** and **KP124**, including a higher molecular weight band above 180 kDa for **KP68**. MS followed by proteomics analysis identified several proteins as possible binding partners of **KP68**. These include ornithine aminotransferase, EMP1-trafficking protein, S-adenosylmethionine, and glyceraldehyde-3-phosphate dehydrogenase. According to proteomics analysis, ornithine aminotransferase is the most probable binding partner of **KP68.** This protein plays a significant role in polyamine biosynthesis, which is essential for cell replication.[5] It is necessary for the parasite's growth and development and a chemically validated target.[5,6] Ornithine aminotransferase was determined as the most probable binding partner due to the amount of protein "pulled down" during the experiment. However, this protein is very abundant (11265 ppm) in the parasite and could account for this observation. On the other hand, the high molecular weight band observed on the SDS-Page gel corresponded to the

plasmodium falciparum erythrocyte membrane protein1 (P*f*EMP1)-trafficking protein (244 kDa) with an abundance of 22 ppm in the parasite. P*f*EMP1 has been shown to localize in the lumen-facing lipid bilayer of the mitochondrial envelope,[7] where it serves as an adenosine diphosphate (ADP) and adenosine triphosphate (ATP) transmembrane transporter.[7] However, its primary role after intraerythrocytic stage infection is to form a complex with knobs at the surface of *Plasmodium falciparum*-infected erythrocytes.[8] The malaria parasite traffics this virulent protein to the surface of the infected erythrocytes through organelles called Maurer's clefts.[9] This occurs a few hours after intraerythrocytic stage infections, and P*f*EMP1 is transported with the help of other proteins such as the *Plasmodium falciparum* skeleton binding protein 1, which was equally identified as the binding partner of **KP68**.[9] The P*f*EMP1-knobs complex at the surface of parasite-infected RBCs are responsible for the virulent adhesion-related pathologies such as cerebral and placental malaria.[10] Recent work has implicated the P*f*EMP1 in the action of dihydroartemisinin.[11] It has also been investigated as an immune target for the development of a malaria vaccine candidate.[12]

It is evident from the combination of results from the live-cell imaging, *in vitro* resistance selection, and chemical proteomics approaches to studying the MOA of **KP68** that the compound does not act by inhibiting the formation of hemozoin, and the parasite's mitochondrion is linked to its primary mode of action. More importantly, it is evident that this compound interferes with many processes in the parasite. While that may be advantageous in delaying parasite resistance to this compound, deconvoluting its target is challenging.

Regarding **KP124**, all protein binding partners identified have direct or indirect effects on protein synthesis. Aside from its ability to inhibit the formation of hemozoin and cause the build-up of toxic heme that subsequently leads to the parasite's death, it is also implicated in protein synthesis in the parasite.

This work has provided more profound insights into the compounds' mode of action (s). The importance of identifying novel targets for the treatment of malaria cannot be overemphasized. The phenotypic whole-cell screening approach to drug discovery presents the unique opportunity to discover novel target (s) as an appropriate starting point for target-based drug discovery. Therefore, chemically validated protein targets

identified here can serve as potential drug targets in future antimalarial drug discovery campaigns.

7.2. Future Work

For future work, target validation is a priority. This will aid in assessing each protein's contribution to the compounds' action. As earlier described in Chapter 1, there are four levels of target validation. These are genetic, chemical (where inhibitors are assessed against the whole cell parasites and the target protein), and clinical validation. For this work, chemical validation of these proteins will be employed as the first step to target validation. The availability of biochemical assays helps to chemically validate protein targets. Of the many proteins identified in this work as protein binding partners of **KP68** and **KP124**, the ornithine aminotransferase and the P*f*EMP1 are the most essential and widely studied. These proteins have been fully characterized, and biochemical assays have been developed to identify small molecules that inhibit their function.[5,13,14] To validate the direct effect of **KP68** on these protein targets, the compound should be assessed in these biochemical assays as the first step to validating these proteins as targets of **KP68.** Other PBIs analogues from the series should also be evaluated in these biochemical assays to contribute more information about the mode of action of the chemical series.

Although the chemical proteomics approach employed in this work effectively identifies protein binding partners of molecules, it has several limitations. Firstly, the need to derivatize the molecules for their attachment to a stationary phase can completely alter the molecule and change its MOA. The choice of a stationary phase and linker chain, although considered carefully, does impact the binding of the target compound to the protein of interest. Also, using parasite lysates instead of intact cells is a limitation in this work. This is because only soluble proteins can effectively bind to the affinity matrices. Therefore, all insoluble proteins are not considered for binding. This fraction of insoluble proteins could contain a protein of interest to the compounds. Furthermore, the freeze and thaw and sonication processes of cell lysis employed in this work can compromise the integrity of some proteins and possibly denature them. Another limitation of this approach is that, for an effective competition elution, the compounds must be considerably soluble in the aqueous buffers in which these experiments are conducted.

However, the compounds studied in this work have moderate to poor aqueous solubility, making it challenging to perform the competition elution required to eliminate non-specific binding effectively.

To mitigate these challenges that significantly affected the outcome of this experiment, the chemical proteomics experiment on these compounds should be repeated using matrix-free and label-free chemical proteomics techniques in intact cells. An example of such is photo-affinity labelling. This chemoproteomics technique involves using a chemical probe to bind its target in response to activation by light covalently. It is a powerful tool used for the study of protein-ligand interactions and is used for the detection of the unknown target (s) of ligands. This technique mitigates the limitations associated with affinity chromatography. Other label-free proteomics techniques include target proteome profiling and drug affinity responsive target stability (DARTS).

As shown in this study, fluorescently labelled analogues of the target compounds serve as valuable tools for probing the localization of drugs in the cells. While NBD was chosen for this study due to its properties previously described, such as its small size and favourable photophysical properties, alternative reporter fluorophores may be used to prepare additional novel derivatives of these compounds. An example of a more photochemically stable fluorophore with high fluorescence quantum yields and good solubility is the boron-dipyrromethane (BODIPY) dyes.[15,16] Particularly for **DM253**, fluorescent derivatives using a hydrophilic fluorophore must be prepared to evaluate the accumulation of the compound in hydrophilic environments. Also, although Airyscan and SR-SIM were employed in this work, more powerful super-resolution techniques are likely to reveal deeper insights into these compounds' localization patterns within *P. falciparum*. Examples of such methods include stimulated emission depletion microscopy (STED) and stochastic optical reconstruction microscopy (STORM), which usually require fluorophores with distinctive photophysical properties.

Although this work has developed new tools for generating insights into the MOA of the compounds investigated, further details of this mechanism (s) remain unsolved. Additional work should be done employing other techniques that circumvent the limitations of the approaches described here. This work has demonstrated the importance of employing a holistic approach to mode of action studies and the value of using different

tools and techniques complementarily. The multi-disciplinary approach to target deconvolution presented in this work is arguably more efficient than single techniques used in isolation. It can be utilized to generate insights into the mode of action of new molecules.

7.3. References

(1) Flannery, E. L.; Chatterjee, A. K.; Winzeler, E. A. Antimalarial Drug Discovery Approaches, and Progress towards New Medicines. *Nat. Rev. Microbiol.* **2013**, *11* (12), 849–862.

(2) Ghana Health Service. Malaria Facts https://www.severemalaria.org/countries/ghana.

(3) Singh, K.; Okombo, J.; Brunschwig, C.; Ndubi, F.; Barnard, L.; Wilkinson, C.; Njogu, P. M.; Njoroge, M.; Laing, L.; Machado, M.; Prudêncio, M.; Reader, J.; Botha, M.; Nondaba, S.; Birkholtz, L.-M.; Lauterbach, S.; Churchyard, A.; Coetzer, T. L.; Burrows, J. N.; Yeates, C.; Denti, P.; Wiesner, L.; Egan, T. J.; Wittlin, S.; Chibale, K. Antimalarial Pyrido[1,2- a]Benzimidazoles: Lead Optimization, Parasite Life Cycle Stage Profile, Mechanistic Evaluation, Killing Kinetics, and in Vivo Oral Efficacy in a Mouse Model. *J. Med. Chem.* **2017**, *60* (4), 1432–1448.

(4) Ndakala, A. J.; Gessner, R. K.; Gitari, P. W.; October, N.; White, K. L.; Hudson, A.; Fakorede, F.; Shackleford, D. M.; Kaiser, M.; Yeates, C.; Charman, S. A.; Chibale, K. Antimalarial Pyrido[1,2-a]Benzimidazoles. *J. Med. Chem.* **2011**, *54* (13), 4581–4589.

(5) Berger, B. J. Antimalarial Activities of Aminooxy Compounds. *Antimicrob. Agents Chemother.* **2000**, *44* (9), 2540–2542.

(6) Bolkenius, F. N.; Knödgen, B.; Seiler, N. DL-Canaline and 5-Fluoromethylornithine. Comparison of Two Inactivators of Ornithine Aminotransferase. *Biochem. J.* **1990**, *268* (2), 409–414.

(7) Https://www.uniprot.org/.

(8) Looker, O.; Blanch, A. J.; Liu, B.; Nunez-Iglesias, J.; McMillan, P. J.; Tilley, L.; Dixon, M. W. A. The Knob Protein KAHRP Assembles into a Ring-Shaped Structure That Underpins Virulence Complex Assembly. *PLOS Pathog.* **2019**, *15* (5), e1007761.

(9) McHugh, E.; Carmo, O. M. S.; Blanch, A.; Looker, O.; Liu, B.; Tiash, S.; Andrew, D.; Batinovic, S.; Low, A. J. Y.; Cho, H.-J.; McMillan, P.; Tilley, L.; Dixon, M. W. A. Role of Plasmodium Falciparum Protein GEXP07 in Maurer's Cleft Morphology, Knob

Architecture, and P. Falciparum EMP1 Trafficking. *MBio* **2020**, *11* (2).

(10) Rowe, J. A.; Claessens, A.; Corrigan, R. A.; Arman, M. Adhesion of Plasmodium Falciparum-Infected Erythrocytes to Human Cells: Molecular Mechanisms and Therapeutic Implications. *Expert Rev. Mol. Med.* **2009**, *11*.

(11) Chen, L.; Zheng, Z.; Liu, H.; Wang, X.; Qu, S.; Yang, Y.; Deng, S.; Zhang, Y.; Tuo, L.; Zhao, Y.; Li, Y. Combined Transcriptome and Proteome Profiling for Role of PfEMP1 in Antimalarial Mechanism of Action of Dihydroartemisinin. *Microbiol. Spectr.* **2021**, *9* (3).

(12) Beeson, J. G.; Chan, J.-A.; Fowkes, F. J. PfEMP1 as a Target of Human Immunity and a Vaccine Candidate against Malaria. *Expert Rev. Vaccines* **2013**, *12* (2), 105–108.

(13) Gafan, C.; Wilson, J.; Berger, L. C.; Berger, B. J. Characterization of the Ornithine Aminotransferase from Plasmodium Falciparum. *Mol. Biochem. Parasitol.* **2001**, *118* (1), 1–10.

(14) Kriek, N.; Tilley, L.; Horrocks, P.; Pinches, R.; Elford, B. C.; Ferguson, D. J. P.; Lingelbach, K.; Newbold, C. I. Characterization of the Pathway for Transport of the Cytoadherence-Mediating Protein, P*f*EMP1, to the Host Cell Surface in Malaria Parasite-Infected Erythrocytes. *Mol. Microbiol.* **2003**, *50* (4), 1215–1227.

(15) Ulrich, G.; Ziessel, R.; Harriman, A. The Chemistry of Fluorescent Bodipy Dyes: Versatility Unsurpassed. *Angew. Chemie Int. Ed.* **2008**, *47* (7), 1184–1201.

(16) Loudet, A.; Burgess, K. BODIPY Dyes and Their Derivatives: Syntheses and Spectroscopic Properties. *Chem. Rev.* **2007**, *107* (11), 4891–4932.

Chapter Eight

Experimental Methods

8.1. Chapter Overview

This chapter will describe the experimental protocols used in this thesis. The following sections will discuss the supplementary information for the synthetic procedures, physicochemical property analysis, and biological assays. The chapter describes the chemistry and characterization information of all synthesized intermediates and target compounds. This is followed by describing the biological assays used to evaluate the compounds.

8.2. Chemistry

8.2.1. Solvents & Reagents

All commercially available chemicals and reagents were purchased from Sigma Aldrich, now known as Merck (South Africa, SA) and Combi block (USA). Absolute ethanol (EtOH), methanol (MeOH), *n*-hexane, acetone, ethyl acetate (EtOAc), and Dichloromethane (DCM) were purchased as analytical grade solvents from Kimix and Protea Chemicals Pty Ltd (SA). Anhydrous solvents tetrahydrofuran (THF) and dimethylformamide (DMF) were bought from Merck (SA). High-performance liquid chromatography (HPLC) grade solvents were purchased from Sigma Aldrich and Merck. Bovine haemin (Fe(III)PPIX-Cl) was obtained from Fluka. NP-40 was obtained from Pierce Biotechnology (Rockford, IL, USA). A Millipore Direct-Q3 water purification system provided double-distilled deionized water (dH2O). DRAQ 5, LysoTracker Red, ER-Tracker Red, and MitoTracker Deep Red were obtained from Molecular Probes (Oregon, USA) and ThermoFisher Scientific. Nile Red was obtained from Sigma-Aldrich. Absorption spectra were recorded on a Varian Cary 100 UV-Vis or a Shimadzu UV-1800 spectrophotometer and were baseline-corrected. Fluorescence spectra were measured using a Varian Cary Eclipse spectrofluorometer. Assay plates were read using a SpectraMax 340 PC 384 Absorbance Microplate Reader (Molecular Devices).

All stock solutions were stored in the dark, and working solutions were made up immediately before use. Unless otherwise stated, the temperature was maintained at 25

°C using a thermostat-controlled water bath. A Hamilton syringe delivered aliquots of solutions into quartz cuvettes (1.00 mm or 10.00 mm). Cuvettes were thoroughly washed with 0.2 M NaOH, followed by several rinses with water, the addition of 1 M HNO_3, and several additional rinses with water to remove adsorbed Fe(III)PPIX.[1]

8.2.2. Spectroscopic Characterization

8.2.2.1. Liquid Chromatography with Mass Spectrometer (LC-MS)

LC-MS analysis was performed on an Agilent 1260 Infinity Binary Pump, Agilent 1260 Infinity Diode Array Detector (DAD), Agilent 1290 Infinity Column Compartment, Agilent 1260 Infinity Standard Autosampler, and an Agilent 6120 Quadrupole Mass Spectrometer with APCI and ESI multimode ionization source. Agilent LC-MS using a Kinetex Core C18 2.6 µm column (50 × 3 mm) was used to determine the purity of all synthesized compounds. The aqueous mobile phase (Mobile Phase A) was made up of 0.4% acetic acid in 10 mM ammonium acetate in HPLC grade water, while the organic phase (Mobile phase B) was comprised of 0.4% acetic acid, 10 mM ammonium acetate in a 9:1 ratio of HPLC grade methanol and Type-1 water. The compounds were run at a flow rate of 0.9 $mL.min^{-1}$, and the purity of all target compounds was confirmed to be greater than 95%.

Table 8.1. LC-MS gradient employed for determining the purity (%), retention time (t_R), and mass (m/z) of compounds

Time (min)	% **A**	% **B**
0.00	75	25
1.00	75	15
3.00	0	100
4.50	0	100
5.20	75	25
6.00	75	25

8.2.2.2. Liquid Chromatography with Mass Spectrometer (LC-MS)

All NMR spectra were recorded on Varian Mercury (^{1}H NMR on 300 MHz) or Bruker (^{1}H NMR on 400 or 600 MHz and 13C NMR on 101 or 151 MHz). Samples were prepared in either deuterated dimethyl sulfoxide (DMSO-*d6*), chloroform ($CDCl_3$), or methanol (MeOD-*d4*). Chemical shifts are reported in parts per million and rounded to two decimal places. Coupling constants (J) are reported in hertz (Hz) and are rounded off to two decimal places. Abbreviations used in assigning ^{1}H NMR signals are d (doublet), dd (doublet of doublets), ddd (doublet of doublet of doublets), s (singlet), and t (triplet), q (quartet), m (multiplets). ^{13}C NMR spectra were recorded in proton-decoupled mode, with chemical shifts recorded in parts per million and rounded off to two decimal places.

8.2.2.3. Melting Points (m.p.)

Melting points were assessed using a Reichert-Jung Thermovar hot-stage microscope attached to a digital thermometer.

8.2.3. Thin Layer Chromatography (TLC)

TLC plates were bought from either Merck or Sigma Aldrich as F_{254} aluminium-backed pre-coated silica gel plates. Compound spots were detected and visualized using UV lights at wavelengths 254 and 366 nm. Other visualization reagents such as Ninhydrin reagent were used when required. Compound purification was done using either gravity glass column chromatography.

8.2.4. Spectroscopic Characterization

8.2.4.1. Synthesis of Fluorescent Analogues of KP68 and KP124.

8.2.4.1.1. Synthesis of Directly Attached CKM08 Fluorescent Analogue (14)

To **8** (1.00, equiv), NBD chloride (1.2 equiv) was added and dissolved in *N, N*-dimethyl formamide (DMF). The mixture was heated in the microwave at 80 ^{o}C for one hour. Excess triethylamine was added to mop up the HCl produced during the reaction. The reaction mixture was purified using column chromatography followed by preparative TLC.

6-((2-(ethyl(7-nitrobenzo[c][1,2,5]oxadiazol-4-yl)amino)ethyl)amino)-8-(4-(trifluoromethyl)phenyl)imidazo[1,2-a:4,5-b']dipyridine-9-carbonitrile (14)

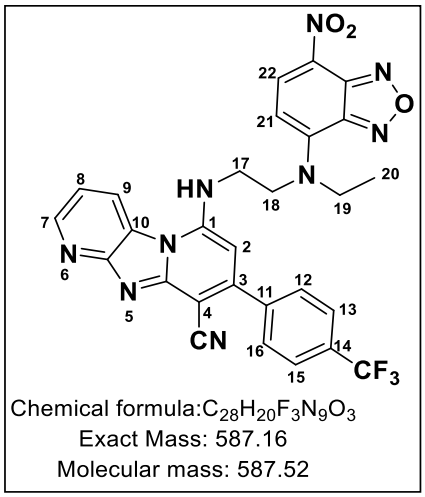

Obtained from **8** (100 mg, 0.27 mmols) as a dark red solid (35% , 56 mg); R_f (DCM: MeOH: 9:1) 0.64: ^{1}H NMR (600 MHz, DMSO-d_6) δ 8.31 (d, J = 9.1 Hz, 1H, H^{22}), 8.26 (dd, J = 4.8, 1.4 Hz, 1H, H^7), 8.22 (dd, J = 8.2, 1.4 Hz, 1H, H^9), 7.95 (d, J = 8.6 Hz, 2H, $H^{13,15}$), 7.93 (d, J = 8.6 Hz, 2H, $H^{12,14}$), 7.60 (dd, J = 8.2, 4.8 Hz, 1H, H^8), 6.55 (d, J = 9.2 Hz, 1H, H^{21}), 6.49 (s, 1H, H^2), 4.50 (t, J = 6.2 Hz, 2H, H^{17}), 4.15 (t, J = 6.1 Hz, 2H, H^{18}), 4.00 (q, J = 7.1 Hz, 2H, H^{19}), 1.31 (t, J = 7.1 Hz, 3H, H^{20}). ^{13}C NMR (151 MHz, DMSO) δ 152.44, 149.32, 148.81, 145.66, 144.97, 144.84, 143.84, 141.83, 140.22, 137.77, 136.16, 130.63, 130.35, 129.96 (4C), 126.77, 125.96, 122.27, 121.26, 116.82, 103.46, 90.47, 82.40, 52.09, 48.47, 12.23. HPLC-MS (ESI): Purity = 98%, t_R = 2.8 min, m/z $[M+H]^+$ = 588.09

8.2.4.1.2. Synthesis of Two-Carbon Linked Fluorescent Analogues of 6 and 8 (18 and 21)

To synthesize the two-carbon linked fluorescent analogues of **6 and 8,** the appropriate target PBI was condensed with *N*-Boc-glycinal under reductive amination conditions using $NaBH_3CN$ to generate *N*-Boc-protected amine (**16**,**19**). This was followed by *N*-Boc deprotection using TFA (20 equiv) in DCM to generate a key intermediate (**17, 20**) which was used in a nucleophilic aromatic substitution with the 4-chloro derivative of the NBD fluorophore to afford the NBD labelled fluorescent analogues (**18, 21**). These intermediates **(17, 20)** could also serve as suitable intermediates for immobilizing an agarose bead in proteomics studies. The compounds were purified using column chromatography.

***tert*-butyl(2-((2-((7,9-dichloro-4-cyano-3-(4 (trifluoromethyl)phenyl)benzo [4,5]imidazo[1,2-a]pyridin-1-yl)amino)ethyl)(ethyl)amino)ethyl)carbamate (19)**

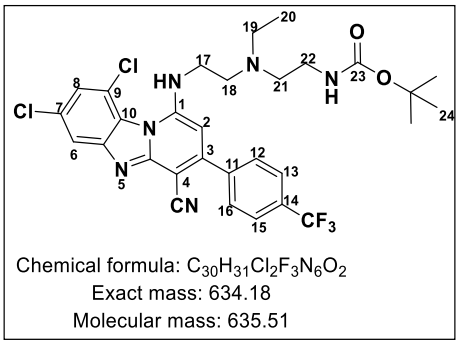

Obtained from **6** (100 mg, 0.27 mmols) as a yellow oil (75%, 38 mg); R_f (Hexane: Ethyl acetate: 6:4) 0.47: ^{1}H NMR (600 MHz, Methanol-d_4) δ 8.08 (d, J = 1.9, 1H, H^6), 7.86 (d, J = 8.0 Hz, 2H, $H^{13,15}$), 7.80 (d, J = 8.0 Hz, 2H, $H^{12,16}$), 7.57 (d, J = 1.8, 1H, H^8), 6.23 (s, 1H, H^2), 3.60 (t, J = 6.1 Hz, 2H, H^{17}), 3.20 (t, J = 6.7 Hz, 2H, H^{22}), 3.01 (t, J = 6.0 Hz, 2H, H^{18}), 2.80 (q, J = 7.1 Hz, 2H, H^{19}), 2.71 (t, J = 6.7 Hz, 2H, H^{21}), 1.20 (s, 9H, H^{24}), 0.89 (t, J = 7.1 Hz, 3H, H^{20}). ^{13}C NMR (151 MHz, MeOD) δ 157.01, 152.04, 150.09, 148.48, 140.85, 140.75, 131.42, 129.22 (2C), 128.79, 125.79 (2C), 125.76 (2C), 125.28, 123.48, 115.85, 112.54, 91.68, 83.45, 78.55, 60.05, 51.80, 50.99, 40.47, 38.23, 29.32, 27.15, 13.05, 10.94. HPLC-MS (ESI): Purity = 99%, t_R = 2.8 min, m/z $[M+H]^+$ = 635.3

***tert*-butyl(2-((2-((9-cyano-8-(4-(trifluoromethyl)phenyl)imidazo[1,2-a:4,5-b']dipyridin-6-yl)amino)ethyl)(ethyl)amino)ethyl)carbamate (16)**

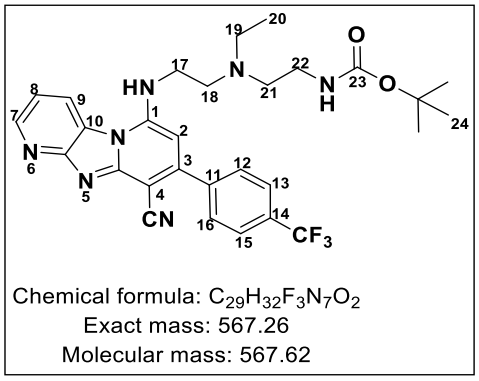

Obtained from **8** (100 mg, 0.20 mmols) as a yellow oil (89%, 100 mg); R_f (Hexane: Ethyl acetate: 6:4) 0.47: ^{1}H NMR (400 MHz, Methanol-d_4) δ 8.34 (dd, J = 4.8, 1.3 Hz, 1H, H^7), 8.06 (dd, J = 8.2, 1.3 Hz, 1H, H^9), 7.82 (d, J = 8.4 Hz, 2H, $H^{13,15}$), 7.78 (d, J = 8.3 Hz, 2H, $H^{12,16}$), 7.52 (dd, J = 8.2, 4.8 Hz, 1H, H^8), 6.13 (s, 1H, H^2), 3.58 (t, J = 6.6 Hz, 2H, H^{17}), 3.20 (t, J = 6.4 Hz, 2H, H^{22}), 2.92 (t, J = 6.6, 2H, H^{18}), 2.71 (q, J = 7.1 Hz, 2H H^{19}), 2.64 (t, J = 6.4 Hz, 2H, H^{21}), 1.44 (s, 9H, H^{24}), 1.15 (t, J = 7.1 Hz, 3H, H^{20}). ^{13}C NMR (101 MHz, MeOD) δ 156.68, 154.92, 152.86, 148.84, 148.54, 141.18, 141.16, 141.15, 140.35, 137.02, 137.01, 129.14 (2C), 125.32, 125.28, 125.24, 122.67, 121.71, 116.01, 89.86, 80.09, 53.76, 53.61, 52.29, 51.07, 43.19, 40.28, 27.26, 11.29. HPLC-MS (ESI): Purity = 97 %, t_R = 2.7 min, m/z $[M+H]^+$ = 568.1

1-((2-((2-aminoethyl)(ethyl)amino)ethyl)amino)-7,9-dichloro-3-(4-(trifluoromethyl)phenyl)benzo[4,5]imidazo[1,2-a]pyridine-4-carbonitrile(20)

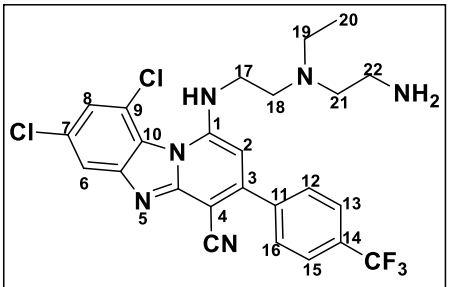

Chemical formula: $C_{25}H_{23}Cl_2F_3N_6$
Exact mass: 534.13
Molecular mass: 535.40

Obtained from **19** (100 mg, 0.27 mmols) as a yellow solid (60%, 87 mg); R_f (100% MeOH) 0.3: ^{1}H NMR (600 MHz, Methanol-d_4) δ 8.23 (d, J = 1.7 Hz, 1H, H^6), 7.81 (d, J = 8.1 Hz, 2H, $H^{13,15}$), 7.67 (d, J = 8.2 Hz, 2H, $H^{12,16}$), 7.26 (d, J = 1.6 Hz, 1H, H^8), 6.40 (s, 1H, H^2), 4.15 (t, J = 6.7 Hz, 2H, H^{17}), 3.85 (t, J = 6.7 Hz, 2H, H^{18}), 3.80 – 3.61 (m, 4H, $H^{21,22}$), 3.53 (q, J = 7.2 Hz, 2H, H^{19}), 1.48 (t, J = 7.2 Hz, 3H, H^{20}). ^{13}C NMR (151 MHz, DMSO) δ 152.44, 149.32, 148.81, 145.66, 144.97, 144.84, 143.84, 141.83, 140.22, 137.77, 136.16, 130.63, 129.96 (2C), 126.77, 125.96, 122.27, 121.26, 116.82, 103.46, 90.47, 82.40, 52.09, 48.47, 12.23. HPLC-MS (ESI): Purity = 98%, t_R = 2.8 min, m/z $[M+H]^{+\,a}$ = 535.1

6-((2-((2-aminoethyl)(ethyl)amino)ethyl)amino)-8-(4 (trifluoromethyl)phenyl)imidazo[1,2-a:4,5-b']dipyridine-9-carbonitrile (17)

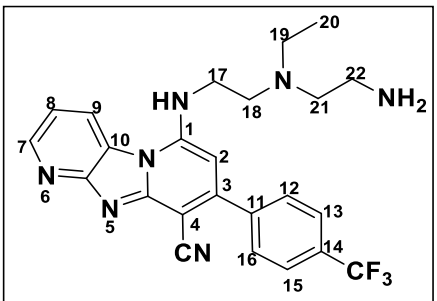

Chemical formula: $C_{24}H_{24}F_3N_7$
Exact mass: 467.20
Molecular mass: 467.50

Obtained from **16** (140 mg, 0.24 mmols) as a yellow solid (69%, 87 mg); R_f (100% MeOH) 0.2: ^{1}H NMR (400 MHz, Methanol-d_4) δ 8.48 (dd, J = 4.8, 1.3 Hz,1H, H^7), 8.10 (dd, J = 8.3, 1.4 Hz, 1H, H^9), 7.90 (d, J = 8.2 Hz, 2H, $H^{13,15}$), 7.81 (d, J = 8.2 Hz, 2H, $H^{12,16}$), 7.63 (dd, J = 8.3, 4.9 Hz, 1H, H^8), 6.67 (s, 1H, H^2), 4.26 (t, J = 6.5 Hz, 2H, H^{17}), 3.76 (t, J = 6.5 Hz, 2H, H^{18}), 3.66 (t, J = 5.7 Hz, 2H, H^{21}), 3.56 – 3.44 (m, 4H, $H^{19,22}$), 1.43 (t, J = 7.2 Hz, 3H, H^{20}).^{13}C NMR (101 MHz, DMSO) δ 153.92, 152.86, 149.10, 148.54, 144.16, 141.11, 141.55, 140.35, 137.02, 137.01, 129.14 (2C), 125.32, 125.28, 125.24, 122.67, 121.71, 116.01, 80.19, 43.19, 40.28, 53.4, 27.26, 11.29. HPLC-MS (ESI): Purity = 96%, t_R = 2.7 min, m/z $[M+H]^+$ = 468.1

7,9-dichloro-1-((2-(ethyl(2((7nitrobenzo[c][1,2,5]oxadiazolyl)amino)ethyl)amino)ethyl)amino)-3-(4(trifluoromethyl)phenyl)benzo[4,5]imidazo[1,2-a]pyridine-4-carbonitrile (21)

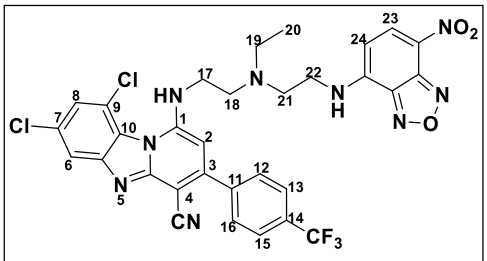

Obtained from **19** (120 mg, 0.22 mmols) as dark red solid (32%, 49 mg); R_f (DCM: MeOH: 9:1) 0.68: ^{1}H NMR (600 MHz, DMSO-d_6) δ 8.15 (d, J = 8.9 Hz, 1H, H^{23}), 8.10 (d, 1H, J = 1.7 Hz,1H, H^6), 7.95-7.93 (m, 4H, $H^{12,13,15,16}$), 7.53 (d, J = 1.7 Hz, 1H, H^8), 6.24 (s, 1H, H^2), 6.20 (d, J = 8.9, Hz, 1H, H^{24}), 3.61 – 3.55 (m, 4H, $H^{17,18}$), 2.94 – 2.86 (m, 4H, $H^{21,22}$), 2.79 (q, J = 7.1 Hz, 2H, H^{19}), 1.13 (t, J = 7.1 Hz, 3H, H^{20}). ^{13}C NMR (151 MHz, DMSO) δ 151.30, 150.27, 148.97, 144.17, 143.90, 141.61, 141.39, 137.14, 129.95 (2C), 129.04, 126.02 (2C), 125.99, 125.80, 125.61, 125.41, 124.53, 123.61, 123.31, 116.88, 114.15, 113.50, 92.24, 92.18, 51.50, 48.32, 41.83, 38.10, 29.39 12.49. HPLC-MS (ESI): Purity = 96%, t_R = 2.8 min, m/z $[M+H]^+$ = 698.1.

6-((2-(ethyl(2-((7-nitrobenzo[c][1,2,5]oxadiazol-4-yl)amino)ethyl)amino) ethyl) amino)-8-(4-(trifluoromethyl)phenyl)imidazo[1,2-a:4,5-b']dipyridine-9-carbonitrile (18)

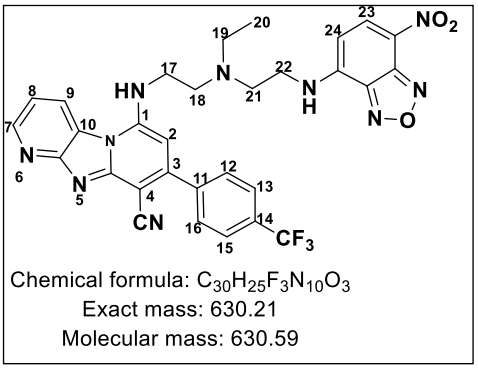

Obtained from **16** (100 mg, 0.21 mmols) as a dark red solid (36%, 50 mg); R_f (DCM: MeOH: 9:1) 0.55: ^{1}H NMR (600 MHz, DMSO-d_6) δ 9.56 (d, J = 9.1, 1H, H^{23}), 8.06-8.03 (m, Hz, 2H, $H^{7,9}$), 7.98 (d, J = 8.1 Hz, 2H, $H^{13,15}$), 7.93 (d, J = 8.1 Hz, 2H, $H^{12,16}$), 7.40 (dd, J = 8.1, 4.8 Hz, 1H, H^8), 6.25 (d, J = 9.0 Hz, 1H, H^{24}), 6.08 (s, 1H, H^2), 3.60 – 3.52 (m, 4H, $H^{17,18}$), 2.87 – 2.83 (m, 4H, $H^{21,22}$), 2.75 (q, J = 7.0 Hz, 2H, H^{19}), 1.20 (t, J = 7.1 Hz, 3H, H^{20}). ^{13}C NMR (151 MHz, DMSO) δ 152.02, 148.40, 145.66, 143.98, 143.35, 143.26, 141.98, 139.82, 137.40, 137.32, 129.96 (2C), 126.21, 126.08, 125.44, 123.63, 121.82, 120.09, 117.17, 99.11, 89.86, 81.19, 51.79, 51.11, 48.38, 42.28, 40.88, 40.73, 40.52, 12.92. HPLC-MS (ESI): Purity = 97%, t_R = 2.7 min, m/z $[M+H]^+$ = 631.1.

8.2.4.2. Synthesis of Benzimidazole lead, DM253

The synthesis of **DM253** progressed with the preparation of a phenethyl bromide intermediate through an Appel reaction and a $BF_3(OEt)_3$-mediated ring closure. A separate reaction involving the alkylation of 2-chloro-1H-benzo[d]imidazole at N-1, followed by a coupling reaction with tert-butyl 4-aminopiperidine-1-carboxylate delivered intermediate **4.** Finally, acidic deprotonation resulting in the formation of intermediate **5**, coupled with a substitution reaction between intermediates **3** and **5,** afforded the target compound **DM253.**

4-(2-bromoethyl)benzonitrile (1)

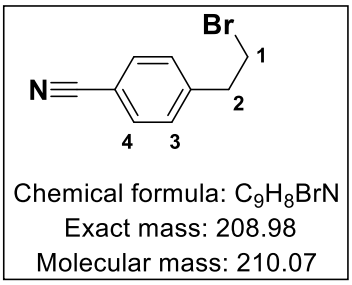

Chemical formula: C_9H_8BrN
Exact mass: 208.98
Molecular mass: 210.07

Obtained from 4-(2-hydroxyethyl)benzonitrile (10.0 g, 67.9 mmol) as a white crystalline solid (11.6 g, 81%). R*f* (20% EtOAc/Hexanes) 0.74. ^{1}H NMR (600 MHz, DMSO-*d*6) δ 7.78 (d, *J* = 8.3 Hz, 2H. H^4), 7.49 (d, *J* = 8.3 Hz, 2H, H^3), 3.78 (t, *J* = 7.0 Hz, 2H, H^1), 3.23 (t, *J* = 7.0 Hz, 2H, H^2). Purity: 96%, tR = 2.753 min.

4-(2-bromoethyl)-N-hydroxybenzimidamide (2).

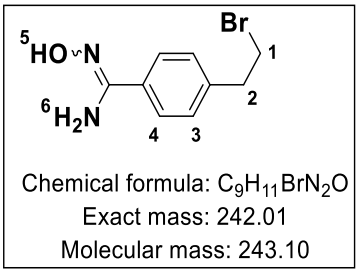

Chemical formula: $C_9H_{11}BrN_2O$
Exact mass: 242.01
Molecular mass: 243.10

To a solution of 4-(2-bromoethyl) benzonitrile (1.5 g, 7.14 mmol) in absolute ethanol (40 ml) was added hydroxylamine hydrochloride (0.59 g, 8.56 mmol), followed by TEA (1.2 ml, 8.56 mmol) and 8-hydroxyquinolone (0.01 eq). The resulting mixture was refluxed at 79 °C for 1.5 hour. After completion (monitored by TLC), the solvent was evaporated *in vacuo*, the residue was dissolved with H_2O (10 ml) and acidified to pH 3 using 10% HCl. The precipitate was filtered off and again washed with 10% HCl and dried. Light green crystalline solid (1.42 g, 82%). R_f(50% EtOAc/Hexanes) 0.25. ^{1}H NMR (300 MHz, DMSO-d_6) δ 9.57 (s, 1H, H^5), 7.61 (d, *J* = 8.3 Hz, 2H, H^4), 7.27 (d, *J* = 8.3 Hz, 2H, H^3), 5.75 (s, 2H, H^6), 3.74 (t, *J* = 7.1 Hz, 2H, H^1), 3.14 (t, *J* = 7.1 Hz, 2H, H^2). LC-MS (APCI$^+$/ESI): found *m/z* = 244.0, 245.0 $[M+H]^+$ Purity: 98%, t_R = 2.135 min.

3-(4-(2-bromoethyl)phenyl)-5-(trifluoromethyl)-1,2,4-oxadiazole (3).

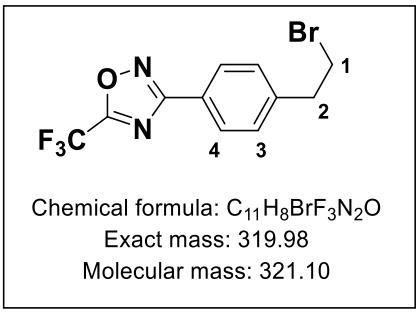

Chemical formula: $C_{11}H_8BrF_3N_2O$
Exact mass: 319.98
Molecular mass: 321.10

A mixture of **2** (1.0 g, 4.1 mmol) in 4 ml pyridine and trifluoroacetic acid anhydride (1.14 ml, 8.2 mmol) was stirred at room temperature (19 °C) for 20 min. The mixture was poured into ice H_2O (10 ml) and extracted with ethyl acetate (3 × 15 ml). The combined organic extracts were washed with brine and dried over anhydrous Na_2SO_4. The product was obtained after flash column chromatography using 0 – 10% EtOAc/Hexanes as a pale-yellow oil (1.00 g, 76%). R_f(40% EtOAc/Hexanes) 0.92. ^{1}HNMR (300 MHz, DMSO-d_6) δ 8.16 (d, J = 8.2, 2H, H^4), 7.49 (d, J = 8.2, 2H, H^3), 3.80 (t, J = 7.0 Hz, 2H, H^1), 3.24 (t, J = 7.0 Hz, 2H, H^2). Purity: 97%, t_R = 2.631 min.

tert-butyl 4-((1H-benzo[d]imidazol-2-yl)amino)piperidine-1-carboxylate (4).

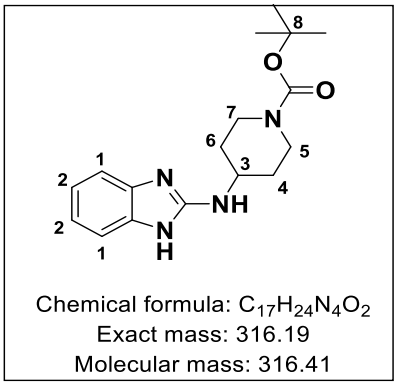

Chemical formula: $C_{17}H_{24}N_4O_2$
Exact mass: 316.19
Molecular mass: 316.41

A mixture of 2-chlorobenzimidazole (5.0 g, 32.8 mmol), ethyl 4-aminopiperidine-1-carboxylate (8.46 g, 49.1 mmol), and TEA (2.0 equiv) was stirred at 155 °C in a seal tube for 6 – 36 hours. After completion (monitored *via* TLC), the residue was cooled and diluted with 10% MeOH/DCM. The mixture was washed with saturated $NaHCO_3$ solution (×3), then brine (×1), and dried over anhydrous Na_2SO_4. The solvent was evaporated *in vacuo* to obtain a crude residue which was purified *via* flash column chromatography to afford product as a light brown solid (8.22 g, 79%). R_f(10% MeOH/DCM), 0.35. ^{1}H NMR (600 MHz, Methanol-d_4) δ 7.18 (dd, J = 5.8, 3.2 Hz, 2H, H^2), 6.95 (dd, J = 5.8, 3.2 Hz, 2H, H^1), 4.11 (q, J = 7.1 Hz, 2H, H^6), 4.09 (m, 2H, H^5), 3.80 (tt, J = 10.6, 4.0 Hz, 1H, H^3), 3.05 – 2.99 (m, 2H, H^5), 2.08 – 2.01 (m, 2H, H^4), 1.48 – 1.39 (m, 2H, H^4), 1.25 (t, J = 7.1 Hz, 3H, H^7). LC-MS (APCI$^+$/ESI): found m/z = 289.0 $[M+H]^+$ Purity: 98%, t_R = 2.258 min.

N-(piperidin-4-yl)-1H-benzo[*d*]imidazol-2-amine (5).

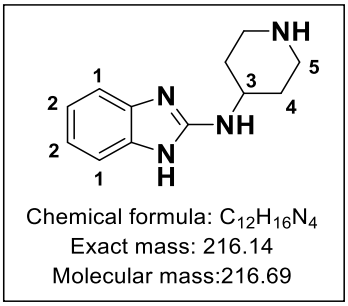

Chemical formula: $C_{12}H_{16}N_4$
Exact mass: 216.14
Molecular mass:216.69

Intermediate **9** (8.00 g, 28.0 mmol) was refluxed in 48% HBr solution for 3 hr at 120 °C. After completion, the reaction mixture was cooled and diluted with deionized water, followed by neutralizing with 15% NaOH. The aqueous solution was extracted with DCM (3 × 60 ml), and the combined organic layers washed with brine and dried over anhydrous Na_2SO_4. Evaporating off the solvent *in vacuo* and washing residue in diethyl ether afforded product as a white crystalline solid (3.52 g, 58%). R_f(10% MeOH/DCM), 0.08. ^{1}H NMR (600 MHz, Methanol-d_4) δ 7.43 (dd, J = 6.0, 3.1 Hz, 2H, H^2), 7.30 (dd, J = 6.0, 3.1 Hz, 2H, H^1), 4.03 (tt, J = 10.6, 4.1 Hz, 1H, H^3), 3.59 – 3.54 (m, 2H, H^{5e}), 3.30 – 3.24 (m, 2H, H^{5a}), 2.39 – 2.33 (m, 2H, H^{4e}), 2.04 – 1.96 (m, 2H, H^{4a}). LC-MS (APCI$^+$/ESI): found m/z = 217.2 [M+H] $^+$ (cal. For $C_{12}H_{16}N_4$, 216.29). Purity: 98%, t_R = 0.621 min.

N-(1-(4-(3-(Trifluoromethyl)-1,2,4-oxadiazol-5-yl)phenethyl)piperidin-4-yl)-1H-benzo[d]imidazol-2-amine (DM253).

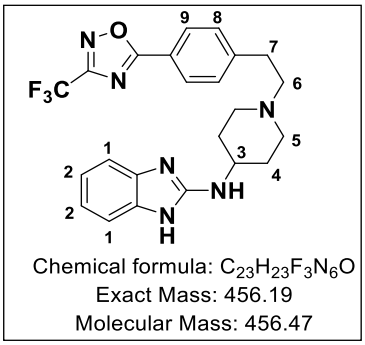

Chemical formula: $C_{23}H_{23}F_3N_6O$
Exact Mass: 456.19
Molecular Mass: 456.47

Using the procedure for compound **8**, obtained from **10** (0.250 g, 1.16 mmol) and **11** (0.474 g, 1.39 mmol) as a white crystalline solid (0.290 g, 55%). m.p.: 102 – 104 °C; R_f(10% MeOH/DCM), 0.38. ^{1}H NMR (600 MHz, Methanol-d_4) δ 8.06 (d, J = 8.0 Hz, $2H^9$), 7.48 (d, J = 8.0 Hz, $2H^8$), 7.25 – 7.24 (m, $2H^1$), 7.06 – 7.04 (m, $2H^2$), 3.74 (tt, J = 10.5, 4.2 Hz, $1H^3$), 3.21 (dt, J = 12.3, 4.0 Hz, $2H^5$), 3.04 – 2.96 (m, $2H^6$), 2.92 – 2.85 (m, $2H^7$), 2.56 (td, J = 11.9, 2.7 Hz, $2H^5$), 2.21 – 2.13 (m, $2H^4$), 1.79 – 1.69 (m, $2H^4$). ^{13}C NMR (101 MHz, Methanol-d_4) δ 169.05, 167.50, 153.15, 144.18, 135.53, 129.34 (2C), 127.50 (2C), 123.11, 120.87 (2C), 111.28 (2C), 58.70 (2C), 51.70, 49.10, 32.14, 30.94 (2C). LC-MS (APCI$^+$/ESI): found m/z = 457.2 [M+H] $^+$ (cal. For $C_{23}H_{23}F_3N_6O$, 456.19). Purity: 98%, t_R = 2.246 min.

8.2.4.2.1. Synthesis of Fluorescent labelled DM253

Briefly, the nucleophilic aromatic substitution of 2-fluoro nitro benzene by *N*-Boc ethylenediamine is followed by the reduction of the nitro group under H_2/Pd conditions.

The product of the reduced intermediate then undergoes a DCC-mediated cyclocondensation. *N*-Boc deprotection followed by nucleophilic substitution with NBD-Cl yields the target compound.

Tert-butyl 4-isothiocyanatopiperidine-1-carboxylate (1).

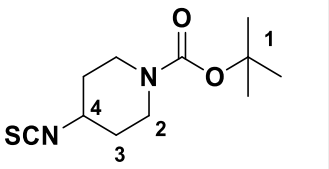

Chemical formula:$C_{11}H_{18}N_2O_2S$
Exact mass: 242.11
Molecular mass: 242.34

To a solution of *tert*-butyl 4-aminopiperidine-1-carboxylate (8.00 g, 39.9 mmol) in DMF (50 ml) at 0 °C was added 1,1'-thiocarbonyldiimidazole (7.82 g, 43.9 mmol). The reaction mixture was allowed to rise to room temperature (24 °C) and stirred for 20 hours at that temperature. The solvent was taken off *in vacuo*, the residue dissolved in EtOAc, and washed with H_2O (3 × 50 ml). The solvent was removed *in vacuo*, the residue triturated with hexane, and filtered. The filtrate was treated with activated charcoal and filtered through Celite. Removal of solvent afforded product as a colourless oil (7.52 g, 78%). ^{1}H NMR (400 MHz, DMSO-d_6) δ 4.11 – 3.98 (m, 2H, H^2), 3.69 (tt, J = 11.3, 4.1 Hz, 1H, H^4), 3.09 – 2.94 (m, 2H, H^2), 2.17 – 2.05 (m, 2H, H^3), 1.92 – 1.83 (m, 2H, H^3), 1.45 (s, 9H, H^1).

Tert-butyl (2-((2-nitrophenyl)amino)ethyl)carbamate (4).

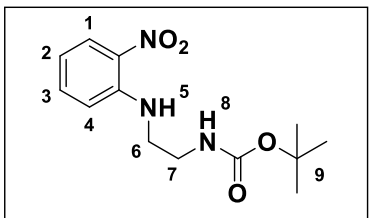

Chemical formula: $C_{13}H_{19}N_3O_4$
Exact Mass: 281.14
Molecular Mass: 281.31

1-fluoro-2-nitrobenzene (1.60 g, 5.70 mmol), *tert*-butyl (2-aminoethyl) carbamate (1.10 g, 6.84 mmol), and K_2CO_3 (1.18 g, 8.55 mmol) were mixed in MeCN (30 ml). Triethylamine, Et_3N (1.20 ml, 8.55 mmol) was added, and the resulting mixture stirred at 65 °C for 4 hr. After completion, the mixture was cooled to room temperature (18 °C), followed by the addition of H_2O (25 ml) and EtOAc (60 ml). The mixture was separated, and the aqueous phase further extracted with EtOAc (2 × 20 ml). Combined organic phases were dried over anhydrous Na_2SO_4, and solvent evaporated *in vacuo*. The pure *o*-amino-nitrobenzene intermediates were obtained following recrystallization from ethanol. Orange solid (1.54 g, 96%). R_f (20% EtOAc/Hexane), 0.28. ^{1}H NMR (300 MHz, DMSO-d_6) δ 8.18 (t, J = 5.7 Hz, 1H, H^8), 8.05 (dd, J = 8.6, 1.6 Hz, 1H, H^1), 7.52 (ddd, J = 8.6, 6.8, 1.7 Hz, 1H, H^2), 7.09 (dd, J = 8.8, 1.2 Hz, 1H, H^4), 7.00 (t, J = 5.8 Hz, 1H, H^5), 6.68 (ddd, J =

8.8, 6.8, 1.2 Hz, 1H, H^3), 3.46 – 3.35 (m, 2H, H^7), 3.25 – 3.14 (m, 2H, H^6), 1.36 (s, 9H, H^9). LC-MS (APCI$^+$/ESI): found m/z = 282.1 $[M+H]^+$ Purity: 98%, t_R = 2.314 min.

Tert-butyl(2-((2-aminophenyl)amino)ethyl)carbamate (5).

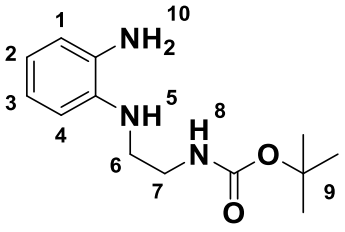

Chemical formula: $C_{13}H_{21}N_3O_2$
Exact Mass: 251.16
Molecular Mass: 251.33

To a solution **4** (1.40 g, 4.98 mmol) in 1:1 MeOH/EtOAc (30 ml) was added 10% Pd/C (0.1 equiv), and the reaction mixture was stirred at 21 °C under a hydrogen (H_2) atmosphere using a double padded balloon for 12 hr. After completion, the reaction mixture was filtered through a bed of Celite, and the filtrate concentrated *in vacuo* to afford products. Flash column chromatography using 20 – 70% EtOAc/Hexanes was performed to obtained product as a dark brown solid (1.12 g, 90%). R_f (40% EtOAc/Hexane), 0.21. ^{1}H NMR (300 MHz, DMSO-d_6) δ 6.88 (t, J = 5.7 Hz, 1H, H^8), 6.55 (dd, J = 7.3, 1.6 Hz, 1H, H^1), 6.52 – 6.37 (m, 3H, $H^{2,3,4}$), 4.39 (br-s, 3H, $H^{5,10}$), 3.21 – 3.11 (m, 2H, H^7), 3.11 – 3.00 (m, 2H, H^6), 1.40 (s, 9H, H^9). LC-MS (APCI$^+$/ESI): found m/z = 252.1 $[M+H]^+$. Purity: 98%, t_R = 0.189 min.

1-(2-aminoethyl)-N-(piperidin-4-yl)-1H-benzo[d]imidazol-2-amine (7).

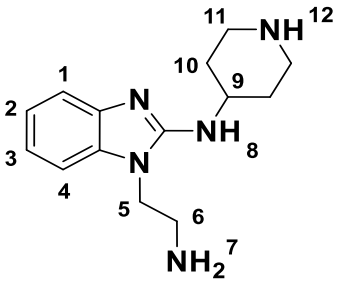

Chemical formula: $C_{14}H_{21}N_5$
Exact Mass: 259.18
Molecular Mass: 259.36

Intermediate **6** (0.490 g, 10.7 mmol) was stirred in DCM (20 ml) and TFA (10 equiv) at 23 °C for 2 hours. Following completion, DCM and TFA were evaporated *in vacuo*, and the residue taken up 50% MeOH/DCM. This solution was stirred with Amberlyst® A-21 free base resin at room temperature (23 °C) until pH was neutral. The mixture was then filtered, and the filtrate evaporated *in vacuo* to afford product. White solid (0.235 g, 85%). R_f(10% MeOH/DCM), 0.09. ^{1}H NMR (300 MHz, DMSO-d_6) δ 8.45 (br-s, 3H, $H^{7,12}$), 7.30 (dd, J = 7.1, 1.7 Hz, 1H, H^1), 7.26 (dd, J = 7.1, 1.6 Hz, 1H, H^4), 7.07 – 6.92 (m, 2H, $H^{2,3}$), 4.28 (t, J = 6.6 Hz, 2H, H^5), 4.00 (tt, J = 10.3, 3.8 Hz, 1H, H^9), 3.42 – 3.29 (m, 2H, H^{10e}), 3.22 – 2.90 (m, 4H, $H^{6,10a}$), 2.24 – 2.03 (m, 2H, H^{11e}), 1.78 (dtd, J = 14.2, 10.9, 3.9 Hz, 2H, H^{11a}). LC-MS (APCI$^+$/ESI): found m/z = 260.2 $[M+H]^+$. Purity: 98%, t_R = 0.186 min.

1-(2-aminoethyl)-N-(1-(4-(5-(trifluoromethyl)-1,2,4-oxadiazol-3 yl) phenethyl) piperidin-4-yl)-1H-benzo[d]imidazol-2-amine (8).

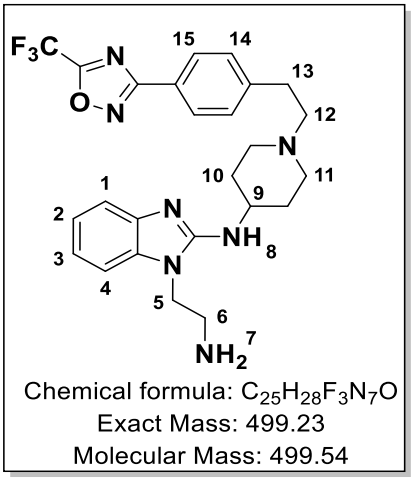

Chemical formula: $C_{25}H_{28}F_3N_7O$
Exact Mass: 499.23
Molecular Mass: 499.54

A solution of **7** (0.300 g, 1.16 mmol) and K_2CO_3 (0.240 g, 1.74 mmol) in MeCN (10 ml) was stirred under reflux at 80 °C for 30 minutes. **3** (0.446 g, 1.39 mmol) was added, and the mixture further stirred under reflux at 85 °C for 6 hours. After completion, MeCN was taken off under reduced pressure, the residue taken up in 10% MeOH/DCM and filtered. The filtrate was adsorbed on silica gel, after which column chromatography was performed using a 3 – 10% MeOH/DCM gradient as eluent, to afford product as a pale-yellow solid (0.365 g, 63%). m.p.: 66 – 68 °C. R_f(10% MeOH/DCM), 0.18. ^{1}H NMR (600 MHz, DMSO-d_6) δ 8.61 – 8.00 (br-s, 2H, H^7), 8.00 (d, *J* = 7.9 Hz, 2H, H^{15}), 7.52 (d, *J* = 7.9 Hz, 2H, H^{14}), 7.26 (dd, *J* = 7.9, 1.2 Hz, 1H, H^1), 7.23 (dd, *J* = 7.7, 1.5 Hz, 1H, H^4), 6.98 (ddd, *J* = 7.9, 6.2, 1.2 Hz, 1H, H^2), 6.93 (ddd, *J* = 7.7, 6.2, 1.3 Hz, 1H, H^3), 6.69 (d, J = 6.5 Hz, 1H, H^8), 4.26 (t, *J* = 6.7 Hz, 2H, H^5), 3.82 (tt, *J* = 11.0, 4.2 Hz, 1H, H^9), 3.18 – 3.02 (m, 4H, H^{6,11e}), 2.95 – 2.91 (m, 2H, H^{12}), 2.89 – 2.77 (m, 2H, H^{13}), 2.51 – 2.33 (m, 2H, H^{11a}), 2.14 – 1.95 (m, 2H, H^{10e}), 1.78 – 1.65 (m, 2H, H^{10a}). LC-MS (APCI$^+$/ESI): found m/z = 500.2 [M+H]$^+$. Purity: 98%, t_R = 2.082 min.

7-nitro-N-(2-(2-((1-(4-(5-(trifluoromethyl)-1,2,4-oxadiazol-3-yl)phenethyl) piperidin-4-yl)amino)-1H-benzo[d]imidazol-1-yl)ethyl)benzo[c][1,2,5]oxadiazo 4-amine (DM253-NBD).

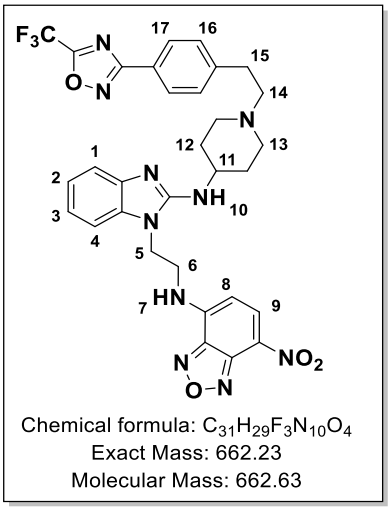

Chemical formula: $C_{31}H_{29}F_3N_{10}O_4$
Exact Mass: 662.23
Molecular Mass: 662.63

A mixture of **8** (0.150 g, 0.30 mmol) and $NaHCO_3$ (0.076 g, 0.90 mmol) in 5 ml H_2O was stirred at 65 °C for 10 min. A solution of 4-chloro-7-nitrobenzo[c][1,2,5]oxadiazole, NBD-Cl (0.060 g, 0.30 mmol) in MeCN (5 ml) was then added to the heated mixture dropwise *via* syringe. The resulting reaction mixture was stirred at 65 °C for 2 hr, during which a gradual colour change from yellow to dark brown was observed. After completion, the mixture was cooled and MeCN was removed *in vacuo*. The aqueous

residue was then filtered and extracted with EtOAc (3 × 20 ml). Combined organic phases were washed with brine and dried over anhydrous Na_2SO_4. Column chromatography using 8 – 10% MeOH/DCM was performed to obtain the product as a blackish solid (0.145 g, 73%). m.p.: 53 – 54 °C. R_f(10% MeOH/DCM), 0.51. ^{1}H NMR (300 MHz, DMSO-d_6) δ 8.67 – 8.60 (br-s, 2H, H^7), 8.47 (d, J = 8.7 Hz, 1H, H^9), 8.21 (d, J = 8.7 Hz, 1H, H^8), 8.04 (d, J = 7.9 Hz, 1H, H^{17}), 7.56 (d, J = 7.9 Hz, 1H, H^{16}), 7.36 (d, J = 7.5 Hz, 1H, H^1), 7.29 – 7.18 (m, 1H, H^4), 7.15 – 7.08 (m, 1H, H^2), 7.03 – 6.95 (m, 1H, H^3), 6.47 (d, J = 6.2 Hz, 1H, H^{10}), 4.58 (m, 2H, H^5), 4.13 – 4.08 (m, 1H, H^{11}), 3.99 – 3.83 (m, 2H, H^{13e}), 3.77 – 3.62 (m, 4H, H^{6,14}), 3.29 – 3.16 (m, 4H, H^{13a,15}), 2.38 – 1.97 (m, 4H, H^{12}). LC-MS (APCI$^+$/ESI): found m/z = 663.2 $[M+H]^+$. Purity: 98%, t_R = 2.658 min.

8.3. Biological Evaluation

8.3.1. *P. falciparum* Culture

Continuous *in vitro* cultures of asexual erythrocyte stages of a CQ-sensitive *P. falciparum* strain (NF54) were maintained using a modified method described by Trager and Jensen.[2] The parasitemia and hematocrit of the cultures were held at 5–8% and 3–6%, respectively. The culture was synchronized at the ring stage by incubating with D-sorbitol. Blood for i*n vitro* cultures was obtained from the Groote Schuur blood bank in Cape Town, with permission from the bank's director. Ethics clearance was obtained from the University of Cape Town ethics committee, and the blood type was O+.

8.3.2. *In vitro* Antiplasmodium Activity Assay

8.3.2.1. Lactate Dehydrogenase Assay

The target compounds' antiplasmodium activities were evaluated using the parasite lactate dehydrogenase assay as an indicator for parasite survival. Briefly, the stock solutions of CQ diphosphate and test compounds were prepared at 2mg/mL in distilled water for CQ and 100% DMSO for the test compounds. These stock solutions are stored at -20 and further diluted on the day of the experiment. In the trophozoite stage, the synchronous cultures of P*f*NF54 CQS and multidrug- resistant strain, P*f*K1 were prepared at 2% parasitemia and 2% hematocrit. The compounds were tested at a starting concentration of 10,000 ng/ml. From this starting concentration, the compounds were serially diluted 2-fold in a complete medium to give ten concentrations with a final volume

of 200 µL in each well. Parasites were incubated in the presence of the compounds at 37 °C under hypoxic conditions (4% CO_2 and 3% O_2 in N_2) For 48 h. Post incubation, 100 µL of MalStat reagent and 15 µL of resuspended culture combined. This is followed by adding 25 µL of nitro blue tetrazolium chloride (NBT). The assay plates were kept in the dark for 10 min to develop fully. The absorbance was then measured at 620 nm on a microplate reader. The data generated is then processed using Microsoft Excel to analyze the dose-response.

8.3.2.2. Hypoxanthine Incorporation Assay

Some of the compounds described in this work were also tested using the modified [^{3}H]-hypoxanthine incorporation assay against the CQS (NF54) and multi-drug resistant strains (K1) of *P. falciparum*. The compounds investigated were dissolved in DMSO to a concentration of 10 mg/mL of stock solutions, which were diluted in the culture medium without hypoxanthine. *P. falciparum*-infected RBCs (100 µL/well with 2.5% hematocrit and 0.3 % parasitemia) were added to each and properly mixed in 100 µL media. This mixture was incubated for 48 h. Further, 0.5 microCi of [^{3}H]-hypoxanthine in 50 µL media was added, and the culture plates were further incubated for 24 h. Radioactivity was assessed from the parasites harvested on glass fiber filters using a β-plate liquid scintillation counter. Each compound's radioactivity was recorded as counts/min/well. This was analyzed as a percentage relative to the untreated controls. IC_{50} values were determined by linear interpolation.

8.3.2.3. *In vitro* β-Hematin Inhibition Assay

The β-hematin formation inhibition assay was performed according to Carter et al. and modified for manual handling.[3,4] 20 mM stock solutions of the compounds investigated were made by dissolving the already weighed compound in DMSO. Specific volumes of this stock were pipetted into a 96-well plate in triplicate to give concentrations from 0 to 1000 µM, where 1000 is the concentration of the final well. The volume of DMSO was maintained at 10 µL in each well. Thereafter, 70 µL of deionized water and 20 µL of a 30.55 µM NP-40 were added. The absorbances of plate wells were pre-read at 405 nm on a SpectraMax 340 PC384 Absorbance Microplate Reader (Molecular Devices, Sunnyvale, CA, USA). A hematin stock 25 mM concentration was made by sonicating hemin dissolved in DMSO for 60 secods. This mixture was then suspended in 178 µL of 1 M

acetate buffer (pH 4.8) and mixed thoroughly by sonication. 100 µL of this mixture was transferred to the wells to obtain a buffer concentration of 0.5 M and hematin concentration of 100 µM. The final assay plate was covered with incubated plate at 37 °C for 5-6 hours. Post incubation, the presence of free heme free was assessed by exploiting the affinity of pyridine for iron according to the methods described by Ncokazi and Egan.[5] Briefly, a mixture of 50% pyridine, 30% water, 20% acetone all (v/v), and 0.2 M Hepes was made. 32 µL of this mixture was added was transferred to every well to obtain a final pyridine concentration of 5% (v/v). 60 µL of acetone was added to help hematin dissipate. Thereafter, the absorbances of the content of the wells were obtained again at 405 nm. This new absorbance was then subtracted from the pre-read values. A dose-response curve of these values was plotted in GraphPad Prism. Each compound's IC_{50} was obtained using the variable slopes that were fitted to the absorbance data. The data was fitted according to the equation below, where the IC_{50} is obtained at the curve's midpoint, and H represents the hill slope. This describes the steepnes of the curve. T and B defines the curve's lower and upper baselines respectively

$$Y = \frac{B+(T-B)}{1+ 10^{(\log IC50 - X)H}}$$

Equation 8.1

8.3.2.4. Parasite Cellular Heme Speciation Assay

Ring stage *Pf*NF54 parasites (5% parasitemia and 2% hematocrit) were synchronized and incubated with different concentrations of the compounds investigated for 36h as well. A no drug control was also included. After 36 h, the rings mature to trophozoites. The matured trophozoites were liberated from the RBCs through saponin lysis. The liberated trophozoites were resuspended in 100 µL PBS and prescisely transferred into a 0.5 mL round-bottomed, 96-well plate (Axygen Scientific). This plate is known as the "stock plate." Similarly, another plate was made by transferring 10 µL of the resuspended trophozoites to a SYBR green-based cell counting (FACS) solution made up of PBS pH 7.5 containing 0.125% (v/v) glutaraldehyde and 0.5% (v/v) DNase. This is the "counting plate". Together, the total volume of each well in the counting plate becomes 200 µL. The counting plate is stored in the fridge at 4 °C. Cells were counted and evaluated using flow cytometry on a Becton Dickinson (BD) Accuri™ C6 Plus system with SSC/FL1530 nm

using BD Accuri™ C6 Plus software. To prepare the cells for sorting on the flow cytometer, 20 µL of thoroughly resuspended cells from the counting plate were transferred into a flat-bottomed, 96-well plate. This plate already contains 160 µL of a solution of 1× SYBR Green in PBS. 20 µL of Trucount™ beads (BD) were then added to this solution to make a final volume of 200 µL. This ensure that the number of beads contained in this final volume is fixed. This plate was kept in an aluminium foil to prevent light interference and incubated at 37 °C for 30 minutes. Before reading on the flow cytometer the mixture is properly resuspended. Usually, about 10 000 total events were counted for each sample. The concentration of cells in the wells was calculated according to equation 8.2:

$$C_F = (T/B) \times C_{B,}$$

Equation 8.2

where C_F is the cells' concentration in 1mL; T is the number of trophozoites gated; B is the number of Trucount™ beads gated, and C_B is the concentration of Trucount™ beads in each well per mL (calibrated bead count according to supplier stipulation).

FlowJo software (V10) is used to analyze the data. The stock plate was stored at −20 °C for at least a day. A series of cellular fraction steps were performed to quantify hemoglobin, heme, and hemozoin amounts in the cell after compound action. The content of the stock plate is thawed after freezing to lyse the parasite's membrane. 100 µL of water was added, and the contents of the plate was sonicated for 5 min. 50 µL of a 0.02 M Hepes buffer at pH 7.5 was added, and the sample was centrifuged at 3600 rpm for 20 min. The supernatant of this solution was transferred to an adjacent set of wells on the same plate. 50 µL of 4% SDS was added to this supernatant and sonicated for 5 min. After that, the plate was incubated on the bench for 30 minutes. This was followed by the addition of 50 µL of 0.3 M NaCl and 25% pyridine (v/v) in 0.2 M Hepes pH 7.5. 200 µL of this supernatant was pipetted to a flat-bottomed, 96-well plate referred to as the "reading plate."

50 µL water and 50 µL of 4% SDS were added to the pellets remaining and mixed well. After sonicating for 5 minutes and incubation for 30 minutes to promote the solubilization of free heme, 50 µL of 0.2 M Hepes pH 7.5, 50 µL of 0.3 M NaCl, and 25% pyridine were added. The plate was then centrifuged at 3600 rpm for 20 min. On the same plate, the supernatants after centrifugation were transferred to the wells adjacent and diluted with 150 µL of water to give a final volume of 400 µL with water. 200 µL of this solution was transferred to the reading plate. To the remaining pellets, representing the hemozoin fraction, 50 µL of water and 0.3 M NaOH was added and sonicated for 15 minutes to dissolve hemozoin. The plate was kept on the bench for 20 minutes to incubate at room temprature. Finally, 50 µL of 0.2 M Hepes buffer, 50 µL of 0.3 M HCl, and 50 µL of 25% pyridine solution were added, and the supernatant was diluted with water to a final volume of 400 µL. 200 µL was transferred to the reading plate was also transferred to the reading plate. The UV-visible spectra of these fractions were recorded between 400 nm and 415 nm on a multi-well plate reader (Spectramax 340PC, Molecular Devices). hemoglobin, heme, and hemozoin percentages were obtained from the absorbance values of the three fractions. Standard curve was used to assess the total heme in each of these samples. Final analysis was performed on GraphPad Prism (v5) where significance tests were performed. All analysis were performed in four technical repeats and three biological repeats. P values were obtained using unpaired 2-tailed *t*-test, 95 % CI.

8.3.2.5. *In-vitro* Resistance Selection and Whole-Genome Sequencing

***In vitro* Resistance Selection.** Resistance selection experiments were carried out with **KP68**. Two flasks containing 2 x 10^9 Dd2 parasites were cultured under 5x IC_{50} of **KP68** (300 nM). Parasites appeared to die slowly and form gametocytes, but all healthy trophozoites and rings were cleared by day 12. Recrudescence was observed only on day 42 in one flask, with no parasites in the other flasks until day 60. Three clones with diverse profiles were selected for sequencing, whereby parasitized RBCs were lysed with saponin to harvest trophozoites. Their genomic DNA (gDNA) was extracted with a QIAamp DNA Blood Midi Kit.

Whole-Genome Sequencing Analysis (WGS). WGS of gDNA from parental and resistant clones employed an Illumina TruSeqDNA PCR-Free library preparation protocol and a MiSeq sequencing platform. Briefly, 2mg of genomic DNA were sheared to a mean

length of 550 bp, end-repaired, adenylated on their 3' ends, and ligated to indexed adaptors. Samples were pooled and sequenced on Illumina MiSeq flow cells to obtain 300 bp paired-end reads. Sequence data were aligned to the *P. falciparum* Dd2 genome (PlasmoDB version 48) using BWA (Burrow-Wheeler Alignment). Samtools and Picard were used to remove PCR duplicates and reads that did not map to the reference genome.

Reads were realigned around indels using GATK Realigner Target Creator, and base quality scores were recalibrated using GATK Table-Recalibration. GATK HaplotypeCaller (version 4.1.8; Min Base quality scoreR18) was used with the clones to identify all possible variants, which were filtered based on quality scores (variant quality as a function of depth QD > 1.5, mapping quality > 40) and read depth (depth of reading > 5) to obtain high-quality single nucleotide polymorphisms (SNPs). These SNPs were annotated using snpEFF. The variants from the resistant clones were compared against the Dd2 parent to obtain homozygous SNPs that were present exclusively in the resistant clones. IGV was used to confirm the SNPs present in the resistant clones. BicSeq was used to discover copy number variants (CNVs) against the Dd2 parent.

8.3.2.6. *In-vivo* Efficacy Studies in *P. Berghei*-infected Mice

In vivo antimalarial efficacy of the target compounds was assessed for a group of five female Naval Research Institute mice with weight between 20 – 22 g at the Swiss TPH. This were injected intravenously on day 0 with *P. berghei* GFP ANKA malaria strain (2×10^7 parasitized erythrocytes donated from A.P Waters and C.J Janse, Leiden University). Untreated control mice die between the 6^{th} and 7^{th} days after infection. The compounds investigated were formulated in 0.5% methylcellulose / 0.5% Tween 80 and administered orally in four consecutive doses of 50 mg/kg at 4, 24, 48, and 72 h after infection. Levels of parasitemia were determined 72 h after infection using flow cytometric techniques. The activity of compounds was evaluated as the difference between the mean percent parasitemia for the treated and untreated groups expressed as a percent relative to the untreated group. Parasite survival, measured in days was recorded up to 30 days after infection. A mouse is said to be cured if it survived up to day 30 after infection with no parasites detected on a slide. The Swiss TPH in Basel is approved for animal studies by the veterinary authorities of the Canton Basel-Stadt (Permit No. 1731 and 2303) based on Swiss Cantonal and National Regulations.

8.4. Fluorescence Live-Cell Microscopy

8.4.1. General Methods

Microscope chamber slides were purchased from ThermoFisher Scientific, Massachusetts, USA. Specifically, the Nunc Lab-Tek II eight-well chamber slides made of cover glass of 1.5 thickness. 150 µL of 0.01% (w/v) poly-L-lysine solution was used to coat the chamber slides for ten minutes. The solution was removed, and the plate was air-dried on the bench. For imaging, Ringer's solution is required. This solution contains all the necessary salts required to mimic the biological environment needed to keep parasite live-cells out of culture. This solution was prepared based on previously described compositions.[6] This compositions are outlined in Table 8.2. After preparation, the pH was adjusted to 7.4, and the solution was filtered through a 0.22 µm nylon syringe filter.

Table 8.2. Constituents of the Ringer's solution for live-cell imaging of the *P. falciparum*

Component	Molecular weight	Final Concentration	Mass required for 100mL
NaCl	58.44	122.5 mM	715.9 mg
KCl	74.56	5.4 mM	40.3 mg
$CaCl_2$	147.02	1.2 mM	17.6 mg
$MgCl_2$	95.21	0.8 mM	7.6 mg
D-glucose	180.16	11 mM	198.2 mg
Hepes	238.30	25 mM	595.8 mg
NaH_2PO_4	119.98	1 mM	12.0 mg

RBCs infected with *P. falciparum* trophozoites (NF54 strain) and schizonts were cultured according to the methods described by Trager and Jensen. 5 µL of the parasitized-RBC were resuspended in the Ringer's solution after parasites were harvested, centrifuged and the supernatant culture media was removed. This mixture was vortexed gently to prevent the clustering of cells. The imaging chamber slides were filled with 150 µL of suspended cells. This was incubated for 30 minutes to allow the parasites to stick to the chamber slide's cover glass. The excess Ringer's solution post incubation was removed, and a fresh

solution was added. By doing After this, all the cells that did not stick to the chamber slide were removed. A fresh Ringer's solution was added, which was also subsequently removed. Finally, 150 µL of Ringer's solution, containing the required concentrations of fluorescence compounds was added to the cells. The parasites were incubated with the fluorophores for 30 minutes prior to imaging.

8.4.1. Live-Cell Confocal Microscopy

Zeiss Axiovert 200 M LSM 150-META was used to obtain confocal and Airyscan images. The images were taken at the University of Cape Town's Confocal and Light Microscope Imaging Facility. SR-SIM images were captured on the Zeiss Elyra 7 microscope. A Plan-Apochromat 63x/1.40 Oil DIC M27 objective lens was used, and the cells were incubated at 37 °C. Images were captured and processed with ZEN 2018 (Carl Zeiss Microscopy GmbH). Laser transmission was kept as low as possible to minimize cell phototoxicity.[7] Dye concentrations with respective excitation and emission settings are listed in Table 8.3. Conclusion on accumulation we made after studying more than ten images obtained at different imaging sessions.

Table 8.3. Concentrations of fluorescent dyes used for confocal imaging of *P. falciparum* with respective excitation lasers and emission filter settings

Dye	Concentration	Excitation Laser	Emission filter
DRAQ 5	500 nM	580 nm	633-647 nm
LysoTracker	100 nM	560 nm	575-590 nm
Nile Red	100 nM	561 nm	575-630 nm
ER-Tracker	100 nM	561 nm	575-630 nm
MitoTracker	100 nM	561 nm	650-710 nm
KP68	50 nM	420 nm	500-550 nm

8.5. Affinity Detection and Proteomic Identification of Binding Target (s)

8.5.1. Preparation of Biological Material for Affinity Detection Experiments

8.5.1.1 Saponin Lysis of Erythrocytes

P. falciparum-infected trophozoites were cultured, harvested, and donated by colleagues from the Swiss Tropical and Public Health Institute and the University of Pretoria.

Parasites were liberated from the erythrocytes using 1% Saponin Solution in 0.01 M phosphate-buffered saline (PBS) at pH 7.4. This was incubated at room temperature for 15 minutes and centrifuged at 1500 rcf for ten minutes to remove the erythrocyte debris. This was further washed with 3 × 20 mL PBS. The trophozoites obtained were stored at -80 °C.

8.5.1.2. Rupturing the Digestive Vacuole Membrane

Freezing the parasite pellets at -80 °C and subsequent thawing resulted in the lysis of the trophozoites but not the digestive vacuole membrane. This was observed under a Giemsa-stained slide. A protease inhibitor cocktail solution was prepared by dissolving one tablet of the SigmaFAST Protease Inhibitor cocktail in 10 mL of acidified deionized water at pH 4.5-5.5. 500 µL of this solution was added to the trophozoites pellets. This mixture is divided into small portions of approximately 1 mL each. Each fraction was centrifuged at 10 900 rpm for five minutes. The supernatant of each fraction was collected, pooled, and stored at -20 °C. To the pellet of each fraction, 1 mL of the protease inhibitor cocktail was added to the pellets of each fraction and mixed thoroughly. Fractions were frozen at -80 °C for 20 minutes and then thawed at 37 °C for ten minutes. After the fractions were vortexed and centrifuged for two minutes at 10 900 rpm. The supernatants were removed and pooled together. This freeze and thaw cycle was continued over several days, after which the digestive vacuole lysis was judged to be complete when no distinct shapes were observed under the microscope. The pooled lysate was stored at -20 °C.

8.5.1.2. Ultracentrifugation and Quantification

The pooled lysate was thawed, transferred into a Beckman polymer centrifuge, and filled with acidified water. The parasite lysate's soluble and insoluble (membrane) fractions were separated using the Beckman centrifuge model L7-65 ultracentrifuge with an SW40-TI rotor. The samples were centrifuged at 31 000 rpm for an hour at 4 °C to pellet out the insoluble membrane material. The supernatant from here was transferred to Merck Amicon Ultra-15 Centrifugal Filter Devices with a 10 kDa molecular weight cut-off. These were spun on a Beckman J2-21M/E centrifuge with JA-14 rotor at 7000 rpm for 20 mins at 4 °C. The insoluble fraction was resuspended with a 0.1% Triton detergent and mixed

gently to help with mixing. All protein fractions were quantified using the Bio-Rad Quick Start Bradford Protein Assay using Bovine serum albumin as a standard.

8.5.2. Preparation of Drug-labelled agarose Beads

About 500 µL packed beads of NHS-activated Sepharose 4 Fast Flow (GE Healthcare) were washed three times with 1 mM cold HCl (1 mL). Afterward, the beads were incubated with a coupling solution of enough moles of the derivatized ligand necessary for a 3 µmol/mL loading capacity dissolved in 100 mM Hepes at pH 8.3. This was rotated at room temperature for one hour, after which the sample was washed three times with 100 mM Hepes at pH 8.3, containing no ligand. The supernatant from each wash step was collected and made up to a known volume for quantification by spectrophotometry to determine the amount of derivatized ligand remaining. The beads were then incubated in a "blocking solution" comprising 100 mM Tris at pH 8.5 and rotated at room temperature for one hour. Following centrifugation, the blocking solution was removed, and the beads were washed with Hepes buffer (100 mM, pH 8.3) followed by acetate buffer (100 mM, pH 4.5). This wash routine was repeated, alternating between high and low pH values, was repeated three times. The beads were stored in 20% aqueous ethanol to avoid microbial contamination.

8.5.3. Matrix-based Affinity Chromatography

An aliquot of 150 µL suspended beads (approximately 100 µL packed beads) was equilibrated by washing three times with 1x affinity buffer (1 mL). About 60 µg of *P. falciparum* lysate was added to the beads, and the total volume was up to 500 µL. This mixture was gently rocked at 4 °C for half an hour. The beads were centrifuged at 4 °C for two minutes at 13 500 x *g,* and the supernatant was removed. They were resuspended in an 800 µL affinity buffer (1x) and washed six times. For solid-phase elution, 40 µL sample application buffer (4x) was added to the samples, followed by mixing, centrifugation, and dry-boiling at 95 °C for five minutes. Samples were then loaded onto the gel directly. Alternatively, for competition elution, 450 µL of a concentrated solution of the drug in affinity buffer (1x) was added to the beads, and this was rotated at 4°C for 20 minutes. Concentrations were 5 mM for **KP124** and 3 mM for **KP68**. Following centrifugation, the supernatant was loaded onto a Pall Nanosep Centrifugal Device with Omega Membrane with a 10 kDa molecular weight cut-off. This was concentrated at 13

500 x *g* at 4°C for about six minutes until approximately 40-50 µL of each sample remained. The remaining supernatant was removed and placed in a new microfuge tube. To this was added 15 µL sample application buffer (4x) followed by mixing, centrifugation, and dry boiling at 95 °C for five minutes. Samples were then loaded onto the SDS-Page gel directly.

8.5.4. SDS-polyacrylamide Gel Electrophoresis

The resolving or separating gel buffer was prepared from 18.2g Tris and 0.4 g SDS, made up to 100 mL, and adjusted to pH 8.8 to give a concentration of 150 mM Tris and 0.4 % SDS. The stacking gel buffer was prepared from 6.05 g Tris and 0.4 g SDS, made up to 100 mL and adjusted to pH 6.8. This gave concentrations of 50 mM Tris and 0.4% SDS. For the running buffer (5x), 15.1 Tris, 72 g glycine, and 5 g SDS were made up to 1L. This was further diluted to 1x to give a concentration of 25 mM Tris, 200 mM glycine, and 0.1% SDS. Finally, 20 mL of sample application buffer (4x) was made from a mixture of 10 mL of stacking buffer and was added to 8 mL glycerol, 0.8 g SDS, 0.8 mL β-mercaptoethanol, 0.2 mg bromophenol blue indicator, and 1.2 mL dH_2O.

8.5.4.1. Casting gels

The equipment was thoroughly cleaned with 70% (v/v) aqueous ethanol. 1.0 mm gels were cast as per the standard procedure. Briefly, the solution for the separating gel was prepared and inserted into the casting apparatus. Isopropanol was used to level out the gel surface. After polymerization, the isopropanol was removed, and the stacking gel was prepared. This was added to the casting apparatus, and a ten-lane comb was gently inserted. Once the stacking gel had been set, the apparatus was placed in the running chamber of a Bio-Rad Mini-PROTEAN Tetra System. The comb was removed, and a running buffer (1x) was added. Samples were prepared by diluting an appropriate volume of sample application buffer (4x) followed by dry-boiling for five minutes at 95°C using a Thermo Scientific Reacti-Therm I #TS-18822 heating mantle with a Reacti-Block #TS-18819 attachment for microfuge tubes. 15 µL of the sample was loaded on the gel. 5 µL of the PageRuler Pre-Stained Protein Ladder 10 to 180 kDa (Thermo Fischer Scientific #26616) was also loaded on each gel. 5 µL sample application buffer (1x) was added to empty wells. For electrophoresis, a Bio-Rad PowerPac Basic was used. Single gels were

run at 20 mA for 45 minutes, and double gels were run at 30 mA for 90 minutes. After the run, the plates were gently prised and placed in dH_2O.

8.5.4.2. Staining

The gels were stained with Coomassie Brilliant Blue and Silver Stain. For Coomassie staining, the gel was incubated with Coomassie Brilliant Blue R-250 Staining Solution (Bio-Rad #1610436) and gently rocked at room temperature overnight. This staining solution was prepared by dissolving 0.1% Coomassie Brilliant Blue R-250 (w/v) in 50: 40: 10 (v/v/v) methanol: water: acetic acid. Following staining, gels were destained using Coomassie Brilliant Blue R-250 Destaining Solution (Bio-Rad #1610438) by washing the gel with water and then covering the gel with a destaining solution. This was gently rocked at room temperature for several hours, during which the destaining solution was changed at least three times. The destaining solution was also prepared by mixing 50:40:10 (v/v/v) water: methanol: and acetic acid. Alternatively, gels were silver-stained using the procedure described in the Sigma-Aldrich ProteoSilver Plus Silver Stain Kit.

8.5.5. Sample Preparation

Samples were digested in solution and in gel. For in-gel digestion, gel bands were gently cut out of the gel and subjected to in-gel digestion. In-gel digestions were performed according to Macek *et al.*, with slight modifications. Briefly, 1 Mm dithiothreitol (DTT) for an hour at room temperature to reduce the protein disulfides. This is subsequently alkylated with 5.5 mM iodoacetamide (IAA) for an hour at room temperature in the dark. Proteins were digested with Sequence-grade trypsin (New England Biolabs, Ipswich, MA, USA) at an enzyme protein ratio of 1: 50 for 18 h at 37 °C, followed by a 4-fold dilution with water. Samples were further digested overnight. Protease activity was quenched by acidification with trifluoracetic acid (TFA) to a final concentration of 1 - 2%. The resulting peptide was desalted and concentrated on a reverse-phase Sep-Pak C18 Cartridge. The resulting peptides were eluted with 80% acetonitrile (ACN) and 6% TFA. The ACN used was later removed by vacuum centrifugation for an hour. The peptide concentration was subsequently estimated by measuring the absorbance at 280 nm using Nanodrop 2000C, Thermo Scientific.

8.5.6. Liquid Chromatography-Tandem Mass Spectrometry Analysis

Chromatographic separation was achieved using a 100 µm ID, 20 mm pre-column attached to a 75 µm, 300 mm analytical column packed with C18 Luna beads connected to an Ultimate 3,500 RS nano UPLC system. About 600 ng of desalted peptides per sample were loaded onto the column, starting with a mobile phase of 2% ACN, 0.1% formic acid, and separated at a constant flow rate of 400 nl/min over a 70 min gradient as follows: 10 min at 2% ACN, increased to 6% ACN over 2 min, to 40% ACN over 70 minutes, and to 80% ACN over 5 min, and held at 80% for 15 minutes as a column wash.

Mass spectra were collected on a Q Exactive mass spectrometer (Thermo Fisher Scientific, Waltham, MA, USA) operating in a positive mode using a data-dependent acquisition and a top-10 method. Intensity threshold for MS^2 ion selection was 1.3e4 with charge exclusion of z = 1 and z > 5. Peptides were ionized by electrospray ionization, and MS spectra were acquired at a resolution of 70,000 for MS^1 and 17,500 for MS^2.
The automated gain control (AGC) target was set to 3e6 with a maximum integration time of 250ms (MS1) and 1e5 with a maximum integration time of 80 ms (MS^2). MS^1 scan range was 300–1,750 Da, and peptide fragmentation was performed using higher-energy collision dissociation (HCD) and setting the energy to 28 Normalised Collision Energy (NCE) and the product ion scan range to 200–2,000 Da. Subsequently, the data from these samples were reacquired. MS acquisition parameters were unchanged, while chromatographic conditions differed in that the 70 min gradient was from 6% ACN to 23%, rather than 40%. The raw files generated by the mass spectrometer were imported into Proteome Discoverer (Version 1.4, Thermo Scientific) and processed using the SequestHT algorithm. Data analysis was structured to allow for methylthio as a fixed modification, deamidation, and oxidation. The precursor tolerance was set to 10 ppm and fragment ion tolerance to 0.02 Da. Databases for *P. falciparum* and *H. sapiens* were obtained from UniProt (www.uniprot.org). The raw files generated were converted to Mascot generic format (mgf), and the files were interrogated using the Myrimatch algorithm through SearchGUI. Search parameters were set for the Sequest HT search. The results files were imported into Scaffold (Version 1.4.4, Proteome Software Inc.) and identified peptides validated using the X! Tandem search algorithm included in Scaffold. Peptide and Protein validation was done using the Peptide and Protein Prophet

algorithms. Further analysis was performed using Scaffold Viewer (Version 4.5.3, Proteome Software Inc.).[8]

8.6. Physicochemical Evaluation of Target Compounds

8.6.1. Relative Fluorescence Quantum Yields

Relative fluorescence quantum yields were calculated according to Equation 8.1, in which Φ represents the comparable fluorescence quantum yield, A is the absorbance of the sample at the excitation wavelength, F is the area under the fluorescence emission curve, and n is the refractive index of the solvent system. The subscripts S and X refer to the standard and the unknown samples, respectively.[9]

$$\Phi = \left(\frac{AS}{AX}\right)\left(\frac{FX}{FS}\right)\left(\frac{nx}{ns}\right)$$

Equation 8.3

The reported measurement by Melhuish of Φ 0.546 for quinine sulfate in 0.5 M sulfuric acid was used as a standard value.[10] Absorbance values were kept below 0.1 to minimize inner filter effects. In each case, the area under the fluorescence emission curve was determined by summing the fluorescence intensities across the entire emission range. Refractive indices of 1.346, 1.3614, and 1.3885 were used for sulfuric acid, ethanol, and 40% DMSO (v/v) in 20 mM Hepes, pH 7.5, respectively. The final value was calculated by interpolation.[11]

8.6.2. Kinetic Turbidimetric Method (pH 7.4)

The test compounds were dissolved in DMSO to a 10 mM stock concentration. A pre-dilution plate was prepared by serially diluting each stock solution in triplicates to obtain concentrations from 0.25 mM to 10.0 mM in a 96-well plate. A secondary dilution of the compounds in both DMSO and 0.01 M Ph 7.4 PBS was made from each pre-dilution in triplicate on a second 96-well plate. The first six wells contained compounds dissolved in DMSO, while the last six wells contained the samples dissolved in PBS at the same nominal concentration as those in DMSO. The final solvent volume in each assay plate was kept at 200 µL. This was done by adding 4 µL of each solution from the pre-dilution plate to the corresponding well containing 196 µL of DMSO and PBS. This maintains the final concentration of DMSO in the aqueous PBS buffer below 2% v/v. Additionally, a

second plate containing compound concentrations of 60, 100, and 120 μM. Controls made up of different concentrations in DMSO were prepared to rule out false turbidimetric absorbance readings due to the absorption of incident rays by test compounds in solution at the test wavelength. After preparation, the assay plate was covered and left to equilibrate for 2 h, after which the UV-vis absorbance of each well on the plate was measured at 620 nm using a SpectraMax^{384} microplate reader. The corrected absorbance was plotted against compound concentration and computed using MS Excel. Hydrocortisone and Reserpine were used as negative and positive controls, respectively.

8.6.3. Kinetic Solubility by HPLC (pH 6.5)

The kinetic solubility assay carried out in this work is based on the shake flask method.[12] Calibration standards were prepared from a DMSO stock solution of 10 mM of test compounds (10 to 220 μM). The stock solution was used to spike in a ratio of 1:50 duplicate aqueous samples in PBS at pH 6.5. The DMSO was dried off using a GeneVac (MiVac, 90 min, 37 °C). The samples were incubated for 20 h while shaking. After incubation, the samples were filtered, and their absorbance was measured using HPLC-DAD (Agilent 1200 Rapid Resolution HPLC with a diode array detector). Calibration curves were plotted from the standards earlier prepared. These calibration curves were used to evaluate the solubility of the aqueous samples.

8.7. References

(1) de Villiers, K. A.; Kaschula, C. H.; Egan, T. J.; Marques, H. M. Speciation and Structure of Ferriprotoporphyrin IX in Aqueous Solution: Spectroscopic and Diffusion Measurements Demonstrate Dimerization, but Not μ-Oxo Dimer Formation. *JBIC J. Biol. Inorg. Chem.* **2007**, *12* (1), 101–117.

(2) Trager, W.; Jensen, J. Human Malaria Parasites in Continuous Culture. *Science (80.).* **1976**, *193* (4254), 673–675.

(3) Sandlin, R. D.; Carter, M. D.; Lee, P. J.; Auschwitz, J. M.; Leed, S. E.; Johnson, J. D.; Wright, D. W. Use of the NP-40 Detergent-Mediated Assay in Discovery of Inhibitors of β-Hematin Crystallization. *Antimicrob. Agents Chemother.* **2011**, *55* (7), 3363–3369.

(4) Wicht, K. J.; Combrinck, J. M.; Smith, P. J.; Hunter, R.; Egan, T. J. Identification and Mechanistic Evaluation of Hemozoin-Inhibiting Triarylimidazoles Active

against Plasmodium Falciparum. *ACS Med. Chem. Lett.* **2017**, *8* (2), 201–205.

(5) Ncokazi, K. K.; Egan, T. J. A Colorimetric High-Throughput β-Hematin Inhibition Screening Assay for Use in the Search for Antimalarial Compounds. *Anal. Biochem.* **2005**, *338* (2), 306–319.

(6) Pisciotta, J. M.; Coppens, I.; Tripathi, A. K.; Scholl, P. F.; Shuman, J.; Bajad, S.; Shulaev, V.; Sullivan, D. J. The Role of Neutral Lipid Nanospheres in *Plasmodium falciparum* Haem Crystallization. *Biochem. J.* **2007**, *402* (1), 197–204.

(7) Wissing, F.; Sanchez, C. P.; Rohrbach, P.; Ricken, S.; Lanzer, M. Illumination of the Malaria Parasite *Plasmodium falciparum* Alters Intracellular PH. *J. Biol. Chem.* **2002**, *277* (40), 37747–37755.

(8) Giddey, A. D.; Ganief, T. A.; Ganief, N.; Koch, A.; Warner, D. F.; Soares, N. C.; Blackburn, J. M. Cell Wall Proteomics Reveal Phenotypic Adaption of Drug-Resistant Mycobacterium Smegmatis to Subinhibitory Rifampicin Exposure. *Front. Med.* **2021**, *8*.

(9) Fery-Forgues, S.; Lavabre, D. Are Fluorescence Quantum Yields So Tricky to Measure? A Demonstration Using Familiar Stationery Products. *J. Chem. Educ.* **1999**, *76* (9), 1260.

(10) Melhuish, W. H. Quantum Efficiencies of Fluorescence of Organic Substances: Effect of Solvent and Concentration of the Fluorescent Solute 1. *J. Phys. Chem.* **1961**, *65* (2), 229–235.

(11) Aminabhavi, T. M.; Gopalakrishna, B. Density, Viscosity, Refractive Index, and Speed of Sound in Aqueous Mixtures of N, N-Dimethylformamide, Dimethyl Sulfoxide, N, N-Dimethylacetamide, Acetonitrile, Ethylene Glycol, Diethylene Glycol, 1,4-Dioxane, Tetrahydrofuran, 2-Methoxyethanol, and 2-Ethox. *J. Chem. Eng. Data* **1995**, *40* (4), 856–861.

(12) Hill, A. P.; Young, R. J. Getting Physical in Drug Discovery: A Contemporary Perspective on Solubility and Hydrophobicity. *Drug Discov. Today* **2010**, *15* (15–16), 648–655.

8.8. Appendix

8.8.1. ^{1}H-NMR Characterization of Relevant Intermediates (KP68)

8.8.1.1 Spectroscopic Analysis of the Benzimidazole Intermediate g/h

The characteristic features of the ^{1}H-NMR spectrum (300 MHz, DMSO) of **g/h** shows the appearance of two doublets at 6.50 and 6.54 ppm, corresponding to a proton each (H-9 and H-7, respectively). The aliphatic region shows the appearance of a singlet at 5.14 ppm, which corresponds to the two protons on the acetonitrile moiety.

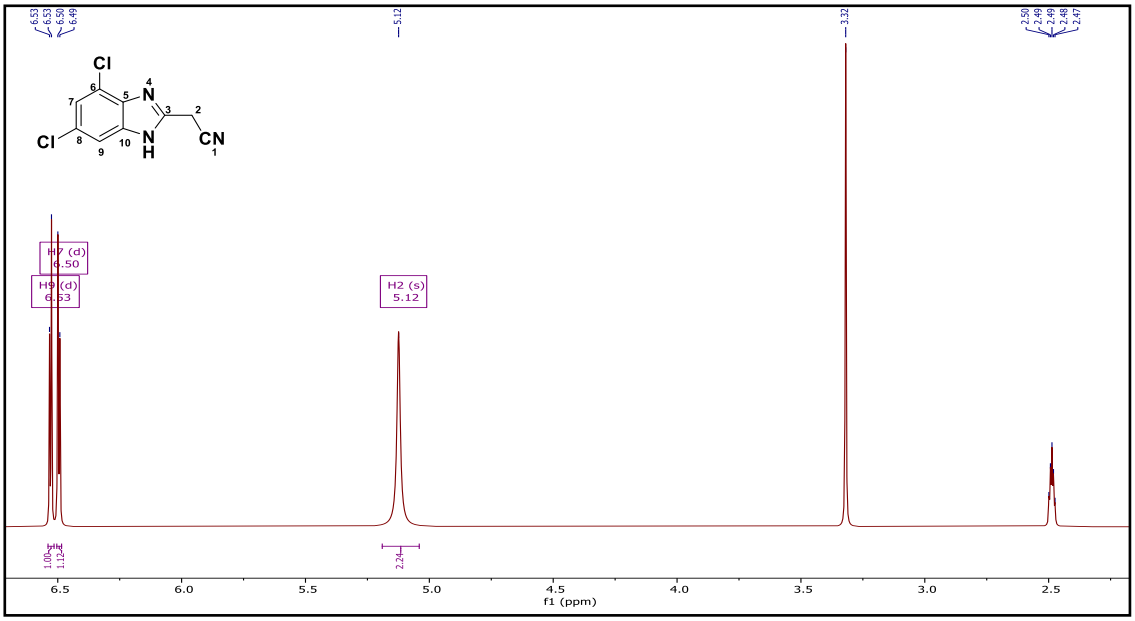

Figure 8.1. ^{1}H-nuclear magnetic resonance spectrum (NMR; 600 MHz, deuterated dimethyl sulfoxide, DMSO-d6) of the benzimidazole intermediate **g/h**

8.7.1.2. Spectroscopic Analysis of the Hydroxyl Intermediate q

The ^{1}H-NMR spectrum (600 MHz, DMSO-*d6*) of compound **q** shows the presence of two doublets occurring at 8.50 and 7.49 ppm, corresponding to H-6 and H-8, respectively (Figure 5). The splitting pattern of the four protons H-13 and H-15 (7.83 ppm) and H-12 and H-16 (7.87 ppm) of the para-substituted benzene are seen as two doublets, corresponding to two protons each according to the symmetry of the moiety. The proton H-2 appears as a singlet occurring at 5.60 ppm, corresponding to one proton.

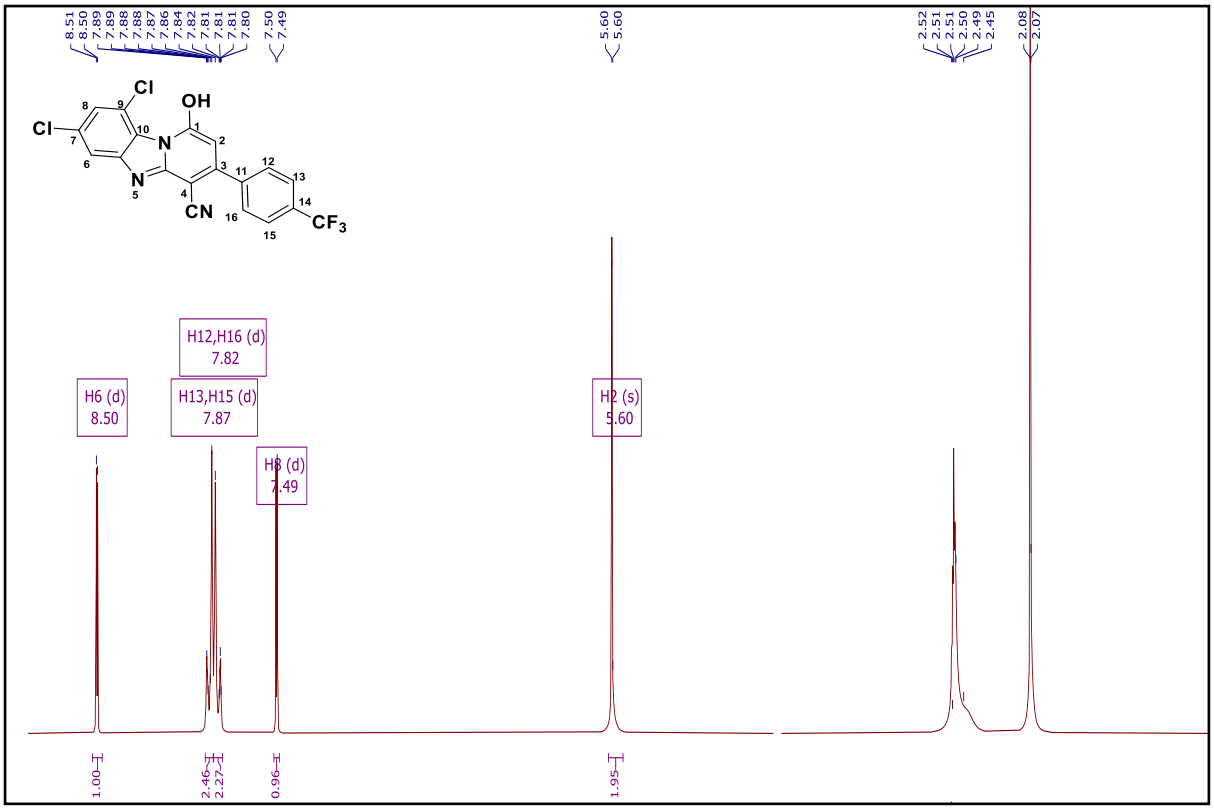

Figure 8.2. [1]H-nuclear magnetic resonance spectrum (NMR; 600 MHz, DMSO-d6) of the hydroxy intermediate **q**

8.7.1.3. Spectroscopic Analysis of the Hydroxyl Intermediate u

The [1]H-NMR spectrum (600 MHz, DMSO-*d6*) of **u** confirmed the formation of the chlorinated intermediate (Figure 3.3). All seven aromatic protons were observed in the region 7.63-8.65 ppm. The shifts in this spectrum are downfield compared to those observed for the hydroxy intermediate (Figure 3.2). This shift is attributed to the electron-withdrawing effect of the chloro group, which deshields the protons more than the hydroxy group.

Figure 8.3. [1]H-nuclear magnetic resonance spectrum (NMR; 600 MHz DMSO-d_6) of the chlorinated intermediate **u**

8.7.2. [1]H-NMR Characterization of Relevant Intermediates (DM253)

8.7.2.1 Spectroscopic Analysis of Intermediate 1

1H-NMR further confirms the formation of intermediate **1** by the disappearance of the hydroxy proton singlet at 5.16 ppm.

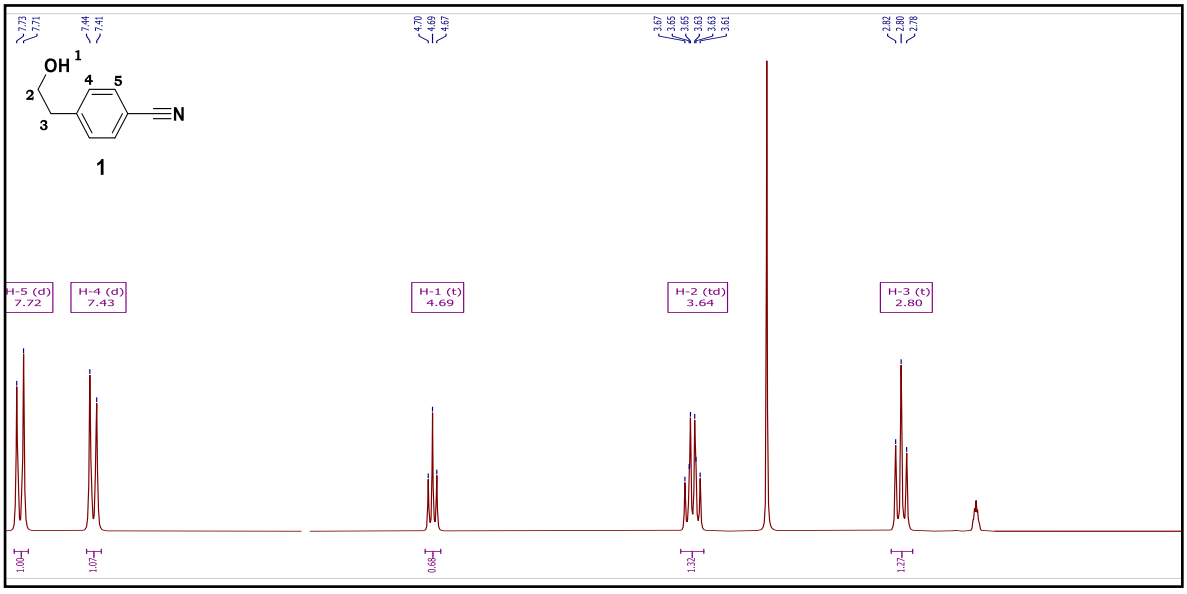

Figure 8.4. [1]H-nuclear magnetic resonance spectrum (NMR; 600 MHz, DMSO-d6) of the hydroxy intermediate **1**

8.7.2.2 Spectroscopic Analysis of Intermediate 3

The formation of intermediate **3** was confirmed by the loss of amidoxime amino (NH_2) and hydroxy (OH) proton signals and the appearance of a singlet downfield (δ = 9.24 ppm), integrating for one proton using ^{1}H NMR.

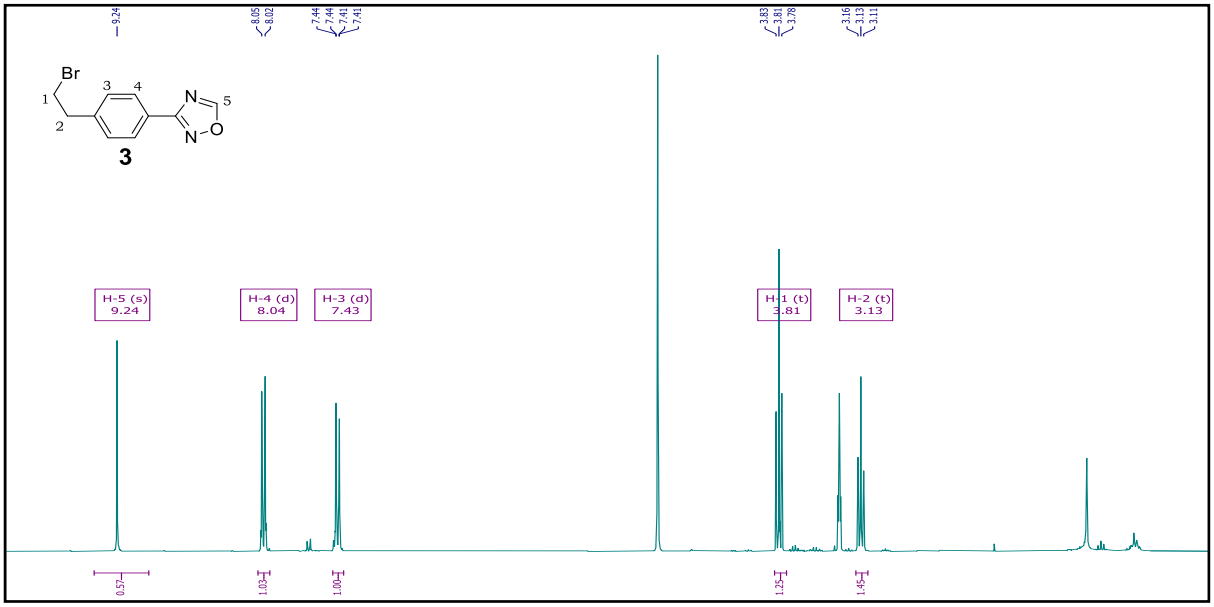

Figure 8.5. ^{1}H-nuclear magnetic resonance spectrum (NMR; 600 MHz, DMSO-d6) of the hydroxy intermediate **3**

8.7.2.3 Spectroscopic Analysis of Intermediate 4

The disappearance of the singlet signal upfield in ^{1}H-NMR, accounting for 9 protons, confirmed the successful N-Boc deprotection. (Figure 8.6)

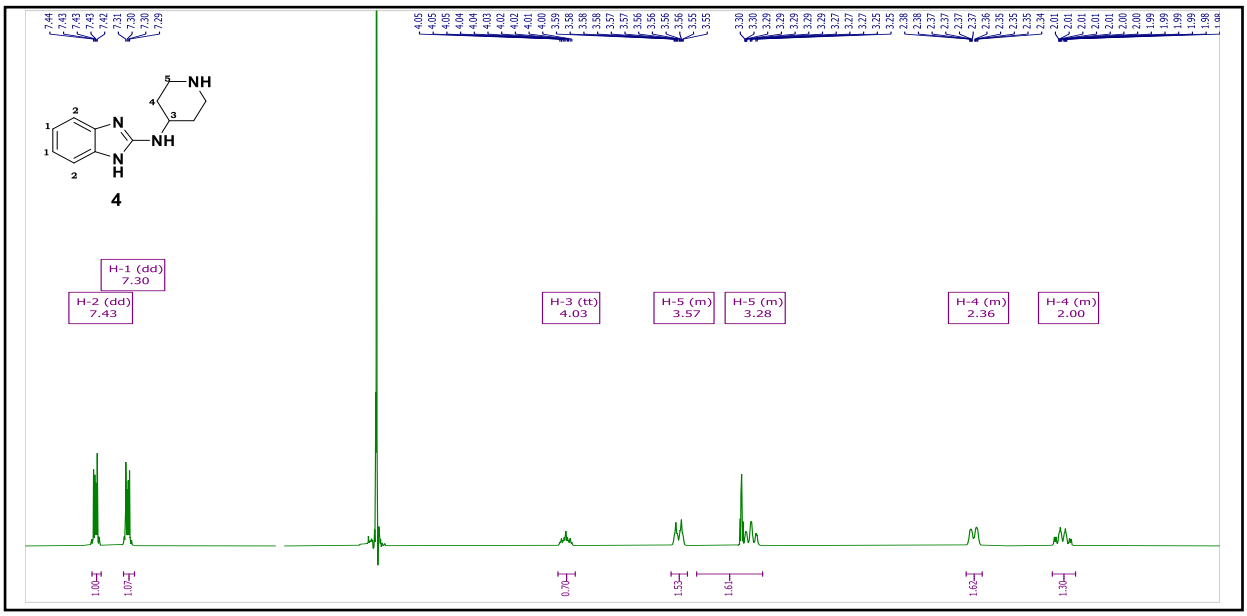

Figure 8.6. [1]H-nuclear magnetic resonance spectrum (NMR; 600 MHz, DMSO-d6) of intermediate **5**

8.7.3. [1]H-NMR Characterization of Relevant Intermediates (KP68-NBD)

8.7.3.1 Spectroscopic Analysis of Intermediate 19

The [1]H-NMR spectrum of **19** is shown in Figure 8.7. A new singlet corresponding to nine protons occurring at 1.2 ppm confirms the introduction of the *t-butyl* group of Boc. The aromatic region of the spectrum remains unchanged as there was no substitution in the aromatic region of **KP68**. Two new triplets corresponding to H-21 and H-22 are observed in the aliphatic region, corresponding to two protons each.

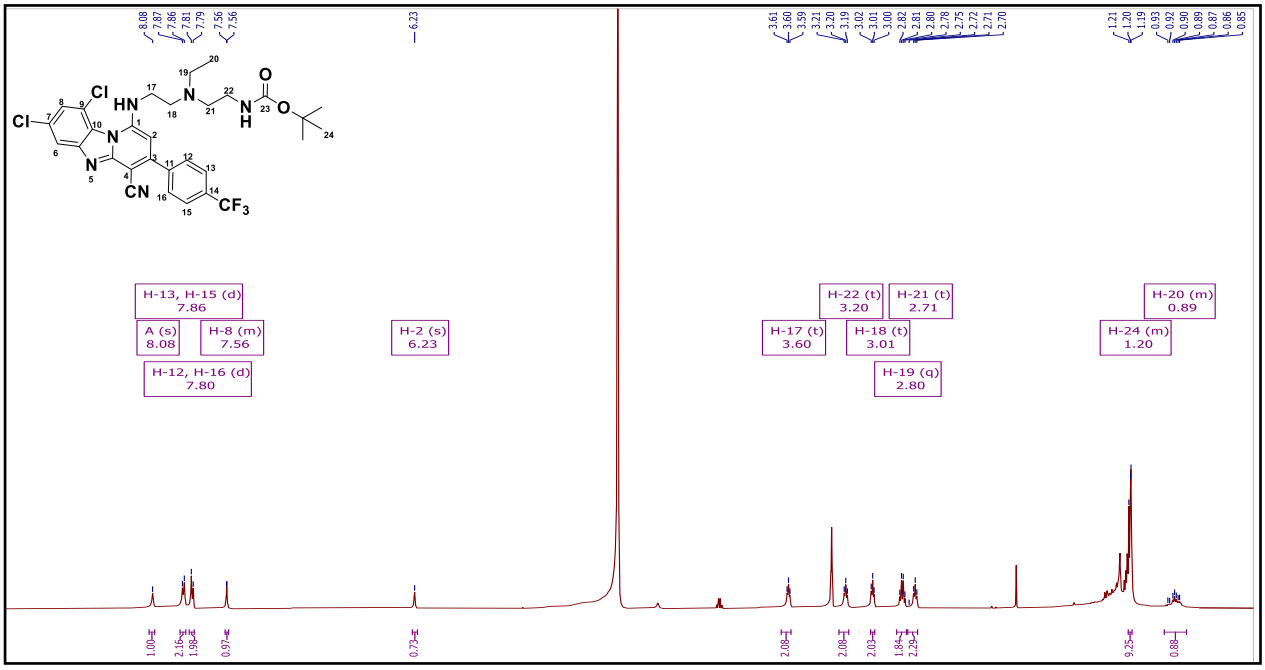

Figure 8.7. [1]H-nuclear magnetic resonance spectrum (NMR; 600 MHz, DMSO-d6) of intermediate **19**

8.7.3.2 Spectroscopic Analysis of Intermediate 20

The [1]H-NMR spectrum (600 MHz DMSO-*d6*) of intermediate **20** is shown in Figure 8.8. The disappearance of the singlet at 1.2 ppm corresponding to the nine protons of the t-butyl group of Boc suggests the success of the Boc deprotection.

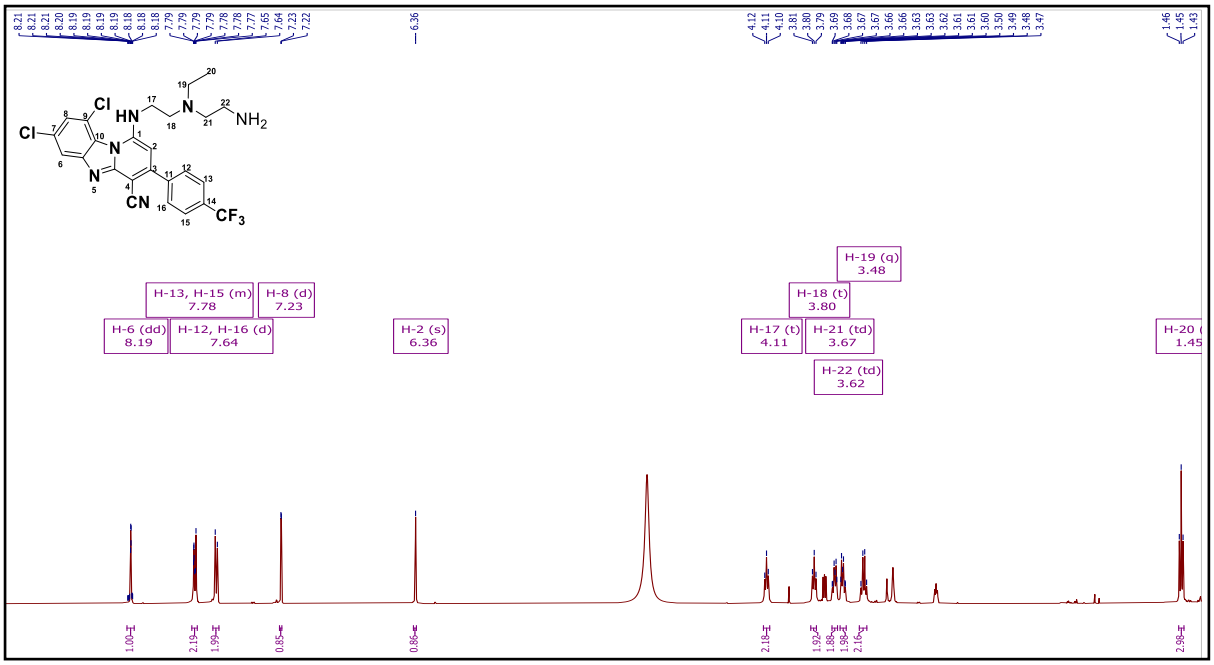

Figure 8.8. [1]H-nuclear magnetic resonance spectrum (NMR; 600 MHz, DMSO-d6) of intermediate **19.**

8.7.4. [1]H-NMR Characterization of Relevant Intermediates (DM253 -NBD)

8.7.4.1 Spectroscopic Analysis of Intermediate 20

The [1]H-NMR spectrum (600 MHz DMSO-*d6*) of intermediate **4** shown in Figure 8.9 reveals the appearance of the characteristic singlet at 1.37 ppm corresponding to the nine protons of the t-butyl group of Boc and the appearance of two quartets integrating for two protons each confirms the successful formation of intermediate **4.** Following the S_NAR reaction, the nitro group is reduced under H_2/Pd conditions to yield **5.** Further, intermediate **1** is reacted with **5** through a dicyclohexylcarbodiimide (DCC) cyclocondensation to yield **6**. The [1]H-NMR spectrum of intermediate **6** reveals the appearance of the diagnostic two singlets corresponding to 9 protons, each con the formation of **6.**

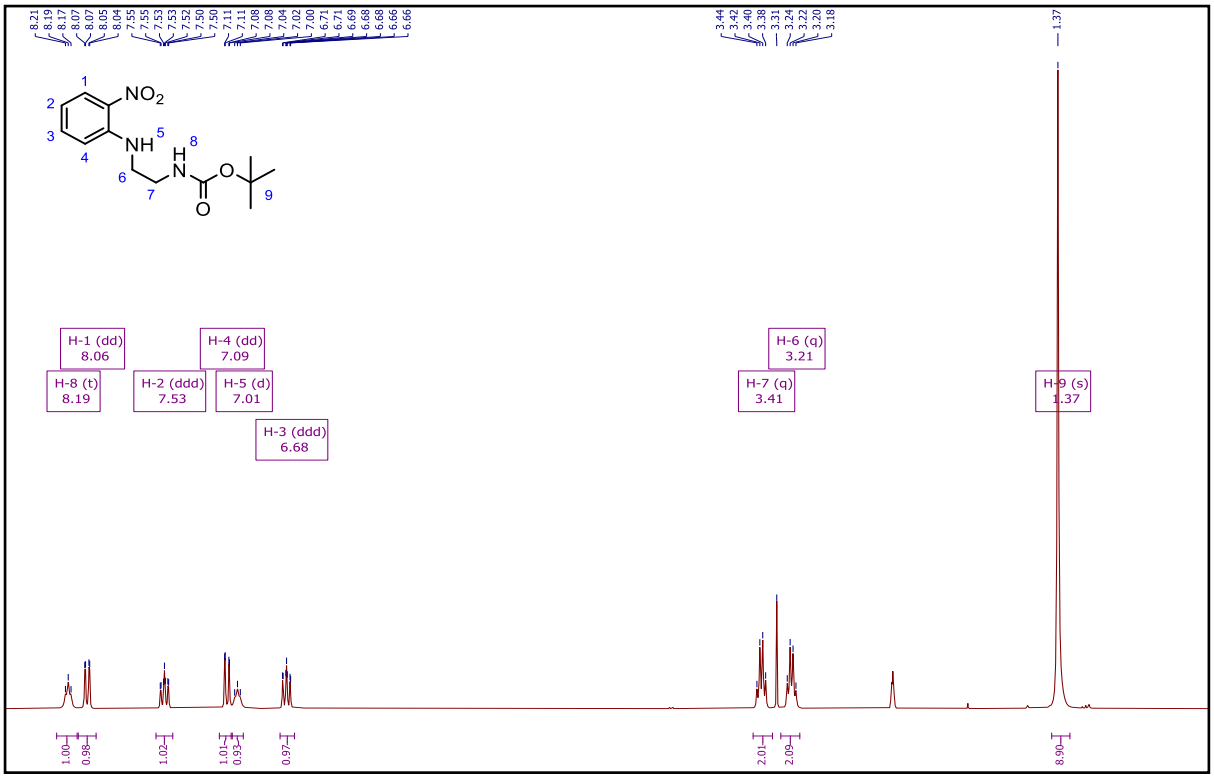

Figure 8.9. [1]H-nuclear magnetic resonance spectrum (NMR; 600 MHz, DMSO-d6) of intermediate **4**

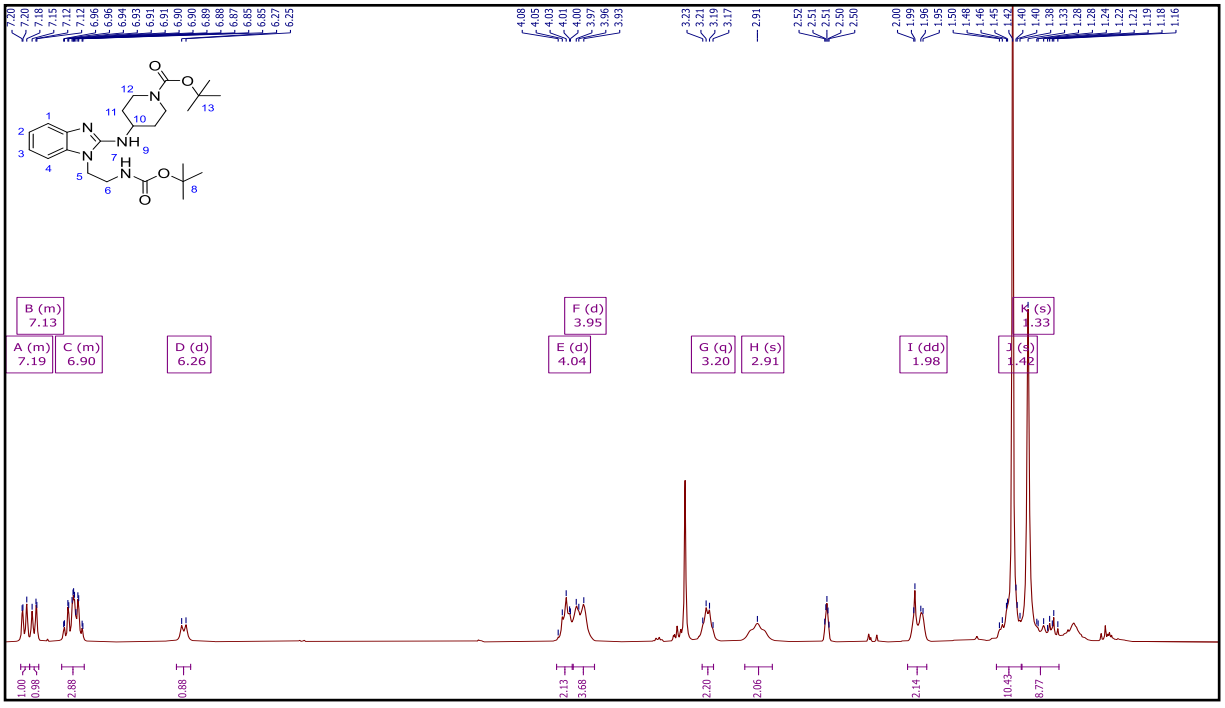

Figure 8.10. [1]H-nuclear magnetic resonance spectrum (NMR; 600 MHz, DMSO-d6) of intermediate **6**